
The function of IQD-KLCR modules in macromolecular complex assembly

DISSERTATION

ZUR ERLANGUNG DES

DOKTORGRADES DER

NATURWISSENSCHAFTEN (DR. RER. NAT.)

DER NATURWISSENSCHAFTLICHEN FAKULTÄT I

"BIOWISSENSCHAFTEN"

DER MARTIN-LUTHER-UNIVERSITÄT HALLE-WITTENBERG

VORGELEGT VON

HERR MALTE KÖLLING

GEB. AM 07.07.1993 IN ITZEHOE

1. Gutachter: Prof. Dr. Steffen Abel
2. Gutachter: Prof. Dr. Ingo Heilmann
3. Gutachter: Prof. Dr. Wayne Snedden

Datum der Verteidigung: 01.03.2023

EIDESSTATTLICHE ERKLÄRUNG

Hiermit versichere ich, **Malte Kölling**, die vorgelegte Dissertation mit dem Titel

"The function of IQD-KLCR modules in macromolecular complex assembly"

selbstständig und ausschließlich unter Zuhilfenahme der angegebenen Quellen und Hilfsmittel angefertigt zu haben. Daten, die aus der Arbeit Dritter stammen, sind als solche gekennzeichnet und wurden entweder unter meiner Betreuung oder in Rücksprache mit mir und auf Basis von mir zur Verfügung gestellter Materialien produziert. Stellen, an denen sinngemäß der Inhalt bereits publizierten Materials wiedergegeben wird, sind entsprechend gekennzeichnet und die jeweilige Referenz aufgeführt.

Halle (Saale), 18.05.2022

ACKNOWLEDGEMENTS

My deepest gratitude goes to Dr. Katharina Bürstenbinder for supervising my thesis, for providing constant, insightful and constructive feedback, helping me stay positive even in the face of less-than-optimal circumstances, and fanning my passion for science.

Furthermore, I am thankful for my colleagues Sandra Klemm, Gina Stamm, Jonas Buhl, Dr. Pradeep Dahiya, and Sven Papsdorf for offering their opinions and assistance, and for contributing to a welcoming and supportive working environment. Additional thanks go to my former students Jacqueline Patzsch and Mariyam Gaysaeva for contributing some of the data presented and discussed in this thesis, and my former colleague Dr. Michael Niemeyer for teaching me most of what I know about protein biochemistry. I would also like to thank Prof. Andrea Sinz, Dr. Christian Ihling, Dr. Christian Tüting, Dr. Susanne Matschi, and Carsten Proksch for their assistance with mass spectrometric identification of proteins, analysis of cross-linking experiments, and *in silico* protein model generation.

Moreover, I would like to thank Prof. Steffen Abel for giving me the opportunity to produce this thesis in the department Molecular Signal Processing at the Leibniz Institute of Plant Biochemistry, and my mentors, Prof. Edgar Peiter and Dr. Justin Lee, for their constructive feedback and sound advice.

Last but not least, I want to thank my friends, my family, and my partner, Virve Fischer, for constant moral support and an open ear and shoulder to lean on, whenever necessary. Without them, this thesis would not have been possible.

Contents

List of Figures	ix
List of Tables	xiii
Abbreviations	xiv
Zusammenfassung/Abstract	1
1 Introduction	3
1.1 Scaffold proteins	3
1.1.1 Types of scaffold proteins	6
1.1.2 Biochemical and structural properties of ordered scaffold proteins	6
1.1.3 Disordered scaffold proteins confer binding flexibility	9
1.2 The plant cytoskeleton	11
1.2.1 The actin cytoskeleton	14
1.2.2 Regulation of the microtubule network	15
1.3 The KLCR-IQD module - a potential hub for macromolecular complex assembly	18
1.3.1 KINESIN LIGHT CHAIN-RELATED proteins are a central adaptor for protein-protein interactions	18
1.3.2 IQ67 DOMAIN proteins comprise disordered scaffolds	20
1.3.3 The NETWORKED protein family links KLCR-IQD modules to the actin cytoskeleton	23
1.4 Calcium signalling at the microtubule cytoskeleton	23
1.4.1 Calmodulins and Calmodulin-like proteins	26
1.5 Regulation of the cytoskeleton by calcium and scaffold proteins	28
1.6 Goals of this thesis	29
2 Results	31
2.1 Biochemical characterisation of KLCRs and their binding partners	31
2.1.1 <i>In silico</i> assessment of KLCRs	31
2.1.2 Expression and purification of KLCRs for <i>in vitro</i> characterisation	35
2.1.3 KLCRs may form dimers	36
2.2 KLCR-CaM interactions	40
2.2.1 Dynamics of KLCR1-CaM interactions	43

2.2.2	Fine-mapping of KLCR-CaM interactions	46
2.2.3	Cross-linking of KLCRs and CaMs	51
2.2.4	<i>In silico</i> model of the KLCR1-CaM2-complex	56
2.3	Determinants of the subcellular localisation of KLCRs	61
2.4	KLCR-IQD interactions	66
2.4.1	<i>In silico</i> assessment of IQD2	66
2.4.2	Subcellular localisation of IQD2	69
2.4.3	Binding mode of KLCRs and IQD2	73
2.4.4	Subcellular localisation of IQD2-KLCR complexes	78
2.5	IQD2-CaM interactions	80
2.5.1	Subcellular localisation of IQD2-CaM complexes	84
2.6	Ternary interactions between KLCR1, IQD2, and CaMs	86
2.7	KLCR-NET3 interactions	92
2.7.1	<i>In silico</i> assessment of NET3C	92
2.7.2	Interaction of NET3s with KLCRs	94
2.7.3	CaM-mediated regulation of NET3s	95
3	Discussion	97
3.1	TPR-mediated homo-interaction of KLCRs	97
3.2	Adaptors, scaffolds, and dockers	100
3.2.1	IQDs but not KLCRs associate directly with microtubules	100
3.2.2	IQD2 binds KLCRs and recruits them to the microtubule cytoskeleton	102
3.3	CaM-mediated calcium-signalling as a regulatory mechanism of the KLCR-IQD core module	104
3.3.1	Regulation of KLCRs by CaM-mediated calcium-signalling	105
3.3.2	IQD2 as a mediator of CaM-signalling	109
3.3.3	Calcium-signalling as a regulator of the subcellular localisation of NET3s	110
3.3.4	Assembly of calcium-signalling modules by ternary interactions between KLCRs, IQD2, and apo-CaM	111
3.4	Assembly and regulation of KLCR-IQD-mediated complexes by the interplay between docking, scaffolding, and cellular signalling	114
4	Materials and Methods	117
4.1	Equipment and consumables	117
4.1.1	Chromatography	118

4.1.2	Chemicals & software	119
4.2	Buffers and media	120
4.2.1	Bacterial strains, cell cultures, and plant material	123
4.3	Primers	123
4.4	Cloning	125
4.4.1	Vectors	125
4.4.2	PCR & Protein fragment generation	126
4.4.3	Restriction cloning	127
4.4.4	Gateway cloning	128
4.4.5	Circular Polymerase Extension Cloning	129
4.4.6	Generation of chemically competent <i>E. coli</i>	129
4.4.7	Heat-shock mediated transformation of <i>E. coli</i>	130
4.4.8	Generation of chemically competent <i>A. tumefaciens</i>	130
4.4.9	Heat-shock mediated transformation of <i>A. tumefaciens</i>	130
4.5	Protein production	131
4.5.1	Protein expression	131
4.5.2	Native protein purification	131
4.5.3	Chromatography	132
4.5.4	Denaturing polyacrylamide gel electrophoresis (PAGE)	133
4.5.5	Semi-dry Western blotting	134
4.5.6	Protein identification via LC/MS/MS	134
4.6	Biochemical assays	135
4.6.1	<i>In vitro</i> pulldown assays	135
4.6.2	<i>In vivo</i> pulldowns	136
4.6.3	Microscale Thermophoresis (MST)	137
4.6.4	Chemical cross-linking	137
4.6.5	LC/MS/MS analysis of cross-linking data	138
4.6.6	<i>In silico</i> modelling of KLCR1-CaM2 complexes	139
4.6.7	Microtubule spin-down assays	139
4.6.8	GAL4 Yeast-two-hybrid (Y2H) experiments	140
4.7	Microscopy	140
4.7.1	Transient transformation of <i>N. benthamiana</i>	140
4.7.2	Confocal laser scanning microscopy (LSM)	141

5 References

A Appendix	172
B Publications	208
C Curriculum vitae	209

List of Figures

1	Types of scaffold proteins.	7
2	The plant cytoskeleton.	12
3	The plant cytoskeleton during mitosis.	13
4	Schematic depiction of the PINK complex.	19
5	The IQ67 domain family in <i>A. thaliana</i>	22
6	Calcium signalling in plant cells.	25
7	3D models of Calmodulin.	26
8	<i>In silico</i> analysis of KLCR1.	33
9	<i>In silico</i> analysis of the charge distribution in KLCR1.	34
10	Purification of His-KLCR1.	37
11	In-depth analysis of KLCR1 regarding homo-dimerisation.	39
12	BiFC of KLCR1 and KLCR2 in <i>N. benthamiana</i> leaves.	41
13	CaM-pulldown of His-KLCRs.	42
14	GST-pulldown of His-KLCR1 with GST-CaMs.	42
15	BiFC of KLCR1 with CaM2 or CaM7 in <i>N. benthamiana</i> leaves.	44
16	Purification of His-CaM2.	45
17	MST affinity measurements between His-KLCR1 and His-CaM2, -CaM4, and -CaM7.	47
18	CaM-pulldowns of truncations of KLCR1.	48
19	CaM-pulldowns of truncations of KLCR2.	50
20	Cross-linking of KLCR1 and KLCR2 with CaM2 or CaM4.	52
21	Generation of tag-free KLCR1.	54
22	Cross-linking of tag-free KLCR1 and CaM2.	55
23	Cross-linking results of tag-free KLCR1 and CaM2.	56
24	Single AlphaFold models of CaM2 and KLCR1 used in MD simulations.	57
25	Models of KLCR1-CaM2 complexes generated by HADDOCK or AlphaFold mul- timer.	60
26	Subcellular localisation of GFP-KLCR1 and its truncations.	63
27	Microtubule spin-down of KLCR1, CaM2, and CaM7.	64
28	Microtubule spin-down concentration curve of KLCR1.	65
29	<i>In silico</i> analysis of IQD2.	67
30	<i>In silico</i> analysis of the charge distribution in IQD2.	69
31	Subcellular localisation of GFP-IQD2.	71

32	Microtubule spin-down of His-SUMO-IQD2 together with GH-CaM2.	72
33	GST-pulldown of His-IQD2 with GST-KLCR1.	73
34	Interaction of IQD2 truncations with KLCRs in yeast-two-hybrid experiments. .	75
35	His-pulldown of GST-KLCR1 with HS-IQD2 and its truncations.	76
36	His-pulldown of GST-KLCR1 truncations with HS-IQD2.	77
37	Co-localisation of IQD2 and KLCR1 in <i>N. benthamiana</i> leaves.	79
38	Subcellular localisation of KLCR-dimers co-expressed with CFP-IQD2 in <i>N. benthamiana</i> leaves.	81
39	Fine-mapping of IQD2-CaM interactions.	82
40	His-pulldowns of GST-CaMs with HS-IQD2.	83
41	Co-localisation of IQD2 and CaM2 in <i>N. benthamiana</i> leaves.	85
42	Co-interaction of IQD2 with KLCRs and CaM.	87
43	Apo-CaM pulldown assays with IQD2 truncations and KLCR1.	89
44	Subcellular localisation of KLCR1 and CaMs co-expressed with CFP-IQD2 in <i>N. benthamiana</i> leaves.	91
45	<i>In silico</i> analysis of NET3C.	93
46	Y2H experiment and <i>in vitro</i> GST-pulldowns showing interaction of NET3s with KLCRs.	94
47	Y2H experiment and <i>in vitro</i> CaM-pulldowns showing interaction of NET3s with CaM.	96
48	Putative binding regions for interaction partners in KLCR1.	108
49	Putative binding regions for interaction partners in IQD2.	111
50	Modes of IQD-KLCR apo-CaM interaction.	113
51	Configurations of KLCR-IQD complex components on the cytoskeleton.	115
A.1	Alignment of KLCR1, KLCR2, and KLCR3.	172
A.2	Gene model of KLCR1 and its splice variant.	173
A.3	<i>In silico</i> analysis of KLCR2.	173
A.4	<i>In silico</i> analysis of KLCR3.	174
A.5	Analysis of His-KLCR2 regarding homo-dimerisation.	175
A.6	GST-pulldown of His-KLCR1 with GST-KLCR1.	176
A.7	Uncropped western blots from Fig. 11.	176
A.8	BiFC of TRM1 and TON1 control in <i>N. benthamiana</i> leaves.	177
A.9	Alignment of all <i>A. thaliana</i> CaM isoforms.	178
A.10	Charge plots of <i>BtCaM</i> , <i>AtCaM2</i> , and <i>AtCaM7</i>	179

A.11 Co-IP of KLCR1 with CaM2 from <i>N. benthamiana</i> leaves.	180
A.12 Purification of His-CaM4.	181
A.13 Purification of His-CaM7.	182
A.14 CaM-binding score of KLCR1.	183
A.15 CaM-binding score of KLCR2.	183
A.16 Cross-linking of KLCR1 and KLCR2.	184
A.17 Generation of tag-free CaM2.	185
A.18 Mass spectrometric identification of tag-free KLCR1 and CaM2.	186
A.19 Cross-linking results of tag-free KLCR1 and CaM2 as bar plots.	187
A.20 Quality scores of the Alphafold generated models of CaM2 and KLCR1.	188
A.21 Alphafold multimer models of KLCR1-CaM2 complexes.	189
A.22 Energy variations in HADDOCK MD simulations of KLCR1-CaM2 complexes. .	190
A.23 HADDOCK scores of KLCR1-CaM2 models generated in the presence of 1 mM CaCl ₂	191
A.24 HADDOCK scores of KLCR1-CaM2 models generated in the absence of added CaCl ₂	192
A.25 Sub-cellular localisation of GFP-KLCR1 and its truncations.	193
A.26 Sub-cellular localisation of GFP-KLCR2 and its truncations.	194
A.27 Purification of His-SUMO-IQD2.	194
A.28 His-pulldown of GST-KLCR1 with HS-IQD2 and its truncations under low salt conditions.	195
A.29 Phospho-sites in IQD2 and the KLCRs annotated in the PhosPhAt database. .	195
A.30 Y2H experiment showing interaction of IQD2 truncations with KLCR1 truncations.	196
A.31 Co-localisation of IQD2 and KLCR2 in <i>N. benthamiana</i> leaves.	197
A.32 Co-localisation of IQD2 and KLCR3 in <i>N. benthamiana</i> leaves.	198
A.33 Co-localisation of IQD2 ₉₈₋₃₂₇ and all KLCRs in <i>N. benthamiana</i> leaves.	199
A.34 Co-localisation of IQD2 and KLCR1 truncations in <i>N. benthamiana</i> leaves. . .	200
A.35 Co-localisation of IQD2 and KLCR1 truncations in <i>N. benthamiana</i> leaves. . .	201
A.36 CaM-binding score of IQD2.	202
A.37 Co-localisation of IQD2 and CaM4 in <i>N. benthamiana</i> leaves.	203
A.38 Co-localisation of IQD2 and CaM7 in <i>N. benthamiana</i> leaves.	204
A.39 Concentration dependency of the co-interaction of IQD2 with KLCRs and CaM.	205
A.40 Fine-mapping of IQD2-KLCR1-CaM interactions.	205
A.41 Pulldowns with IQD2 and KLCR1 in the presence of 1 M NaCl.	206

A.42 CaM-binding score of NET3A and NET3C. 207

List of Tables

2	KLCR expression constructs used in this thesis.	36
3	Equipment	117
4	Resins	118
5	ÄKTApure columns	118
6	Standards, kits, and specialised consumables	119
7	Buffers – protein work and purifications	120
8	Buffers – general utility	121
9	Buffers – MS/MS analysis	122
10	Media	122
11	List of primers used in this thesis. Non-gene specific overhangs are marked as <i>italic</i>	123
12	Vectors used in this thesis.	125
13	Protein constructs	126
14	Phusion PCR mix and program for fragment generation	126
15	Restriction digest of IQD2 constructs for cloning	127
16	Restriction digest	127
17	Ligation setup	128
18	BP-reaction	128
19	LR-reaction	129
20	CPEC PCR	129
21	Expression constructs and expression conditions	131
22	Recipe – SDS-PAGEs	133
23	Antibodies	134
24	MST labelling results	137

Abbreviations

35S	Cauliflower Mosaic Virus 35S Promoter
3-AT	3-Amino-1,2,4-Triazole
<i>A. thaliana</i>	<i>Arabidopsis thaliana</i>
ABP	Actin Binding Protein
ACA	Autoinhibited Ca ²⁺ -ATPase
ACN	Acetonitrile
ADP	Adenosine Diphosphate
AKAP	A-Kinase Anchoring Protein
Ank	Ankyrin
ATP	Adenosine Triphosphate
AUX/IAA	Auxin/Indole-3-Acetic Acid
BiFC	Bimolecular Fluorescence Complementation
BIN2	Brassinosteroid Insensitive 2
BSA	Bovine Serum Albumin
Cα_{avg}	Average C α Distance
Ca²⁺	Calcium Ions
CaM	Calmodulin
cAMP	Cyclic Adenosine Monophosphate
CAX	Ca ²⁺ -exchanger
CBB	Coomassie Brilliant Blue
CBL	Calcineurin-B Like
CdC16	Cell division Cycle 16
CDK	Cyclin-Dependent Kinase
CDPK	Ca ²⁺ -Dependent Protein Kinase
CFP	Cyan Fluorescent Protein
CIPK	CBL Interacting Protein Kinase
CLASP	Cytoplasmic Linker Associated Protein
CML	CaM-Like Proteins
CMU	CELLULOSE MICROTUBULE UNCOUPLING
CNGC	Cyclic Nucleotide Gated Channel
co-IP	Co-Immunoprecipitation
CTPR	Consensus TPR Protein

DDO	Double Drop-Out
DNA	Desoxyribonucleic Acid
DOL	Degree Of Labeling
DS	Desolvation
DUF4005	Domain of Unknown Function 4005
<i>E. coli</i>	<i>Escherichia coli</i>
ECA	ER-type Ca ²⁺ -ATPase
EDTA	Ethylenediaminetetraacetic Acid
EGTA	Ethylene Glycol-bis(β -aminoethyl ether)-N,N,N',N'-Tetraacetic Acid
EF3	Elongation Factor 3
EM	Electron Microscope/Microscopy
EPCS	ER-PM Contact Sites
ER	Endoplasmatic Reticulum
ES	Electrostatic
F-actin	Fibrous Actin
FPLC	Fast Protein Liquid Chromatography
FRA1	FRAGILE FIBER 1
FtsA	Filamentous Temperature Sensitive A
G-actin	Globular Actin
g-force	Gravitational force
GAI	Gibberellic Acid Insensitive
GDP	Guanosine Diphosphate
GFP	Green Fluorescent Protein
GLR	Glutamate Receptor-Like channel
GRAS	GAI, RGA And SCR
GSH	Glutathione
GSK3	Glycogen Synthase Kinase 3
GST	GSH S-Transferase
GTB	General Tubulin Buffer
GTP	Guanosine Triphosphate
HEAT	Huntingtin, EF3, PP2A, TOR1
HMA1	P1-ATPase
HOP	HSP Organising Protein
HSP	Heat Shock Protein


IDP	Intrinsically Disordered Protein
IDR	Intrinsically Disordered Region
IMAC	Immobilised Metal Affinity Chromatography
IpgC	Invasion plasmid gene C
IQD	IQ67 DOMAIN Protein
JIP	JNK Interacting Protein
JNK	c-Jun N-terminal Kinase
KHC	Kinesin Heavy Chain
KLC	Kinesin Light Chain
KLCR	KINESIN LIGHT CHAIN RELATED
LC/MS/MS	Liquid Chromatography/Mass Spectrometry/Mass Spectrometry
LEA	Late Embryogenesis Abundant
LRR	Leucine Rich Repeat
LSM	Laser Scanning Microscope/Microscopy
MAP	Microtubule Associated Protein
MCA	Mechanosensitive channel
MCUC	Mitochondrial Ca ²⁺ -Uniporter Complex
MD	Molecular dynamic
MORF	Molecular Recognition Feature
MPK	MAP Kinase
MSD	Major Sperm Domain
MST	Microscale Thermophoresis
MT	Microtubule(s)
MTB	Microtubule Binding region
<i>N. benthamiana</i>	<i>Nicotiana benthamiana</i>
NAB	NETWORKED ACTIN BINDING
NET	NETWORKED Protein
NTA	Nitrilotriacetic Acid
OSCA	Reduced HyperOSmolality induced CA ²⁺ increase
PAE	Predicted Alignment Error
PAGE	Polyacrylamide Gel Electrophoresis
PBS	Phosphate-buffered Saline
PHGAP	PLECKSTRIN HOMOLOGY GTPase ACTIVATING Protein
PIInsP	Phosphatidylinositol Phosphate

PKA	Protein Kinase A
PKC	Protein Kinase C
PM	Plasma Membrane
PMT	Photomultiplier Tube
POI	Protein Of Interest
POK	Phragmoplast Orienting Kinesin
PP2A	Protein Phosphatase 2 A
PPB	Pre-Prophase Band
PPR	Pentatricopeptide Repeat
PTM	Post-translational Modification
QDO	Quadruple Drop-Out
RACK1	Receptor for Activated C Kinase 1
RCD1	Radical Induced Cell Death 1
RFP	Red Fluorescent Protein
RGA	Repressor of GAI
RNA	Ribonucleic Acid
ROS	Reactive Oxygen Species
RT	Room Temperature
<i>S. cerevisiae</i>	<i>Saccharomyces cerevisiae</i>
<i>S. pombe</i>	<i>Schizosaccharomyces pombe</i>
SCR	Scarecrow
SDS	Sodium Dodecyl Sulfate
SEC	Size Exclusion Chromatography
SGT1	Suppressor of G2 allele of <i>skp1</i>
SUMO	Small Ubiquitin-like Modifier
TBS	Tris-buffered Saline
TDO	Triple Drop-Out
TF	Transcription Factor
TIR1	TRANSPORT INHIBITOR RESPONSE 1
TON1	TONNEAU 1
TPC	Two-Pore Channel
TPR	Tetratricopeptide Repeat
TRM1	TON1 Recruiting Motif 1
Ub10	Ubiquitin 10 Promoter

UPS	Ubiquitin Proteasome System
VAMP	Vesicle Associated Membrane Protein
VAP27	(VAMP) Associated Protein 27
VdW	Van der Waals
Y2H	Yeast Two Hybrid
YFP	Yellow Fluorescent Protein


BIOLOGY IS LARGELY SOLVED. DNA IS THE SOURCE CODE FOR OUR BODIES. NOW THAT GENE SEQUENCING IS EASY, WE JUST HAVE TO READ IT.

IT'S NOT JUST "SOURCE CODE." THERE'S A TON OF FEEDBACK AND EXTERNAL PROCESSING.

A stick figure with a hat and a bag is talking to a stick figure with a ponytail.

BUT EVEN IF IT WERE, DNA IS THE RESULT OF THE MOST AGGRESSIVE OPTIMIZATION PROCESS IN THE UNIVERSE, RUNNING IN PARALLEL AT EVERY LEVEL, IN EVERY LIVING THING, FOR FOUR BILLION YEARS.

IT'S STILL JUST CODE.


A stick figure with a hat is sitting at a desk with a chair, talking to a stick figure with a ponytail.

OK, TRY OPENING GOOGLE.COM AND CLICKING "VIEW SOURCE."

OK, I-... OH MY GOD.

THAT'S JUST A FEW YEARS OF OPTIMIZATION BY GOOGLE DEVS. DNA IS THOUSANDS OF TIMES LONGER AND WAY, WAY WORSE.

WOW, BIOLOGY IS IMPOSSIBLE.

A stick figure with a hat is sitting at a desk with a computer, talking to a stick figure with a ponytail.

xkcd 1605: DNA

Zusammenfassung

Pflanzenzellen befinden sich stets in der Situation, sich einer Vielzahl externer und interner Stimuli anpassen zu müssen. Das Zytoskelett und damit assoziierte Proteine spielen dabei essenzielle Rollen bei der Koordination des Zellinneren und der Aufrechterhaltung zellulärer Signalkaskaden und metabolischer Prozesse. Kürzlich wurde ein neuartiger Multiproteinkomplex in der Modellpflanze *Arabidopsis thaliana* identifiziert. Dieser besteht aus dem (VAMP)-assoziierten Protein 27-1 (VAP27-1), dem IQ67-Domänen Protein 2 (IQD2), NETWORKED 3C (NET3C) und KINESIN LIGHT CHAIN-RELATED 1 (KLCR1) und wird als PINK Komplex bezeichnet. Er verbindet das Aktin Zytoskelett, die Mikrotubuli, die Plasmamembran (PM) und das endoplasmatische Retikulum (ER) an ER-PM-Kontaktstellen. KLCR1 und IQD2 bilden das Kernmodul dieses Komplexes. Da weder IQD2, noch NET3C, noch KLCR1 über enzymatische Aktivität verfügen, handelt es sich bei diesem Komplex möglicherweise um einen Super-Hub aus Gerüstproteinen, der wesentlich im Pflanzenwachstum involviert ist. Zusätzlich wurden IQD2 und KLCR1 in der Vergangenheit als Interaktoren des Ca^{2+} -Sensors Calmodulin (CaM) identifiziert, sodass eine Regulation dieses Komplexes durch CaM-vermittelte Ca^{2+} -Signale plausibel erscheint. Diese Arbeit verfolgt das Ziel der Charakterisierung der Dynamik und Mechanismen hinter der Assemblierung von Proteinkomplexen aus der Perspektive von KLCR1 durch biochemische, zellbiologische und strukturelle Ansätze.

Die Charakterisierung KLCR1-IQD2 vermittelter Proteinkomplexe führte zur Entdeckung potenzieller KLCR1-Dimere, sowie der Fähigkeit von KLCR1 auch mit anderen KLCRs *in vitro* und *in vivo* Komplexe zu bilden. Darüber hinaus wurden die Interaktionsmodi von KLCR1 und KLCR2 mit CaM eingehend untersucht und ihre Bindestellen kartiert. Diese Ergebnisse deuten auf präferenzielle Interaktion bestimmter KLCRs mit bestimmten CaM-Isoformen hin. Auf Basis von cross-linking Experimenten wurde zudem das erste datenbasierte *in silico* Modell von KLCR-CaM-Komplexen generiert. Die Untersuchung binärer und trinärer Interaktionen zwischen KLCR1, IQD2 und CaM deutete auf eine wichtige Funktion von IQD2 bei der Rekrutierung von KLCRs und ihren Komplexen an Mikrotubuli und bei der Integration CaM-vermittelter Ca^{2+} -Signale zur Proteinkomplexbildung hin. Zu guter Letzt wiesen Experimente mit NET3C die direkte Interaktion mit KLCR1 und CaM nach und fügten eine weitere Ebene potenzieller Ca^{2+} -Regulation von KLCR1-IQD2 vermittelten Proteinkomplexen hinzu.

In Summe verschafft diese Arbeit einen umfassenden Einblick in die molekularen Mechanismen hinter der Bildung und Regulation von Proteinkomplexen. Sie dient zudem durch die Etablierung von Expressions- und Aufreinigungsprotokollen als Fundament für weitere strukturelle Analysen von KLCR-IQD-CaM Komplexen und den Transfer in pflanzliche Systeme.

Abstract

Plant cells are in a constant process of adaptation to a plethora of external and internal stimuli. The cytoskeleton and cytoskeleton-associated proteins play crucial roles in coordinating the cellular interior and ensuring the efficient flow of internal processes. Recent research has identified a novel multi-protein complex in the model plant *Arabidopsis thaliana* with proposed functions as a scaffold in cellular calcium signalling. This complex, consists of the (VAMP) ASSOCIATED PROTEIN 27-1 (VAP27-1), IQ67 DOMAIN protein 2 (IQD2), NETWORKED 3C (NET3C), and KINESIN LIGHT CHAIN-RELATED 1 (KLCR1), and was termed the PINK complex. It connects the actin cytoskeleton, the microtubule cytoskeleton, the plasma membrane (PM), and the endoplasmatic reticulum (ER) at ER-PM-contact-sites (EPCS). KLCR1 and IQD2 form the core module of this complex. Interestingly, neither IQD2, nor NET3C, nor KLCR1 have known enzymatic activities, suggesting that this complex may be a super-hub of scaffold- and adaptor-proteins with functions in plant growth and development. Furthermore, IQD2 and KLCR1 were previously known as interactors of the Ca^{2+} -sensor Calmodulin (CaM), suggesting regulation of the KLCR-IQD2 module by CaM-mediated Ca^{2+} -signalling. This thesis focused on elucidating the dynamics and mechanisms of core-module-mediated protein-complex formation from the viewpoint of KLCR1 by biochemical, cell biological, and structural biology approaches.

The characterisation of KLCR1-IQD2 mediated protein complexes uncovered dimerisation of KLCR1 with itself and other KLCR family members *in vitro* and *in vivo*. Furthermore, CaM-binding sites in KLCRs were mapped to the terminal regions of their TPR domain, and differential binding of KLCR1 to different CaM-isoforms was discovered. Cross-linking firmly placed CaM-binding in the C-terminus of KLCR1 and formed the basis for the generation of the first data-based *in silico* model of KLCR-CaM-complexes. The investigation of KLCR1-IQD2 binary and KLCR1-IQD2-CaM ternary interactions pointed toward a role for IQD2 in recruiting KLCRs and their complexes to microtubules and in integrating CaM-mediated Ca^{2+} -signalling to protein complex formation. Lastly, NET3s were found to physically interact with KLCR1, and CaM, adding an additional layer of possible Ca^{2+} -regulation to KLCR1-IQD2 modules.

This thesis provides comprehensive insights into the molecular mechanisms orchestrating the formation of multi-protein complexes and their regulation. It lays the foundation for further research into the structural determinants underlying KLCR-IQD-CaM complexes by establishing expression and purification protocols and experimental pipelines for structure elucidation of their interactions. These will allow transfer into plant systems to further understand the role of CaM-mediated Ca^{2+} -signalling at the PM-cytoskeleton-nexus.

1 Introduction

Cells form the basic unit of life. In multi-cellular organisms cells are specialised in different tissues and organs, fulfilling a plethora of essential functions. Internally, all eukaryotic cells are sub-divided into organelles, specialised compartments with a unique biochemical composition that enables functional specialisation [1]. Within these compartments as well as outside of them, eukaryotic cells require additional means of structuring their interior and maintain their cellular pathways. Prokaryotic cells (i.e. bacteria and archaea) do not possess organelles or compartments, but still efficiently maintain their cellular processes. Recent estimates place the abundance of proteins in living bacteria between 2 and 4 million protein molecules per μl cell volume [2]. While the same estimate assumes that number to be approx. three to ten times lower for yeast and animals, and probably even smaller for plants, those numbers are still staggering. The genome of the model plant *Arabidopsis thaliana* encodes for approx. 20,000 protein coding genes [3], many of which may give rise to multiple protein isoforms via alternative splicing. In this potential chaos, components of distinct signalling or metabolic pathways require specialised guidance to assemble efficiently. To add to this complexity, plant cells constantly need to adapt to external and internal stimuli to maintain a functioning organism [4].

The cytoskeleton and scaffold proteins are critical facilitators of intracellular order. The cytoskeleton is an intracellular structure that acts as an internal skeleton and provides stability to cells, mediates organelle positioning, confers contact between different membrane systems within a cell, and fulfils crucial roles in intracellular transport [5]. The assembly of functional units for efficient cellular signalling and metabolic flux is conferred by scaffold proteins that aid in the assembly of protein-complexes in the crowded environment of the cellular interior [6].

1.1 Scaffold proteins

Scaffold proteins are crucial contributors to intracellular organisation. The term "scaffold protein" has a number of different, and partially overlapping meanings, primarily referring to proteins that provide a structural scaffold to a cell or intercellular matrices, or to proteins that serve as assembly platforms for protein complexes. While the former usually includes components of the cytoskeleton, or related proteins, the latter are more diverse in terms of structure and function. This section focuses on scaffold proteins as modes of assembly for other proteins. Scaffold proteins as assembly platforms for other proteins were first discovered in *Saccharomyces cerevisiae*. The zinc-finger protein Ste5 was found to be essential for the formation of a multi-kinase complex comprised of several MAP kinases (MPKs) [7]. Since then, the number of

known scaffold proteins has increased greatly [8]. Current research classifies scaffold proteins into four main functional groups: Assembly platforms for components of signalling pathways, anchors/dockers that direct their interacting proteins to distinct subcellular sites, regulators of signal transduction or metabolic pathways, and isolators between different (signalling) pathways [9]. None of these functions exclude any of the others and multiple proteins belonging to more than one of these classes exist. Prominent examples of the first class are the previously mentioned Ste5 [7] and related proteins. Since the characterisation of multi-protein complexes *in vitro* poses a significant challenge, a plethora of work has been done on *in silico* simulations and mathematical models describing the regulation of scaffold protein complexes and possible effects of binding affinities and complex stoichiometry on their assembly, using Ste5-mediated complexes as a model system [10] [11]. Other examples of assembly platforms include the cullin-component of cullin-ring-ligases in the ubiquitin-proteasome-system (UPS). Cullins can bind a number of target-specific F-box proteins and E2-interactors, allowing for an intricately fine-tuned mode of specific protein ubiquitylation [12]. The A-kinase anchoring proteins (AKAPs) are prime examples for anchoring proteins that target the eponymous protein kinase A (PKA) to regions of cAMP production, therefore confining phosphorylation by PKAs to a small subset of target proteins by spatial limitation. Differential targeting of different splice variants of the same AKAP diversifies AKAP functions, as does feedback-regulation of AKAPs by phosphorylation via PKAs [13]. Isolating properties of scaffold proteins were shown for AKAP7 α and protein kinase C (PKC), whereby PKC tethered to AKAP7 α was less susceptible to competitive inhibition by the ATP-competitor Gö6976 or the substrate competitor PKC20-28 [14]. The concept of pathway regulation by scaffold proteins is mainly attributed to mathematical models of scaffold protein function, whereby scaffolds with different binding affinities to their partners either accelerate or decelerate intracellular signalling processes [10] [15]. Real-life examples of pathway regulation by scaffold proteins are reported in the c-Jun N-terminal kinase (JNK) signalling pathway. Four distinct JNK interacting proteins (JIPs) serve as scaffolds for components of the JNK pathway, conferring differential levels of activity to the resulting JNK signal cascade [16].

Since their initial discovery, scaffold proteins have been implicated in a number of signalling pathways and other cellular processes. They serve as putative intracellular hubs for kinase and ubiquitin signalling, and assembly platforms for the protein folding machinery [17]. Due to their central role in cellular signalling, they are targets for the engineering of novel pathway behaviours, and for the disruption of cellular signalling by invading pathogens [17]. In intracellular networks scaffold proteins are proposed to function as central coordinating hubs [18] [19].

Most commonly, scaffold proteins fulfil their function through enforced proximity of their binding partners, or through conformational fine-tuning, e.g. by activating a bound enzyme, or exposing an interaction surface for modification [17] [20]. A key function of scaffold proteins is the integration of different signalling pathways by anchoring their components to the same subcellular site or acting as adaptors between them [21]. A degree of modularity observed in many scaffold proteins confers a certain freedom to modify pathways or to form new integration hubs through the evolution of existing scaffold proteins, or even the creation of artificial scaffold proteins by directed mutation [22]. Interestingly, artificial scaffolds have in recent years been candidates for the development of inhibitors of protein-protein interactions by creating synthetic scaffolds for target proteins that out-compete naturally occurring interactions [23]. Recent advances in computational biology allow for more detailed studies of the influence of the biochemical and biophysical properties of scaffold proteins on their function in protein-complex assembly through *in silico* simulations [24].

Although lagging behind the animal and yeast field, an increasing number of plant-specific scaffold and adaptor proteins have been described in recent decades [25] [26] [27]. The WD40 repeat containing protein Receptor for Activated C-Kinase 1 (RACK1) has been proposed as a scaffold protein for plant PKCs, with critical roles in plant hormone signalling [25], and in the regulation of cross-talk between kinase and ROS signalling [28] [29]. The polarity protein POLAR has been implicated as a scaffold for the kinase BIN2/GSK3. By recruiting BIN2, POLAR spatially modulates the ratio of nuclear to cytosolic BIN2 in favour of cytosolic localisation, thus changing the target profile of BIN2. Recruitment of BIN2 by POLAR has been implicated in asymmetric cell division in stomata cells in *A. thaliana* [30]. The GRAS [gibberellic acid insensitive (**GAI**), repressor of GAI (**RGA**), and scarecrow (**SCR**)] proteins are proposed to act as scaffolds in plant hormone signalling [31]. IQ67 domain (IQD) proteins, a plant-specific group of Calmodulin (CaM)-targets, have in recent years been established as scaffold proteins with a wide range of functions in plant defense and development [32] [33] [26]. As interactors of the Ca²⁺-sensor CaM and CaM-like proteins (CMLs), they are believed to integrate CaM-mediated Ca²⁺-signals at various subcellular sites, such as the microtubule cytoskeleton, plasma membrane subdomains, and the nucleus [34]. Furthermore, they may function as hubs in cellular signalling, linking Ca²⁺-signalling and auxin-signalling, therefore affecting plant cell and organ shape [35]. Lastly, KINESIN LIGHT CHAIN-RELATED (KLCR) proteins have been implicated as putative bridging scaffolds between different cytoskeleton components [36] [27]. KLCRs and IQDs act in the same pathways in plant growth and development. Different KLCRs and IQDs have been shown to interact, putatively forming scaffold protein hubs [27].

1.1.1 Types of scaffold proteins

Scaffold proteins are grouped by their mode of interaction with their respective targets into the following practical categories: Adaptors [6], scaffolds/anchors [37] [38], and dockers [39] (**Fig. 1**). Adaptors are usually small proteins that interact with precisely two interaction partners at the same time via distinct interaction domains, thus conferring enforced proximity between the two to enable immediate signal transfer from e.g. a receptor to a target protein [40] (**Fig. 1 A**). Like adaptors, scaffolds/anchors also serve to enforce proximity between their interactors but are usually larger multi-domain proteins that can bind more than two proteins at the same time (**Fig. 1 B**). Thereby, scaffolds anchor whole signalling cascades on a single docking platform [37]. In addition to the spatial assembly of signalling cascades, adaptors and scaffolds can affect cascade activity by allosteric modification of their binding partners, or by protecting certain components from degradation [9] [20]. Distinct combinations of binding partners with the same scaffold protein result in different outcomes, allowing for regulatory mechanisms by post-translational modification of scaffolds/anchors to influence the binding affinities for different interactors, or by translational regulation of interactor abundance [41]. Lastly, dockers specifically dock interactors to distinct subcellular sites, e.g. the plasma membrane or the cytoskeleton, thus spatially limiting signalling pathways or ensuring efficient processing of external or internal stimuli or nutrients/metabolites by pre-assembly of the processing machinery at the site of arrival [39] (**Fig. 1 C**). A considerable overlap exists between these groups, e.g. dockers can also fall into the categories of adaptors or scaffolds, depending on their structural properties outside of their domain(s) conferring subcellular localisation [6]. This overlap gives rise to a plethora of modes of intracellular coordination by assembly of whole signalling cascades at e.g. the plasma membrane or near receptors or transporters initiating signalling or metabolic cascades. Combinatorial action by different scaffolds or adaptors may additionally facilitate the integration of multiple cellular signalling or metabolic pathways [21] [17].

1.1.2 Biochemical and structural properties of ordered scaffold proteins

To fulfil their role as mediators of protein-protein interactions and complex assembly platforms, scaffold proteins require certain biochemical and structural properties such as the presence of protein-protein interaction motifs and domains. Many protein-protein interaction domains are characterised by tandem repeat domains, i.e. repeating arrays of small, conserved motifs [42]. Known tandem repeats include ankyrin repeats (Ank) [43], Armadillo repeats [44], HEAT repeats [45], leucine-rich-repeats (LRRs) [46], tetratricopeptide repeats (TPR) [47], and WD40 repeats [48], and several more. Repeat domains are usually characterised by small,

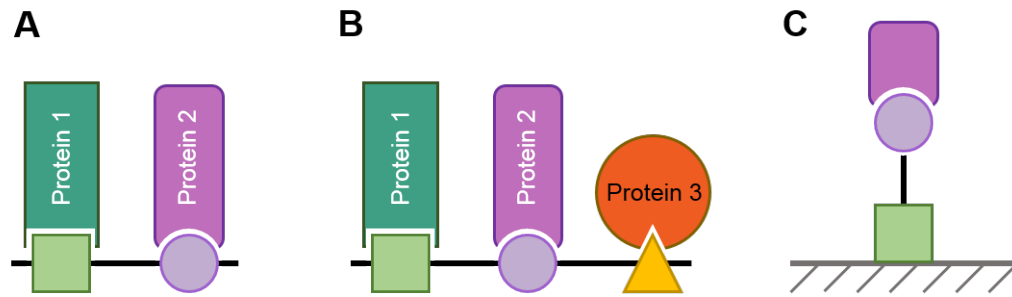


Figure 1: Types of scaffold proteins by target-interaction. **A:** Adaptor protein with two binding partners that bind to distinct domains. **B:** Scaffold/anchor with three binding partners bound by different binding domains. **C:** Docker with one binding partner tethered to a subcellular site.

structurally conserved units that are repeated multiple times, forming an extended protein-protein interaction surface. Most commonly, a single unit of a repeat contains multiple short α -helices connected by loops (Ank, Armadillo, HEAT, and TPR), and in some cases also β -sheets (LRR and WD40) [42]. Ligand binding sites are much more variable between different repeat proteins of the same type than the amino acids conferring 3D protein structure. Amino acid residues in tandem repeat motifs can thereby be categorised as structure-determining, and ligand specificity-determining residues [49]. The generation of artificial tandem repeat domain proteins highlights the role of both short-range molecular interactions and long-range electrostatic forces in tertiary structure assembly and ligand binding specificity of tandem repeat domains, suggesting diverse binding modes with target proteins [50] [51]. Tandem repeats are relatively rigid and maintain their conformation upon ligand binding, indicating that rather than changing to fit their ligand, ligands change conformation to fit into repeat domain proteins [52]. Due to the modularity conferred by repeat motifs, tandem repeat domains can – in theory – extend *ad infinitum* by adding more repeats. This allows for the assembly of large tandem repeat proteins with extensive protein-protein interaction surfaces. Tandem repeat proteins have thus been implicated as scaffold proteins in the assembly of a number of protein complexes. HEAT domains, for example, are found in the protein phosphatase 2A (PP2A) complex, where the A subunits act as scaffolds for the regulatory B and catalytic C subunits, binding both with different HEAT repeat domains [53]. Interactome studies have identified WD40 domains as "promiscuous" interactors present in a number of putative signalling hubs, thereby contributing to cellular signalling networks by facilitating signalling cascade assembly and conferring network cross-talk [54]. The assembly of various heat shock proteins (HSPs) by the HSP organising protein (HOP), on the other hand, is orchestrated by binding of different HSPs to distinct sets of TPR motifs within HOP, thereby bringing HSPs into close proximity to promote the folding of

HSP target proteins [55]. Components of the repeat-domain-mediated multi-protein chaperone machinery have also been identified in plants [56], suggesting a high degree of conservation. In plants, tandem repeat proteins are reported to regulate growth, development, and stress response, as well as hormone signalling [57] [58]. A repetitive organisation of TPR motifs, e.g. is characteristic for the KLCR protein family from *A. thaliana*, which emerged as putative adaptor proteins between components of the cytoskeleton in intracellular coordination [27]. TPR motifs arrange in an anti-parallel helix-loop-helix conformation of 34 amino acids [42]. Consistent with the high degree of variability found in tandem repeats, no position within TPR motifs is fully conserved. Certain preferences, however, are found in various TPR motifs which tend to feature amino acids tryptophan at position 4, leucine at position 7, glycine at position 8, tyrosine at position 11, alanine at positions 20 and 27, phenylalanine at position 24, and proline at position 32. Positions 20 and 27 show a higher degree of conservation than the other positions [59]. Despite proline's known function as a helix-breaker, due to its unique stereochemical properties [60], the consensus proline in TPR motifs appears to mediate a tighter 3D structure of TPR domains when present in a TPR motif, rather than disrupting the motif [61]. TPR motifs are known to occur in repeats of three to sixteen motifs, that form a protein-protein interaction groove by adopting a helical arrangement of helices in higher order TPR domains [62]. The inner cylinder formed by multiple TPR motifs is thought to serve as the primary interaction interface between TPR domains and interacting proteins. Due to the structural rigidity of TPR domains, interactors tend to adopt an extended conformation when binding to a TPR domain, contacting multiple TPR motifs at once [63]. Research on human TPR-containing KLCs has provided insights into the structural mechanism of ligand binding by TPR domains through specific amino acid residues as well as target selection through changes in the helix orientation within the TPR domain for steric regulation [64] [65]. Interestingly, helix-loop-helix motifs have also been implicated in CaM-binding [66], hinting at possible, non-canonical roles for TPR motifs in Ca²⁺-signalling. In addition to facilitating protein-complex formation, TPR domain proteins have been shown to self-associate, forming dimers or higher order oligomers both in plants and other kingdoms of life [67] [68] [69] [70] [71]. Oligomerisation of TPR domain proteins is mediated by the TPR domains, resulting in diverse modes of self-association. Most commonly, TPR domains "twist" into each other by interaction of the inner groove of their N- or C-terminal helices [62]. The capping helices of TPR domains have been identified as putative regulators of TPR-TPR association by steric inhibition of the interaction [69]. While TPR domain proteins are found in all kingdoms of life, a plant-specific TPR-related motif has been identified. The pentatricopeptide repeat (PPR) motif consists of

35 amino acids instead of 34 and shares a high degree of structural and sequence similarity with the TPR motif [72]. Over 400 putative PPR proteins have been identified in various plant species. The majority of PPR domain proteins function as putative scaffold proteins in chloroplast and mitochondrial gene regulation and biogenesis, and RNA binding [73], pointing toward diversification of scaffold protein functions in plants compared to animals.

1.1.3 Disordered scaffold proteins confer binding flexibility

While a large number of scaffold proteins adopt a defined 3D structure, thereby providing a rigid scaffold for interacting proteins, a number of scaffold proteins identified in more recent time are intrinsically disordered proteins (IDPs) or contain intrinsically disordered regions (IDRs) crucial for their scaffolding function [74]. IDPs contain little to no tertiary structure under native conditions and instead rely on short molecular recognition features (MORFs) connected by flexible regions to bind to their interactors [75] [74]. Notably 20 to 30 % of all eukaryotic proteins are believed to be disordered, out of which many may function in cellular signalling [76] [77]. Intrinsic disorder has been shown to assist in promoting the assembly of protein complexes [78], and IDRs are thus widely found in subunits of protein complex components. The prevalence of IDRs in signalling and metabolic network hubs suggests that IDRs are advantageous when assembling multi-protein machineries that require tight regulation [79].

Functions of IDPs and IDRs can be broadly categorised as molecular recognition, molecular assembly, protein modification, and entropic chain activities [80] [81], with the former two being more crucial for scaffold proteins. Protein-protein interactions with IDPs are conferred by MORFs that bind to diverse binding partners. Commonly observed binding mechanisms of IDPs are coupled or concomitant binding and folding, i.e. either the adoption of a defined 3D structure *while* binding to an interactor [82] [80], or sequential adoption of a defined structure *after* binding to an interactor [83]. Usually, the initial interaction between an IDP and an interactor is mediated by pre-formed elements in their MORFs, regions that possess residual secondary structure and serve as starting points for folding after or during protein-protein binding [84]. The arrangement of different MORFs within the same scaffold protein allows for differential binding to different interaction partners with the same IDR and provides a mechanism for binding inhibition, whereby a MORF may be inaccessible under certain conditions [85]. An additional mode of interaction between a scaffold and a binding partner unique to IDPs is "fuzzy" binding, i.e. a dynamic bound state [86]. Fuzzy binding describes a situation where instead of adopting a defined fold after binding to an interactor, an IDP remains in a state of disorder while bound. Fuzzy binding is believed to allow rapid dis-association and re-association between the

IDP and its interactor(s) in fuzzy complexes [86]. In protein complexes IDPs not only confer protein-protein interactions, but also serve to provide contextual spatial arrangements of their binding partners due to their flexibility [74]. Intrinsic disorder in scaffold proteins can also serve to isolate binding partners through the adoption of a more defined structure of the scaffold, which leads to masking or unmasking of intra- or inter-molecular interaction sites within bound partners, or confer allosteric modification of bound proteins [87] [22] [74]. Post-translational modifications (PTMs) have been shown to regulate the structure of IDPs. Phosphorylation, for example, affects disorder-to-order switching in synaptogamin 1 [88], and induces disorder-to-order transition in 4E-BP2, thereby modulating its affinity for its binding partner eIF4E [89]. PTMs thus allow for efficient switching of the localisation or binding behaviour of IDPs, modulating cross-talk between different cellular signalling and metabolic networks [90] [13] [91] [92]. The presence of multiple or promiscuous kinase consensus sites has been suggested to facilitate integration of different signalling pathways [93]. IDPs may thus integrate kinase signalling by various kinases at different subcellular sites.

Based on the research focusing on IDPs and IDRs, several *in silico* prediction servers have been established in the past two decades that predict protein disorder based on amino acid composition, hydrophobicity, net charge, and other biophysical characteristics [94]. The underlying algorithms differ in their respective method of predicting disorder, window length for averaging predicted disorder scores, and consequently their accuracy. Quality, however, is steadily improving, allowing for more and more reliable prediction of IDRs in proteins of interest. MORFs tend to appear as sharp drops in predicted disorder propensity in the graphs produced by these predictors due to the presence of residual secondary structure often found in MORFs [84] [95]. In plants IDPs contribute to the plasticity required to master their sessile lifestyle [96]. IDPs, and more specifically intrinsically disordered scaffold proteins, have been implicated in cell cycle control, regulation of plant metabolism, plant hormone signalling, the regulation of gene expression, plant cell development, and stress response [96] [97] [98]. Known and characterised IDPs in plants include but are not limited to the LEA proteins, regulators of stress response that undergo disorder-to-order transition under drought stress, a number of chloroplast-specific proteins involved in photosynthesis, coordinators of MPK-signalling in plant immunity, members of the WRKY family of transcription factors (TFs), the TF interactor RCD1, and a number of members of various other signalling pathways [99] [97] [100]. Among the latter are the GRAS proteins, which are intrinsically disordered DELLA proteins implicated in gibberelic acid signalling [31]. GRAS proteins are involved in various growth and developmental processes and signal transduction. They are believed to undergo disorder-to-order transition as part of their

function [101]. Other plant IDPs with functions in intracellular signalling include the AUX/IAA proteins involved in auxin signalling [102]. The putatively disordered IQ67 domain (IQD) proteins [26] function as regulators of cytoskeleton organisation and dynamics. They interact with KLCRs, putatively contributing to the formation of super-hubs of disordered and ordered scaffold proteins. KLCR-IQD modules have been implicated in the facilitation of cross-talk between the actin and the microtubule cytoskeleton. The function of KLCR-IQD modules in the regulation of the cytoskeleton points towards more general mechanisms of cytoskeletal regulation by scaffold proteins in the green lineage.

1.2 The plant cytoskeleton

The cytoskeleton forms a second, but no less critical mechanism to provide structure and order to the cellular interior. It forms a highly dynamic three-dimensional network inside eukaryotic cells [5]. While a "proper" cytoskeleton is believed to be exclusive to eukaryotes, rudimentary precursors of cytoskeleton components are found in bacteria [103]. The term "cytoskeleton" was first coined by Paul Wintrebert to describe a structure providing physical stability to cells [104]. To date, the cytoskeleton or its precursors have been shown to be involved in almost all major processes in living organisms. It provides both plasticity and structural stability to cells [5], while simultaneously serving as an intracellular transport network for cell components, as well as whole organelles [105] [106]. It is crucial for cell division and cytokinesis, assisting in chromosome separation during cell division [107], and the creation of new daughter cells [108]. The plant cytoskeleton consist of two key components: Actin microfilaments and microtubules [105] (**Fig. 2**). The actin and the microtubule cytoskeleton form filamentous structures, assembled from single units. Actin microfilaments consist of actin subunits that assemble into fibres. Microtubules are formed by tubulin dimers that polymerise into hollow tubes. The different cytoskeletal structures differ in their respective dynamic properties, with actin filaments exhibiting a higher degree of dynamicity compared to microtubules. Microfilaments and microtubules exhibit polarity, with plus- and minus-ends in microtubules or barbed and pointed ends in actin filaments. Directionality of cytoskeleton components allows for directed cell growth and transport along these structures [109]. Microfilaments and microtubules both exhibit a behaviour referred to as "treadmilling", i.e. simultaneous net-gain at the fast-growing end and net-loss at the slow-growing end, that is crucial to their regulation and their roles as transport networks and facilitators of cell integrity [5]. Cytoskeleton dynamics, their bundling, cross-linking, or tethering to different cytoskeleton components and various membrane systems are mediated by multiple, functionally distinct cytoskeleton associated proteins and cross-linking

factors [110] [111].

In plants the cytoskeleton is involved in providing the specific cell shape required to form

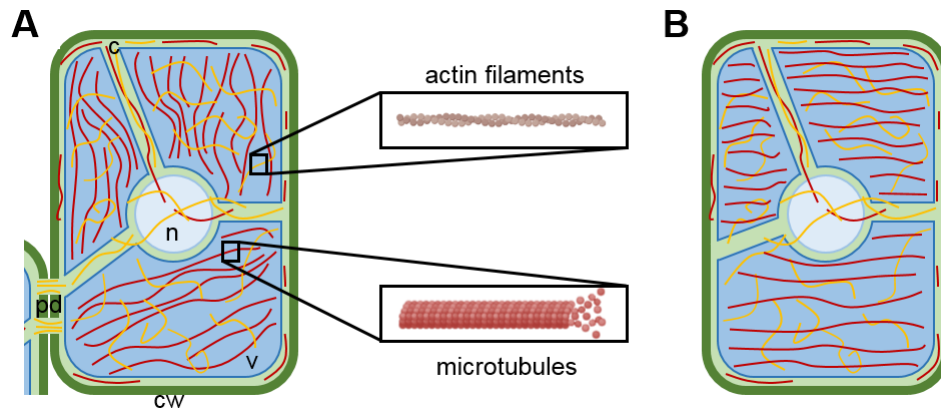


Figure 2: The plant cytoskeleton. Orientation of the cytoskeleton in non-growing cells (**A**) and cells showing diffuse, anisotropic growth (**B**). Microtubules are depicted in red, actin microfilaments in yellow. c: cytosol, cw: cell wall, n: nucleus, pd: plasmodesmata, v: vacuole. Figure modified from Kost and Chua, 2002 [105].

distinct plant organs. It contributes to the characteristic "puzzle" shape observed in leaf epidermis pavement cells, the forked trichomes found on the leaf surface, and the unidirectional growth of root hairs and pollen tubes, by directing cellulose deposition during cell wall formation and restricting growth in certain regions of the cell [112] [113] [114]. Furthermore, the plant cytoskeleton is involved in the generation of plant-specific structures required for correct cell division and cytokinesis (**Fig. 3**). The rigid cell wall in plant cells inhibits cell division by cleavage and requires a mechanism of separating the daughter cells by the insertion of a new cell wall in the middle of the mother cell. Both microtubules and actin are crucial for the determination of the cell division plane by forming the pre-prophase band (PPB) [115] [116]. At the onset of G2 to M transition microtubules and actin reorganise into a dense ring-like structure around the cell periphery that predicts the future division site (**Fig. 3 A**). After PPB disassembly, microtubules and actin depart the cellular division zone (CDZ), forming an actin-depleted zone (**Fig. 3 B**). Markers of the positional information remain at the CDZ, allowing for correct fusion of the newly formed cell wall. Additionally, both cytoskeleton components are required for the formation of the phragmoplast, the intracellular structure assembling the cell plate and ultimately the newly formed cell wall (**Fig. 3 C**). It has been suggested that microtubules and actin fulfil distinct functions within the phragmoplast, with actin providing stability, and microtubules being involved in guiding the cell plate to its future site of fusion with the mother cell wall [117]. To fulfil this function, microtubules re-organise dynamically. They depolymerise at the inner edge of the phragmoplast and polymerise at the growing edge, allowing for centrifu-

gal expansion [108]. While in animals the cytoskeleton is crucial for maintaining cell stability, in plants this function is taken over by the cell wall. This leaves the plant cytoskeleton with more functions in intracellular organisation and transport during interphase [118] [105]. Cell wall biosynthesis relies on the cytoskeleton for both cellulose synthesis and the delivery of non-cellulosic materials via the secretory pathway [119]. Microtubules act as "rails" for the cellulose synthase complex, directing cellulose deposition and thereby cell wall rigidity. Uncoupling of microtubules from the plasma membrane results in loss of directed cellulose deposition and cell morphology defects [120]. Actin is additionally crucial for cytoplasmic streaming and the transport of organelles within the cell. Consequently, actin is critical for nuclear positioning prior to chromosome separation during cell division [105] [121].

Microtubule binding proteins (MAPs) and actin binding proteins (ABPs) play essential roles in the regulation and rapid remodelling of the plant cytoskeleton in response to various biotic and abiotic stresses and in the context of various signalling pathways, such as CaM-mediated Ca^{2+} -signalling and phospholipid signalling. While most MAPs and ABPs bind exclusively to microtubules *or* actin, certain MAPs and ABPs possess dual affinity for both cytoskeleton components and confer regulation to both [122]. Additionally, interaction between MAPs and ABPs can facilitate cross-talk between actin and microtubules. IQDs are MAPs that recruit KLCRs to the microtubule cytoskeleton [123]. KLCR-IQD modules are crucial for the assembly of regulatory multi-protein complexes at the microtubule cytoskeleton. The extension of the base KLCR-IQD module by interaction of KLCRs with the actin-binding NETWORKED (NET) proteins links microtubules and actin through the formation a bridging complex [27].

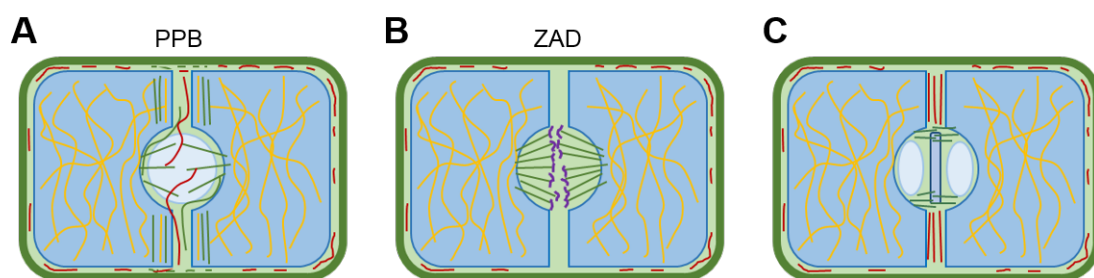


Figure 3: The plant cytoskeleton during mitosis. Orientation of the cytoskeleton during the pre-prophase/prophase (**A**) mitosis (**B**), and cytokinesis (**C**). Cortical microtubules are depicted in red, perinuclear microtubules, the spindle apparatus, and the phragmoplast in green, and actin microfilaments in yellow. Chromosomes are depicted in purple. The newly growing cell plate is depicted between the daughter nuclei in **C**. PPB: pre-prophase band, ZAD: zone of actin depletion. Figure modified from Kost and Chua, 2002 [105].

1.2.1 The actin cytoskeleton

Actin microfilaments are highly conserved structures throughout the kingdoms of life. They were originally identified as components of blood plasma in the late 19th century [124]. Predecessors of actin have been identified as crucial facilitators of cell division in the form of the protein FtsA in *Escherichia coli* [125]. While actin is highly conserved between animals and plants, recent research points towards distinct functions of the actin cytoskeleton in the regulation of plant growth and morphology and the interplay with their environment. To fulfil these functions, plants possess ABPs that are conserved in eukaryotes, and additional plant-specific ABPs [126]. Actin microfilaments measure approx. 7 nm in diameter [105]. They consist of globular actin monomers (G-actin), that assemble into fibrous actin filaments (F-actin) through the hydrolysis of ATP into ADP [127]. The ATP required for polymerisation is sandwiched within the actin-monomers and hydrolysed during formation of actin microfilaments [128]. The conformational change underlying actin-polymerisation consists of a 20 degree rotation of two domains within G-actin that results in a comparatively flat structure and the conversion to F-actin [129]. In forming actin filaments, actin monomers arrange themselves in a helical structure [130], that is capable of forming both dense bundles consisting of multiple filaments, as well as intricate three-dimensional networks [5].

The most important transport proteins using actin filaments as tracks for ATP-dependent intracellular transport are myosins [131]. Myosins consist of a motor or head domain, that binds actin and generates force through ATP-hydrolysis, a neck region, and a tail domain that is required for cargo binding. The tail region also confers interaction with the Ca^{2+} -sensor CaM in many myosins as a putative mode of regulating myosin activity [132]. A total of 18 myosin families are known [133], with myosins VIII and XI being plant-specific [134]. Both of these plant-specific myosins are involved in cell division. Myosin VIII is found at the phragmoplast [135], while myosin XI has been identified at the mitotic spindle [136]. Furthermore, myosin XI has been implicated in intracellular organelle trafficking [137], hormone transport by affecting the polar localisation of auxin transporters, and root organogenesis [138], suggesting distinct roles for the actin cytoskeleton in intracellular signalling exclusive to plants.

The genome of *A. thaliana* encodes for ten different actins, suggesting remarkable diversity in actin filament composition and thus a possible multitude of functions [139]. The actin cytoskeleton has been implicated as a signalling hub in directional cell growth, by integrating GTPase-, Ca^{2+} -, and lipid-signalling via its associated proteins [140]. It confers cytoplasmic streaming in plants, a means by which the cytoplasm is kept in motion in controlled flow patterns as a product of intracellular microfilament organisation [141]. In addition to the distribution of cellular com-

ponents to their destination, cytoplasmic streaming can be used to transport organelles within the cell [106]. Recent research has highlighted the role of the actin cytoskeleton in intercellular transport through plasmodesmata [142], and the importance of the actin-nucleator formin for rapid actin remodelling in innate immunity in plants [81]. The NET protein family has recently been identified as a novel class of ABPs [143]. The most recent findings point towards roles for NET2s in regulating cortical actin in pollen tube growth [144] and for the NET3 proteins in linking the actin cytoskeleton to microtubules and the plasma membrane through a bridging multi-protein complex through interaction with KLCRs [27]. The dynamics and exact roles of KLCR-NET3 complexes in cellular regulation are not fully understood.

1.2.2 Regulation of the microtubule network

Like the actin cytoskeleton, microtubules are a crucial intracellular structure conferring form and stability to cells [105]. They are highly conserved and rudimentary precursors were identified in bacteria in recent years [145]. In contrast to microfilaments, microtubules form hollow, tubular arrangements of up to 50 μm in length and an outer diameter of approx. 27 nm [146]. Microtubules consist of single units that polymerise to form the larger structure. These units are dimers of α - and β -tubulin [147], with GTP sandwiched between them and an exposed GDP bound on the surface-accessible side of β -tubulin [148]. α - and β -tubulin are roughly 50 % identical in their sequence and share a molecular weight of approx. 50 kDa [149]. A third type of tubulin, γ -tubulin, plays an essential role in the nucleation of new microtubules by forming the γ -tubulin ring complex [150] [122]. The *A. thaliana* genome encodes nine α -tubulins and six β -tubulins, allowing for remarkable diversity within microtubules through a concept termed "isovariant dynamics". Isovariant dynamics confer increased functionality, responsiveness, and resilience of the microtubule cytoskeleton through diverse array composition and partial functional redundancy between different tubulin isoforms [139]. Microtubule polymerisation occurs by end-to-end association of tubulin dimers. The β -subunit of one dimer contacts the α -subunit of the following dimer. The resulting proto-filament has an α -tubulin exposed on its (−) end and a β -tubulin exposed on its (+) end [151]. Proto-filaments assemble in a pseudo-helical arrangement of 13 proto-filaments to form the microtubule lattice. The disordered, negatively charged C-terminal tails of tubulin are presented on the surface of the microtubule lattice [152]. Microtubules consisting of different numbers of proto-filaments have been reported, pointing to diverse functions, depending on their composition [153]. The process of microtubule polymerisation also functions in cell-free environments when tubulin and GTP are present [154]. Microtubule elongation primarily occurs at the (+) end and microtubule directionality is crucial

for their function [155].

Microtubule growth and stability are affected by several factors, including temperature, Ca^{2+} -concentration, PTMs of tubulin, and differential activities of MAPs [147] [156]. MAPs fulfil many functions, such as regulating microtubule nucleation and growth, (de-)stabilisation, bundling, or tethering of microtubules to subcellular sites [157] [122]. Katanin is a microtubule severing protein with putative roles in promoting microtubule nucleation in plant cortical microtubule arrays [158]. Catastrophins, i.e. proteins that promote microtubule catastrophe, were identified in humans as regulators of microtubule stability and microtubule dependent vesicle transport [159]. Homologues in plants are not known. The tau proteins promote microtubule stability and the formation of parallel microtubule arrays via two distinct microtubule binding sites [157] [160]. Other microtubule stabilisers include CLASP and XMAP215 [161], the former of which is also conserved in plants [162]. Modification and regulation of MAPs is crucial for the orchestration of cellular processes. Many MAPs bind microtubules via electrostatic interaction between polybasic stretches and the acidic tubulin tails [152]. Phosphorylation of MAPs in proximity to polybasic regions locally changes their charge and regulates their association with microtubules [163].

In plants the primary transport proteins associated with microtubules are the kinesin family, which play important roles in the intracellular transport of single proteins and whole organelles [164] [165]. Kinesins consist of an ATP-dependent motor domain and a coiled-coil domain that facilitates interaction with a second kinesin. Two kinesins assemble into a functional kinesin complex that allows transport along microtubules by "stepping" of the motor domains on the microtubule lattice [165]. Kinesins either bind their cargoes directly via specific interaction domains, or indirectly by the formation of a multi-protein complex with a target adaptor. The use of target adaptors allows for increased diversity in the set of potential targets for the same kinesin and for context-dependent regulation of kinesin specificity by adaptor exchange. Target adaptors of the Kinesin-1 family are the Kinesin Light Chains (KLCs) that interact with the motor-domain containing Kinesin Heavy Chains (KHCs) [165]. The KLCs are more variable than the KHCs, conferring cargo specificity to Kinesin-1s [166]. The plant-specific KLCRs are homologues of KLCs found in animals [123]. Overall, kinesins have been grouped into 14 subclasses, based on sequence homology between their motor domains [167]. While most kinesins are (+) end directed, Kinesin-14 instead moves cargoes towards the (−) end of microtubules [168]. Distinct Kinesin-13 family members facilitate microtubule depolymerisation instead of transport [165], indicating regulatory roles for kinesins in addition to their function as transporters. Plant kinesins have diversified from animals, with a large increase in

kinesin genes encoded in plant genomes [167] [169] [170]. As kinesins have diversified in plants, so have their functions. Several plant kinesins, such as the PHRAGMOPLAST ORIENTING KINESINS (POKs), are involved in PPB formation and cell division plane selection during cytokinesis [171] [172].

Microtubules are crucial for cell division. They form the centrioles and the spindle apparatus during mitosis in all kingdoms of life, thereby contributing to chromosome separation [173] [107] [174]. In plant cells, microtubules are the main contributor to the formation of the PPB as the first visible marker of the future cell division plane [175] [176] [177]. Intact microtubules at the PPB are crucial for the formation of the PPB's actin-component. Correct cell division has been observed in the presence of actin-destabilising drugs, indicating that the role of microtubules in cell division is more important than that of actin [115] [105]. Furthermore, microtubules are essential components of the phragmoplast, a cylindrical structure of anti-parallel microtubules that overlap in the mid-zone of dividing cells and serves to deliver cell wall components to the newly forming cell plate as well as guide the cell plate to the future site of fusion with the mother cell wall [178] [179]. Within this structure, members of the MAP65 protein family, MAP65-1, MAP65-2, and MAP65-3, cross-link plus-ends of microtubules at the midzone, regulating microtubule stability and depolymerisation. MAP65s are subject to MPK mediated regulation [180] [181] [182] and MAP65-hubs may play a role in controlling phragmoplast orientation and expansion speed [183]. Furthermore, members of the plant-specific IQD protein family have been implicated as crucial contributors to PPB formation and division-plane orientation in *A. thaliana* by interacting with Kinesin-12 family members POK1 and POK2 as well as GTPase activators PLECKSTRIN HOMOLOGY GTPase ACTIVATING Protein (PHGAP) 1 and PHGAP2, and anchoring these proteins to the PPB and CDZ [184].

Outside of their role in cell division and cytokinesis, plant microtubules are believed to function as sensor arrays for the response to abiotic stresses, such as salt stress, cold stress, or drought stress by sensing mechanical tension within the cell and orchestrating the cellular response [185]. Additionally, the plant microtubule cytoskeleton has been implicated as a crucial component for monitoring Ca^{2+} -levels and integrating Ca^{2+} -signalling and ROS-signalling for efficient signal transduction [186]. CML24 has been shown to directly bind and regulate cortical microtubule arrays [187]. Furthermore, recent reviews have highlighted functions for MAPs in the integration of Ca^{2+} -signalling at the microtubule cytoskeleton and the facilitation of cross-talk with other signalling pathways through the formation of signalling hubs and regulatory multi-protein complexes at the microtubule cytoskeleton [188] [122] [27].

1.3 The KLCR-IQD module - a potential hub for macromolecular complex assembly

Recent studies identified a novel multi-protein complex in *A. thaliana* [27]. It consists of the (VAMP) ASSOCIATED PROTEIN 27 (VAP27-1), IQ67 DOMAIN protein 2 (IQD2), NETWORKED 3C (NET3C), and KINESIN LIGHT CHAIN-RELATED 1 (KLCR1) and has been termed the PINK complex. The PINK complex acts as a bridging complex between the microtubule cytoskeleton, the actin cytoskeleton, the plasma membrane (PM), and the endoplasmic reticulum (ER) at ER-PM contact sites (EPCS) (**Fig. 4**). Loss of function mutants in members of this complex exhibit altered leaf cell shapes and root morphology, and defects in cytoskeleton and ER organisation. This suggests that the PINK complex plays a crucial role in plant growth and development by organising the cellular interior [120] [27]. KLCRs and IQDs constitute the core protein-protein interaction module of the PINK complex. The interaction of putative structured adaptor proteins in the form of the KLCRs, and putatively disordered scaffold proteins in the form of IQDs serves as the basis for the formation of a signalling super-hub. IQDs interact with microtubules, the plasma membrane, and the Ca²⁺-sensor CaM [32] [123]. KLCRs are TPR domain proteins that act as adaptors for the KLCR-IQD module. They interact with the NET protein family, thereby linking the KLCR-IQD core module to the actin cytoskeleton [123] [27]. Neither component of the KLCR-IQD module has known enzymatic activity. Therefore, this core module may be crucial for regulating the interplay between the microtubule and actin cytoskeleton, the PM, and the ER by acting as a calcium signalling hub in cellular coordination.

1.3.1 KINESIN LIGHT CHAIN-RELATED proteins are a central adaptor for protein-protein interactions

The KINESIN LIGHT CHAIN-RELATED proteins, also known as CELLULOSE MICROTUBULE UNCOUPLING (CMU) [120], form a small family of three proteins in *A. thaliana*. KLCRs feature a TPR domain in their C-terminus, consisting of 10 to 11 TPR motifs, characteristic for tandem-repeat proteins [123]. KLCRs are named by their similarity to the light chains of animal Kinesin-1, and were originally proposed to function in plant kinesin transport along the microtubule cytoskeleton by binding to KHCs. The static localisation of KLCRs along microtubules, the lack of typical Kinesin-1 family members in plants, and the lack of the coiled-coil domain typically conferring KHC-interaction suggests that plant KLCRs do not function as kinesin subunits [27].

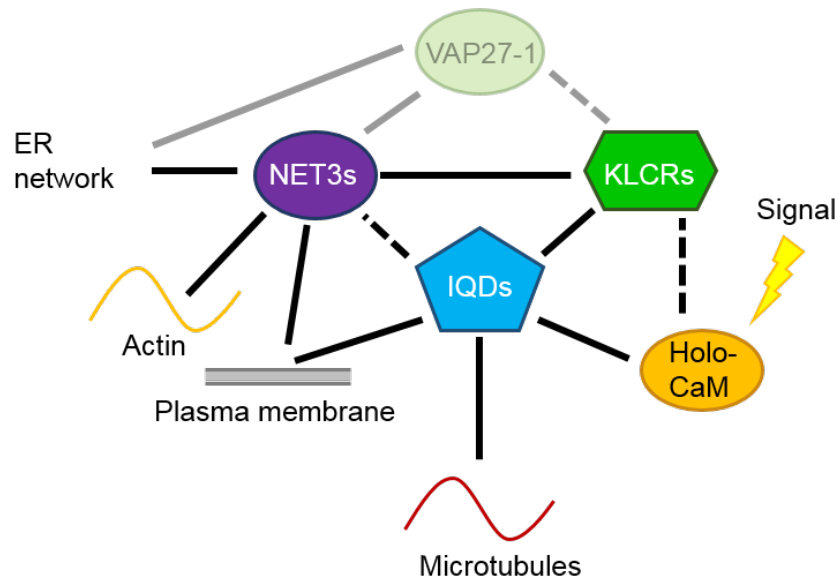


Figure 4: Schematic depiction of the PINK complex. (VAMP)-ASSOCIATED protein 27-1 (VAP27-1), the NETWORKED 3 proteins (NET3s), IQ67 domain proteins (IQDs), and the KINESIN LIGHT CHAIN RELATED proteins (KLCRs) form the PINK complex, linking actin, microtubules, the plasma membrane, the endoplasmic reticulum, and Ca^{2+} -signalling. Dashed lines indicated indirect or suspected interactions. Solid lines show known interactions. VAP27-1 was not investigated in this thesis. Modified from Zang and Klemm *et al.*, 2021 [27].

KLCRs are proposed to anchor cortical microtubules to the plasma membrane thereby stabilising microtubules against the pushing force of the cellulose synthase complex and directing cellulose deposition [120]. Direct interaction of KLCRs with microtubules, however, is disputed. KLCRs were originally identified as interactors of IQD proteins IQD1 and IQD2 [123] [36]. Due to their known microtubule interaction, IQDs are believed to recruit KLCRs to the microtubule cytoskeleton to fulfil their function in the regulation of cellulose deposition [123] [36]. KLCR1 additionally interacts with IQD9 in the regulation of cellulose synthesis during the formation of seed mucilage [189].

Functions of KLCRs as adaptors are supported by the identification of KLCR2 as a central hub in cellular signalling networks [190]. KLCR2 was found to interact with members of hormone and kinase signalling pathways, TFs, RNA binding proteins, and components of Ca^{2+} -signalling pathways in the form of IQD2 and IQD23. Furthermore, KLCR1 and KLCR2 have been found to interact with the kinesin FRA1. FRA1 affects protein levels and microtubule localisation of KLCR1 and KLCR2, potentially regulating sites of cell wall synthesis [191]. Phosphorylation of FRA1 reduces its binding affinity for KLCRs, suggesting that the composition of KLCR-mediated protein complexes can be fine-tuned by PTMs. Phosphorylation of KLCRs as a putative mode

of regulation was suggested by the identification of KLCRs as targets for calcium dependent protein kinases (CDPKs), MPKs, and sugar nonfermenting kinases (SnRK) [192] [36]. KLCRs together with IQD2 and the NET3s were implicated in plant growth and morphology by affecting leaf and root development [27]. By interacting with IQDs and NET3s, KLCRs serve to link the microtubule and actin cytoskeleton with EPCS. Known regulation of KLCs by CaM-binding and phosphorylation may be the basis for similar modes of regulation for KLCR-IQD modules through modification of KLCRs [193]. The mechanisms behind KLCR-IQD interaction, and thus the modes of protein complex formation exerted by KLCRs are not understood, yet.

1.3.2 IQ67 DOMAIN proteins comprise disordered scaffolds

IQ67 domain proteins were originally identified as plant-specific CaM-targets in *A. thaliana* and *O. sativa* [32]. Since their original discovery, IQD families have been annotated in several angiosperms, including commercially relevant plant species, such as soybean (*Glycine max*) [194], maize (*Zea mays*) [195], tomato (*Solanum lycopersicum*) [196], and wheat (*Triticum aestivum* L.) [197], and the moss *Physcomitrium patens*, indicating early evolution of IQDs in the land plant lineage [32]. In angiosperms, alterations in the expression of *IQD* genes has been reported to affect fruit size or shape, or plant morphology, establishing IQDs as potential critical regulators of plant growth and development.

The genome of *A. thaliana* encodes for 33 IQDs (**Fig. 5 A**), which are characterised by their eponymous IQ67 domain, a 67 amino acid spanning domain containing up to three IQ motifs, separated by stretches of 11 and 15 amino acids, as well as varying numbers of 1-5-10 and 1-8-14 motifs [32] (**Fig. 5 C**). IQ motifs are thought to confer Ca²⁺-independent CaM-binding, while the other motifs are reported to confer Ca²⁺-dependent CaM-binding, making IQDs versatile CaM-interactors with putative roles in Ca²⁺-signal integration [198] [32] [123]. Outside of the IQ67 domain IQDs are characterised by hyper-variable regions that differ widely in length and amino acid composition. They possess no known conserved domains or enzymatic activity and are predicted to be intrinsically disordered [32]. The IQ67 domain has been shown to be sufficient and required for CaM-binding of IQDs [123]. Recently, conserved motif #8 has been identified as part of a microtubule binding DUF4005 domain in IQD16 that shares similarity with the microtubule binding domain in animal Kif18A proteins [199]. Additionally, IQDs contain short, conserved motifs with mostly unknown function (**Fig. 5 B**). IQDs cluster into four phylogenetic groups that differ mostly in the size and distribution of conserved motifs (**Fig. 5 A**). Unpublished data suggest that clade III IQDs represent the most evolutionarily conserved IQDs, characterised by the specific arrangement of conserved motifs. IQDs localise to PM

subdomains, the nucleus, or the microtubule cytoskeleton, putatively conferring CaM-mediated Ca²⁺-signalling to other proteins at these subcellular sites by differential recruitment of CaMs and CMLs [34].

IQDs are involved in a plethora of biological networks. Often their function is conferred by interaction with distinct binding partners and is subject to strict regulation. IQD1 has been suggested to be involved in the recruitment of KLCRs and CaMs to the microtubule cytoskeleton by co-expression in *N. benthamiana* leaves. It differentially interacts with CaM- and CML-isoforms, indicating context-specific modes of Ca²⁺-signal mediation by and regulation of IQDs [123]. More recent research also showed interaction of IQD1 with MPKs and hints at phosphorylation of IQD1 by these kinases in its hyper-variable regions [36]. Furthermore, rice IQD protein GW5 was identified as a phosphorylation target of GSK2/BIN2 [200]. Other IQDs, such as IQD2 have been identified as phosphorylation targets by various kinases, such as the TOR kinase [201], and in various contexts, such as circadian clock controlled processes [202]. The identification of phosphorylation events in various IQDs suggests PTMs as a general mode of regulation for IQD localisation and function.

IQDs and their interactors are involved in several processes of plant growth and development. Overexpression of IQD11, IQD14, and IQD16 affects microtubule organisation and cell shape in *A. thaliana* [34], and *Osl*IQD14 regulates microtubule dynamics in rice in a CaM-dependent manner [203]. IQD13 has been linked to the regulation of ROP GTPase domains in the PM through the formation of "lateral fences" of cortical microtubules that restrict PM subdomain size. Overexpression or loss of *IQD13* also affects the size and shape of secondary cell wall pits, indicating that IQD13 indirectly regulates cell wall architecture [204]. IQD2 and IQD5 are involved in the establishment of the characteristic puzzle shape of leaf epidermis cells [205] [114] [27], while IQD2 together with KLCRs also appears to regulate root growth, with mutants showing deviations in touch response [27]. IQD6 to 8 are essential regulators of PPB formation and cell division plane selection during cytokinesis through their interaction with POKs and PHGAPs [184]. Fine-mapping of POK- and PHGAP-interaction sites in IQD8 has revealed a prominent role for the C-terminus of IQDs in protein-protein interactions, indicating protein-protein binding via putative MORFs in IQDs. IQD9 interacts with KLCR1 and the IQD9-KLCR1 module regulates seed mucilage formation by affecting cellulose synthase speed [189]. IQD15 to 18 have been implicated in the integration of auxin- and Ca²⁺-signalling and the regulation of the activity of SPIRAL2 at the microtubule cytoskeleton [206].

Due to their biochemical properties and their multitude of known or putative interactors, IQD proteins have been suggested to function as cellular scaffolds and signalling hubs with diverse

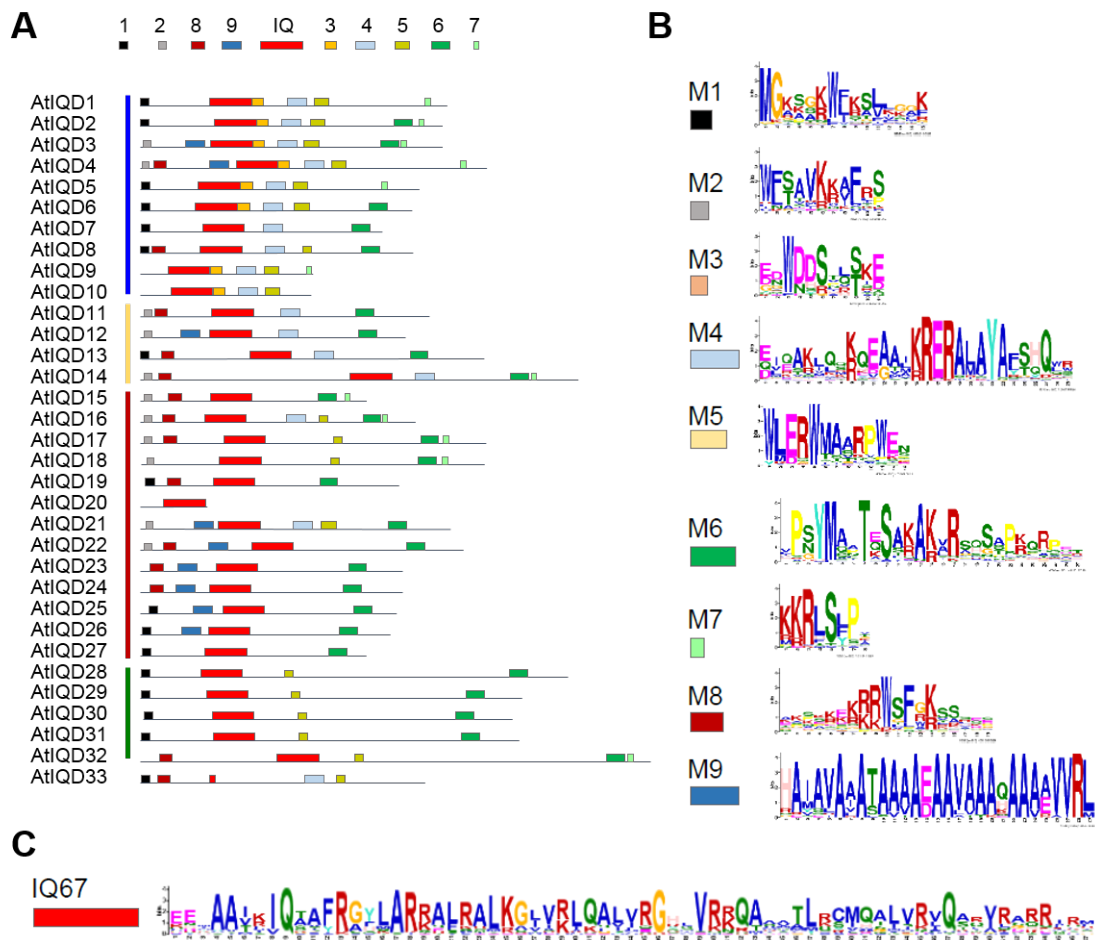


Figure 5: The IQ67 domain family in *A. thaliana*. **A:** Domain organisation of the IQ67 domain family in *A. thaliana*. All IQDs share the eponymous IQ67 domain. Outside of this domain, they differ in size and amino acid composition. IQDs are organised into clades, showing clades I (red line), clade II (yellow line), clade III (blue line), and clade IV (green line). IQD33 only possesses a truncated IQ67 domain. Conserved motifs are marked as coloured boxes and numbered 1 to 9 from N- to C-terminus. **B:** Consensus logos of the conserved motifs found in IQDs. Motif #8 corresponds to the DUF4005 domain [199] **C:** Consensus logo of the IQ 67 domain found in *A. thaliana* IQDs. Modified from Kumari *et al.*, 2021 [184].

functions depending on their expression and localisation [26] [35]. They may be important in integrating Ca^{2+} -signalling, auxin-signalling, and kinase signalling at the PM and the cytoskeleton [35]. Their predicted disorder coupled with short, conserved motifs of lower disorder propensity (**Fig. 29 B**), their ability to localise to the plasma membrane, bind microtubules through the DUF4005 domain [199], and CaMs through the IQ67 domain [123] singles IQDs out as *bona fide* disordered scaffold proteins, interspersed with MORFs.

1.3.3 The NETWORKED protein family links KLCR-IQD modules to the actin cytoskeleton

The NETWORKED proteins were identified as a novel superfamily of 13 actin-binding proteins acting in concert with VAP27s at the actin-PM-nexus [110]. They are divided into four phylogenetic groups with diverging subcellular localisation and functions. They do, however, share the eponymous NETWORKED ACTIN BINDING (NAB) domain in their N-terminus and coiled-coil domains of varying sizes in their C-terminus [143]. Homologues of the NET family have been identified in other plant species by the conservation of the NAB domain [207]. Coiled-coil domains have been implicated as mediators of protein-protein interactions in some protein families in the past, suggesting protein-protein interactions of NETs through this domain [208] [209]. NETs are believed to function in the regulation of the actin cytoskeleton in directional cell growth through their NAB domain [144]. NET3A and NET3C interact with VAP27-1 to link the ER and the actin cytoskeleton to the PM [210]. They were also shown to interact with KLCRs, thus forming a bridge to IQDs and the microtubule cytoskeleton [27]. Their lack of enzymatic activity, small size, actin binding domain, and coiled-coil domain mark NET3A and NET3C as putative adaptor proteins or dockers of KLCR-IQD modules to the actin cytoskeleton.

1.4 Calcium signalling at the microtubule cytoskeleton

Calcium is one of the most important second messengers in all kingdoms of life [211]. Despite its high degree of conservation between the kingdoms, Ca^{2+} -sensor and -transducer families have largely expanded in plants compared to animals, suggesting extended roles for calcium signalling [212] [213] (**Fig. 6**). Calcium signalling has been implicated in virtually every process of plant life, including but not limited to growth and development, nutrient sensing, stress response, and plant immunity [214] [215] [216] [217]. Studies carried out in microgravity have additionally provided evidence, linking Ca^{2+} -signalling to gravitropic growth [218]. Ca^{2+} further contributes to cell wall stability, the regulation of polar cell growth, cell cycle progression,

cytoskeleton organisation and dynamics, various hormone signalling pathways, and hormone transport [219] [213] [220] [221] [200] [222] [188].

Due to its tendency to form insoluble compounds with phosphate, thereby hindering the ATP metabolism crucial to every living cell, cytosolic Ca^{2+} -concentrations are constantly kept at low levels of approx. 100 nM. The low cytosolic calcium levels allows for small *absolute* changes in the local Ca^{2+} -concentration to exert large *relative* effects in cellular signalling cascades [211]. To avoid Ca^{2+} -toxicity, Ca^{2+} -transport across membranes is tightly regulated against an approx. 20,000-fold gradient between the cellular interior and its exterior, as well as certain organelles [211] [223]. In plant cells, the ER and the vacuole act as Ca^{2+} -stores with Ca^{2+} -concentrations in the millimolar range that would be lethal in the cytosol [223]. EPCS are believed to be crucial to the re-filling of internal Ca^{2+} stores of cells by allowing transport of Ca^{2+} directly into the ER [224]. Ca^{2+} -transport maintaining the trans-membrane gradient is carefully orchestrated by the interplay of Ca^{2+} -influx and efflux. Influx transporters, such as ligand- or voltage-gated ion channels and Ca^{2+} -permeable channels (**Fig. 6, left**) act in concert with ATP-dependent efflux carriers and Ca^{2+} -antiporters that transport protons in exchange for Ca^{2+} ions [225] [226] [227] (**Fig. 6, middle**). External stimuli to plant cells result in intricately regulated patterns of Ca^{2+} -influx and -efflux by these transporters. This intricate interplay leads to specific Ca^{2+} -gradients across the cell interior that vary in their amplitude and frequency. Collectively, these Ca^{2+} -oscillations are known as the " Ca^{2+} -signature" [225] [228]. The exact contribution of different transporters and organelles to this signature is not fully understood [223].

The Ca^{2+} -signature is read out by a diverse set of more than 400 Ca^{2+} -sensors and more than 200 Ca^{2+} -targets, indicating a possible signalling network of staggering complexity [230] (**Fig. 6, right**). While some proteins are directly affected by Ca^{2+} -binding, the gamut of Ca^{2+} -signalling is conferred by specific sensors [231] [232]. The main Ca^{2+} -sensors are the CaMs and CMLs [233], the CDPKs [234], and the calcineurin-B-likes (CBLs) [235]. These sensors bind Ca^{2+} via their conserved EF-hands, a helix-loop-helix domain that confers Ca^{2+} -binding by sandwiching the ion between its two helices [211] [212] [236]. Ca^{2+} -binding in EF-hands usually results in conformational changes in binding proteins, causing a switch from a "closed" (apo) to an "open" (holo) conformation, thus changing protein-protein interaction properties [237] [238]. CaMs possess four EF-hands and directly bind to a diverse array of target proteins, either in their Ca^{2+} -bound or their Ca^{2+} -free state. CMLs are more diverse in size, composition, and number of EF-hands than CaMs, ranging from one to six EF hands [239] [240] [233]. CDPKs are comprised of a CaM-like domain containing four EF-hands and a kinase domain. Upon

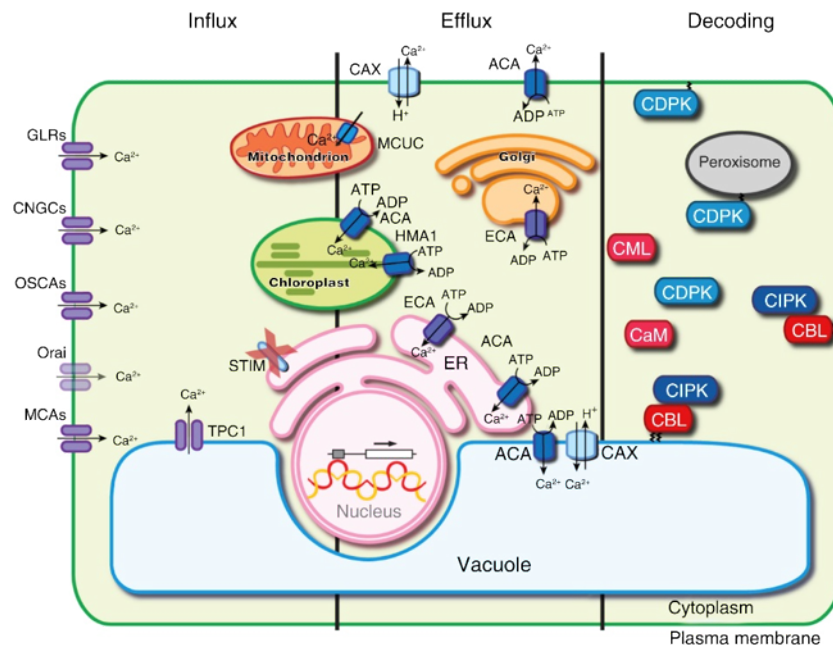


Figure 6: Calcium signalling in plant cells. Schematic depiction of Ca²⁺-signalling coordinated by Ca²⁺-influx, -efflux, and signal decoding. **Left: Ca²⁺-influx channels:** GLR: Glutamate Receptor-Like channel; CNGC: Cyclic Nucleotide Gated Channel; OSCA: Reduced HyperOSmolality induced CA²⁺ increase; MCA: Mechanosensitive channel; TPC: Two-Pore Channel; **Middle: Ca²⁺-efflux transporters:** ACA: Autoinhibited Ca²⁺-ATPase; ECA: ER-type Ca²⁺-ATPase; HMA1: P1-ATPase; MCUC: Mitochondrial Ca²⁺-Uniporter Complex; CAX: Ca²⁺-exchanger; **Right: Ca²⁺-sensors:** CaM: Calmodulin; CML: CaM-Like; CDPK: Ca²⁺-Dependent Protein Kinase; CBL: Calcineurin-B Like; CIPK: CBL-Interacting Protein Kinase. Figure taken from Edel *et al.*, 2017 [229].

Ca²⁺-binding they can phosphorylate their targets, causing downstream effects [212]. CBLs usually contain only three EF-hands and confer Ca²⁺-signalling via CBL-interacting protein kinases (CIPKs) that phosphorylate target proteins following CBL-binding [212] [241]. The various sensors and signal transducers translate Ca²⁺-signals into protein-phosphorylation or protein-protein-interactions, thereby leading to alterations in protein localisation or activity, or changes in gene expression by interaction with TFs [242]. While there are only a few groups of major Ca²⁺-sensors and -signal transducers, these families have expanded in plants, compared to animals. The genome of *A. thaliana* alone encodes for seven CaMs, and 50 CMLs [233], 34 CDPKs [234], and ten CBLs [235]. Only three CaMs and no CMLs are known in humans, indicating much more intricate mechanisms of Ca²⁺-signal control in plants compared to the animal kingdom.

1.4.1 Calmodulins and Calmodulin-like proteins

Calmodulin is *the* archetypal Ca^{2+} -sensor. It is highly conserved between animals and plants and precursors of CaM have even been identified in bacterial genomes [243]. In *A. thaliana* seven genes encode for four different CaM isoforms. *A. thaliana* CaMs possess the canonical four globular EF-hands and share a sequence identity of 97 to 99 % between them and above 95 % identity to animal CaMs, suggesting largely similar CaM-binding targets and functions. CMLs are exclusive to plants. The genome of *A. thaliana* encodes for 50 CMLs that share only 15 % identity with CaMs on average and are much more diverse in their make-up and putative targets and functions. In contrast to CaMs, CMLs possess between one and six EF-hands [240] [244] [236]. The regulation of cortical microtubule arrays in plant roots by CML24 [187], and the interaction of CaMs/CMLs with the microtubule-associated IQDs suggests distinct functions in cytoskeleton regulation by CaMs/CMLs in plants [206].

The expansion of CaMs and CMLs in plants suggests the need for more diverse and varied

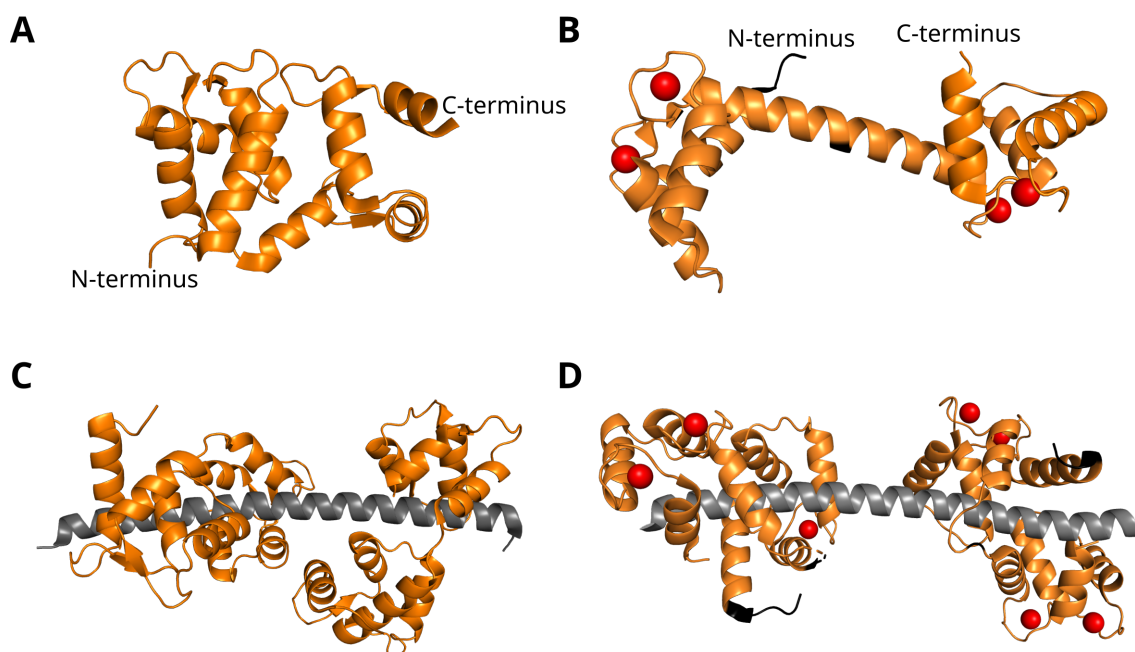


Figure 7: 3D models of Calmodulin. **A:** Crystal structure of apo-CaM from *R. norvegicus* in cartoon depiction, showing the compact fold of apo-CaM. Based on PDB entry 1QX5 [245]. **B:** Crystal structure of holo-AtCaM7, showing its two globular EF-hand domains, each consisting of two EF-hands bound to Ca^{2+} . Ca^{2+} is depicted as red spheres. Based on PDB entry 5A2H [246]. **C:** Crystal structure of apo-CaM from *M. musculus* (orange) bound to an IQ domain of myosin V (grey). Based on PDB entry 2IX7 [247]. **D:** Multiple holo-AtCaMs (orange) bound to the amphiphatic helix of Aca8R (grey). Ca^{2+} is depicted as red spheres. Based on PDB entry 4AQR [248].

functions of Ca^{2+} -signalling. It also points toward possible Ca^{2+} -independent roles for some

CMLs in cellular signalling and organisation [233] [244]. While the seven CaMs found in *A. thaliana* are all expressed at high levels throughout the plant, they differ in their expression levels relative to each other, suggesting context-specific roles for different CaM-isoforms despite their high similarity [239] [233]. Additionally, different splice variants of *AtCaMs* are known. CaM1/4 possesses multiple splice variants with differences in their N-terminal EF-hand domain. Splice variants of CaM2/3/5 differ in the linker between their first two EF-hands and in their C-terminus. CaM6 has no known splice variants, while splice variants of CaM7 differ in both termini. This diversity further support an expansion of CaM-signalling in plants. Different CaM-isoforms and the different EF-hands within a single CaM possess different binding affinities for Ca^{2+} -ions [66] [249] [250] [251]. Competition for Ca^{2+} between the different CaM-isoforms [252], changes in Ca^{2+} -affinity in the presence of target proteins [253], different binding affinities for the same CaM-targets, and differential effects of different CaM-isoforms on target proteins when binding to the same CaM-target [254] support the hypothesis of a vast degree of sophistication in CaM-mediated Ca^{2+} -signalling in plants.

Ca^{2+} -binding induces a conformational switch in CaM. Apo-CaM adopts a compact fold with few surface-accessible residues in the linker between the EF-hands [255] (**Fig. 7 A**). Ca^{2+} -binding results in a more extended conformation in holo-CaM (**Fig. 7 B**), with a higher surface area available for protein-protein interactions in the flexible linker [256]. It has been suggested that burying of the surface-exposed residues in holo-CaM may be a major contributor to holo-CaM complex formation [256], resulting in high stability of holo-CaM binding to target proteins, and consequently weaker interaction between apo-CaM and its targets due to lower accessible interaction surface area. Because of their low pI of approx. 4, CaMs carry a high negative net-charge in native pH between 7 and 8, indicating a crucial role for electrostatic interactions in CaM-target protein binding [257].

CaM- and CML-targets include transcription factors, receptors, kinases, F-box proteins, ion-channels, cytoskeleton regulators, and putatively many more [258] [259] [260] [261]. Despite the high degree of diversity between CaM- and CML-targets, they share some similarity. Canonical CaM/CML-binding domains consist of short, amphiphatic α -helical regions that interact with hydrophobic regions in CaMs/CMLs – found within the linker between EF-hands 2 and 3 [262] [236]. In the canonical CaM-target protein interaction, holo-CaM has been found to wrap around helical interaction domains (**Fig. 7 D**), thereby affecting the biochemical properties of its targets [132]. Binding of holo-CaM to target proteins in an extended conformation has been additionally reported, e.g. for Small-conductance Ca^{2+} -activated potassium channel (SK2) [263]. Active site remodelling as a consequence of holo-CaM-binding has been observed

in anthrax edema factor [263]. Electrostatic interactions between CaMs/CMLs and their targets have been found to stabilise CaM/CML-target-complexes and consequently the target proteins, themselves [250] [264]. CaMs/CMLs have additionally been found to interact with a number of targets – including myosins and Ca²⁺-channels – in the absence of Ca²⁺, suggesting a plethora of regulatory functions for apo-CaM [198] [264] [265]. Apo-CaM-interaction is usually conferred by IQ-motifs (**Fig. 7 C**), conserved motifs found in several ion-channels, myosins, and the IQDs [198] [266] [132], suggesting diverse modes of interaction between CaM and its target proteins in the holo- and apo-form.

As part of their confirmed and putative roles in the regulation of cellular signalling pathways, CaMs have been identified as regulators of scaffold and hub proteins in cellular signalling networks, putatively linking hormone, kinase, and Ca²⁺-signalling to the cytoskeleton and the plasma membrane [34] [35] [267], as well as affecting microtubule stability [268]. Furthermore, CaMs and other EF-hand proteins have been implicated as possible Ca²⁺-dependent adaptor proteins, linking their interactors through the flexibility of the linker between the EF-hand domains [267]. Through their interaction with IQDs, CaMs may play an important role as mediators of Ca²⁺-signalling to KLCR-IQD modules at the cytoskeleton [27].

1.5 Regulation of the cytoskeleton by calcium and scaffold proteins

Rapid remodelling of plant cells in response to external and internal stimuli is critical to their success. The integration of Ca²⁺-signals at the cytoskeleton by direct and indirect regulation of MAPs and ABPs is crucial to this process [188]. Several MAPs and ABPs are subject to subcellular re-localisation and changes in their interaction profiles following Ca²⁺-dependent CaM/CML-binding, including putatively IQDs and KLCRs [188]. KLCR-IQD modules are believed to function as the central unit for the assembly of regulatory multi-protein complexes at the microtubule cytoskeleton. These complexes can be extended to the actin cytoskeleton and EPCS by integration of NET3s [27]. The ability of IQDs, to interact with CaMs/CMLs suggests functions in the integration of Ca²⁺-signals in the assembly and regulation of protein complexes by IQDs.

The exact modes of action of core modules for multi-protein complex assembly remain elusive. The dynamics of complex assembly, the molecular binding mechanisms, the stoichiometry of the KLCR-IQD core module, and the modes of CaM-mediated regulation by Ca²⁺-signals are still unknown. The formation of a putative super-hub of different classes of scaffold proteins provides an intriguing model system for the investigation of cellular coordination by the integration of protein complex assembly and signal transfer. Elucidating the function of KLCR-IQD modules

at the cytoskeleton and the plasma membrane may serve to further the general understanding of the role of scaffold protein hubs in cellular signalling.

1.6 Goals of this thesis

The goal of this thesis was the biochemical characterisation of the KLCR-IQD protein-protein interaction module and its interaction with and regulation by CaM-mediated Ca^{2+} -signalling. This allows us to further our understanding of scaffold proteins as cellular signalling hubs, using the KLCR-IQD module as a model system. Interaction of IQD2 and KLCR1 was chosen as the primary focus over other IQD-KLCR modules, such as KLCR1-IQD9, due to their overlapping phenotypes, and their involvement in the PINK complex. This function singles out IQD2 and KLCR1 as well-established central components of a multi-protein complex that links both contributors of the cytoskeleton, the PM, and the ER. Characterisation of KLCR1-IQD2 modules can therefore serve as a basis for uncovering modes of regulation between the cytoskeleton and cellular membrane systems.

In this thesis, components of the PINK complex in *Arabidopsis thaliana* were characterised comprehensively with regards to their interaction dynamics and mechanisms and with the aim of assessing the integration of KLCR-IQD modules into cellular signalling networks – namely Ca^{2+} -signalling. This thesis takes a KLCR-centric approach, first focusing on a biochemical analysis of possible KLCR-homo-interactions, before expanding into biochemical assays and structure-function studies aimed at investigating the binary interactions between KLCR proteins and CaMs, IQD2, the microtubule cytoskeleton, and NET3 proteins. These *in vitro* and *in vivo* experiments are further supplemented by in-depth *in silico* analyses of the involved proteins, integration of experimental data and *in silico* predictions, and the generation of protein and protein-complex models based on the experimental data. Furthermore, this thesis takes initial steps towards the characterisation of the structural and biochemical determinants underlying the ternary interaction between KLCRs, CaMs, and IQDs, and therefore possible modes of CaM-mediated regulation of the KLCR-IQD core module.

2 Results

2.1 Biochemical characterisation of KLCRs and their binding partners

Previous work performed in this research group and recent publications established KLCRs as central bridging proteins that link functionally diverse interaction partners to the actin and microtubule cytoskeleton and EPCS. The architecture and dynamics of KLCR-mediated protein complexes, and the modes of interaction between individual binding partners, however, are still largely elusive. The comprehensive *in vitro* characterisation of multi-protein complexes is a challenging task, due to the different biochemical properties of the involved proteins and lack of knowledge regarding the spatio-temporal dynamics of complex composition. To reduce the complexity for *in vitro* studies, it is useful to first focus on binary interactions within a putative protein complex before delving into the more intricate interaction dynamics that come with ternary, quaternary, or higher order interactions. KLCRs – specifically KLCR1 – serve as the central linchpin for the characterisation of binary protein-protein interactions in this thesis. The structural determinants of the function of KLCRs and IQDs in the KLCR-IQD core module for protein complex formation, the extension of this core-module by NET3s, and the regulation of KLCR1-IQD2 mediated protein complex assembly will be investigated.

2.1.1 *In silico* assessment of KLCRs

To gain first insights into the characteristics of KLCR proteins, their structural and biochemical properties were assessed *in silico* by interrogation of publicly available databases and bioinformatic tools. KLCR1, KLCR2, and KLCR3 are proteins of 610, 663, and 650 amino acids, and molecular weights of approx. 66, 72, and 71 kDa, respectively. They share a sequence identity of 34.3 % between the three of them, with 243 identical and 176 similar amino acid residues (**Fig. A.1**). KLCR2 and KLCR3 are more similar to each other than to KLCR1, with 52.4 % identity as opposed to 45 and 46 %. KLCRs are characterised by, in the case of KLCR1 and KLCR3 ten, or in the case of KLCR2 eleven TPR motifs in their central to C-terminal region, connected by short linkers (**Figs. 8 A, A.3 A, and A.4 A**). KLCRs are therefore *bona fide* tandem repeat proteins with possible regulatory elements in their terminal regions. The N- and C-termini of KLCRs possess no known conserved domains or motifs.

The first 100 to 190 amino acids and the last 50 to 60 amino acids of all KLCRs are predicted to feature regions of intrinsic disorder, while the TPR motifs are predicted to adopt a helical fold with short regions of higher disorder propensity in the linkers connecting them (**Fig. 8 B, Figs. A.3 B and A.4 B**). While the N-terminal 100 amino acids of KLCR1 are predicted to

be fully disordered, KLCR2 and KLCR3 contain a short region of predicted structure in their N-terminus (**Figs. A.3 B and A.4 B**). This region stretches from residues 20 to 90 in both proteins and is characterised by two sharp drops in disorder propensity connected by a region of higher disorder propensity. These short, ordered regions may confer functions specific to KLCR2 and KLCR3, but have not yet been assessed experimentally. KLCR1 possesses a similar short, likely ordered region with no known conserved motifs or domains just N-terminal of its first TPR motif.

Although no experimentally confirmed 3D structures of KLCRs exist to date, the 3D structure of tandem TPR domains can be predicted with high confidence due to their extensive characterisation as known protein-protein interaction domains [62]. 3D models of all KLCRs were obtained from the AlphaFold 2.0 database [269], or produced with the MODELLER server, using PDB structure 6EOU of human UDP-N-acetylglucosamine-peptide N-acetylglucosaminyltransferase, 110 kDa subunit [270] as a template. 3D models were assessed and curated with PyMol to gain insights into the tertiary structure of KLCRs. The TPR motifs in all KLCRs are predicted to form two short parallel helices connected by a flexible linker, consistent with the secondary structure predictions of KLCRs (**Fig. 8 C and D**). Multiple TPR motifs are predicted to be arranged in a helical structure, in agreement with known structures of multi-TPR-domains [62]. This helical arrangement forms a central cylinder that may be essential for interactions with other proteins (**Fig. 8 E**). Due to their predicted disorder and the resulting low prediction confidence for 3D structures, the positions and orientations of the N- and C-terminus of KLCRs in 3D models are less clear. The predicted ordered regions in the N-terminus of all KLCRs are represented as short, helical motifs in 3D structure predictions and may serve as flexible regulatory elements for KLCR functions. In addition to its canonical form, KLCR1 possesses an alternative splice variant, referred to as KLCR1_{spl}, missing the last exon and consequently the C-terminal 78 amino acids, i.e. the C-terminal disordered region and half of TPR motif #10 (**Fig. A.2**). The disruption of the last TPR motif does not affect secondary structure predictions, or 3D models generated of this splice variant, suggesting that it still adopts a fold largely similar to the canonical version of KLCR1. No information regarding the expression of KLCR1_{spl} relative to its canonical form is currently available.

Charge plots of KLCRs were generated with the EMBOSS charge tool to address their electrostatic properties as possible factors in protein-protein interactions. KLCRs are acidic proteins with pIs of 5.35 for KLCR1, 5.02 for KLCR2, and 4.93 for KLCR3. Charge plots of KLCRs show a charge distribution characterised by basic or acidic patches with few regions showing a more even charge distribution. Basic patches are found as an over-representation of positively charged

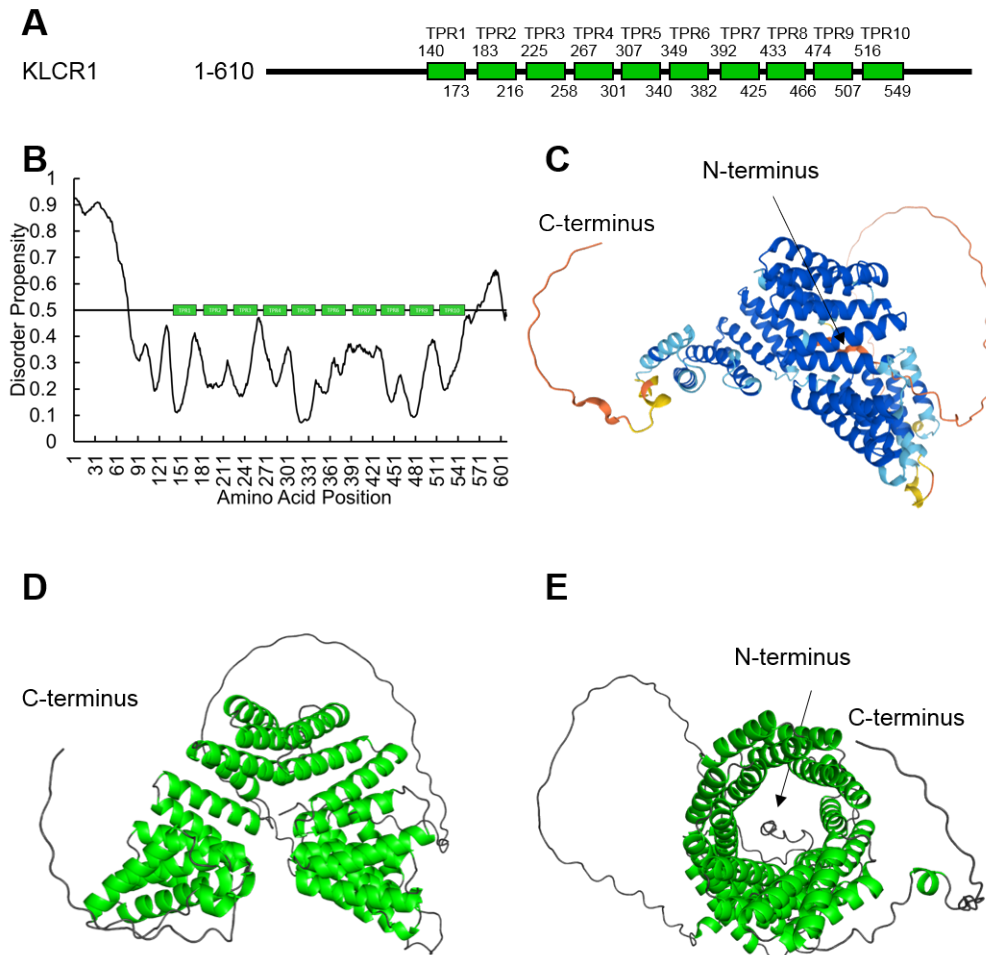


Figure 8: *In silico* analysis of KLCR1. **A:** Schematic representation of KLCR1. TPR motifs are depicted as green boxes. First and last amino acid positions are provided above and below each motif, respectively. **B:** Disorder prediction consensus of KLCR1 with the protein schematic superimposed. A disorder propensity above 0.5 is considered to be likely disordered, a value below 0.5 suggests an ordered secondary structure. **C:** AlphaFold 2.0 model of KLCR1 with prediction confidence from high confidence (dark blue) to low confidence (dark orange). **D:** AlphaFold 2.0 model of KLCR1 in cartoon presentation. Helices are coloured green, while loops are coloured grey. **E:** "Top down" view of the model shown in **D**, showing the inner cylinder formed by the TPR domain of KLCR1.

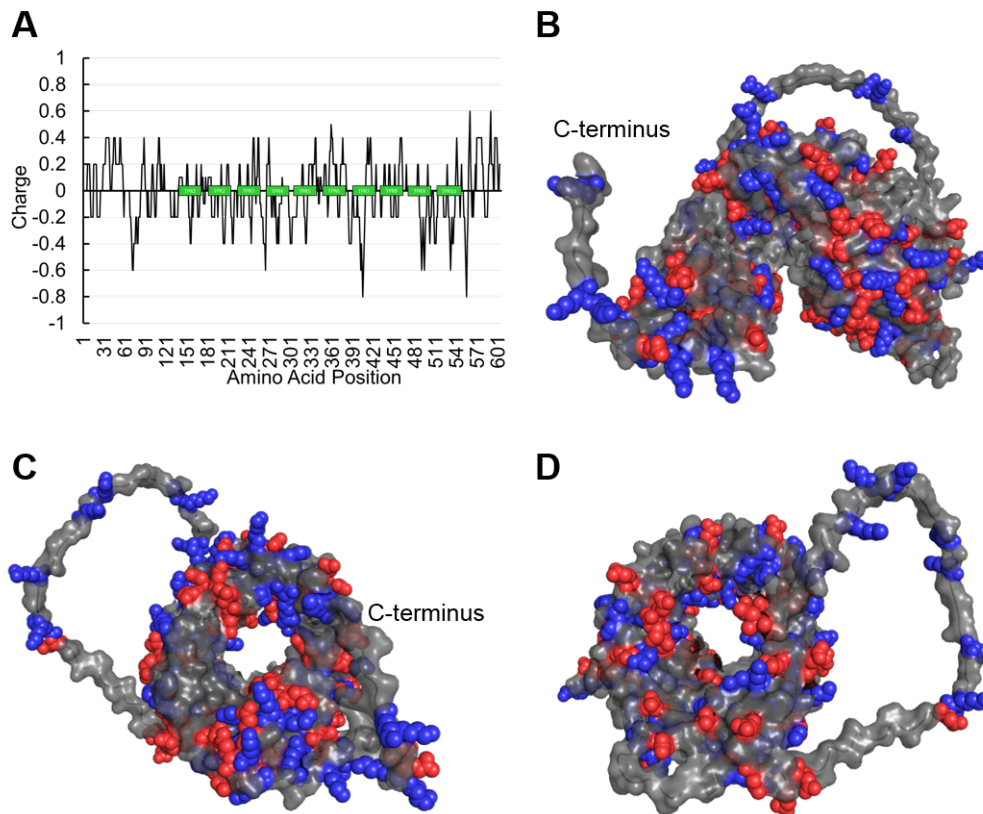


Figure 9: *In silico* analysis of the charge distribution in KLCR1. **A:** Charge plot of KLCR1 generated with the EMBOSS charge tool with the schematic representation of KLCR1 superimposed. **B to D:** Cartoon depiction of the AlphaFold 2.0 model of KLCR1 with a surface of 40 % transparency superimposed. The negatively charged amino acids aspartic acid and glutamic acid are depicted as red spheres, while the positively charged amino acids arginine, histidine, and lysine are depicted as blue spheres.

amino acids N-terminal of the TPR-domain, in TPR motifs #5, and #6, and at the very N- and C-terminus of KLCR1. Acidic patches are present as an over-representation of negatively charged residues in TPR motifs #1 to #4, #7, #9, and #10, respectively. Consistent with the low pI of KLCR1, negatively charged residues are enriched in KLCR1 compared to positively charged residues, with a maximum positive charge of 0.6 and a maximum negative charge of -0.8 (**Fig. 9 A**). The surface accessibility of charged amino acid side chains on KLCR1 or inside its central cylinder may be crucial to its structural and functional integrity (**Fig. 9 B to D**) [65]. KLCR2 and KLCR3 show similar charge distributions to KLCR1 throughout the TPR domain, but differ in their N-termini, which show an over-representation of negatively charged residues, as opposed to positively charged ones in KLCR1 (**Fig. A.3 E and A.4 E**). The negative charge coincides with the short, structured regions in the N-termini of KLCR2 and KLCR3 (**Fig. A.3 B and A.4 B**). The low pI of KLCRs and the enrichment of positively or

negatively charged amino acid residues in distinct regions suggests that KLCRs bind to their diverse interaction partners via electrostatic interactions.

Together, the central cylinder of the TPR domain and the surface accessibility of basic or acidic amino acids may be essential in determining how and where certain binding partners interact with KLCRs. Additionally, post-translational modifications of KLCRs, e.g. via phosphorylation, may serve to regulate the function of KLCR proteins, similar to animal KLCs, where inhibition of Kinesin-1 ATPase activity by CaM-binding to KLCs is blocked by phosphorylation of KLC1 and KLC2 [193]. This hypothesis is further supported by preliminary work carried out in this group showing phosphorylation of all KLCRs by and interaction with MAP kinases MPK3, MPK4, and MPK6 [36]. Annotated phosphorylation sites in the PhosPhAt database [271] and *in silico* predictions of kinase recognition sites in KLCRs point towards phosphorylation of KLCRs in the disordered regions N-terminal of the TPR domain and of KLCR1 and KLCR3 in their C-terminal disordered regions, i.e. their polybasic stretches [36] (**Fig. A.29 B to D**). Phosphorylation in disordered regions has been shown to induce disorder-to-order switching. Alternatively, phosphorylation in proximity to polybasic regions may reduce surface charge and thereby influence electrostatic interactions within KLCRs or with potential binding partners [272].

2.1.2 Expression and purification of KLCRs for *in vitro* characterisation

To experimentally address the structural and biochemical properties of KLCR proteins, KLCRs were expressed in *E. coli* strain KRX and purified using a tandem method of affinity purification coupled with gel filtration. KLCRs were expressed either with a 10x His-tag, a GST-tag, a combined GST-tag and 6x His-tag with a thrombin cleavage site before the protein of interest, or with a combined 8x His-tag followed by a SUMO-tag for use in various different assays and interaction studies (Tab. 2). The highest achieved protein yield during KLCR purifications were approx. 12 mg of pure His-KLCR1 from 3 l expression culture, showing as a prominent band at approx. 70 kDa in denaturing PAGEs (**Fig. 10 A and B**). *In vitro* studies requiring purified protein focused on KLCR1 due to its putative role in KLCR1-IQD2 protein-protein interaction modules. Assays carried out in cell lysates additionally included KLCR2 and/or KLCR3 to assess possible differences in the biochemical properties of these closely related proteins and gain insights into the underlying structural and biochemical determinants.

Relatively pure His-tagged KLCR1 already eluted in the last washing step during affinity purification via Ni-NTA agarose. The last wash fraction of affinity purifications of KLCR1 via Ni-NTA was thus consistently included in further affinity purification or gel filtration. In SDS-PAGEs KLCRs migrated at their expected sizes as a clean band (**Tab. 2, Figs. 10 and A.5**

Table 2: KLCR expression constructs used in this thesis.

Protein	Tag	Trivial name	Expected size [kDa]
KLCR1	10x His	His-KLCR1	69,4
	GST	GST-KLCR1	94,5
	GST, 6x His	GH-KLCR1	98,1
	8x His, SUMO	HS-KLCR1	81,2
KLCR2	10x His	His-KLCR2	75,6
	GST	GST-KLCR2	100,8
	8x His, SUMO	HS-KLCR2	87,4
KLCR3	10x His	His-KLCR3	74,3
	GST	GST-KLCR3	99,5

A and B), although occasionally double bands were observed, even after multiple purification steps (**Fig. 21 A, D, and E**). These double bands may be attributed to modifications of KLCRs or possible DNA contamination. Failure to remove these double bands by the addition of DNaseI to purification buffers or more stringent washing steps point towards modifications of KLCRs as the more likely explanation.

2.1.3 KLCRs may form dimers

During gel filtration, KLCR1 migrated in a sharp peak at a retention volume of 67 ml on a HiLoad 16/600 Superdex 200 pg column, while KLCR2 migrated at a retention volume of 68 ml (**Figs. 10 C and A.5 C**). When compared to a size standard for 16/600 Superdex 200 columns, proteins of 70 kDa are expected to migrate at a retention volume between 70 and 80 ml, while a retention volume just below 70 ml more closely correlates to a molecular weight of 150 kDa (**Fig. 11 A and B**), i.e. roughly twice that of His-KLCR1 or -KLCR2. Silver staining of the protein fractions corresponding to the peaks confirmed the presence of only a single protein – KLCR1 or KLCR2, respectively. The observed migration behaviour during SEC may therefore point towards possible homo-dimerisation of KLCR proteins (**Figs. 11 C and D, and A.5 B and C**).

To assess the possibility of direct interaction between KLCRs, *in vitro* pulldown experiments were carried out. GST-KLCR1 was immobilised on GSH-agarose and incubated with His-KLCR1 over night. GST alone served as a negative control to rule out unspecific interaction between His-KLCR1 and the GST affinity tag. Efficient immobilisation of GST and GST-KLCR1 on GSH-agarose was validated by western blot analysis using an anti-GST antibody which confirmed the presence of GST (at 25 kDa) and GST-KLCR1 (approx. 100 kDa). Weak co-recruitment of His-

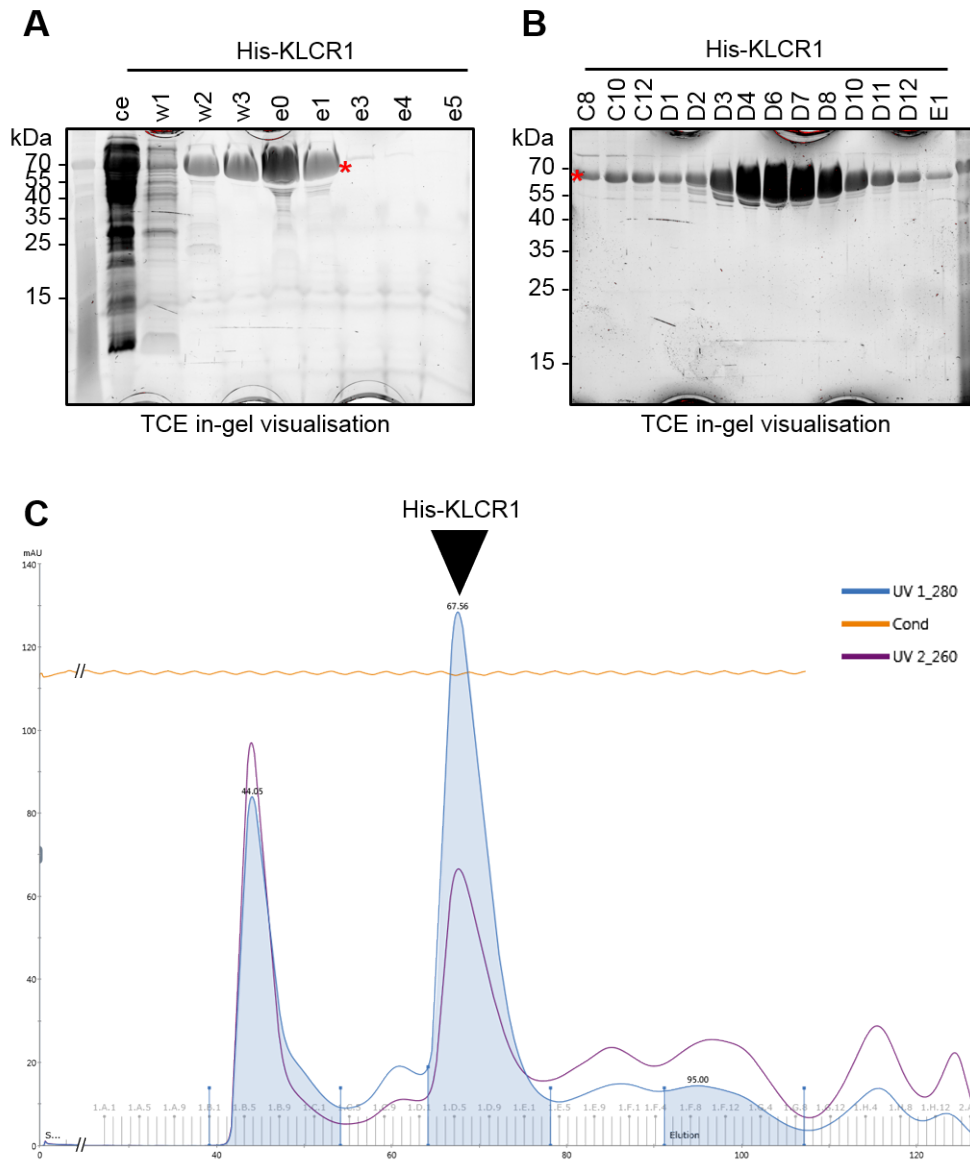


Figure 10: Purification of His-KLCR1. **A:** 15 % SDS-PAGE of crude extract (ce), wash fractions (w1 to w3), and elution fractions (e0 to e5) after affinity purification via Ni-NTA agarose. His-KLCR1 is marked with a red asterisk. **B:** 15 % SDS-PAGE of peak fractions of SEC of His-KLCR1. His-KLCR1 is marked with a red asterisk. **C:** Chromatogram of SEC of His-KLCR1 on a HiLoad 16/600 Superdex 200 pg column showing absorption at 280 nm (blue), 260 nm (violet), and conductivity (orange) plotted against the retention volume. The fractions analysed in **B** correspond to the peak at 67.56 ml.

KLCR1 (at 70 kDa) was detected with an anti-His antibody in combination with GST-KLCR1, but not GST alone (**Fig. A.6**), confirming specific and direct homo-interaction of KLCR1. The low amount of His-KLCR1 recruited by GST-KLCR1 suggested that either the affinity for self-association of KLCRs is low, or that dimerisation of GST-KLCR1 has been saturated by itself in this assay, blocking interaction with His-KLCR1. To test these hypotheses, GST-His-KLCR1 (GH-KLCR1) was co-expressed with His-SUMO-KLCR1 (HS-KLCR1) and subjected to GST-pulldowns. HS-KLCR2 and HS-KLCR1_{spl} were included in this assay to assess the possibility of KLCR-hetero-dimerisation and to test whether the C-terminus of KLCR1 affects dimerisation. Co-expressions of HS-KLCRs with GST-His (GH) alone served as the negative control. A publicly available anti-SUMO antibody was not functional. Recruitment of HS-KLCRs was therefore detected with an anti-His antibody, which recognises both HS-KLCRs and the GH-tag. The expected differences in molecular mass and an apparent preference of the anti-His antibody for the N-terminal 8x His-tag in the HS constructs over the 6x His-tag in the GH constructs allowed for distinction between the different constructs (**Fig. A.7**). GH-KLCR1 and GH were successfully immobilised on GSH-agarose, showing as bands at 100 kDa and 40 kDa when detected with an anti-GST antibody by western blotting. Recruitment of HS-KLCR1 (at 80 kDa), HS-KLCR2 (at 90 kDa), and HS-KLCR1_{spl} (at 70 kDa) was observed with GH-KLCR1, but not with GH alone (**Fig. 11 E**). The observed bands of HS-KLCRs, that co-recruited to GSH-agarose with GH-KLCR1 upon co-expression, were much stronger than those observed for sequential incubation of GSH-agarose with GST-KLCR1 and His-KLCR1. These data confirm the direct physical interaction between KLCR1, and suggest that dimerisation can occur for full length KLCR1 and KLCR1_{spl}. In addition, KLCR1 likely forms hetero-dimers with KLCR2. It further suggests that KLCR-dimers are stable, showing little dis-association and re-association.

To validate the potential KLCR-KLCR interaction in an independent experimental system, bimolecular fluorescence complementation (BiFC) assays with VYNE-KLCR1, VYCE-KLCR1, and VYCE-KLCR2 were carried out in *N. benthamiana* leaves. The MAP TRM1 was used as a negative control for KLCR-interaction, while co-expression of TRM1 with its known interactor TON1 served as a control for the expression of TRM1 [273]. Co-expression of VYCE-KLCR1 with VYNE-KLCR1 or VYNE-KLCR2 resulted in YFP fluorescence complementation, while co-expression of VYNE- or VYCE-KLCRs with VYNE- or VYCE-TRM1, respectively, did not, suggesting specific interaction between KLCRs *in vivo* (**Fig. 12 A to E**). The apparent KLCR-dimers displayed diffuse fluorescence signals, indicative of cytosolic localisation, which is consistent with previously reported localisation of RFP-KLCR1 and RFP-KLCR2 in transient

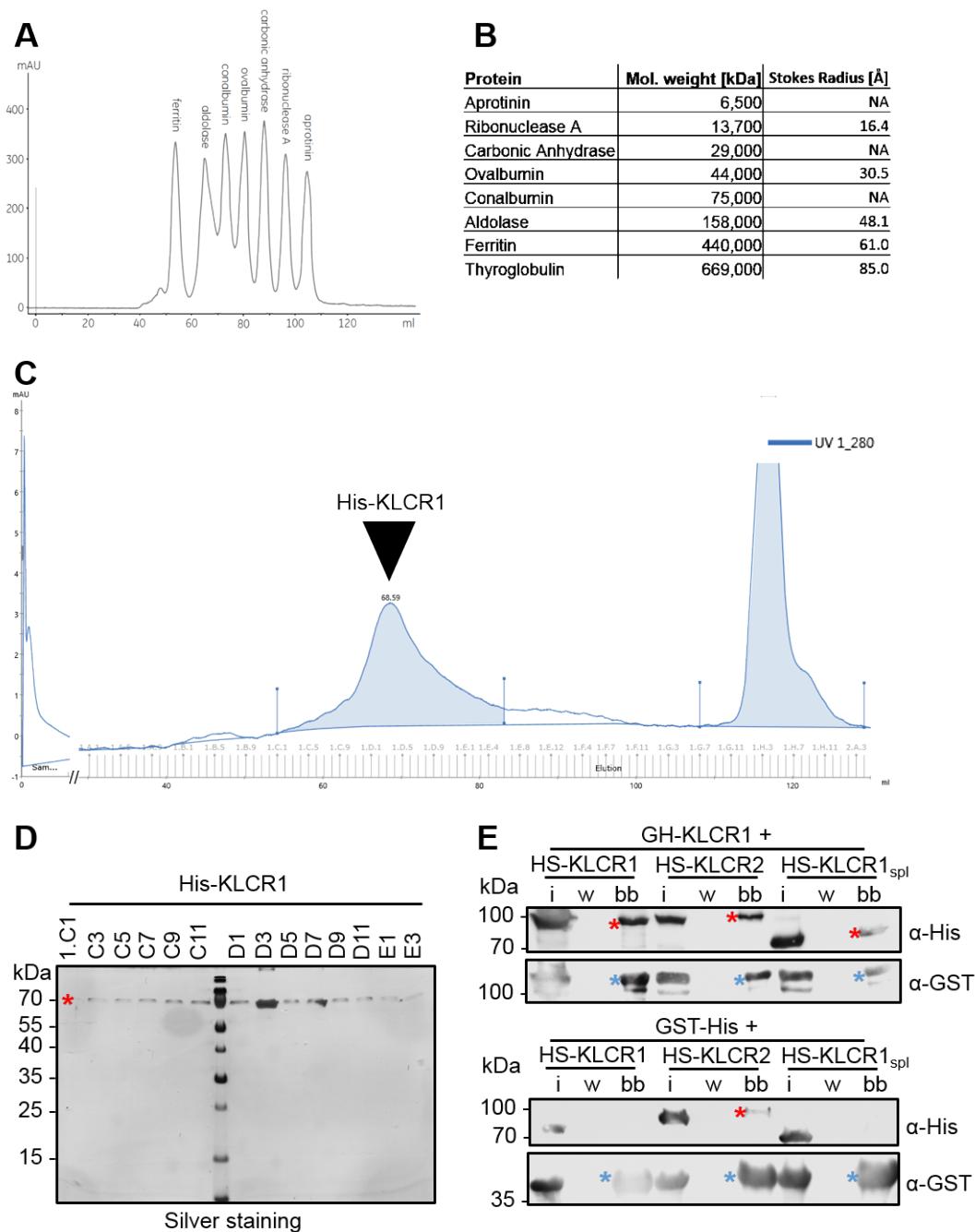


Figure 11: In-depth analysis of KLCR1 regarding homo-dimerisation. **A** and **B**: Size standard for a HiLoad 16/600 Superdex 200 pg column with molecular weights and Stokes Radii of size standard components. **C**: Chromatogram of SEC of His-KLCR1 on HiLoad 16/600 Superdex 200 pg showing absorption at 280 nm plotted against the retention volume. The peak corresponding to His-KLCR1 is marked with a black arrowhead. **D**: 15 % SDS-PAGE of the marked peak from **C** after silver staining. His-KLCR1 is marked with a red asterisk. **E**: Western blot of a GST-pulldown of HS-KLCR1, -KLCR2, and -KLCR1_{spl} with either GH-KLCR1 or GH as negative control. Blue asterisks mark the bait constructs, red asterisks mark the prey constructs. i: input, w: wash, bb: bead-bound.

expression assays in *N. benthamiana* [123] [27]. Co-expression of VYCE- or VYNE-TON1 with TRM1 in either orientation resulted in fluorescence complementation at microtubules and in the cytosol depending on expression strength, confirming expression of TRM1 (**Fig. A.8**). Taken together, these findings support KLCR homo- and -hetero-dimerisation, and point towards the ability of different KLCRs to form stable dimers both *in vitro* and *in vivo*.

2.2 KLCR-CaM interactions

Previous work carried out in our group implicated KLCRs as interactors of holo-CaM, but not of apo-CaM [36]. To validate these findings, CaM-pulldown experiments with all His- and GST-KLCRs were carried out with commercially available bovine CaM immobilised on agarose beads [274]. KLCRs were detected in western blots using either anti-GST or anti-His antibodies. His-KLCRs (70, 75, or 74 kDa) (**Fig. 13**) and GST-KLCRs (95, 100, or 99 kDa) (**Fig. 42 A**) were recruited to CaM-agarose from cell lysate in the presence of 1 mM CaCl₂. KLCR2 and KLCR3 were not recruited in the presence of 5 mM EGTA, a specific Ca²⁺ ion chelator. KLCR1 also showed faint recruitment to CaM-agarose in the presence of EGTA. This observation may be concentration-dependent, as this interaction was only observed at high KLCR1-concentrations in protein solutions incubated with CaM-agarose. These data establish KLCRs as (mostly) specific holo-CaM interactors.

Initial pulldown experiments were carried out with bovine CaM, but not with *A. thaliana* CaM (*AtCaM*). Despite the high conservation between bovine and plant CaM (87 % identity to *AtCaM2* and *AtCaM4*, 88 % identity to *AtCaM7*), possible artifacts caused by inter-kingdom differences between these proteins can not be ruled out. To test the direct interaction between *AtCaMs* and KLCRs, *in vitro* GST-pulldowns of His-tagged KLCR1 with GST-tagged CaM2 or CaM7 were carried out. GST alone served as the negative control. Successful immobilisation of GST-CaMs and GST was detected with an anti-GST antibody in western blots, showing as bands at 45 kDa or 25 kDa, respectively (**Fig. 14 A and B**). His-KLCR1 was co-recruited to the GSH-agarose by holo-GST-CaM2 and -CaM7 (**Fig. 14 A**), but not with either apo-GST-CaM (**Fig. 14 B**). His-KLCR1 was not recruited by GST regardless of the presence or absence of Ca²⁺ (**Fig. 14 A and B**). These findings demonstrate that *A. thaliana* KLCRs can bind to CaMs from *A. thaliana*, establishing them as *bona fide* CaM-targets. Interestingly, the GST-pulldown with holo-GST-CaM7 resulted in slightly stronger recruitment of His-KLCR1 compared to holo-CaM2, hinting at possible differential interaction between KLCR1 and different CaM-isoforms (**Fig. 14 A**).

To assess, whether KLCRs and CaMs interact *in planta*, BiFC-assays in *N. benthamiana*

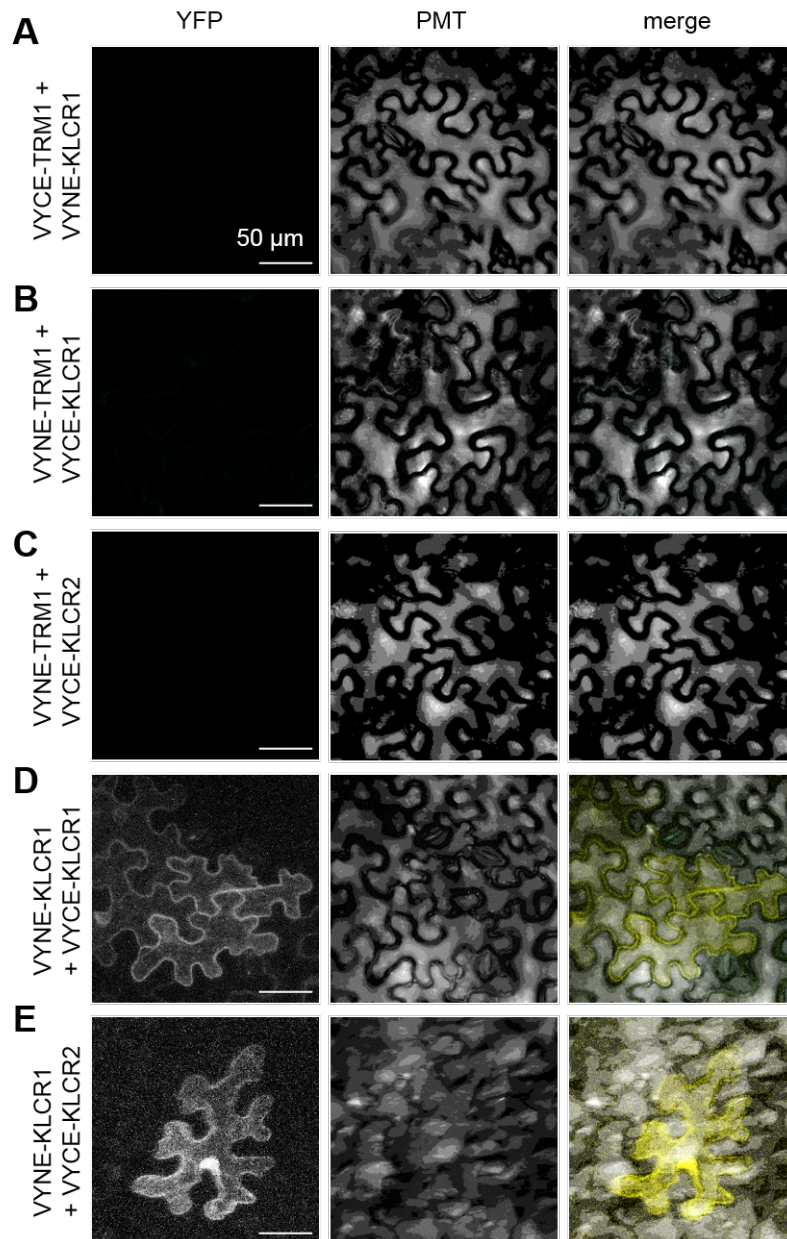


Figure 12: BiFC of KLCR1 and KLCR2 in *N. benthamiana* leaves. **A to C:** Co-expression of negative controls VYCE-TRM1 with VYNE-KLCR1 and VYNE-TRM1 with either VYCE-KLCR1 or VYCE-KLCR2. **D** and **E:** Co-expression of VYNE-KLCR1 with either VYCE-KLCR1 or -KLCR2. YFP fluorescence shows protein interaction, while the T-PMT channel served as a pseudo-bright-field image to visualise cells without fluorescence. Scale bars represent 50 μm . Positive controls for TMRs can be found in Fig. A.8.

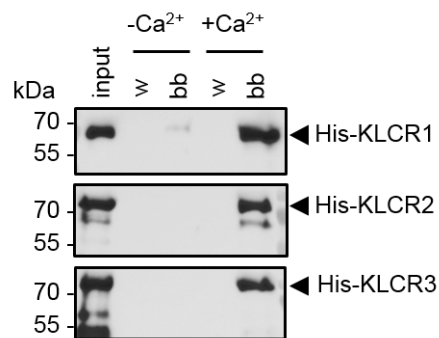


Figure 13: CaM-pulldown of His-KLCRs. Western blots of 15 % SDS-PAGEs of CaM-pulldowns of His-KLCR1, -KLCR2, or -KLCR3 with bovine CaM immobilised on agarose beads in the presence of 1 mM CaCl₂ (+ Ca²⁺) or 5 mM EGTA (– Ca²⁺) from bacterial lysate. The expected positions of His-KLCRs in the blots are marked with black arrowheads. w: wash, bb: bead-bound.

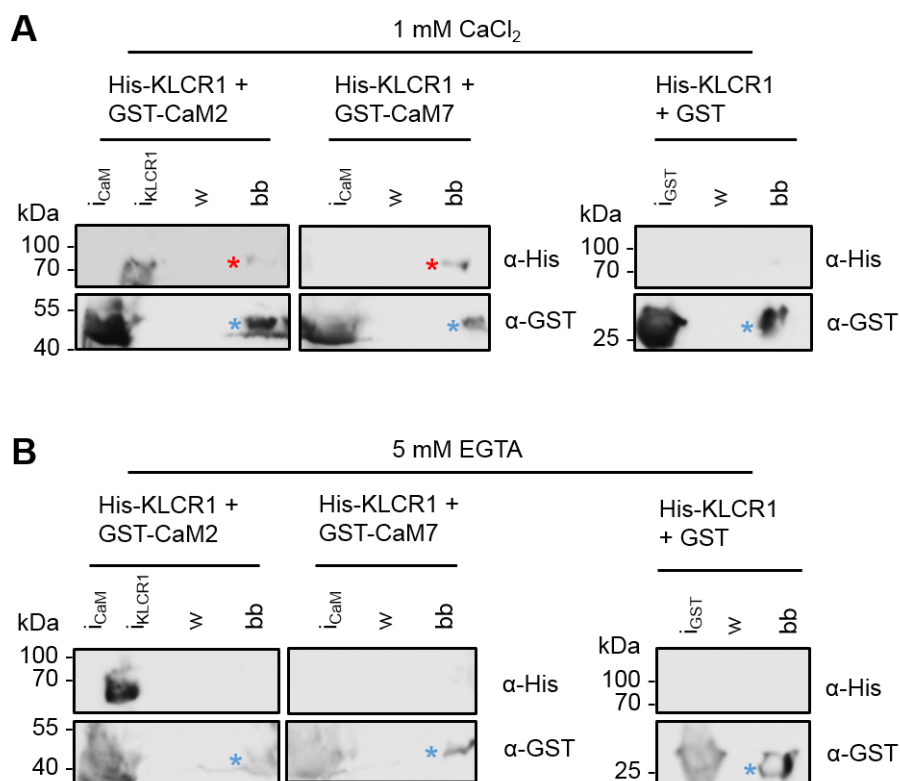


Figure 14: GST-pulldown of His-KLCR1 with GST-CaMs. Western blots of 12 % SDS-PAGEs of GST-pulldowns of His-KLCR1 with either GST-CaM2, -CaM7, or GST alone in the presence of 1 mM CaCl₂ (**A**) or of 5 mM EGTA (**B**) from bacterial lysate. Bait constructs are marked with blue asterisks, prey constructs with red ones. i: input, w: wash, bb: bead-bound.

leaves with VYNE-KLCR1, VYCE-CaM2, and VYCE-CaM7 were carried out, with TRM1 as the negative control. Co-expression of TRM1 with TON1 served as the control for the expression of TRM1 (**Fig. A.8**). Co-expression of VYNE-KLCR1 and VYCE-CaM2 or VYCE-CaM7 resulted in specific YFP fluorescence complementation (**Fig. 15 C and D**). No fluorescence complementation was observed when VYNE-KLCR1 was co-expressed with VYCE-TRM1 or when VYCE-CaMs were co-expressed with VYNE-TRM1 (**Fig. 15 A to C**). KLCR-CaM-complexes displayed diffuse fluorescence signals, pointing towards cytosolic localisation. This is consistent with previously reported findings on the subcellular localisation of KLCR-CaM complexes [36].

To test the direct interaction between KLCR1 and CaMs *in planta*, co-immuno-precipitation (co-IP) assays of GFP-KLCR1 were performed with RFP-CaM2 using RFP-trap beads. Successful immobilisation of RFP-CaM2 on the RFP-traps in the presence and absence of added Ca^{2+} was confirmed with an anti-RFP antibody, showing as a signal at 45 kDa (**Fig. A.11**). Weak recruitment of GFP-KLCR1 (100 kDa) to RFP-traps was already observed in the absence of additionally added Ca^{2+} , which was enhanced upon addition of 1 mM CaCl_2 to the IP-buffer (**A.11**). Residual Ca^{2+} from disruption of plant material (since no EGTA was added) may have been sufficient for weak interaction between GFP-KLCR1 and RFP-CaM2. These data confirm the direct interaction of CaM2 and KLCR1 *in planta* and validate the Ca^{2+} -dependency of their interaction.

2.2.1 Dynamics of KLCR1-CaM interactions

To quantitatively assess the dynamics of KLCR-CaM interactions, affinity measurements between purified KLCRs and CaMs were carried out. To test for differential interaction with different CaM-isoforms, the binding affinity between KLCR1 and CaM2, CaM4, and CaM7 was determined. CaM2, CaM4, and CaM7 were expressed in and purified from *E. coli* strain KRX as 10xHis-tagged constructs. CaMs expressed and purified with a maximum yield of 36 mg protein from 3 l expression culture – albeit the degree of purity was lower than for KLCR1. These yields were achieved with all CaM isoforms, showing as prominent bands at approx. 15 kDa in denaturing PAGEs (**Figs. 16, A.12, and A.13**). CaMs already eluted from Ni-NTA agarose during the washing steps, which led to the last wash step, "w3", consistently being included in further purification steps. CaMs migrated in clean peaks at a retention volume just above 60 ml on a HiPrep Sephacryl S100 HR column in the case of CaM2 and CaM4 (**Figs. 16 and A.12 C**) or at 68 ml on a 16/60 Superdex 75 column in the case of CaM 7 (**Fig. A.13 C**). CaMs showed a tendency for DNA contamination, as indicated by an absorption at 260 nm

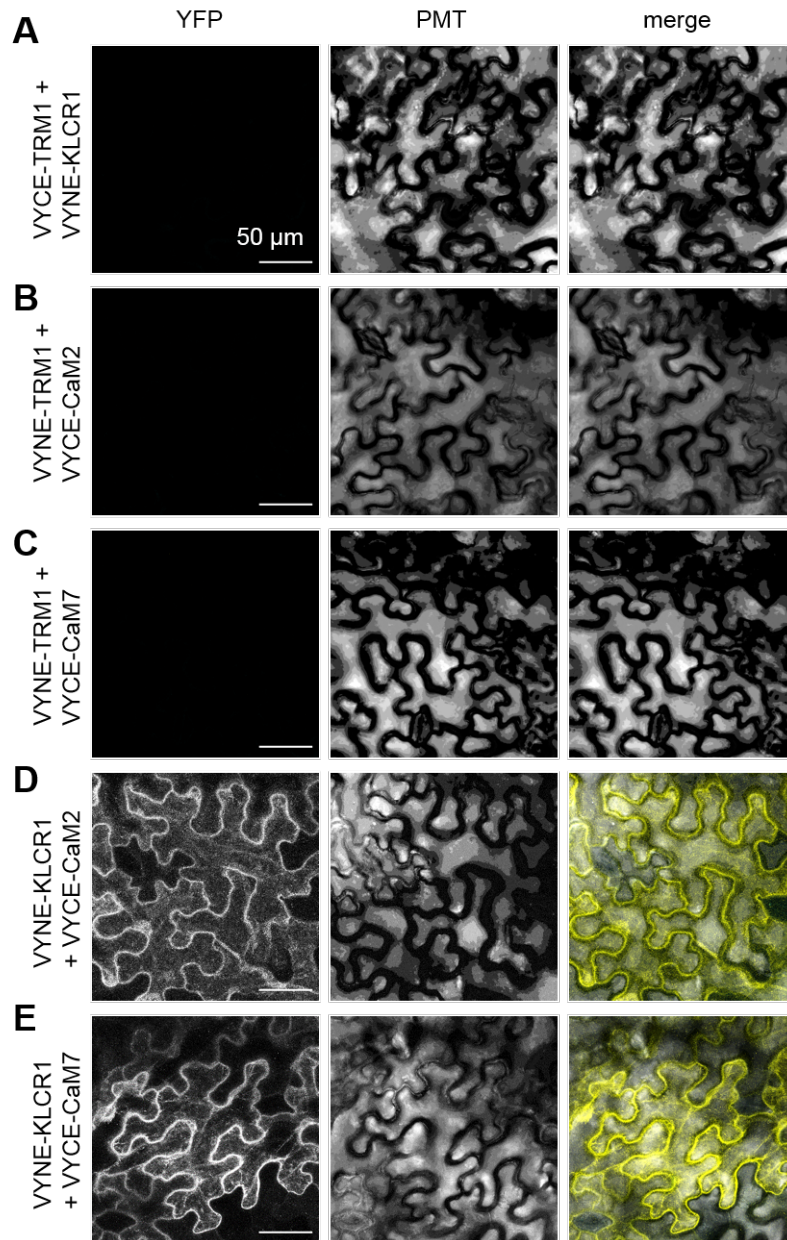


Figure 15: BiFC of KLCR1 with CaM2 or CaM7 in *N. benthamiana* leaves. **A to C:** Co-expression of negative controls VYCE-TRM1 with VYNE-KLCR1 and VYNE-TRM1 with either VYCE-CaM2 or VYCE-CaM7. **D and E:** Co-expression of VYNE-KLCR1 with either VYCE-CaM2 or -CaM7. YFP fluorescence shows protein interaction, while the T-PMT channel serves as a pseudo-bright-field image to visualise cells without fluorescence. The same positive controls for TMRs were used as in Fig. 12 and can be found in Fig. A.8. Scale bars represent 50 μm .

higher than that at 280 nm in the protein peak in SEC chromatograms (**Fig. A.13 C**). For biochemical assays, special care was taken to avoid this contamination through the inclusion of DNaseI in purification buffers.

To determine binding affinities between KLCRs and CaMs, purified His-KLCR1, -CaM2, -

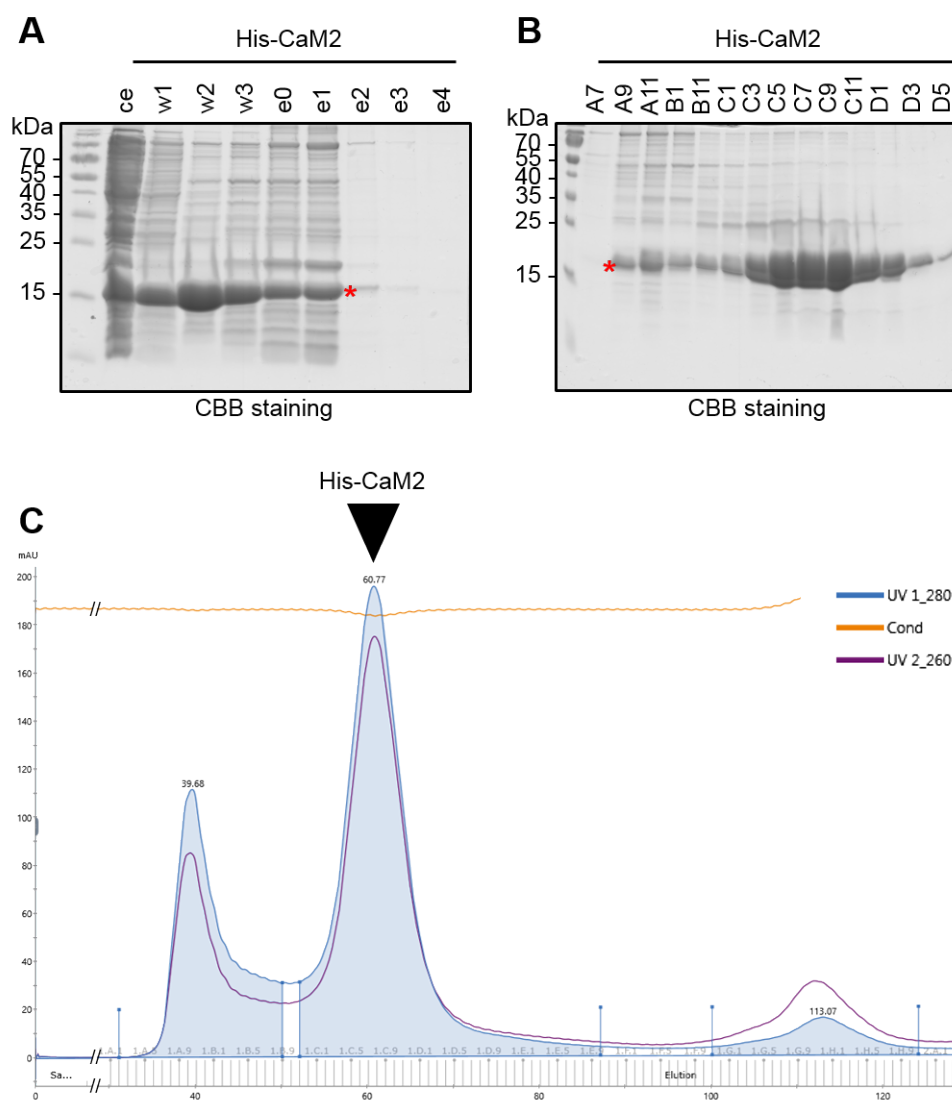


Figure 16: Purification of His-CaM2. **A:** 15 % SDS-PAGE of crude extract (ce), wash fractions (w1 to w3), and elution fractions (e0 to e4) after affinity purification via Ni-NTA agarose. His-CaM2 is marked with a red asterisk. **B:** 15 % SDS-PAGE of peak fractions of SEC of His-CaM2. His-CaM2 is marked with a red asterisk. **C:** Chromatogram of SEC of His-CaM2 on a HiPrep 16/60 Sephacryl S100 HR column showing absorption at 280 nm (blue), 260 nm (violet), and conductivity (orange) plotted against the retention volume. The fractions analysed in **B** correspond to the peak at 60.77 ml.

CaM4, and -CaM7 were subjected to microscale thermophoresis (MST) [275]. MST was the

method of choice due to ease of use and low material requirements. Experiments were carried out on a Nanotemper Monolith at room temperature with 20 nM His-KLCR1 labelled with the NHS-red dye provided by Nanotemper as the target and unlabelled CaMs as the ligand. Labelling of KLCR1 consistently yielded between 2.2 and 6.9 μM labelled KLCR1 with a degree of labelling (DOL), i.e. the average number of dye molecules per protein molecule, between 0.77 and 1.33. KLCR1 was subjected to titration of CaMs in the presence of 1 mM CaCl_2 or 5 mM EGTA and the fraction of KLCR1 bound to CaMs was determined. Titration curves showed little change in the fraction of KLCR1 bound to its ligand below 10 nM of either CaM, a sharp increase between 20 and 200 nM CaM and saturation above 1 μM CaM. Saturation of KLCR1 with CaM7 occurred at lower concentrations than with CaM2 or CaM4. Automatic fits of the resulting binding curves yielded K_D values of 190 ± 65 nM for CaM2, 270 ± 109 nM for CaM4, and 48 ± 23 nM for CaM7 in the presence of Ca^{2+} (**Fig. 17 A**). While data points were recorded in the absence of Ca^{2+} , the analysis software failed to produce any reasonable fitted curves or reliable K_D values based off of these measurements (**Fig. 17 B**). These data confirm the direct interaction observed qualitatively between KLCR1 and CaMs as well as the Ca^{2+} -dependency of their interaction. In addition, they indicate a binding preference of KLCR1 for CaM7, followed by CaM2, and lastly CaM4. These data are consistent with the lower amount of His-KLCR1 pulled from solution by GST-CaM2 compared to GST-CaM7 in pulldown assays (**Fig. 14 A**). This preferential interaction between KLCR1 and different CaM isoforms – despite the high degree of sequence identity between CaM2 and CaM7 (**Fig. A.9**) – may point toward different biochemical effects on KLCR1 as a consequence of binding different CaMs. This effect may depend on the expression levels of different CaM isoforms, or on different Ca^{2+} -binding affinities of individual CaM-isoforms. These data indicate a possible Ca^{2+} -dependent mode of regulation for KLCR1 function through differential CaM interaction.

2.2.2 Fine-mapping of KLCR-CaM interactions

To uncover, which regions in KLCRs contribute to CaM-binding, *in vitro* CaM-pulldown assays were carried out with truncations of KLCR1 and KLCR2 (**Figs. 18 A and 19 A**). The truncations had been generated previously in our group and were designed to maintain the integrity of the TPR motifs within KLCR1 and KLCR2. $\text{KLCR1}_{N\text{-term}}$ encompasses the N-terminal disordered region of KLCR1 and KLCR1_{TR1} to KLCR1_{TR3} cover the N-terminal, central, and C-terminal three TPR motifs of the TPR Rregion of KLCR1. $\text{KLCR1}_{N\text{-half}}$ is a combined truncation, encompassing $\text{KLCR1}_{N\text{-term}}$ and KLCR1_{TR1} , $\text{KLCR1}_{\text{central}}$ combines KLCR1_{TR1} and KLCR1_{TR2} , and $\text{KLCR1}_{C\text{-half}}$ combines KLCR1_{TR2} and KLCR1_{TR3} . $\text{KLCR1}_{\Delta C\text{-term}}$ and

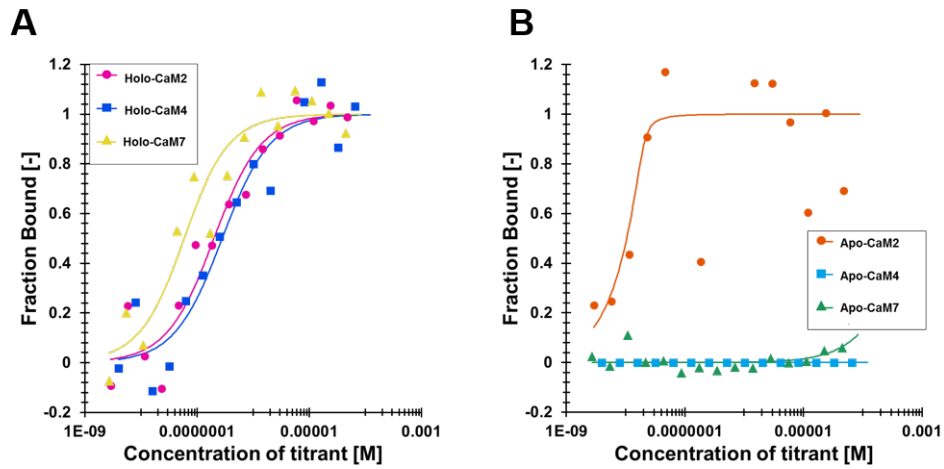


Figure 17: MST affinity measurements between His-KLCR1 and His-CaM2, -CaM4, and -CaM7. **A:** Fitted curves of MST measurements plotting the fraction of KLCR1 bound to CaMs against the CaM-concentration. In the presence of 1 mM CaCl_2 the fit results in K_D values of 190 ± 65 nM for CaM2, 270 ± 109 nM for CaM4, and 48 ± 23 nM for CaM7. **B:** Fitted curves of MST measurements in the presence of 5 mM EGTA acting as a negative control. The fits did not result in reliable K_D values.

$\text{KLCR1}_{\Delta N-term}$ are missing the C- or N-terminal regions of KLCR1, respectively (**Fig. 18 A**). Truncations of KLCR2 differ from those of KLCR1. KLCR2_{N-term} covers the N-terminal disordered region of KLCR2 and the first TPR motif. KLCR2_{TR1} encompasses TPR motifs #2 to #5, and KLCR2_{C-half} the C-terminal six TPR motifs. KLCR2_{N-half} combines KLCR2_{N-term} and KLCR2_{TR1} . $\text{KLCR2}_{\Delta N-term}$ combines KLCR2_{TR1} and KLCR2_{C-half} and is missing the N-terminal disordered region of KLCR2 and the first TPR motif (**Fig. 19 A**).

Due to recent changes in the annotation of TPR motifs in KLCR1, TPR motif #4 is disrupted in these truncations, with the first half being part of KLCR1_{TR1} and the second half being part of KLCR1_{TR2} . The helices of TPR motif #4 are still intact in the truncations because the TPR motif was split in its flexible linker. For KLCR1, the alternative splice variant, KLCR1_{spl} , was included in the CaM-pulldowns to assess possible effects of the C-terminus of KLCR1 on CaM-binding.

Truncations of KLCR1 or KLCR2 were expressed as 10xHis-tagged constructs in *E. coli* KRX and incubated with CaM-agarose in the presence of 1 mM CaCl_2 or 5 mM EGTA. Recruitment to CaM-agarose was detected in western blots using an anti-His antibody. None of the artificial truncations of KLCR1 interacted with CaM in the presence of EGTA, similar to full length KLCR1. His- KLCR1_{N-term} and - KLCR1_{TR1} weakly recruited to holo-CaM. His- KLCR1_{TR3} showed the strongest holo-CaM-recruitment of all short truncations of KLCR1, indicating strong CaM-binding in the C-terminus, and weak CaM-binding in the N-terminus

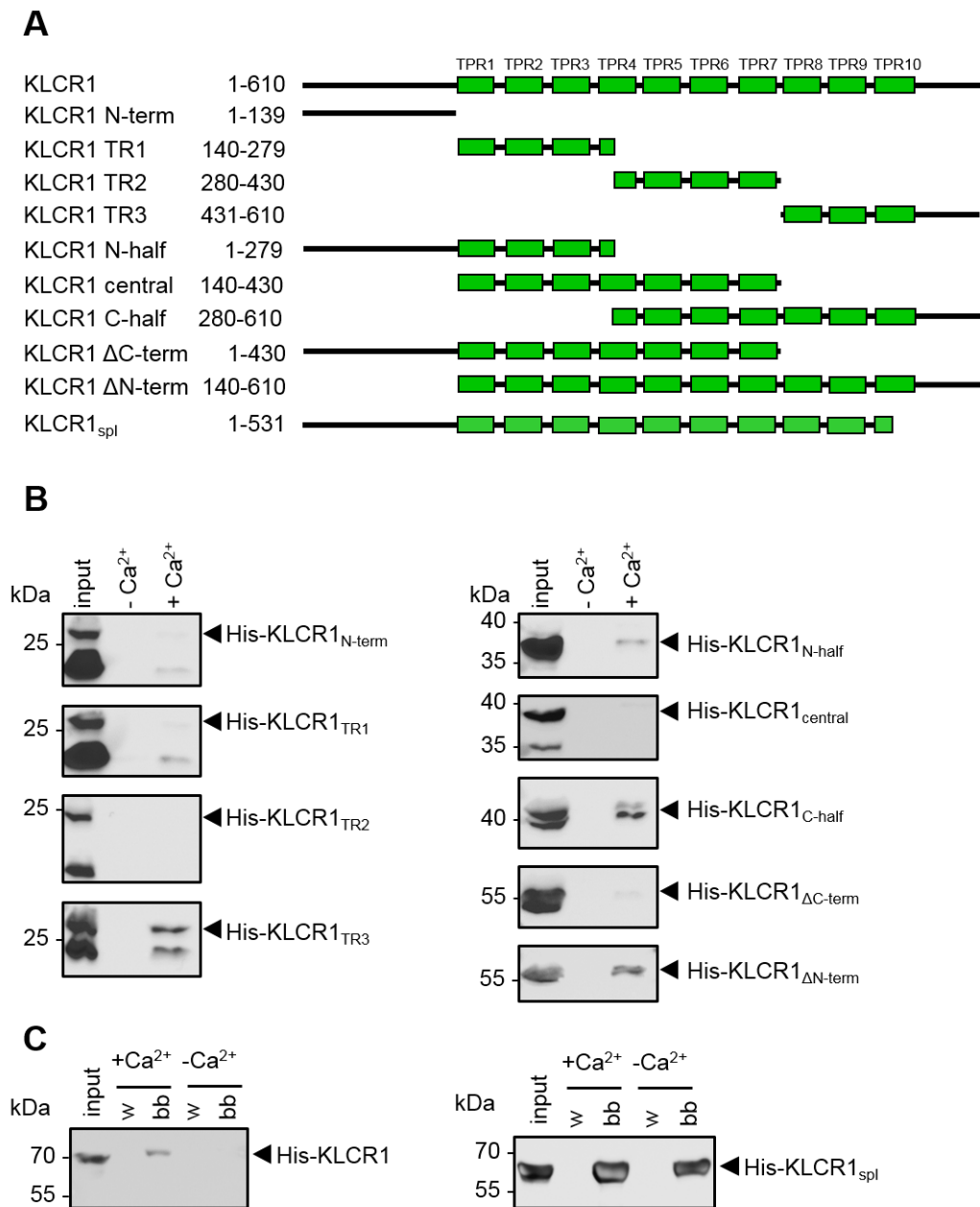


Figure 18: CaM-pulldowns of truncations of KLCR1. **A:** Schematic representation of truncations of KLCR1 (F1 to F9) and the alternative splice variant KLCR1_{spl}, showing the respective TPR motifs present in each truncation as green boxes as well as the exact amino acid positions of each truncation. **B:** Western blots of 15 % SDS-PAGEs of CaM-pulldowns with KLCR1 truncations in the presence of 1 mM CaCl₂ (+ Ca²⁺) or 5 mM EGTA (– Ca²⁺). Expected positions of KLCR1 truncations are marked with black arrowheads. **C:** Western blots of 12 % SDS-PAGEs of CaM-pulldowns of His-KLCR1 or His-KLCR1_{spl} in the presence of 1 mM CaCl₂ (+ Ca²⁺) or 5 mM EGTA (– Ca²⁺). The expected positions of both proteins are marked with black arrowheads. w: wash, bb: bead-bound.

of KLCR1. His-KLCR1_{TR2} was not recruited to CaM-agarose, indicating no CaM-binding in the central region of the TPR domain of KLCR1. Combination of KLCR1_{N-term} and KLCR1_{TR1} in His-KLCR1_{N-half} resulted in recruitment to CaM-agarose comparable to, if somewhat stronger than observed for His-KLCR1_{N-term} and -KLCR1_{TR1}. Combination of His-KLCR1_{N-half} and His-KLCR1_{TR2} in His-KLCR1_{ΔC-term} resulted in weak CaM-binding, comparable to KLCR1_{N-half}, indicating slightly enhanced CaM-binding when combining the disordered N-terminus and the N-terminal three TPR motifs of KLCR1. His-KLCR1_{C-half} and -KLCR1_{ΔN-term} were both recruited to holo-CaM at comparable levels to His-KLCR1_{TR3} and the full length protein. Interestingly, His-KLCR1_{central} showed no recruitment to CaM-agarose (**Fig. 18 B**), indicating that CaM-binding of the N-terminal end of the TPR domain observed in KLCR1_{TR1} may be an artifact of the truncation of KLCR1. These data suggest that the primary CaM-binding region of KLCR1 is located in its C-terminal region, with the N-terminal half possessing residual holo-CaM-binding capabilities. The truncations may render regions of KLCR1 accessible for CaM-binding that would be masked in the full length protein, such as observed for KLCR1_{N-half} and KLCR1_{ΔC-term}.

His-KLCR1_{spl} differed from His-KLCR1 in its CaM-binding and was recruited efficiently to both holo- and apo-CaM (**Fig. 18 C**). Together, the CaM-pulldowns of the truncations of KLCR1 and the altered CaM-binding of KLCR1_{spl} point toward an important role of the C-terminal region of KLCR1 in CaM-binding. CaM-binding of KLCR1 may be conferred by its C-terminal TPR motifs, while its very C-terminal disordered region may be crucial for the regulation of apo-CaM-interaction. These data are consistent with *in silico* predictions of CaM-binding regions in KLCR1 by the CaM-target database and the Calmodulation database. These online resources predict a high CaM binding score in the C-terminal half of KLCR1, although the CaM-target database places the highest CaM-binding score for His-KLCR1 within KLCR1_{TR2}, not KLCR1_{TR3}. Additionally, both databases predict a low CaM-binding probability around TPR motif #1 of KLCR1, i.e. the border between KLCR1_{N-term} and KLCR1_{TR1}. Restoration of this region in KLCR1_{N-half} may explain its stronger CaM-interaction compared to the short truncations. The CaM-binding score of KLCR1_{spl} is largely identical to that of KLCR1, with the exception of an additional high-scoring region within KLCR1_{TR3} that is consistent with the Calmodulation database prediction and the experimental data (**Figs. A.14 and 18 C**).

The CaM-binding patterns of truncations of KLCR2 partially overlap with those observed for KLCR1. None of the truncations of KLCR2 interacted with CaM in the presence of EGTA, similar to full length KLCR2. The N-terminal region of KLCR2, His-KLCR2_{N-term}, showed weak but detectable holo-CaM recruitment, while the combination of TPR motifs #2 to #5

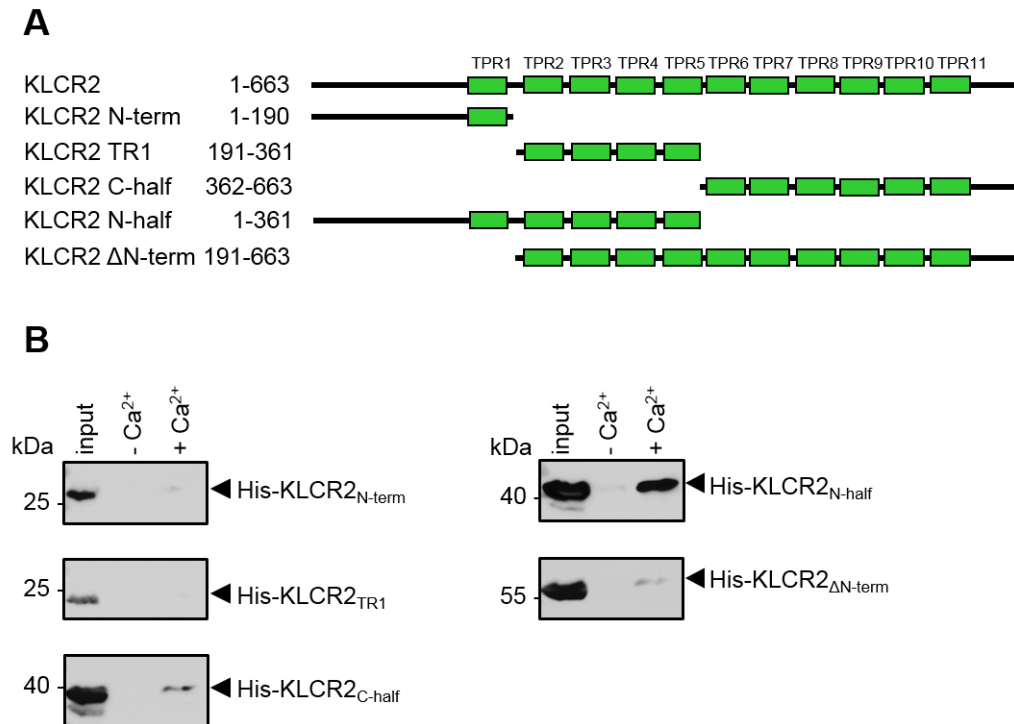


Figure 19: CaM-pulldowns of truncations of KLCR2. **A:** Schematic representation of truncations of KLCR2 (N-term to Δ N-term) showing the respective TPR motifs present in each truncation as green boxes as well as the exact amino acid positions of each truncation. **B:** Western blots of 15 % SDS-PAGEs of CaM-pulldowns with KLCR2 truncations in the presence of 1 mM CaCl_2 (+ Ca^{2+}) or 5 mM EGTA ($-\text{Ca}^{2+}$). Expected positions of KLCR2 truncations are marked with black arrowheads. w: wash, bb: bead-bound.

in His-KLCR2_{TR1} did not result in CaM-recruitment. His-KLCR2_{C-half} was recruited to holo-CaM stronger than His-KLCR2_{N-term} but not as strong as the full length protein (**Fig. 19 B**). In contrast to KLCR1_{N-half}, His-KLCR2_{N-half} exhibited the strongest CaM-binding of the truncations, comparable to full length KLCR2 (**Fig. 13**), while His-KLCR2 _{Δ N-term} showed CaM-binding similar to His-KLCR2_{C-half} in its CaM-recruitment strength (**Fig. 19 B**). Overall, these data indicate differential CaM-interaction of KLCR1 and KLCR2. The main CaM-binding site in KLCR1 is likely located in its C-terminal three TPR motifs and/or the disordered C-terminus. The main CaM-binding site in KLCR2 may be located in the N-terminus of the TPR domain. The N-terminal short truncations of KLCR1 and KLCR2 both showed weak CaM-recruitment that was increased when the the disordered N-terminus and the first three TPR motifs were combined. The CaM-recruitment of His-KLCR2_{C-half} and His-KLCR2 _{Δ N-term} was consistent with KLCR1. The increase in CaM-binding strength observed for His-KLCR2_{N-half} is consistent with a region of a high predicted CaM-binding score around TPR motif #1 in KLCR2 (**Fig. A.15**). In His-KLCR2_{N-term} and His-KLCR2_{TR1} this region

may be disrupted, resulting in decreased CaM-binding capability. The reconstitution of the full CaM-binding region may restore full binding capacity. The *in silico* data also feature a predicted CaM-binding site in the C-terminal region of KLCR2, similar to KLCR1, which is consistent with the experimental data (**Fig. A.15**). Taken together, KLCR1 and KLCR2 are both capable of binding to holo-CaM, although their CaM-binding regions likely differ. Considering the putative role of KLCRs as adaptor proteins, binding to CaM in different regions may confer Ca²⁺ signals to different binding partners that bind either in the N- or C-terminal regions of KLCRs. CaM-mediated Ca²⁺-signalling may additionally affect the stability or changes the dimerisation status of KLCRs by masking putative dimerisation-interfaces.

2.2.3 Cross-linking of KLCRs and CaMs

To gain a more detailed understanding of the structural determinants underlying the differential interaction of KLCR1 and KLCR2 with different CaM-isoforms, cross-linking experiments were carried out. Cross-linking experiments allow for insights into which regions of proteins of interest are in close proximity, by covalently linking the proteins with a chemical cross-linker. In the recent past, cross-linking experiments have been successfully employed in a tandem approach with molecular modelling and existing crystal-structures to generate large-scale 3D models of the endocytic T-plate complex [276]. To assess the binding mode in KLCR-CaM-complexes, as well as suspected KLCR-homo-dimers, KLCRs and CaMs were subjected to chemical cross-linking with the cleavable cross-linker Disuccinimidyl Dibutyric Urea (DSBU) [277]. DSBU is a 12.5 Å molecule that preferentially binds to primary amines, thus linking surface-exposed lysine residues and N-termini in target proteins. DSBU can later be cleaved to identify the linked protein regions by mass spectrometry.

To establish cross-linking conditions for KLCRs and CaMs, initial cross-linking tests were carried out with purified proteins. GST-KLCR1, GST-KLCR2, His-CaM2, and His-CaM4 at a concentration of 5 µM were incubated with a 30- or a 100-fold molar excess of DSBU or a control containing no cross-linker in the presence of 1 mM CaCl₂. Cross-linking efficiency was subsequently assessed by denaturing PAGE. Upon incubation with DSBU input protein bands in the SDS-gels at approx. 100 kDa (KLCRs) or 20 kDa (CaMs) disappeared and a high molecular weight smear of more than 180 kDa appeared in PAGEs, regardless of incubation time or molar excess of DSBU (**Fig. 20**). In the case of CaM4, a second lower molecular weight smear appeared at approx. the same molecular weight as CaM4, indicating residual non-cross-linked CaM4. This was not observed in cross-linking tests carried out with CaM2, which may be attributed to lower amounts of CaM2 in the input samples despite concentration adjustment prior

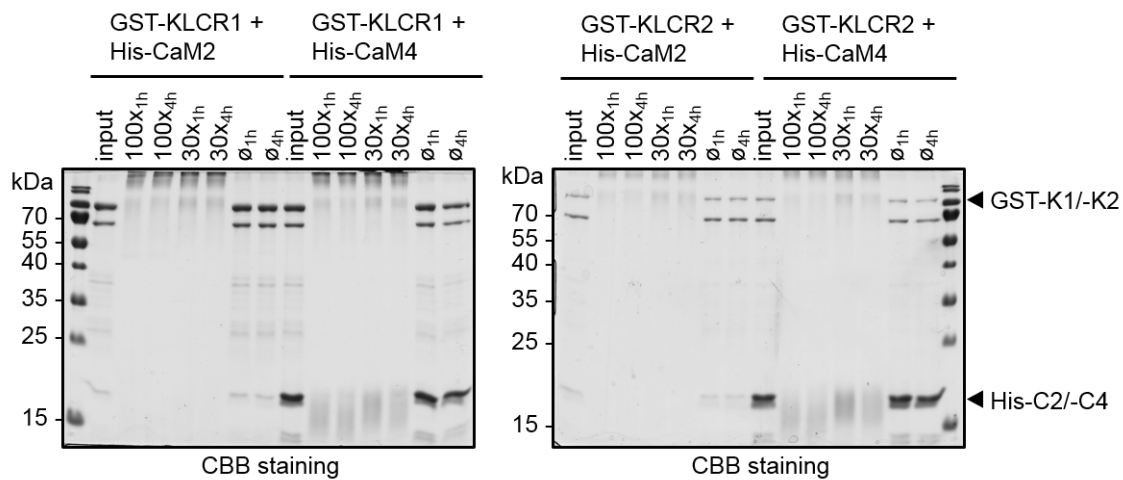


Figure 20: Cross-linking of KLCR1 and KLCR2 with CaM2 or CaM4. 12 % SDS-PAGE of cross-linking results of 5 μ M GST-KLCR1 (K1) and GST-KLCR2 (K2) with His-CaM2 (C2) or His-CaM4 (C4) after one or four hours of incubation without cross-linker (\emptyset) or with 100- or 30-fold molar excess of cross-linker DSBU. Expected positions of GST-KLCRs and His-CaMs are marked with black arrowheads.

to incubation. Incubation of only KLCR1 or KLCR2, or KLCR1 and KLCR2 together resulted in the formation of a similar high molecular weight smear (**Fig. A.16**). These data suggest successful cross-linking of KLCRs with other KLCRs, and with CaMs.

For a comprehensive analysis via LC/MS/MS, the possible effect of protein tags on cross-linking results needed to be eliminated. To generate tag-free KLCRs and CaMs, expression constructs containing a thrombin cleavage site between the affinity tags and the protein of interest were generated and a protocol for purification was established. GH-KLCR1 and -CaM2 were purified via Ni-NTA agarose, showing as bands at approx. 100 kDa or 45 kDa, respectively, in a 12 % denaturing PAGE (**Figs. 21 and A.17 A**). The proteins were immobilised on GSH-agarose and subsequently subjected to tag removal by addition of thrombin, resulting in a shift in molecular weight to 70 kDa for tag-free KLCR1 and 20 kDa for tag-free CaM2 (**Figs. 21 and A.17 B**). KLCR1 was insensitive to unspecific thrombin cleavage, allowing for storage on ice for more than 24 hours in the presence of 50 units of thrombin. CaM2 on the other hand was much more susceptible to thrombin cleavage, making immediate thrombin removal necessary. Both proteins were further purified and separated from remaining thrombin by SEC on either a HiLoad 16/600 Superdex 200 pg column (KLCR1) or a HiPrep Sephacryl S100 HR column (CaM2). Tag-free KLCR1 migrated at a retention volume of 70 ml, while CaM2 was found in a peak at 51 ml. The tag-removal from CaM2 resulted in a significant reduction in its extinction coefficient at 280 nm, making detection via the absorption of its peptide bonds at 230 nm necessary (**Figs. 21 and A.17 C**). After SEC, both proteins showed a sufficient degree of

purity and were concentrated to approx. 1 g/l (KLCR1) or 0.7 g/l (CaM2) (**Figs. 21 and A.17 D and E**). The maximum yield achieved by this method was 300 µg KLCR1 from four liters expression culture and 210 µg CaM2 from three liters expression culture. While these results still leave room for improvement, especially when aiming to generate X-ray structures of these proteins, they were sufficient for cross-linking studies. To confirm successful purification of intact protein, tag-free KLCR1 and CaM2 were subjected to protein identification via mass spectrometry. Both proteins were identified with a sequence coverage of more than 70 % in the case of KLCR1 and 50 % in the case of CaM2. The identification of peptides covering the entire length of both proteins confirmed the purification of intact proteins after tag removal (**Fig. A.18**). The functional integrity of KLCR1 was further confirmed by successful *in vitro* CaM-pulldown of tag-free KLCR1 with CaM-agarose and subsequent detection by denaturing PAGE. Tag-free KLCR1 showed strong recruitment to holo-CaM and only weak recruitment to apo-CaM (**Fig. 22 A**), consistent with previous results. These data suggest the successful generation of stable and intact tag-free KLCR1 and CaM2 for cross-linking experiments and validate that native KLCR1 interacts with CaM.

To gain detailed insights into KLCR-CaM-interactions, tag-free KLCR1 and CaM2 were subjected to cross-linking under the same conditions as previously described. Due to the lack of differences between 100- and 30-fold molar excess of DSBU, 5 µM pure KLCR1 and CaM2 were incubated with 150 µM DSBU for one and three hours in the presence and absence of added CaCl₂ (**Fig. 22 B**). Additionally KLCR1 was incubated alone with DSBU. Cross-linking success was assessed by 10 % denaturing PAGE. Unlike in previous experiments, tag-free KLCR1 did not cross-link with itself, despite the fact that tag-free KLCR1 showed similar migration behaviour during SEC to His-KLCR1. Only faint bands just below 140 kDa appeared after cross-linking. These data suggest a possible need for adjustment of cross-linking conditions for efficient KLCR1-dimerisation. In the case of the KLCR1-CaM2 co-incubation, a band at approx. 100 kDa appeared after cross-linking in addition to the input bands at 70 kDa and 20 kDa, which may correspond to KLCR1-CaM2 complexes (**Fig. 22 C**). In contrast to initial cross-linking tests, the input bands did not disappear completely, suggesting incomplete cross-linking of KLCR1 and CaM2. This may be attributed changes in the biochemical properties of tag-free proteins, or to unfavourable cross-linking conditions that may be improved in future experiments.

To gain further insights into the structural determinants underlying KLCR-CaM interactions, the bands observed at 100 kDa in the samples containing KLCR1 and CaM2 and the faint bands just below 140 kDa in the samples without CaM2 were subjected to LC/MS/MS analysis.

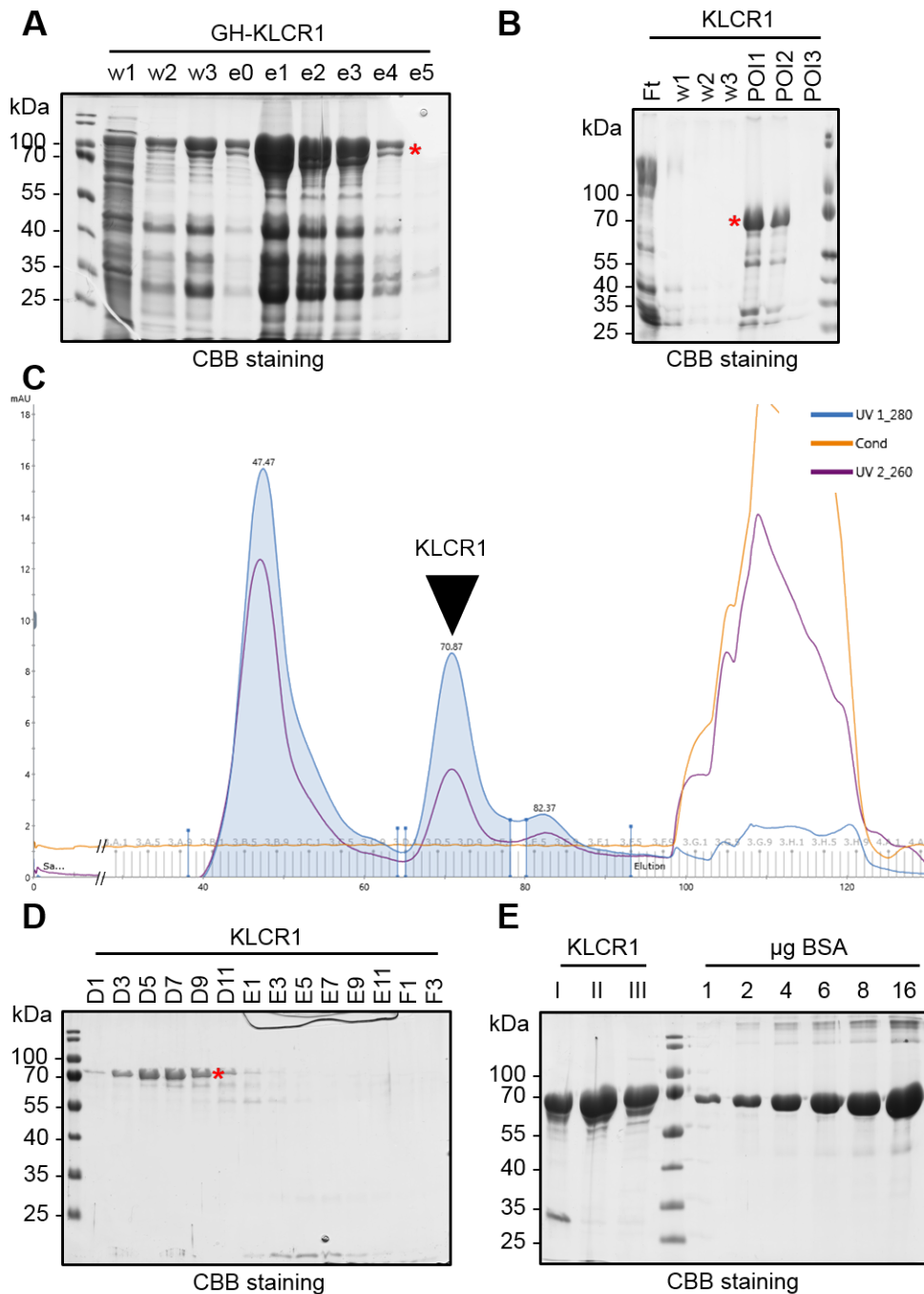


Figure 21: Generation of tag-free KLCR1. **A:** 12 % SDS-PAGE of wash (w1 to w3) and elution (e0 to e5) fractions of affinity purification of GST-His-KLCR1 (GH-KLCR1) via Ni-NTA agarose. GH-KLCR1 is marked with a red asterisk. **B:** 12 % SDS-PAGE of flow-through (Ft), wash (w1 to w3) and protein-of-interest (POI1 to POI3) fractions after tag-removal from GH-KLCR1. **C:** SEC of tag-free KLCR1 on HiLoad 16/600 Superdex 200 pg. The peak corresponding to tag-free KLCR1 is marked with a black arrowhead. **D:** 12 % SDS-PAGE of peak fractions of the SEC in **C**. KLCR1 is marked with a red asterisk. **E:** Concentrated peak fractions of three independent purifications (I to III) of KLCR1 with a BSA calibration curve for concentration determination. KLCR1 can be found at approx. 70 kDa.

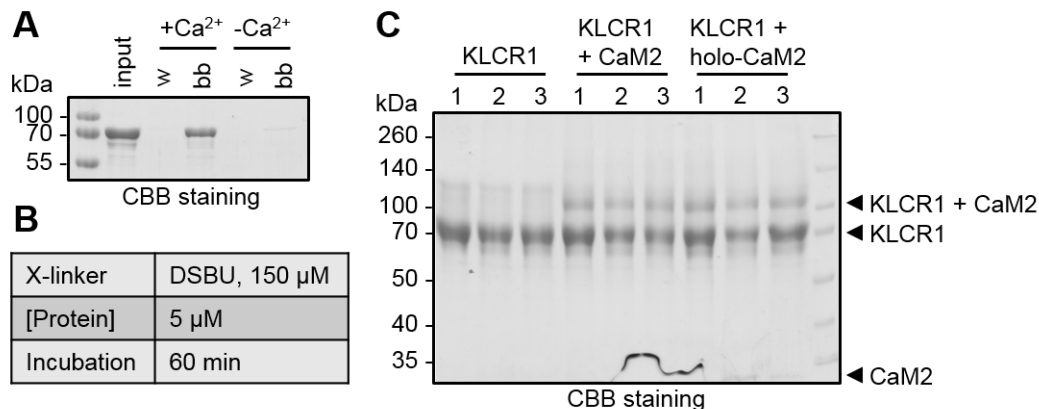


Figure 22: Cross-linking of tag-free KLCR1 and CaM2. **A:** CaM-pulldown of tag-free KLCR1 with CaM-agarose in the presence of 1 mM CaCl₂ (+ Ca²⁺) or 5 mM EGTA (– Ca²⁺). w: wash, bb: bead-bound **B:** Cross-linking conditions used in **C.** **C:** 10 % SDS-PAGE of KLCR1 or KLCR1 and CaM2 after one hour incubation with 30-fold molar excess DSBU in the presence (holo-CaM) or absence of added CaCl₂. Expected positions of KLCR1, CaM2, or the cross-linking product are marked with black arrowheads.

LC/MS/MS analysis followed by assessment of cross-links using the MeroX software identified intra-molecular cross-links within KLCR1 and inter-molecular cross-links between KLCR1 and CaM2. Intra-molecular cross-links within KLCR1 appeared mostly unchanged in the presence of CaM2, suggesting that CaM-binding resulted in no structural changes in KLCR1, or at least no changes in the relative positioning of surface exposed, cross-linked amino acid side-chains (**Fig. A.19**). This is consistent with the reported rigidity of tandem repeat proteins [63]. Interestingly, cross-links between KLCR1 and CaM2 were almost unchanged in samples with 1 mM added CaCl₂ and without the additions of CaCl₂, suggesting either the formation of an artificial complex in the presence of CaCl₂, the presence of residual Ca²⁺ in CaM2 without added CaCl₂, or the stabilisation of an otherwise very transient complex with minor structural differences depending on available Ca²⁺ (**Fig. A.19 B and C**).

The majority of intra-molecular cross-links inside KLCR1 occurred between a short, lysine-rich region within its predicted unstructured, N-terminal region and TPR motifs #5, #7, #8, #10, a short predicted structured region just before TPR motif #1, and the predicted unstructured C-terminus of KLCR1 (**Fig. 23 A**). These data point towards a possible connection between the unstructured N- and C-terminus of KLCR1, or suggest that the N-terminus is very flexible and comes into contact with other, surface exposed regions of the protein. Further cross-links were identified between the flexible linkers connecting TPR motifs #5 and #6 and motifs #6 and #7 and between the linkers connecting TPR motifs #6 and #7 and motifs #7 and #8. These cross-links are likely the result of close proximity between amino acid residues inside the

central cylinder of KLCR1.

Inter-molecular cross-links between KLCR1 and CaM2 concentrated on first and third EF-hand domain of CaM2, the aforementioned lysine-rich region in the N-terminus of KLCR1, the flexible linker between TPR motifs #3 and #4, TPR motif #10, and the flexible C-terminal region of KLCR1 (**Fig. 23 B**). The identified cross-links between CaM2 and the C-terminus of KLCR1 confirm previous findings regarding the *in silico* prediction of CaM-binding sites in KLCR1 and the experimental data suggesting a role for the C-terminus of KLCR1 in CaM-binding (**Figs. A.14 and 18 B**). Cross-links of both termini of KLCR1 with the same regions of CaM2 suggest close proximity of the termini of KLCR1 during CaM-binding. The cross-links to the linker between TPR motifs #3 and #4 may be the result of close proximity between this region and CaM2 through the cylindrical inner groove of KLCR1.

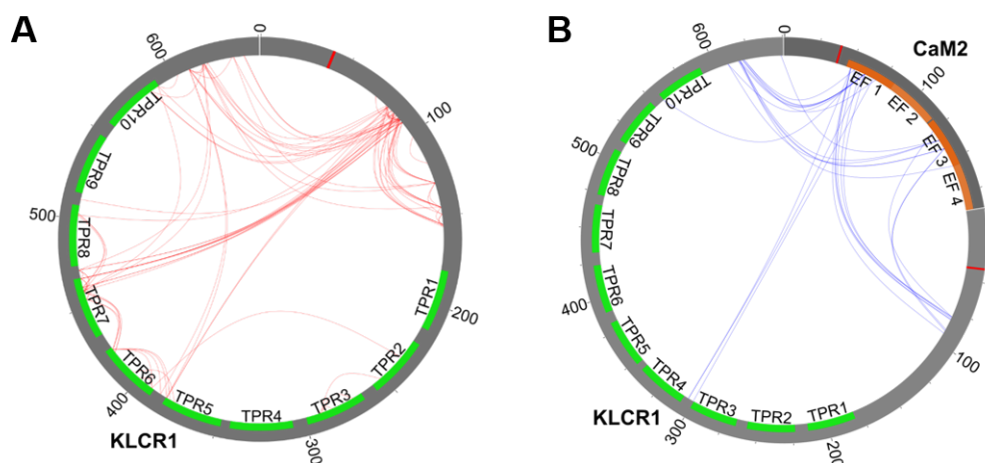


Figure 23: Cross-linking results of tag-free KLCR1 and CaM2. **A:** Intra-molecular cross-links within KLCR1, identified using the MeroX software after LC/MS/MS analysis and visualised using xVis. The TPR motifs of KLCR1 are marked as green boxes. Red lines represent cross-links identified in three independent experiments. **B:** Inter-molecular cross-links between KLCR1 and CaM2. Green boxes represent the TPR motifs in KLCRs, orange boxes the EF-hands in CaM2. Cross-links identified in three independent experiments are represented as blue lines. The bold red lines in **A** and **B** mark the end of the remaining protein tag after protease cleavage. LC/MS/MS measurements and analysis with MeroX were carried out by Dr. Christian Ihling.

2.2.4 *In silico* model of the KLCR1-CaM2-complex

Using the cross-linking data as input, *in silico* models of the KLCR1-CaM2 complex were generated. Monomeric models of KLCR1 and CaM2 were created using the neural network-based prediction algorithm AlphaFold [278]. Model confidence was assessed by Predicted Alignment Error (PAE) and Local Distance Difference Test (IDDT) scores produced by AlphaFold [279]. An IDDT below 50 was considered low confidence and residues were removed for further modelling.

The five best-scored models per protein were assessed and Model 1 of each protein was chosen for further processing. For CaM2, Alphafold identified two domains with high confidence, connected by a linker with low prediction confidence (**Fig. A.20 A**). The two domains correspond to the globular EF-hand domains of CaMs. In KLCR1, the TPR domain was modelled with high confidence, but the putatively disordered N- and C-termini scored below an IDDT of 50, indicating low model confidence due to intrinsic disorder (**Fig. A.20 B**).

To validate the structures, the intra-molecular cross-links detected via LC/MS/MS analysis of

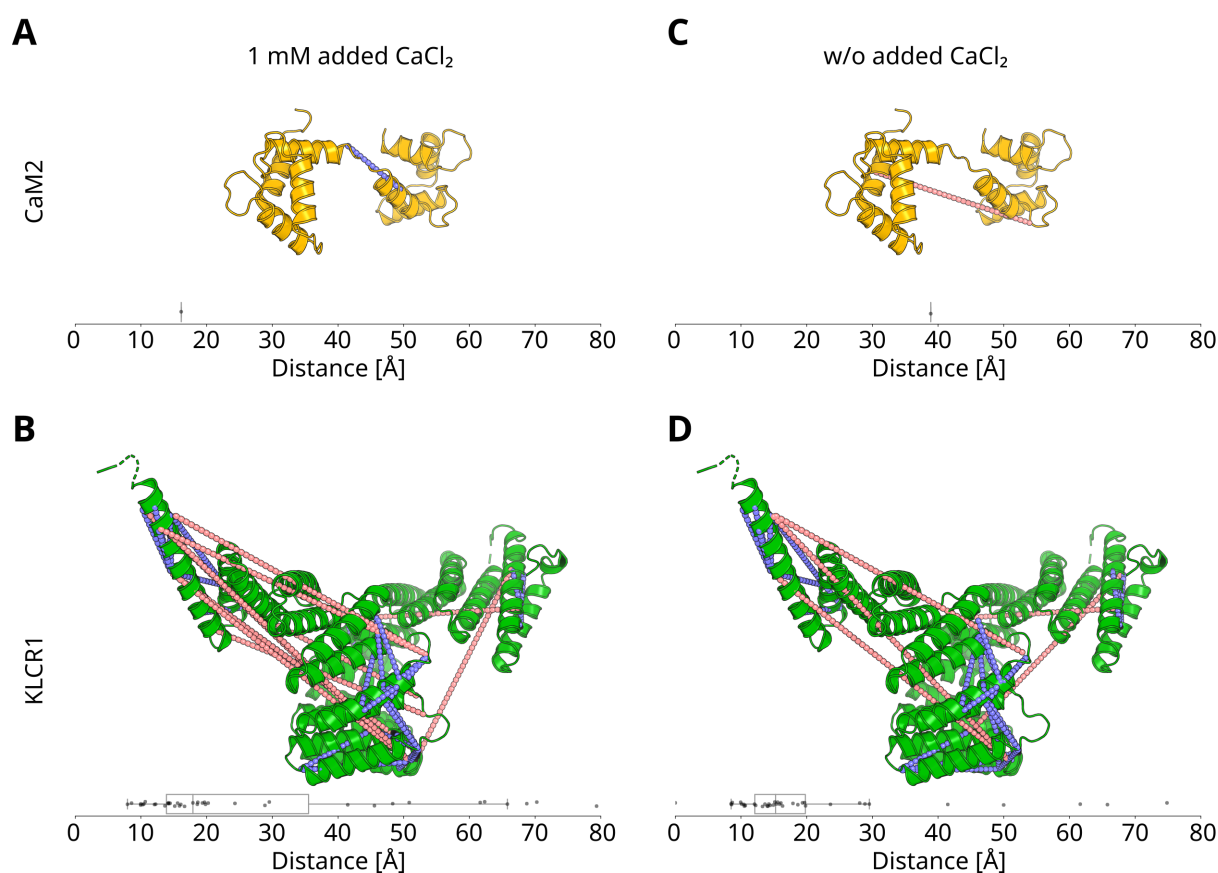


Figure 24: Single Alphafold models of CaM2 and KLCR1 used in MD simulations. Models of CaM2 contain only a single cross-link, each, in the presence (**A**) or absence (**C**) of added 1 mM CaCl₂ with $C\alpha$ -distances of 17 Å and 39 Å between the cross-linked residues. Models of KLCR1 show several intra-molecular cross-links. $C\alpha_{avg}$ between cross-linked residues are 17 Å and 16 Å in the presence (**B**) or absence (**D**) of added 1 mM CaCl₂, respectively. In the presence of CaCl₂, nine cross-links above a $C\alpha$ -distance of 30 Å were mapped, and only five in the absence of added CaCl₂, resulting in a lower spread of $C\alpha$ -distances. Satisfied cross-links below 30 Å are displayed in blue, violated cross-links above 30 Å are displayed in red. Models were generated and curated by Dr. Christian Tüting.

the cross-linking samples of KLCR1 and CaM2 *with* 1 mM added CaCl₂ and *without* added CaCl₂ were mapped onto the models. $C\alpha$ -distances between cross-linked residues were calcu-

lated. Distances below 30 Å were considered satisfied cross-links, and distances above 30 Å were considered violated cross-links. The average distance between the C α atoms of cross-linked residues in a model ($C\alpha_{avg}$) was used as an indicator of model agreement with experimental data. The intra-molecular cross-link detected in CaM2 in the presence of CaCl₂ was satisfied with a C α -distance of 17 Å. The cross-link detected without added CaCl₂ was violated, with a C α -distance of 39 Å, suggesting a different internal orientation of CaM2 to the model (**Fig. 24 A and C**). The presence of a single intra-molecular cross-link in CaM2 allows for no insights into the relative arrangement of the EF-hands and suggests an extended conformation of CaM2 bound to KLCR1 [263]. The intra-molecular cross-links in KLCR1 were mostly satisfied in the absence of added CaCl₂, but showed a larger spread in the presence of added CaCl₂, with a $C\alpha_{avg}$ of 16 Å and 17 Å, respectively (**Fig. 24 B and D**). Both models showed violated cross-links between the C-terminal region of KLCR1 and the core of the TPR domain, but the amount of violated cross-links was lower in the absence of added CaCl₂, indicating better model satisfaction.

Two approaches were used for modelling of KLCR1-CaM2 complexes: (A) The monomeric models were submitted for multimer prediction by AlphaFold multimer [280] and (B) the monomeric models were subjected to *in silico* docking simulations by the HADDOCK docking server [281], using the cross-links as unambiguous distance restraints [282]. Model quality was assessed by $C\alpha_{avg}$. HADDOCK additionally provided insights into the contribution of Van der Waals (VdW), electrostatic (ES), and desolvation (DS) energies on complex formation, allowing for model ranking by energy scores.

AlphaFold multimer generated 25 complex models for each condition, with a wide range of orientations of CaM2 relative to KLCR1 (**Fig. A.21 A**). AlphaFold predicts protein orientation in complexes based on a learned dataset of known protein complexes. The large spread of CaM2-orientations relative to KLCR1 predicted by AlphaFold multimer suggests that the interaction interface between CaMs and KLCRs is not known, yet. Mapping of the cross-links onto the generated models showed that every model was in violation of experimental data, with no model scoring below a $C\alpha_{avg}$ of 30 Å (**Fig. A.21 B**). Most models scored above a $C\alpha_{avg}$ of 40 Å. The best-ranked model by AlphaFold score was model 13 with $C\alpha_{avg}$ of 60 and 52 Å, respectively (**Fig. A.21 B, black arrowheads**). Despite its higher $C\alpha_{avg}$ compared to models 10 (52 and 41 Å), 14 (52 and 40 Å), 17 (58 and 41 Å), or 20 (58 and 41 Å), model 13 was selected for comparative analysis due its AlphaFold score. Model 13 placed CaM2 near the core of the TPR domain of KLCR1 (**Fig. 25 B and D**). HADDOCK models of KLCR1-CaM2 complexes in the presence and absence of 1 mM CaCl₂ were generated by molecular dynamic

(MD) simulations. Water-refined models grouped into clusters by their HADDOCK scores. For each condition, approx. 75 % of water-refined models (148 of 188 and 155 of 192) grouped into a single cluster, indicating a highly confident docking solution (**Figs. A.23 and A.24**). The highest scored model from each condition was used for further analysis. VdW and DS energies differed little within clusters, indicating a minor role in KLCR1-CaM2 interactions. ES energies showed greater variation, correlating with variation in the buried surface area between models, i.e. the protein-protein interaction interface. These data suggest that KLCR1-CaM2 interactions are mainly charge-driven (**Fig. A.22**). HADDOCK models placed CaM2 in the C-terminal region of KLCR1 (**Fig. 25 A and C**), consistent with the fine-mapping of the CaM-binding site of KLCR1 in CaM-pulldowns and the *in silico* CaM-binding scores (**Figs. 18 and A.14**).

To validate model quality, inter-molecular cross-links were mapped onto the best-scored multimeric models created by HADDOCK and Alphafold multimer. Most cross-links were satisfied in the HADDOCK models with a $C\alpha_{avg}$ of 24 Å in the presence of $CaCl_2$, and 25 Å in the absence of $CaCl_2$, indicating good model quality (**Fig. 25 A and C**). Three violated inter-molecular cross-links above a $C\alpha$ -distance of 60 Å were observed in the complex model in the presence of $CaCl_2$, linking CaM2 and the core of the TPR domain of KLCR1 (**Fig. 25 A**). Seven cross-links were violated in the absence of $CaCl_2$, resulting in a greater spread of $C\alpha$ -distances. Distances in violated cross-links were between 30 and 50 Å, connecting CaM2 to the core of the TPR domain and the N-terminus of KLCR1 (**Fig. 25 C**). Model 13 of the Alphafold multimer showed only few satisfied cross-links with a $C\alpha_{avg}$ of 41 Å and 54 Å in the presence and the absence of $CaCl_2$, respectively (**Fig. 25 B and D**). In the presence of $CaCl_2$, two inter-molecular cross-links between CaM2 and the core of the TPR domain were satisfied, but all cross-links between CaM2 and the C-terminus of KLCR1 were violated with $C\alpha$ -distances between 30 and 100 Å (**Fig. 25 B**). No inter-molecular cross-links were satisfied in the model generated in the absence of $CaCl_2$, with $C\alpha$ -distances ranging from 33 to 105 Å (**Fig. 25 D**). Taken together, cross-linking data allowed for the generation of preliminary models of KLCR1-CaM2 complexes with satisfactory quality. Derived Alphafold models of KLCR1 and CaM2 showed high confidence, but complex models generated by Alphafold multimer were lacking in quality. HADDOCK MD simulations indicated that KLCR1-CaM2 interactions are mostly driven by electrostatic interactions. HADDOCK placed the CaM2-binding region in KLCR1 in the C-terminus of the TPR domain, consistent with experimental fine-mapping of the protein-protein interaction site between KLCR1 and CaM2.

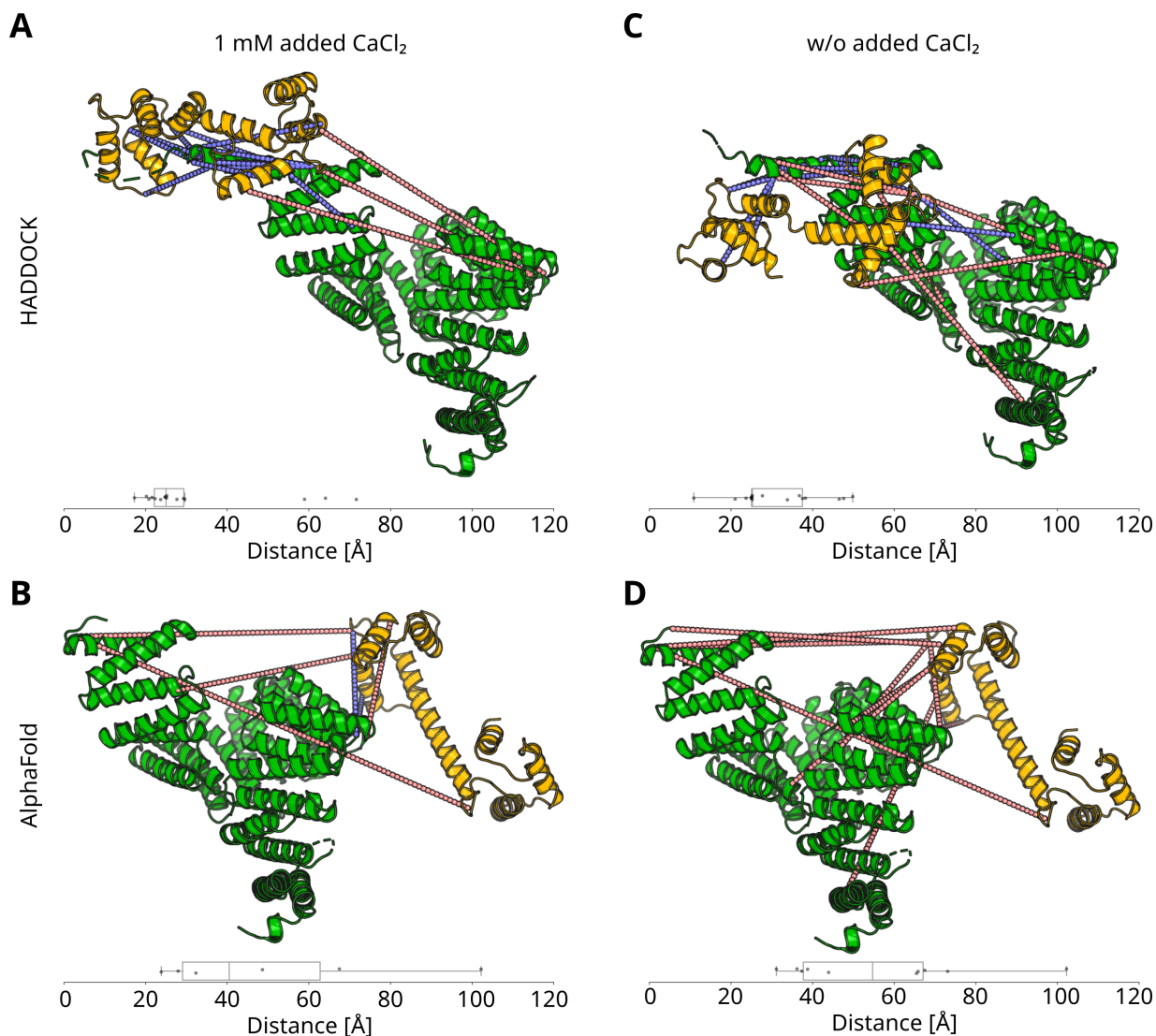


Figure 25: Models of KLCR1-CaM2 complexes generated by HADDOCK or AlphaFold multimer. HADDOCK models were generated using experimentally validated cross-links between KLCR1 and CaM2 in the presence **(A)** or absence **(C)** of 1 mM added CaCl_2 . $C\alpha_{avg}$ in the HADDOCK model in the presence of CaCl_2 is 24 Å with a minor spread in $C\alpha$ -distances and three violated cross-links above 60 Å. $C\alpha_{avg}$ is 25 Å in the absence of added CaCl_2 with seven violated cross-links between 30 and 50 Å. AlphaFold multimer models in the presence **(B)** or absence **(D)** of 1 mM added CaCl_2 show almost no satisfied cross-links with a $C\alpha_{avg}$ 41 Å and 54 Å in the presence and the absence of CaCl_2 , respectively. Two cross-links between CaM2 and the core of KLCR1 was satisfied in the presence of added CaCl_2 . Satisfied cross-links below 30 Å are displayed in blue, violated cross-links above 30 Å are displayed in red. Models were generated and curated by Dr. Christian Tüting.

2.3 Determinants of the subcellular localisation of KLCRs

KLCRs are proposed to play a crucial role in the organisation of protein complex formation at the microtubule cytoskeleton and the plasma membrane. First *in vitro* data suggest that KLCRs possess only weak microtubule binding affinity [120]. When expressed under control of the cauliflower mosaic virus (CMV) 35S promoter in transient assays in *N. benthamiana* leaves, KLCR proteins accumulate in the cytosol (**Fig. 12**). Reduction of expression levels by use of the native, or the Ubiquitin10 (Ub10) promoter results in partial microtubule localisation (**Fig. 26 A**). Microtubule localisation is enhanced in the presence of IQD proteins, suggesting that KLCRs may be recruited by additional adaptor proteins. To identify structural determinants of subcellular localisation of KLCRs, fluorescent protein fusions of KLCR1 and KLCR2 and their truncations were expressed transiently in *N. benthamiana* leaves under the control of different promoters.

When expressed under control of the Ub10 promoter GFP-KLCR1 and -KLCR2 partially localised to the microtubule cytoskeleton, indicated by the labelling of filamentous structures in leaf epidermis cells, while a large fraction remained in a diffuse pattern, indicative of cytosolic localisation (**Figs. 26 and A.26 A**). When expressed under the control of the 35S promoter, the partial microtubule association of both KLCR1 and KLCR2 was abolished and both GFP-fused proteins displayed diffuse fluorescence signals, pointing towards cytosolic localisation (**Figs. A.25 and A.31 A**), consistent with previously published data [123]. Most truncations of KLCR1 (**Fig. 18 A**), except GFP-KLCR1 $\Delta C-term$ and -KLCR1 $\Delta N-term$, showed the same diffuse, likely cytosolic localisation, indicating no interaction with microtubules. This was observed independent of expression strength (**Figs. 26 and A.25 B to H**). Under control of the Ub10 promoter GFP-KLCR1 $\Delta C-term$ and -KLCR1 $\Delta N-term$ both localised to filamentous structures within the leaf cells (**Fig. 26 I and J**), indicating recruitment to microtubules. Under control of the 35S promoter they showed a diffuse, likely cytosolic localisation pattern (**Fig. A.25 I and J**). No truncation of KLCR2 showed microtubule localisation (**Fig. A.26 B to F**).

Partial microtubule localisation of full length KLCR1 and KLCR2 when expressed under control of the Ub10 promoter and abolition of microtubule localisation under control of the 35S promoter suggests that rather than binding directly to microtubules, KLCRs are recruited by an adaptor naturally occurring in *N. benthamiana*. This adaptor may become rate-limiting for efficient microtubule targeting in the presence of an excess of KLCR proteins, leading to masked signals of microtubule-localised KLCRs. The lack of microtubule association of short truncations of either KLCR1 or KLCR2 suggests that no single site in KLCR1 or KLCR2 confers microtubule

binding. The stronger microtubule association of KLCR1 $_{\Delta C-term}$ and -KLCR1 $_{\Delta N-term}$ when compared to full length protein may be an artifact of the truncations. Microtubule association may result from the loss of regulatory elements of microtubule binding in the N- and/or C-terminus of KLCR1, or indicate stronger binding to a potential adaptor protein.

To experimentally assess direct physical association of KLCR1 with the microtubule cytoskeleton, *in vitro* microtubule spin-down assays were carried out with purified GH-KLCR1 and tag-free KLCR1, using *in vitro* assembled and taxol-stabilised microtubules. Earlier publications reported microtubule-binding ability in CaM [283]. GH-CaM2 and -CaM7 were therefore included in spin-down experiments to assess their microtubule association, and possible regulation of microtubule association of KLCR1 via CaM-binding. Proteins of interest were incubated with microtubules for 30 min and subsequently subjected to ultracentrifugation at 50,000 g for 40 min to sediment the microtubules and bound proteins. For co-spin-downs KLCR1 and CaMs were co-incubated with microtubules in the presence of 100 μ M CaCl₂ to facilitate their interaction without disturbing microtubule integrity [284]. A MAP fraction (MAPF) served as the positive control for microtubule binding, while bovine serum albumin (BSA) served as the negative control. Spin-downs were assessed by denaturing PAGE.

Microtubules sedimented after ultracentrifugation, visible at 50 kDa in the pellet. The MAPF control co-sedimented with microtubules, as indicated by a band above 180 kDa in the pellet sample, but remained in the soluble fraction in the absence of microtubules. BSA remained in the soluble fraction in the presence and absence of microtubules, at 70 kDa (**Fig. 27 A and C**). GH-KLCR1 sedimented in the tubulin-free control, indicated by bands at 100 kDa in the soluble fraction and the pellet. The sedimented fraction did not increase upon incubation with microtubules, suggesting no direct binding. GH-CaM2 and -CaM7 remained largely soluble after ultracentrifugation with or without microtubules, indicated by bands just below 50 kDa (**Fig. 27 A and C**). Co-incubation of GH-KLCR1 with either GH-CaM2 or -CaM7 with microtubules resulted in no changes in protein sedimentation compared to incubation of the single proteins with microtubules. Partial sedimentation of GH-KLCR1 and -CaMs was maintained (**Fig. 27 B and D**). These data suggest that KLCR1, CaM2, and CaM7 do not physically interact with microtubules and that CaM-binding of KLCR1 does not affect its microtubule interaction, or its susceptibility to sedimentation.

In vitro interaction between purified KLCR1 and microtubules reported by collaborators had been observed at concentrations of 3.6 μ M KLCR1 (personal communication), while the 5 μ g KLCR1 used for microtubule spin-downs in this thesis resulted in a final KLCR1 concentration of approx. 1 μ M GH-KLCR1 in solution. To assess if KLCR1 interacted with microtubules at

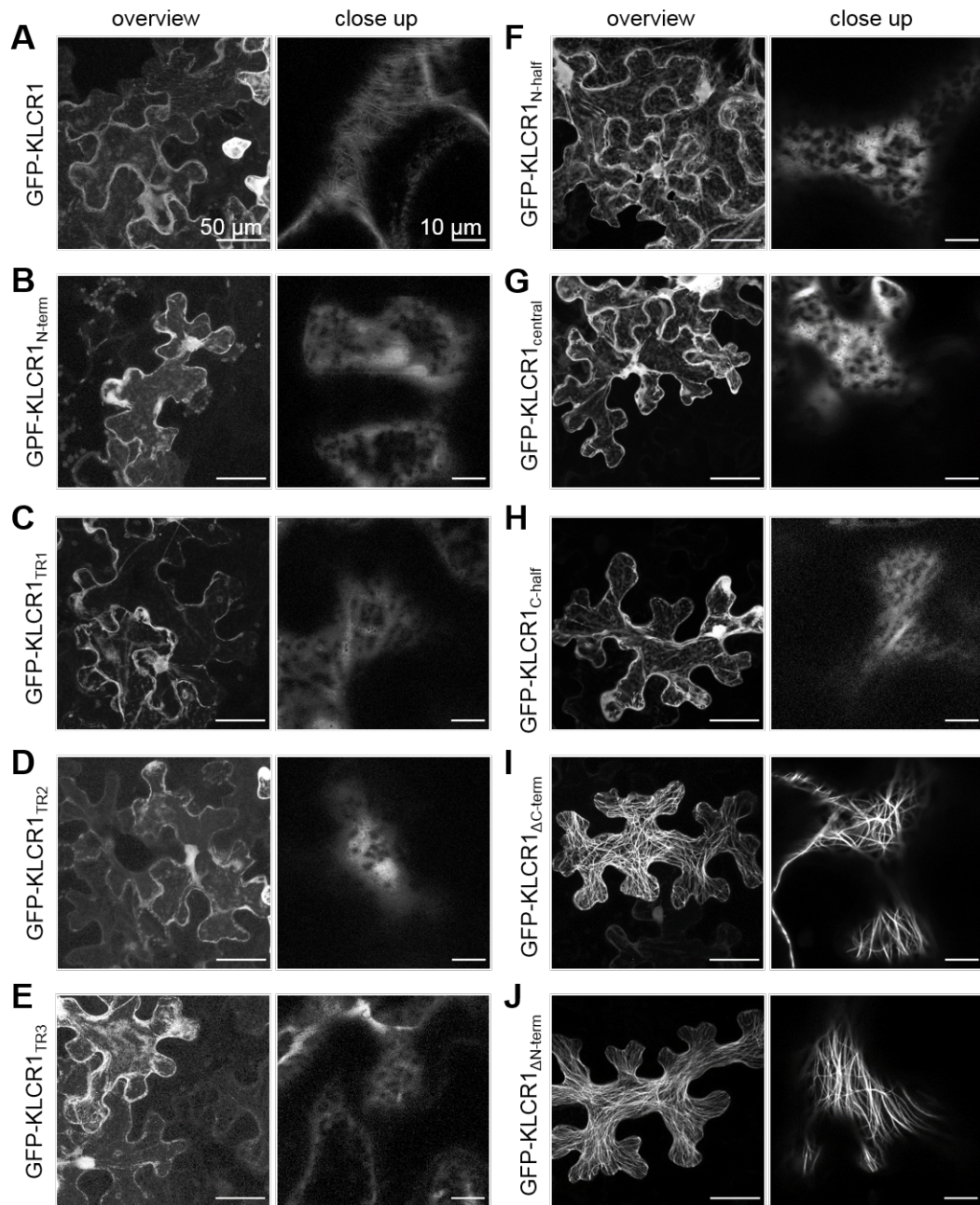


Figure 26: Subcellular localisation of GFP-KLCR1 and its truncations. Subcellular localisation of GFP-KLCR1 (A) or its truncations according to Fig. 18 A (B to J) under the control of the constitutive Ub10 promoter. Scale bars in the overview images represent 50 μm , those in the close up images represent 10 μm .

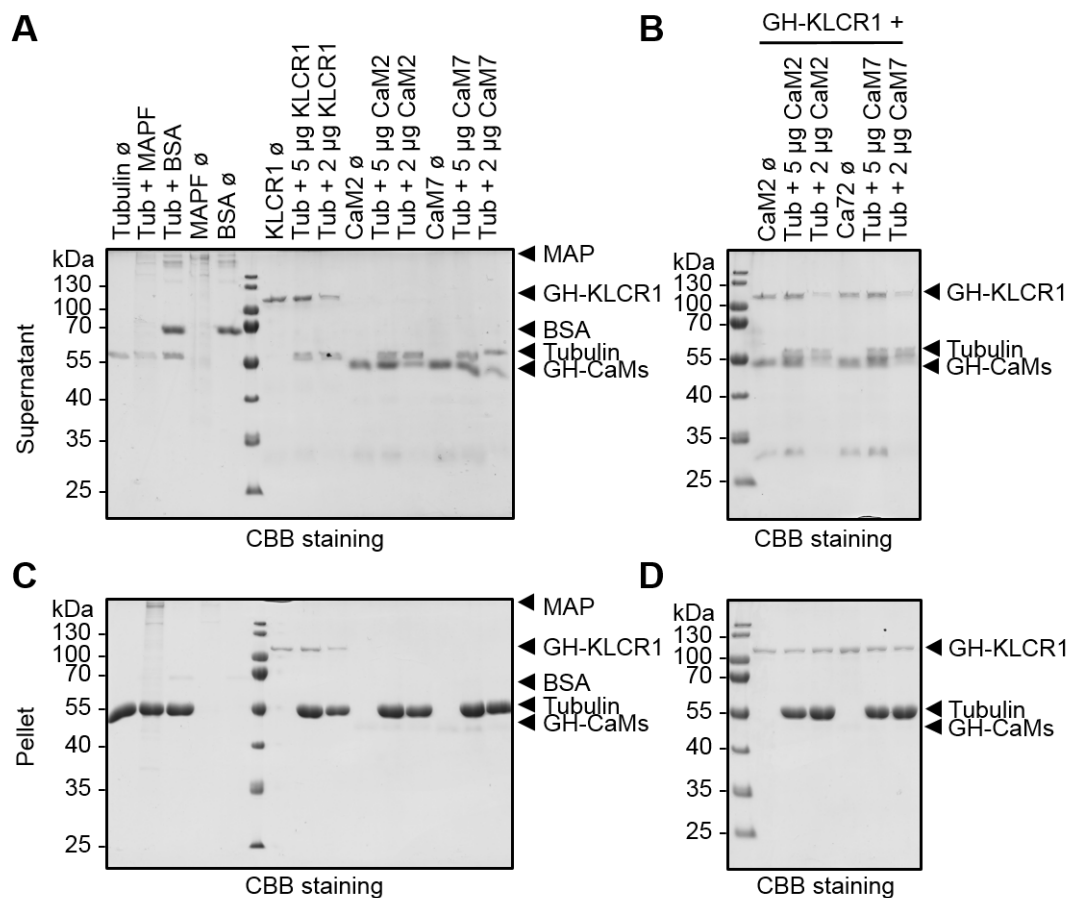


Figure 27: Microtubule spin-down of KLCR1, CaM2, and CaM7. **A:** 12 % SDS-PAGE of supernatant after MT spin-down at 50,000 g for 40 min of control samples, GH-KLCR1, GH-CaM2, and GH-CaM7 with 2 μ M *in vitro* assembled, taxol-stabilised microtubules. Expected positions of the MAP positive control, GH-KLCR1, the BSA negative control, tubulin, and the GH-CaMs are marked with black arrowheads. **B:** Supernatant after MT spin-down of GH-KLCR1 together with GH-CaM2 or GH-CaM7 in the presence of 100 μ M CaCl_2 . **C:** 12 % SDS-PAGE of the pellet corresponding to **A**. **D:** 12 % SDS-PAGE of the pellet corresponding to **B**.

high concentrations, microtubule spin-downs with a concentration gradient of either tag-free KLCR1 against a fixed concentration of 2 μ M tubulin (**Fig. 28 A and B**) or increasing tubulin concentrations against a fixed concentration of 3 μ M tag-free KLCR1 (**Fig. 28 C and D**) were carried out. Spin-downs were assessed by denaturing PAGE. Protein amounts were quantified using ImageJ and MS Excel.

In both spin-down experiments a small fraction of KLCR1 consistently sedimented even in the absence of microtubules, visible as a band at 70 kDa in the soluble fraction (S) and the pellet sample (P). This fraction did not increase with increased concentrations of tubulin from 0 to 8 μ M (**Fig. 28 A**), nor with increasing concentrations of KLCR1 from 0 to 3 μ M (**Fig. 28**

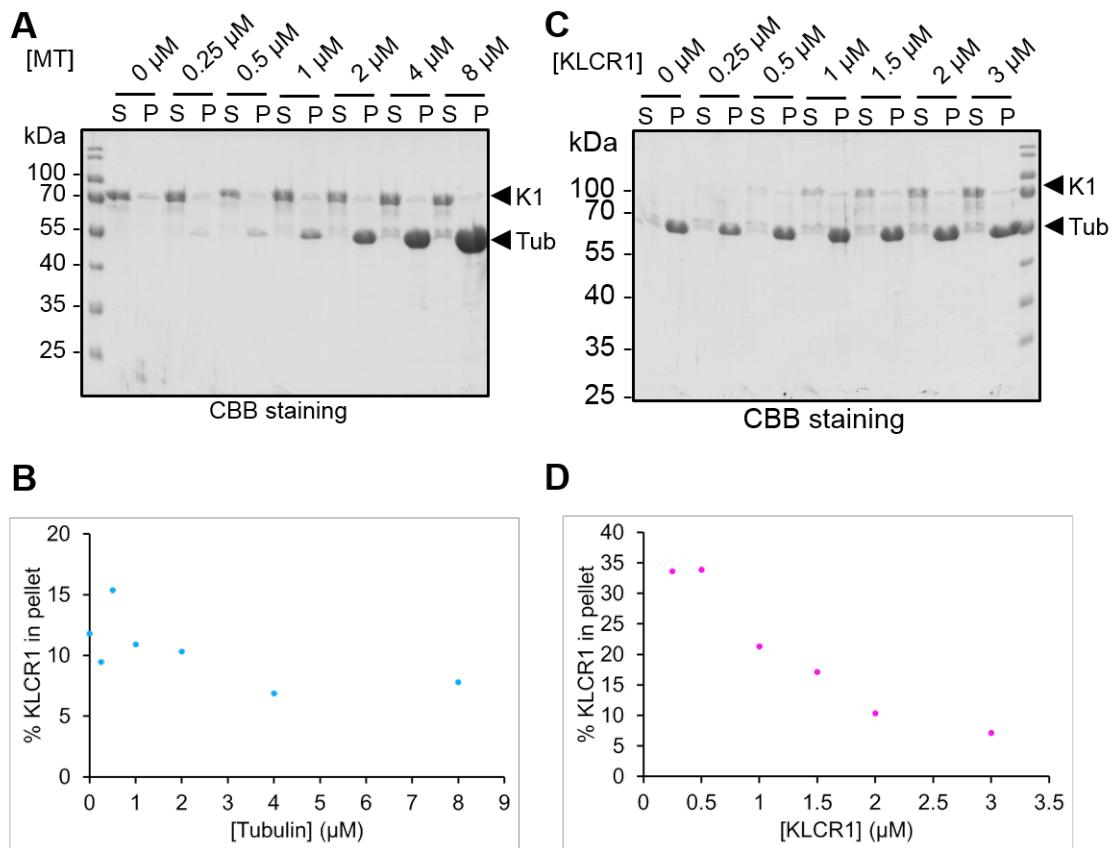


Figure 28: Microtubule spin-down concentration curve of KLCR1. **A:** 12 % SDS-PAGE of MT spin-down of 3 μ M tag-free KLCR1 with increasing concentrations of *in vitro* assembled, taxol-stabilised microtubules, showing supernatant (S) and pellet (P) alongside each other. The expected positions of KLCR1 (K1) and tubulin (Tub) are marked with black arrowheads. **B:** Plot of the percentage of KLCR1 found in the pellet against the tubulin concentration in **A**. **C:** MT spin-down of increasing concentrations of tag-free KLCR1 with 2 μ M *in vitro* assembled, taxol-stabilised microtubules. **D:** Plot of the percentage of KLCR1 found in the pellet against the KLCR1 concentration in **C**.

C). With KLCR1 constant, a fraction of 10 to 15 % of KLCR1 was found in the pellet after ultracentrifugation, regardless of the amount of tubulin added. At tubulin concentrations of 4 μ M and 8 μ M this fraction dipped below 10 % (**Fig. 28 B**). Increasing the KLCR1 concentrations in the presence of a constant amount of tubulin resulted in a steadily decreasing fraction of KLCR1 in the pellet after ultracentrifugation from 35 % to below 10 % of KLCR1 at 3 μ M (**Fig. 28 D**). These data are consistent with the qualitative microtubule spin-downs and confirm that KLCR1 does not interact directly with microtubules.

In conclusion, KLCR1 and KLCR2 localise to filamentous structures that are likely the microtubule cytoskeleton when expressed at low levels in *N. benthamiana* leaves. *In vitro* microtubule spin-downs carried out with GH-KLCR1 as well as tag-free KLCR1 suggest that KLCRs do not

directly bind to microtubules. Co-spin-downs carried out with CaM2 and CaM7 furthermore suggest that CaM-binding of KLCRs does not affect their microtubule affinity. These data point towards an indirect microtubule association of KLCRs through an adaptor protein, rather than direct interaction.

2.4 KLCR-IQD interactions

The plant-specific IQ67 domain proteins (IQDs) have previously been connected to KLCRs and the microtubule cytoskeleton as part of a core-protein-protein interaction module [123] [35]. IQDs thus are likely candidates to act as adaptors between KLCRs and microtubules. Previous work carried out in our group established IQD1, IQD2, and IQD9 as direct interactors of KLCRs [36]. As known CaM-targets IQDs may additionally be involved in Ca_2^+ -signal integration at KLCR-IQD modules, conferring regulatory functions to KLCRs and associated protein complexes [32]. Similar phenotypes in mutants of both *IQD2* and *KLCR1* have recently been identified during root growth and leaf epidermis pavement cell shape formation. Because IQD2 and KLCR1 likely act in the same pathway *in planta* [27], this thesis focused on the characterisation of KLCR-IQD2 interactions as a model for KLCR-IQD modules.

2.4.1 *In silico* assessment of IQD2

To gain initial information about the characteristics of IQD2, its structure and biochemical properties were assessed *in silico* by interrogation of publicly available databases and bioinformatic tools. IQD2 is a protein of 461 amino acids and a molecular weight of 50 kDa. IQD2 possesses the eponymous IQ67 domain, a 67 amino acid long domain containing several CaM-binding motifs, most prominently three IQ-motifs [32]. Outside of the IQ67 domain, IQD2 contains six other motifs of mostly unknown function that are conserved throughout clade III IQDs (**Fig. 29 A**). Motif #6 has recently been identified as part of a DUF4005 domain that confers microtubule association in IQD16 [199].

Disorder prediction of IQD2 marks it as a putative IDP (**Fig. 29 B**), which is further corroborated by the amino acid composition bias of IQD2. Compared to a known set of ordered proteins, the RCSB Protein Data Bank (PDB), IQD2 shows a similar amino acid compositional bias as the Disprot consensus, a database of known IDPs (**Fig. 29 C**). IQD2 displays an over-representation of the amino acids asparagine, arginine, and serine and an under-representation of histidine, aspartic acid, and glycine relative to the Disprot consensus. In the case of histidine and serine, however, the compositional bias of IQD2 is consistent with the Disprot consensus,

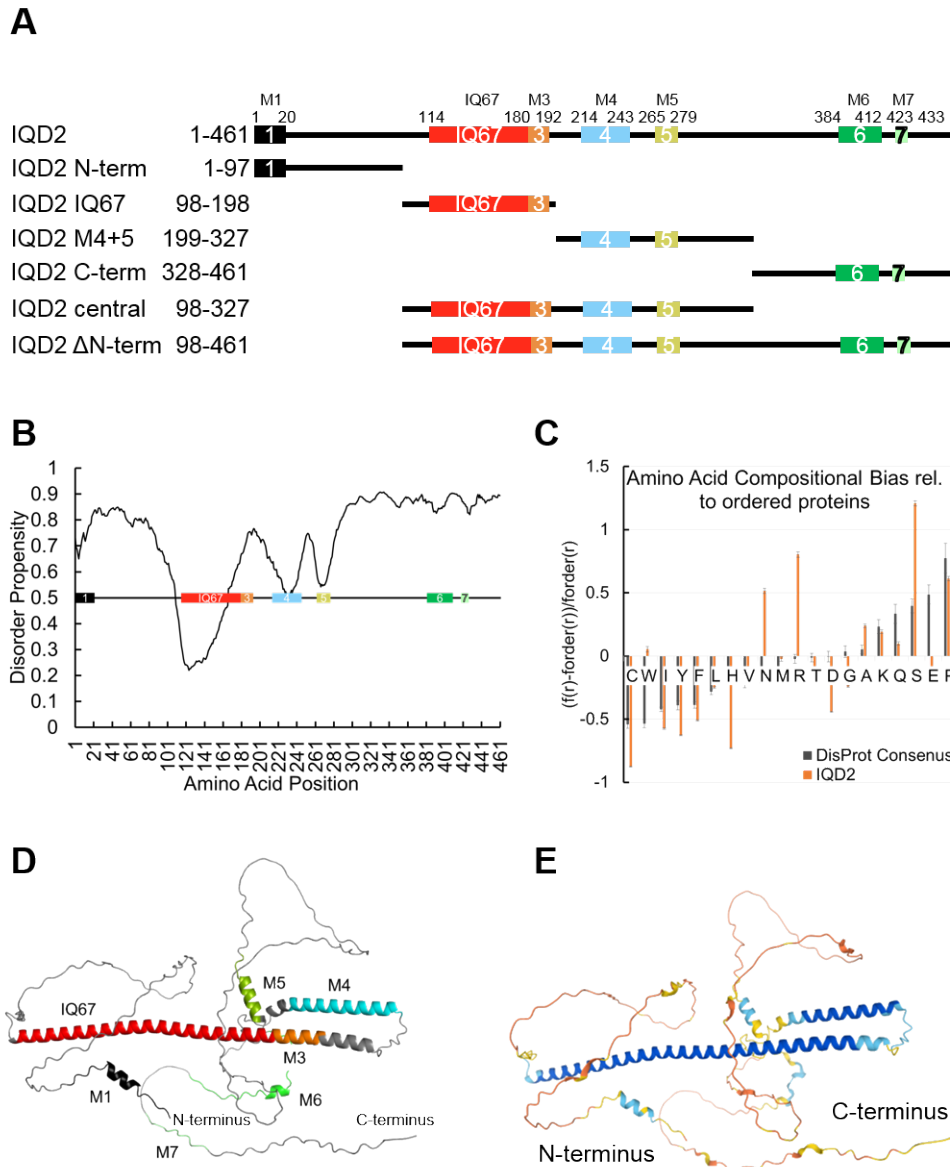


Figure 29: *In silico* analysis of IQD2. **A:** Schematic representation of IQD2 and truncations used in this thesis with conserved motifs as identified by the MEME Suite depicted as coloured boxes. Numbers and amino acid positions of conserved motifs are provided for each motif. The IQ67 domain is marked in red. **B:** Disorder prediction consensus for IQD2. A disorder propensity above 0.5 likely corresponds to a disordered region, while a score below 0.5 is more likely to be structured. **C:** Amino acid compositional bias of IQD2 (orange) and the DisProt consensus (black) relative to known ordered proteins. **D:** AlphaFold 2.0 model of IQD2 with conserved motifs and the IQ67 domain coloured as in **A**. **E:** AlphaFold 2.0 model of IQD2 with prediction confidence indicated by colour scale from high confidence (dark blue) to low confidence (dark orange).

relative to ordered proteins, but exceeds the reference set. Histidine is under-represented in IQD2 compared to ordered proteins, and serine is over-represented, but more so than the Disprot consensus. The majority of the IQD2 sequence is predicted to adopt no defined secondary structure, indicated by a disorder propensity above 0.5. The predicted disorder is interspersed with short regions with a lower disorder propensity. These regions of lower disorder coincide with the conserved motifs found in IQD2, especially the IQ67 domain and motifs #4 and #5 (**Fig. 29 B**), marking them as potential pre-formed MORFs in IQD2.

Currently no 3D structures of IQD proteins exist. The AlphaFold 2.0 model of IQD2 indicates that IQD2 adopts a loose, disordered structure with a low prediction confidence outside of the conserved motifs (**Fig. 29 D and E**). Almost all conserved motifs are predicted to adopt a helical fold with a higher prediction confidence than the putatively disordered regions between them. Likely due to similarity of the IQ67 domain to deposited structures of IQ domains of other CaM-binding proteins (e.g. myosin V, PDB entry 2IX7 [247]), the IQ67 domain shows the highest model confidence. Conserved motif #3 and motif #4 have similarly high modelling confidence, followed by motifs #1, #5, and #6. Motif #7 has a low prediction confidence on par with that of the putative loop regions of IQD2. In agreement with known crystal structures of other CaM-binding helices, the IQ67 domain is predicted to form one long, amphiphatic helix together with conserved motif #3 [132]. Motifs #4 and #5 are predicted to form a second, larger helical arrangement, connected to the IQ67 domain and motif #3 by a short, flexible linker. Conserved motifs, interspersed with disordered regions highlights IQD2 as a putative *bona fide* disordered scaffold protein.

IQD2 has a pI of 10.3 which corresponds to an over-representation of positively charged amino acid residues organised in poly-basic patches (**Fig. 30 A and B**). Poly-basic patches are especially pronounced in conserved motifs #1 and #3, the IQ67 domain and the C-terminal region behind motif #5 of IQD2, while the N-terminal disordered region and motif #5 show a relatively even charge distribution. Electrostatic interactions may mediate binding of IQD2 to negatively charged tubulin tails and membrane lipid head groups, or to overall acidic KL-CRs [285] [152] [286]. The possible reliance on charge-driven interactions may be key to the regulation of IQD localisation and interactions with other proteins through phosphorylation. Phosphorylation of IQD proteins by MPKs MPK3, MPK4, and MPK6 was already shown for IQD1 and IQD2 [36]. Similarly, rice IQD protein GW5 is subject to phosphorylation by GSK2/BIN2 [200]. Further phosphorylation sites of IQDs are annotated in the PhosPhAt database [271], suggesting phosphorylation as a general mode of regulation of IQDs (**Fig. A.29 A**). Due to the putatively flexible nature of IQD2 and the presence of poly-basic stretches, phos-

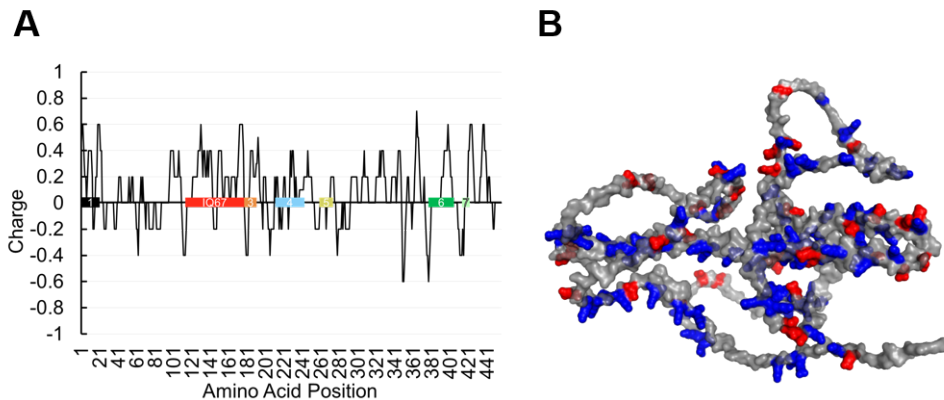


Figure 30: *In silico* analysis of the charge distribution in IQD2. A: Charge plot of IQD2 generated with the EMBOSS charge tool with the schematic representation of IQD2 superimposed. **B:** Cartoon depiction of the AlphaFold 2.0 model of IQD2 with a surface of 40 % transparency superimposed. The negatively charged amino acids aspartic acid and glutamic acid are depicted as red spheres, while the positively charged amino acids arginine, histidine, and lysine are depicted as blue spheres.

phorylation has the potential to alter the organisation and orientation of IQD2 by affecting the local charge. Similar mechanisms were shown for human 4E-BP2, which undergoes disorder-to-order switching upon phosphorylation [287].

Truncations of IQD2 were generated for fine-mapping of the subcellular localisation and protein-protein interactions of IQD2. These truncations divide IQD2 roughly into quarters with the intent to maintain the integrity of the conserved motifs found within them (**Fig. 29 A**). IQD2_{N-term} contains conserved motif #1 and the N-terminal variable region of IQD2. IQD2_{IQ67} encompasses the IQ67 domain and conserved #3. IQD2_{M4+5} covers conserved motifs #4 and #5 of IQD2 and the surrounding variable regions, and IQD2_{C-term} contains the C-terminal variable regions of IQD2 and conserved motifs #6 and #7. IQD2_{central} combines IQD2_{IQ67} and IQD2_{M4+5}, covering the central region of IQD2. IQD2_{ΔN-term} is missing only IQD2_{N-term}, covering the IQ67 domain and the C-terminal half of IQD2.

2.4.2 Subcellular localisation of IQD2

To identify structural determinants of subcellular targeting in IQD2, GFP-fusions of IQD2 and its truncations were transiently expressed in *N. benthamiana* leaves. GFP-IQD2 localised to filamentous structures reminiscent of microtubule localisation *in planta* when expressed under control of the 35S promoter (**Fig. 31 A**). The truncations GFP-IQD2_{N-term}, -IQD2_{IQ67}, and -IQD2_{M4+5} displayed diffuse fluorescence signals, indicating cytosolic localisation of the N-terminus, the IQ67 domain, and motifs #4 and #5 of IQD2 (**Fig. 31 B to D**). GFP-

IQD2_{N-term} and -IQD2_{M4+5} additionally accumulated in punctate structures that suggest either an association with specific membrane sub-domains or the formation of protein aggregates. Considering the size and fluorescence intensity observed in these structures, the accumulation in membrane sub-domains seems more likely for GFP-IQD2_{N-term}, while aggregation seems to be the more likely explanation for GFP-IQD2_{M4+5} (**Fig. 31 B and D, zoomed images**). The C-terminus of IQD2 alone, containing motif #6, partially labelled filamentous structures, indicating microtubule localisation, while a large portion exhibited diffuse, likely cytosolic localisation (**Fig. 31 E**). Combination of IQD2_{IQ67} and IQD2_{M4+5} in GFP-IQD2_{central}, spanning the IQ67 domain and motifs #3 to #5, resulted in partial labelling of filamentous structures, indicating microtubule localisation. GFP-IQD2_{ΔN-term}, spanning IQD2_{central} and IQD2_{C-term}, localised exclusively to filamentous structures in a pattern similar to full length GFP-IQD2, indicating efficient microtubule localisation (**Fig. 31 F and G**).

These findings are consistent with the previously reported subcellular localisation of IQD2 to microtubules [34]. They suggest that direct interaction of IQD2 with microtubules is conferred by the presence of at least two distinct microtubule binding regions (MTBs). Microtubule association of GFP-IQD2_{C-term} points to a conserved role of motif #6, which is part of the DUF4005 identified in IQD16 [199], in mediating microtubule binding in MTB1. A second microtubule binding region (MTB2) is present in GFP-IQD2_{central}. Full microtubule localisation was observed in variants containing both MTBs, suggesting that both microtubule binding regions are required for efficient microtubule binding of IQD2.

To confirm the physical interaction between IQD2 and microtubules, *in vitro* microtubule spin-downs were carried out with purified IQD2 and assessed by denaturing PAGE. IQD proteins have proven challenging to purify due to their low expression rate, sub-optimal solubility in bacterial expression cultures, and low stability after purification. The generation of His-SUMO-tagged IQD2 (HS-IQD2) expression constructs and the establishment of co-expression and co-purification protocols of these constructs with GH-CaMs improved the yield of soluble IQD2 available for *in vitro* studies (**Fig. A.27**). The major drawback of these protocols is the necessary inclusion of GH-CaMs and Ca²⁺ in *in vitro* assays involving HS-IQD2. HS-IQD2 has a calculated molecular weight of 65 kDa. In denaturing PAGEs it migrated at a molecular weight between 70 and 100 kDa. Migration above their expected molecular weight in denaturing PAGEs was consistently observed with all expression constructs of IQD2 and some of its truncations. Whether this deviation from its expected migration pattern is caused by the relatively high pI of IQD2 or other biochemical properties could not be determined conclusively. As controls for unspecific sedimentation of IQD2 and CaMs, spin downs without tubulin were

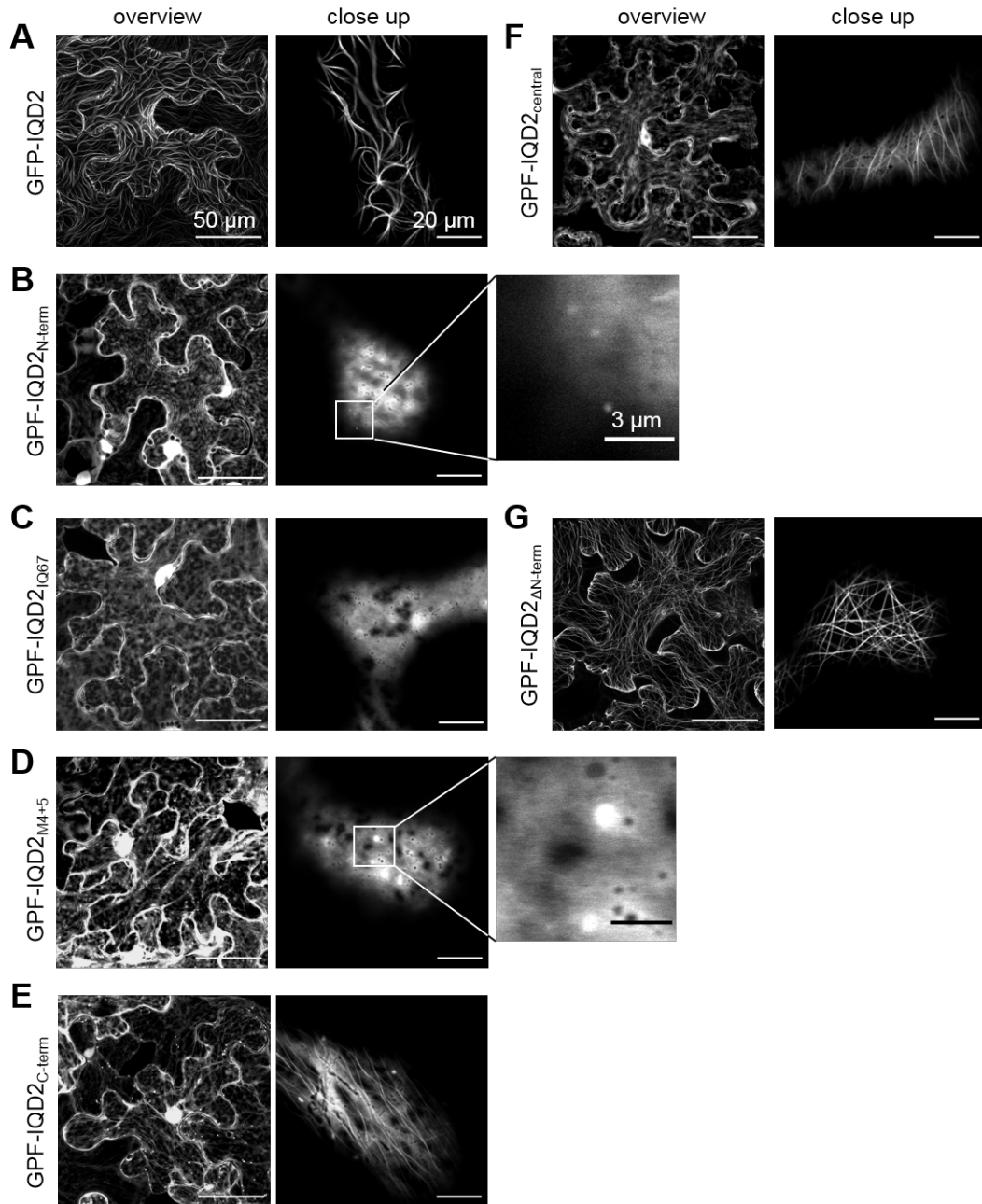


Figure 31: Subcellular localisation of GFP-IQD2. Subcellular localisation of GFP-IQD2 (**A**) or its truncations according to Fig. 29 A (**B** to **J**) under the control of the constitutive 35S promoter. Scale bars in the overview images represent 50 μm , those in the close up images represent 20 μm . Scale bars in the zoomed images in **B** and **D** represent 3 μm . Microscopy was carried out by Jacqueline Patzsch.

performed. MAPF and BSA served as positive and negative control for microtubule interaction. Tubulin controls without added proteins, and MAPF and BSA positive and negative controls showed the same sedimentation described in microtubule spin-downs with KLCR1 and CaMs. MAPF co-sedimented with microtubules, while BSA did not. In microtubule spin-downs in the presence of GH-CaM2 and 100 μ M CaCl_2 HS-IQD2 co-sedimented with microtubules, visible at 70 kDa in the pellet sample, while remaining soluble in the absence of tubulin (**Fig. 32**). Furthermore, IQD2 was capable of recruiting GH-CaM2 to microtubules, detectable as an increase in the amount of CaM2 in the pellet sample in the presence of tubulin compared to spin-downs of CaM2 alone. Due to low solubility and stability of IQD2, these spin-downs could not be carried out with defined protein amounts as was the case for KLCR1 and CaMs. Nonetheless, these findings demonstrate a direct physical interaction between IQD2 and the microtubule cytoskeleton and further support IQD2 as a microtubule-adaptor for CaMs and possibly also KLCRs.

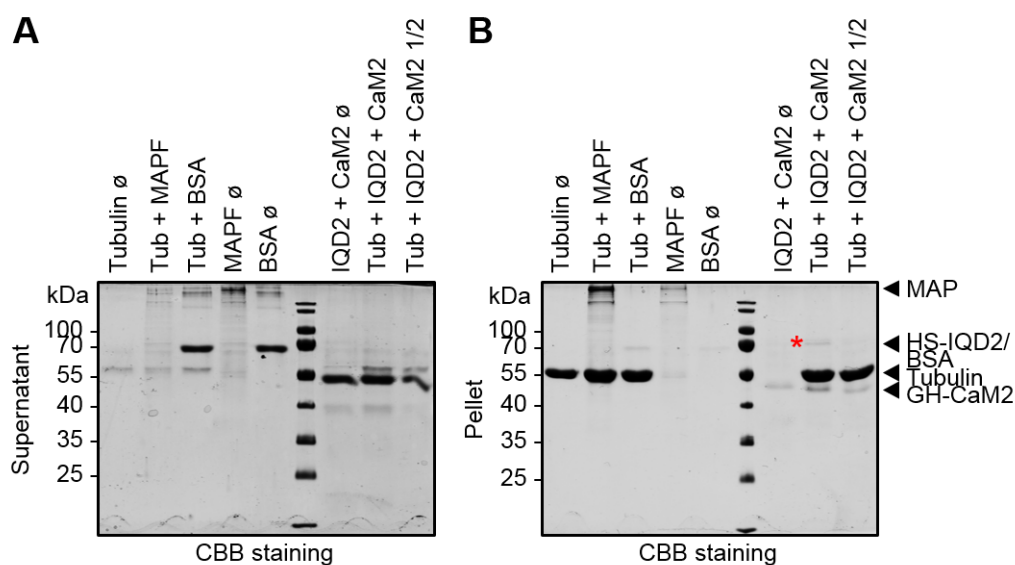


Figure 32: Microtubule spin-down of His-SUMO-IQD2 together with GH-CaM2. **A:** 12 % SDS-PAGE of supernatant after MT spin-down at 50,000 g for 40 min of control samples and His-SUMO-IQD2 (HS-IQD2) together with GH-CaM2 with 2 μ M *in vitro* assembled, taxol-stabilised microtubules in the presence of 100 μ M Ca^{2+} . **B:** Pellet corresponding to **A**. Expected positions of the MAP positive control (MAP), HS-IQD2, the BSA negative control, tubulin, and GH-CaM2 are marked with black arrowheads. The band corresponding to HS-IQD2 is highlighted with a red asterisk.

2.4.3 Binding mode of KLCRs and IQD2

Previous publications showed interactions between KLCRs and IQD1 [123], KLCRs and IQD2 [36] [27] and KLCRs and IQD9 [189]. To further investigate the possible role of IQD2 in KLCR1-recruitment to microtubules, their direct physical interaction was tested in *in vitro* GST-pulldown assays. GST-KLCR1 was immobilised on GSH-agarose beads and incubated with His-IQD2. GST served as the negative control. Immobilisation of GST-KLCR1 and GST was confirmed by detection with an anti-GST antibody in a western blot (**Fig. 33**). Co-recruitment of His-IQD2 to the GSH-agarose by GST-KLCR1 but not by GST was detected with an anti-His antibody as a band at 70 kDa (**Fig. 33**). These data confirm the previously reported direct interaction between IQD2 and KLCR1 [36].

To gain insight into the regions in IQD2 required for interaction with KLCRs a first screen for

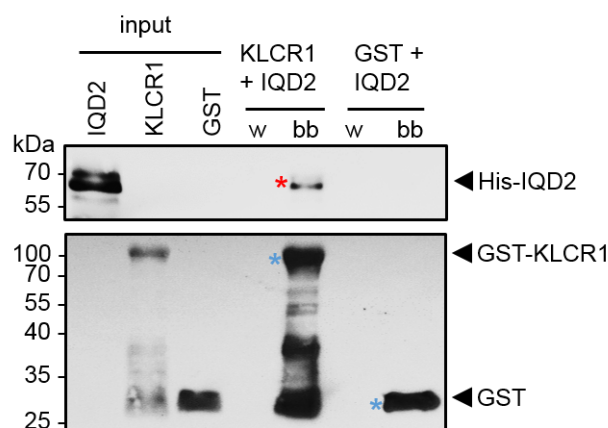


Figure 33: GST-pulldown of His-IQD2 with GST-KLCR1. Western blot of 15 % SDS-PAGE of GST-pulldown of His-IQD2 with GST-KLCR1 or GST alone as a negative control. Expected positions of His-IQD2, GST-KLCR1, and GST are marked with black arrowheads. Bait constructs are additionally marked with blue asterisks, prey constructs with red asterisks. w: wash, bb: bead-bound.

KLCR-binding regions in IQD2 was carried out in the GAL4-based yeast-two-hybrid (Y2H) system. KLCR1, KLCR2, and KLCR3 were expressed as GAL4 activation domain (AD) fusions, due to previously observed auto-activation when fused to the GAL4 DNA binding domain (DBD). IQD2 and its truncations were expressed as DBD fusions. Successful transformation of yeast strain PJ69-4a with both constructs was indicated by growth on vector-selective double drop-out (DDO) medium, while protein-protein interaction between KLCRs and IQD2 constructs was determined by yeast growth on interaction-selective triple drop-out (TDO) and quadruple drop-out (QDO) medium, with medium and high stringency, respectively. TDO with 2.5 mM 3-amino-1,2,4-triazole (3-AT) was used to reduce unspecific growth by inhibition of the His-

metabolism in PJ69-4 [288]. Co-expression of either constructs with the corresponding vector expressing only the AD or the DBD served as a negative control for interaction. All yeast colonies grew on DDO medium, confirming successful transformation with the constructs of interest (**Fig. 34 A**). Growth of colonies expressing full length IQD2 and KLCRs on TDO medium without 3-AT suggests interaction in yeast. Addition of 3-AT reduced yeast growth, suggesting that the interaction (or protein expression) is relatively weak. On high-stringency QDO medium only colonies expressing IQD2 and KLCR2 grew (**Fig. 34 B to D**). No growth was observed for any of the negative controls, confirming that the constructs were not auto-activating and that interactions between the tested protein pairs are specific. These data suggest interaction of IQD2 with all KLCRs, confirming previously reported findings. On medium stringency media, in the absence of 3-AT, auto-activation was observed for IQD2_{M4+5}, IQD2_{C-term}, and IQD2_{central}, as indicated by growth in combination with the empty AD construct (**Fig. 34 B**). Auto-activation was abolished by addition of 3-AT and on high-stringency medium. Co-expression of the short truncations IQD2_{IQ67}, IQD2_{M4+5}, as well as the long truncations containing these two, IQD2_{central} and IQD2_{ΔN-term}, with all KLCRs resulted in yeast growth on TDO containing with 3-AT. Co-expression with KLCR2 and KLCR3 additionally resulted in growth on QDO medium (**Fig. 34 B to D**). These data suggest interaction of IQD2 truncations containing the IQ67 domain and conserved motifs #3, #4, and #5 with all KLCRs. The interaction between IQD2 constructs encompassing motifs #4 and #5 and KLCR3 appeared weaker compared to KLCR2 (**Fig. 34 B to D**). Cells expressing IQD2_{N-term} or IQD2_{C-term} did not grow on TDO or QDO medium when co-expressed with any KLCR, indicating no interaction between the termini of IQD2 and KLCRs, or no expression of these constructs (**Fig. 34 B to D**). These data place the KLCR-interacting region of IQD2 between the IQ67 domain and conserved motif #5. The contribution of motif #3 to KLCR-interaction appears stronger than that of motifs #4 and #5, as indicated by yeast growth on QDO medium. Preliminary data on IQD1 suggest that KLCR1-binding is independent of the IQ67 domain. Interaction of IQD2_{IQ67} may thus be mediated via motif #3, which is part of the truncation. Additional data are needed to fine-map the KLCR binding site in IQD2 to specific amino acid residues. These data suggests partial overlap between the KLCR-binding site in IQD2 and MTB2 required for efficient microtubule recruitment. Additionally, interaction between IQD2 and KLCR2 may be stronger than that between IQD2 and KLCR1.

To further assess the KLCR-binding regions in IQD2 and confirm physical interaction, *in vitro* His-pulldowns were carried out. HS-IQD2 and its truncations were immobilised on Ni-NTA agarose and incubated with GST-KLCR1. GST alone served as the negative control. Due to

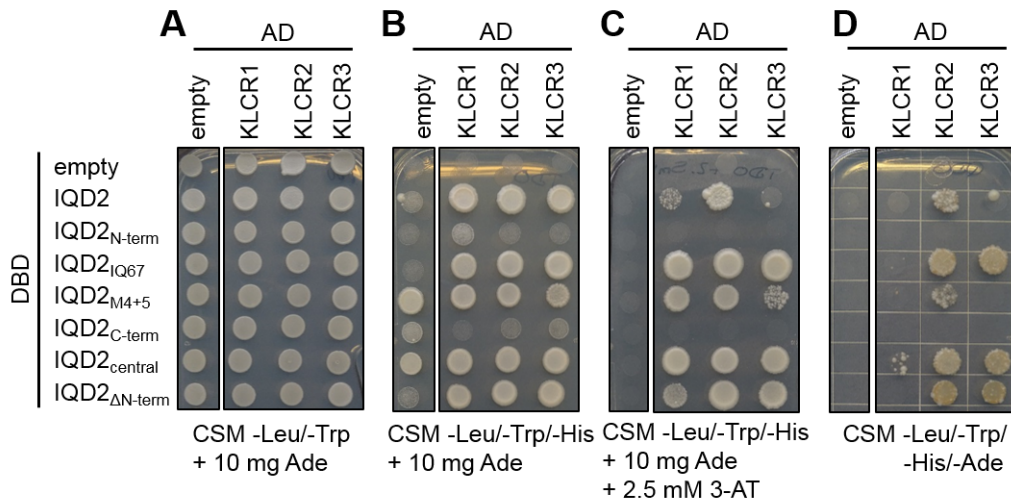


Figure 34: Interaction of IQD2 truncations with KLCRs in yeast-two-hybrid experiments. Yeast-two-hybrid double drop-out (DDO), triple drop-out (TDO), TDO + 2.5 mM 3-AT, and quadruple drop-out (QDO) medium (**A** to **D**, left to right) of IQD2 and its truncations (Fig. 29 A) as DBD fusions and KLCR1, KLCR2, and KLCR3 as AD fusions.

unspecific stickiness of the involved proteins in standard buffer conditions, His-pulldowns were carried out in the presence of 500 mM NaCl to reduce the effect of possible unspecific electrostatic interactions.

Successful immobilisation of HS-IQD2 constructs on Ni-NTA agarose was confirmed by detection with an anti-His antibody in a western blot. Co-recruitment of GST-KLCR1 or GST was detected using an anti-GST antibody. Recruitment of GST-KLCR1 to Ni-NTA agarose was observed with all truncations containing the IQ67 domain and motif #3, or motif #4 to motif #5, i.e. HS-IQD2_{IQ67} (35 kDa), -IQD2_{M4+5} (37 kDa), -IQD2_{central} (50 kDa), and -IQD2_{ΔN-term} (70 kDa), and full length IQD2 (90 kDa), indicating direct interaction with KLCR1 (**Fig. 35 A**). In addition, weak recruitment of GST-KLCR1 was detected in combination with the N-terminal and C-terminal truncations of IQD2 (i.e. HS-IQD2_{N-term} and -IQD2_{C-term}) alone (**Fig. 35 A**). Co-incubation of GST with HS-IQD2 constructs resulted in faint co-recruitment to Ni-NTA with HS-IQD2_{N-term}, HS-IQD2_{M4+5}, and HS-IQD2_{C-term}, but not with any other construct (**Fig. 35 B**), suggesting that these signals result from unspecific binding. These data are consistent with the Y2H experiments in placing the KLCR1-binding site in IQD2 between conserved motifs #3 and #5. Co-incubation of GST-KLCR1 with IQD2_{IQ67} and IQD2_{central} resulted in only slightly less GST-KLCR1 pulled from solution than with IQD2_{M4+5} or IQD2_{ΔN-term}, despite lower amounts of these truncated IQD2 versions bound to the Ni-NTA agarose. These data, together with the preliminary data from IQD1 suggest that motif #3 of IQD2 may be

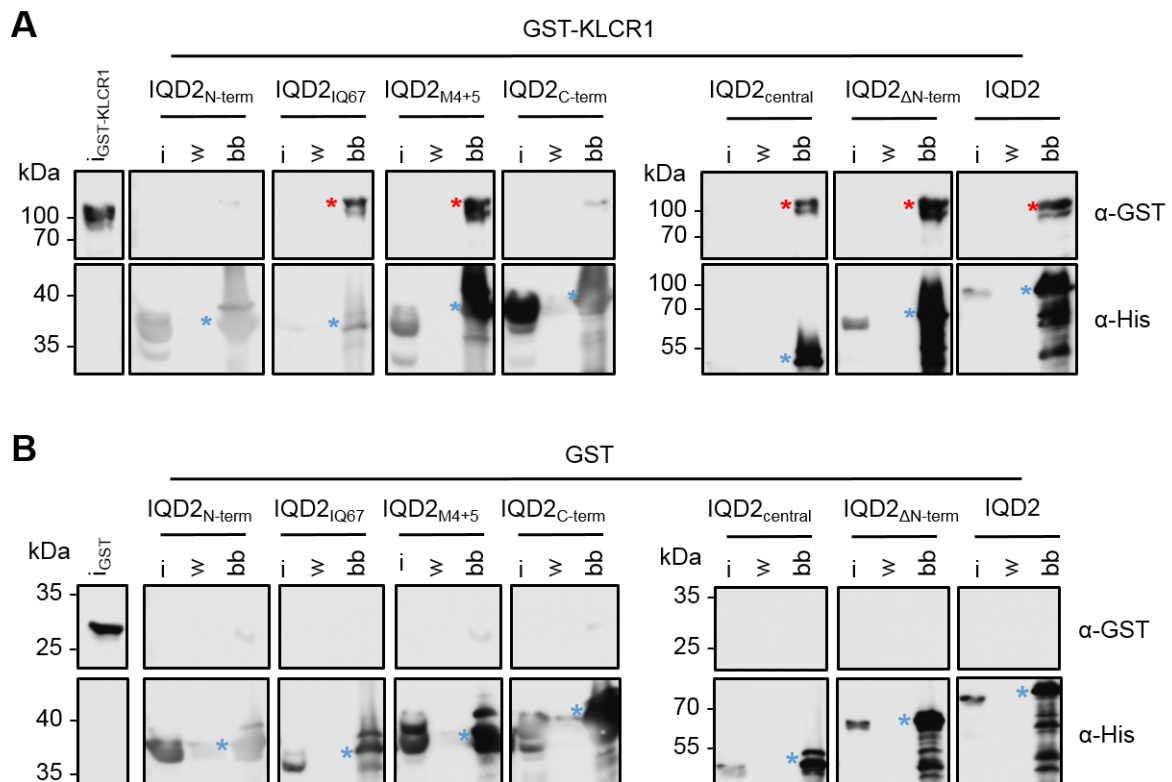


Figure 35: His-pulldown of GST-KLCR1 with HS-IQD2 and its truncations. A: Western blot of 12 % SDS-PAGE of His-pulldown of GST-KLCR1 with HS-IQD2 or its truncations according to Fig. 29 A under high salt conditions (500 mM NaCl). Bait constructs are marked with blue asterisks, prey constructs with red asterisks. i: input, w: wash, bb: bead-bound. **B:** Western blot of the negative control to **A** carried out with GST alone. Bait constructs are marked with blue asterisks.

crucial for efficient KLCR1 interaction. It also supports the putatively relatively minor role of motifs #4 and #5 compared to motif #3 in IQD2-KLCR1 binding. Furthermore, it points to a possible role for the flexible regions in the C-terminus of IQD2 in regulating protein-protein interactions. The outcomes between the pulldowns carried out with different salt concentrations did not differ in principle, but the amount of GST-KLCR1 pulled from solution was reduced under high salt conditions (**Figs. 35 A and A.28**). This observation supports the hypothesis of charge-driven mechanisms as the main facilitator of IQD-KLCR-interactions.

To fine-map the IQD2 binding site in KLCR1, *in vitro* His-pulldowns between HS-IQD2 and GST-tagged truncations of KLCR1 were performed. GST served as a negative control (**Fig. 35 B**). Immobilisation of HS-IQD2 on Ni-NTA agarose was confirmed by detection with an anti-His antibody in a western blot, while GST-tagged KLCR1 constructs were detected with an anti-GST antibody. Co-incubation of HS-IQD2 with any of the short fragments of KLCR1, or

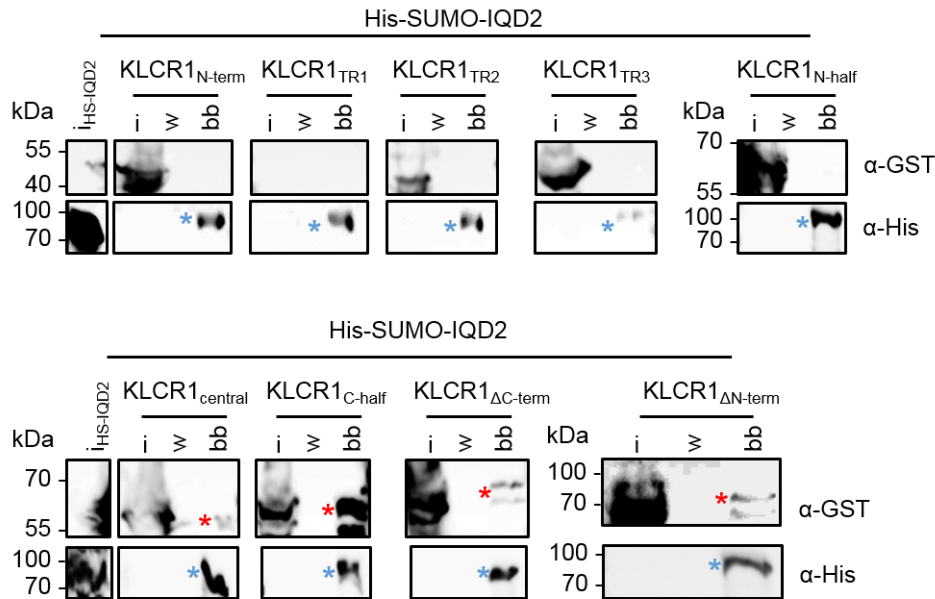


Figure 36: His-pulldown of GST-KLCR1 truncations with HS-IQD2. Western blot of 12 % SDS-PAGEs of His-pulldown of GST-KLCR1 truncations according to Fig. 18 A with HS-IQD2. Bait constructs are marked with blue asterisks, prey constructs with red asterisks. Pulldown of GST-KLCR1 and GST with HS-IQD2 shown in Fig. 35 A and B served as the positive and negative control. The pulldown was carried out by Jacqueline Patzsch. i: input, w: wash, bb: bead-bound.

GST-KLCR1_{N-half} did not result in co-recruitment of the GST-constructs to Ni-NTA agarose (**Fig. 36**), indicating no interaction. GST-KLCR1_{central}, -KLCR1_{C-half}, -KLCR1_{ΔC-term} and -KLCR1_{ΔN-term} were co-recruited to Ni-NTA agarose by co-incubation with HS-IQD2 (**Fig. 36**), indicating direct interaction. These data suggest a role for the C-terminal half of the TPR domain of KLCR1 in IQD2-binding. Interaction between HS-IQD2 and GST-KLCR1_{C-half} appeared stronger than with any other truncation of KLCR1. This points toward the location of the IQD2-interacting region in KLCR1 in its C-terminal half. Considering the strong over-representation of negatively charged amino acid residues in this region of KLCR1 (**Fig. 9 A**), a potential role of electrostatic interactions in IQD2-binding seems plausible. These findings were consistent with Y2H experiments testing for interaction between the truncations of IQD2 and KLCR1 expressed as DBD or AD fusions, respectively. Co-expression of full length KLCR1 with IQD2_{M4+5} and IQD2_{ΔN-term} resulted in strong yeast growth on TDO medium, and faintly with full length IQD2. Co-expression of KLCR1_{C-half} with IQD2_{central} also resulted in weak yeast growth on TDO medium (**Fig. A.30**), confirming previous Y2H experiments and indicating interaction between the C-terminal of KLCR1 and the central region of IQD2.

Taken together, these findings narrow down the location of binding sites required for interac-

tion between KLCR1 and IQD2 to the central region of IQD2, encompassing the IQ67 domain and conserved motifs #3 to #5, and to the C-terminal half of the TPR domain of KLCR1. Combined with preliminary data from IQD1, suggesting that the IQ67 domain does not contribute to KLCR-IQD-binding, conserved motif #3 may contribute the most to KLCR1-binding of IQD2, while motifs #4 and #5 may fulfil a supporting role. On the side of KLCR1, the protein's C-terminus confers IQD2-interaction but a greater resolution of this interaction to a specific TPR motif was not possible. One explanation may be that no single TPR motif confers IQD2 interaction, but rather a certain number of TPR motifs together form an IQD2-binding structure in KLCR1. This may be further investigated by structural elucidation of KLCR1-IQD2 complexes.

2.4.4 Subcellular localisation of IQD2-KLCR complexes

The interaction of IQD2 and KLCRs has been demonstrated, as well as the localisation of IQD2 to microtubules *in planta* and *in vitro*. To assess whether IQD2 is capable of recruiting KLCRs to the microtubule cytoskeleton and to fine-map the regions required for this function, GFP-IQD2 and its truncations were transiently co-expressed with RFP-KLCRs and the truncations of KLCR1 in *N. benthamiana* leaves under control of the 35S promoter.

Consistent with previous data, RFP-KLCRs localised to the cytosol (**Figs. 37, A.31, and A.32 A**), while GFP-IQD2 labelled the microtubule cytoskeleton (**Fig. 31 A**). When co-expressed with GFP-IQD2, RFP-KLCRs were recruited to microtubules as indicated by co-localisation of GFP-IQD2 and RFP-KLCRs (**Figs. 37, A.31, and A.32 B**). This was supported by fluorescence overlap of GFP- and RFP-fluorescence in a fluorescence profile. Co-expression of GFP-IQD2_{central} with RFP-KLCRs mostly resulted in a loss of the microtubule association of IQD2_{central} (**Fig. 31 F**), while RFP-KLCRs remained in the cytosol (**Figs. 37, A.31, and A.32 D**). In a small subset of cells, GFP-IQD2_{central} remained at the microtubule cytoskeleton when co-expressed with RFP-KLCRs, but did not recruit KLCRs (**Fig. A.33**). These findings suggest that KLCR-binding in MTB2 out-competes microtubule binding. It also shows that, while IQD2_{central} is necessary for KLCR-binding of IQD2, it is not sufficient for recruitment of KLCRs to the cytoskeleton. The localisation of IQD2_{central} to microtubules in a subset of cells, but failure to recruit KLCRs further supports the exclusive nature of KLCR- and microtubule-interaction. Co-expression of RFP-KLCRs with GFP-IQD2_{C-term} did not result in changes in subcellular localisation of either construct. GFP-IQD2_{C-term} continued to partially label the cytoskeleton, while the KLCRs remained cytosolic (**Figs. 37, A.31, and A.32 C**), consistent with their lack of interaction. When MTB1 and MTB2 were combined in GFP-IQD2_{ΔN-term},

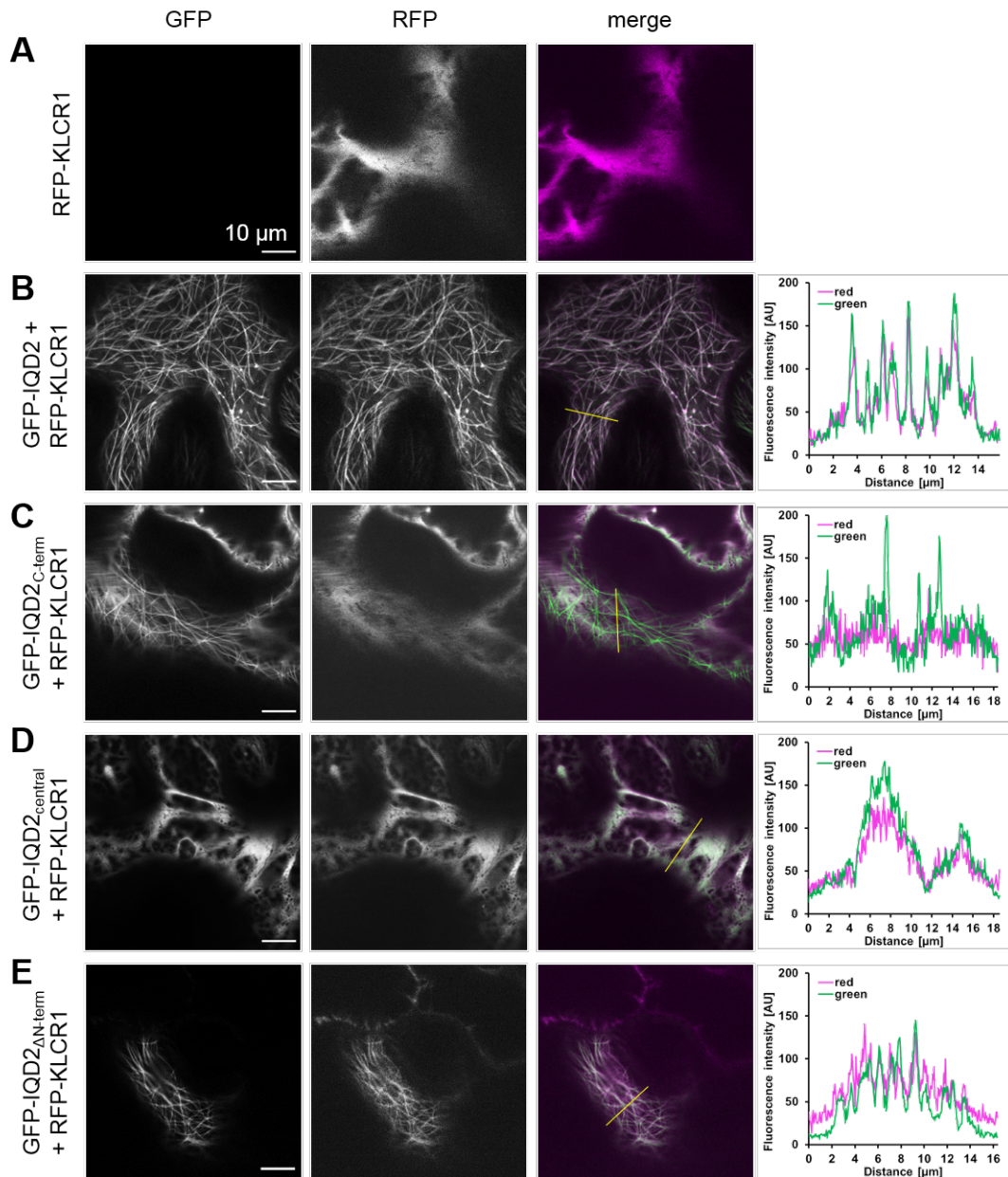


Figure 37: Co-localisation of IQD2 and KLCR1 in *N. benthamiana* leaves. **A:** Subcellular localisation of RFP-KLCR1 under control of the 35S promoter. **B to E:** Co-expression of GFP-IQD2 and its truncations with RFP-KLCR1 under control of the 35S promoter. Scale bars represent 10 μm . Fluorescence profiles were generated along the yellow lines in the "merge" images.

RFP-KLCRs were efficiently recruited to microtubules to levels comparable to full length IQD2 (**Figs. 37, A.31, and A.32 E**). These findings suggest that microtubule binding of the central MTB2 of IQD2 is out-competed by KLCR1 binding and that the C-terminal MTB is required to anchor IQD2-KLCR complexes at microtubules. Results observed upon co-expression of KLCR1, KLCR2 or KLCR3 with IQD2 and truncated IQD2 variants were comparable, indicating no differences of different KLCRs on microtubule localisation of IQD2. These data indicate that regulation of the central MTB2 is conserved for all three KLCR isoforms.

Co-expression of GFP-IQD2 with the truncations of KLCR1 resulted in recruitment of RFP-KLCR1, -KLCR1_{N-half}, -KLCR1_{central}, -KLCR1_{ΔC-term}, and -KLCR1_{ΔN-term} to the microtubule cytoskeleton (**Fig. A.35**), while the short truncated RFP-KLCR1 constructs and RFP-KLCR1_{C-half} exhibited diffuse, likely cytosolic localisation (**Figs. A.34**). These data are mostly consistent with earlier findings, placing the IQD2 binding site in the C-terminus of KLCR1. The recruitment of RFP-KLCR1_{N-half} but not of -KLCR1_{C-half} to the microtubule cytoskeleton by GFP-IQD2 requires further assessment.

Our previous work indicates that KLCRs form homo-dimers and hetero-dimers with other KLCRs (**Fig. 11 and 12**). To assess whether IQD2 interacts with and recruits KLCR-dimers to the microtubule cytoskeleton, CFP-IQD2 was co-expressed with combinations of BiFC-pairs VYNE-KLCR1, VYCE-KLCR1, and VYCE-KLCR2 in *N. benthamiana* leaves. Consistent with previous data, CFP-IQD2 labelled the microtubule cytoskeleton (**Fig. 38 A**), while dimers of VYNE-KLCR1 and VYCE-KLCR1, and of VYNE-KLCR1 and VYCE-KLCR2 accumulated in the cytosol (**Fig. 38 B and C**). Upon co-expression with CFP-IQD2, YFP-fluorescence was observed at microtubules, suggesting that IQD2 efficiently recruited KLCR1-homo-dimers, and KLCR1-KLCR2-hetero-dimers (**Fig. 38 D and E**). These data indicate that IQD2 is capable of interacting with KLCR-dimers *in vivo* and that interaction with KLCR-dimers does not affect the subcellular localisation of IQD2 or its ability to recruit KLCRs to microtubules.

2.5 IQD2-CaM interactions

IQD proteins were originally identified as the largest group of plant-specific CaM-interactors [32], and binding of IQD2 to bovine CaM had been demonstrated previously [36]. Thus, the interaction of KLCRs and IQD2 – and the assembly and dynamics of KLCR-IQD modules – may be subject to CaM-mediated regulation orchestrated by IQD2-CaM interactions. IQDs are named after their IQ67 domain, a domain shown to confer holo- and apo-CaM binding [32]. Previous work demonstrated that the IQ67 domain is required and sufficient for CaM binding in IQD1, which is encoded by the sister gene of IQD2 [123] [36]. To validate that the IQ67 domain

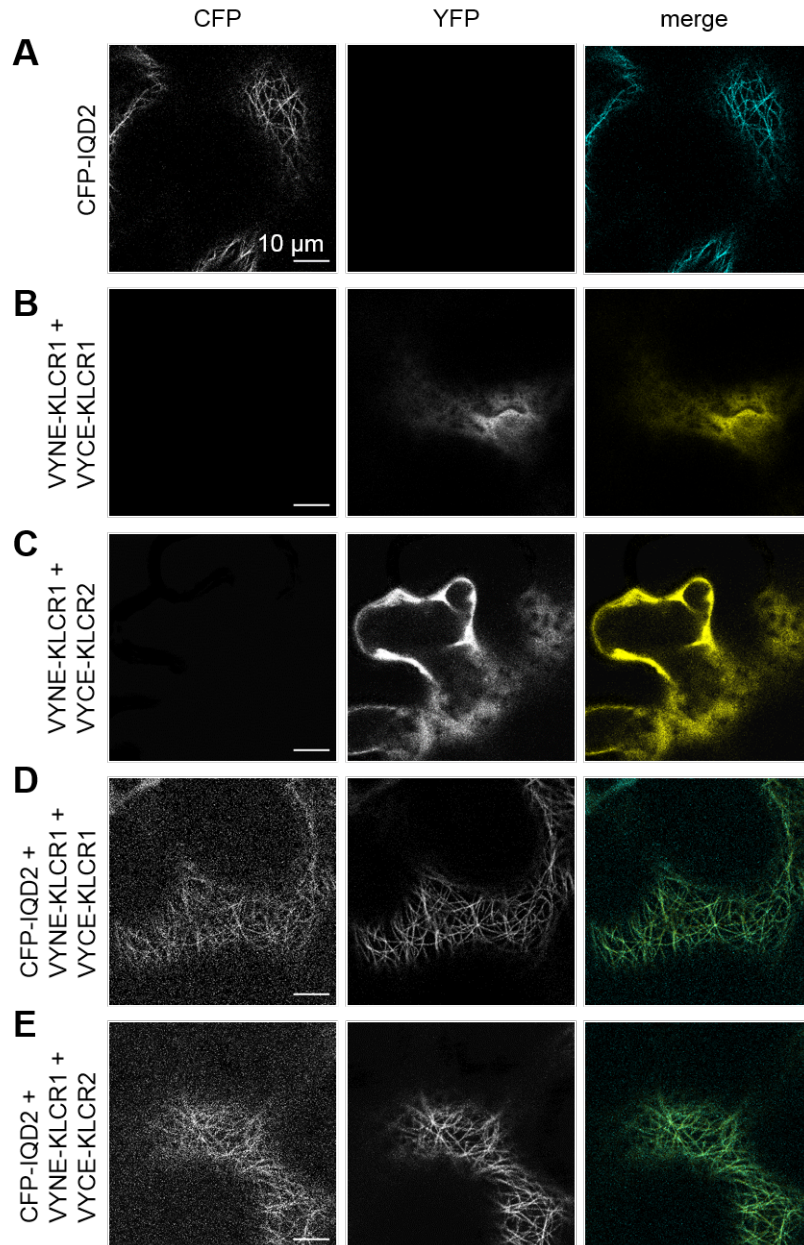


Figure 38: Subcellular localisation of KLCR-dimers co-expressed with CFP-IQD2 in *N. benthamiana* leaves. **A:** Subcellular localisation of CFP-IQD2 under the control of the 35S promoter. **B** and **C:** Subcellular localisation of KLCR1- or KLCR1-KLCR2-dimers. **D** and **E:** Subcellular localisation of KLCR-dimers co-expressed with CFP-IQD2. Scale bars represent 10 μm .

mediates CaM binding in IQD2, truncations of IQD2 were analysed for their CaM binding in Y2H assays.

In Y2H assays IQD2 constructs were expressed as DBD-fusions and CaM-constructs as AD

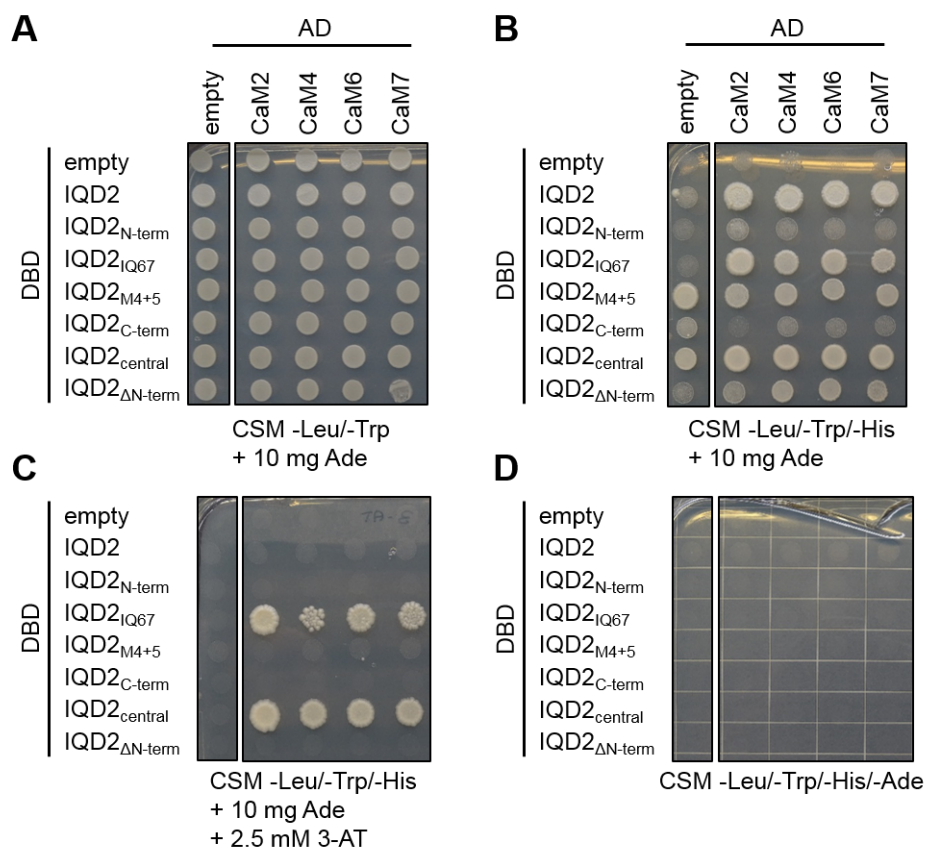


Figure 39: Fine-mapping of IQD2-CaM interactions. Y2H experiment showing interaction of DBD-IQD2 or its truncations with all AD-AtCaM isoforms on DDO (A), TDO (B), TDO + 2.5 mM 3-AT (C), and QDO (D) medium. The same negative controls for AD and DBD were used as in Fig. 34.

fusions. Protein-protein interactions were assessed by yeast growth on vector-selective DDO medium, and interaction-selective TDO, and QDO medium with medium to high stringency. All yeast colonies grew on DDO medium, indicating successful transformation (Fig. 39 A). No negative control of CaM-fusions co-expressed with the DBD showed auto-activation on TDO or QDO medium (Fig. 39 B to D). IQD2_{M4+5} and IQD2_{central} showed auto-activation on TDO medium without 3-AT. This was abolished by the addition of 3-AT and on QDO medium (Fig. 39 B to D). Co-expression of full length IQD2, IQD2_{IQ67}, and IQD2_{ΔN-term} with all CaMs resulted in yeast growth on TDO medium, indicating protein interaction (Fig. 34). Only IQD2_{IQ67} and IQD2_{central} co-expressed with CaMs resulted in yeast growth on TDO

plates containing 2.5 mM 3-AT and no colonies grew on QDO plates, suggesting interaction of IQD2_{IQ67} and IQD2_{central} with all CaMs (**Fig. 39 C and D**). These data indicate specific interaction between all tested CaM-isoforms and those regions of IQD2 containing the IQ67 domain. No colonies grew when IQD2_{N-term} or IQD2_{C-term} were co-expressed with CaMs, indicating no interaction between CaMs and the termini of IQD2, or no expression of these constructs. No differential interaction between IQD2 and the different CaM isoforms was observed. These data are consistent with the previously reported specific CaM-binding of IQD proteins via their IQ67 domain [123].

To test whether IQD2 directly interacts with different CaM-isoforms found in *A. thaliana*, and

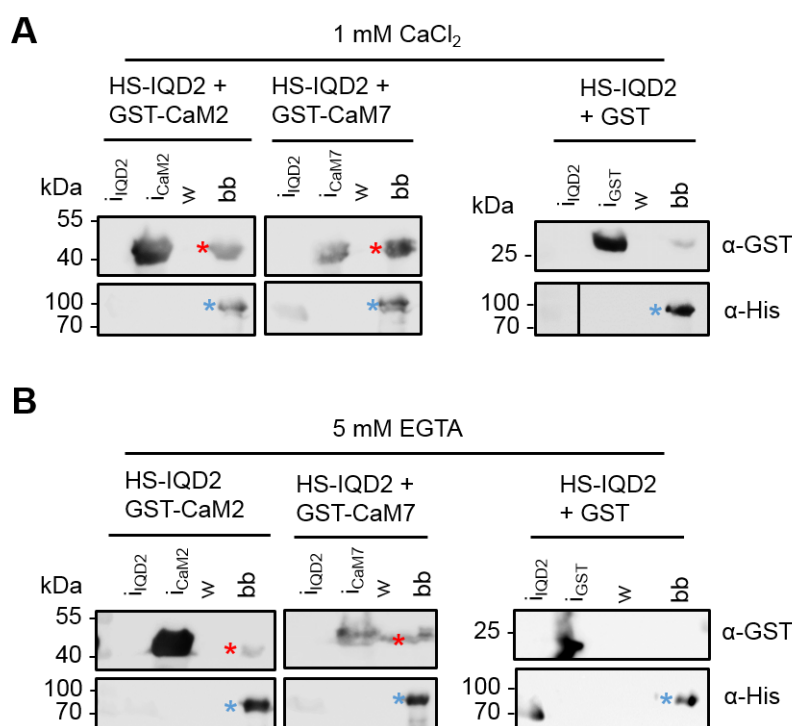


Figure 40: His-pulldowns of GST-CaMs with HS-IQD2. Western blots of 12 % SDS-PAGEs of His-pulldown of GST-CaM2, -CaM7, or GST alone with HS-IQD2 in the presence of 1 mM CaCl₂ (**A**) or of 5 mM EGTA (**B**). Bait constructs are marked with blue asterisks, prey constructs with red asterisks. i: input, w: wash, bb: bead-bound.

assess the Ca²⁺-dependency of IQD2-CaM-interactions *in vitro*, His-pulldowns of GST-CaM2 and -CaM7 in the presence of 1 mM CaCl₂ or 5 mM EGTA were carried out. GST alone served as the negative control. HS-IQD2 was immobilised on Ni-NTA agarose and incubated with the GST-constructs. Successful immobilisation of HS-IQD2 was confirmed with an anti-His antibody and recruitment of GST-constructs with an anti-GST antibody in western blots.

Co-incubation of HS-IQD2 with GST-CaM2 and GST-CaM7 resulted in co-recruitment of the CaMs to Ni-NTA agarose in the presence of CaCl_2 (**Fig. 40 A**). Weak recruitment of GST alone was observed in the presence of CaCl_2 , indicating partial unspecific recruitment. The stronger co-recruitment of GST-CaMs over GST points to physical interaction between IQD2 and holo-CaM2 and holo-CaM7. In the presence of EGTA, GST-CaM2 and GST-CaM7 were recruited to Ni-NTA agarose by HS-IQD2 (**Fig. 40 B**), but no GST was recruited in the presence of EGTA, indicating specific interaction of IQD2 with apo-CaMs. These data are consistent with previously reported apo- and holo-CaM binding of IQD proteins [123] [36]. They establish IQD2 as a *bona fide* interactor of *At*CaM-isoforms that binds to apo-CaM and holo-CaM. Weaker interaction of HS-IQD2 with apo-CaMs compared to holo-CaMs suggests that IQD2 exhibits a binding preference for holo-CaM. The ability of IQD2 to bind apo-CaM may play a role in recruiting other IQD2-binding proteins to apo-CaM that on their own would only interact with holo-CaM, such as KLCRs, and make them available for efficient Ca^{2+} -signal integration. Alternatively, apo-CaM-binding of IQD2 may fulfil regulatory functions distinct from holo-CaM [198].

The CaM-binding scores of IQD2 provided by the CaM-target database and the Calmodulation database are consistent with the observed CaM-binding of IQD2 and its truncations (**Fig. A.36**). Both online resources placed the highest CaM-binding score in the IQ67 domain of IQD2, with an emphasis on the N-terminal half of the IQ67 domain. Furthermore, both databases predicted a moderately high CaM-binding score for motif #4 of IQD2, which did not show CaM-binding on its own. Additionally, the Calmodulation database predicted low CaM-binding scores throughout the N-terminal disordered region of IQD2 and around the DUF4005 domain in its C-terminus. IQ motifs were identified by the Calmodulation database only in the IQ67 domain of IQD2. IQ motifs were reported to bind apo-CaM, suggesting apo-CaM binding of IQD2 specifically through the IQ67 domain [289]. All other CaM-binding motifs identified in IQD2 by the Calmodulation database rely on the presence of Ca^{2+} to associate with CaM.

2.5.1 Subcellular localisation of IQD2-CaM complexes

Mapping of the CaM binding domain in IQD2 via Y2H experiments confirmed that the IQ67 domain is required for CaM binding. This domain partially overlaps with MTB2 of IQD2. To assess whether IQD2 recruits CaMs to the microtubule cytoskeleton and if and how CaM-binding affects the microtubule binding behaviour of IQD2, GFP-IQD2 and its truncations were transiently co-expressed with mCherry-CaM2, RFP-CaM4, or RFP-CaM7 in *N. benthamiana* leaves.

When expressed on their own, all CaMs displayed diffuse fluorescence signals, likely localising

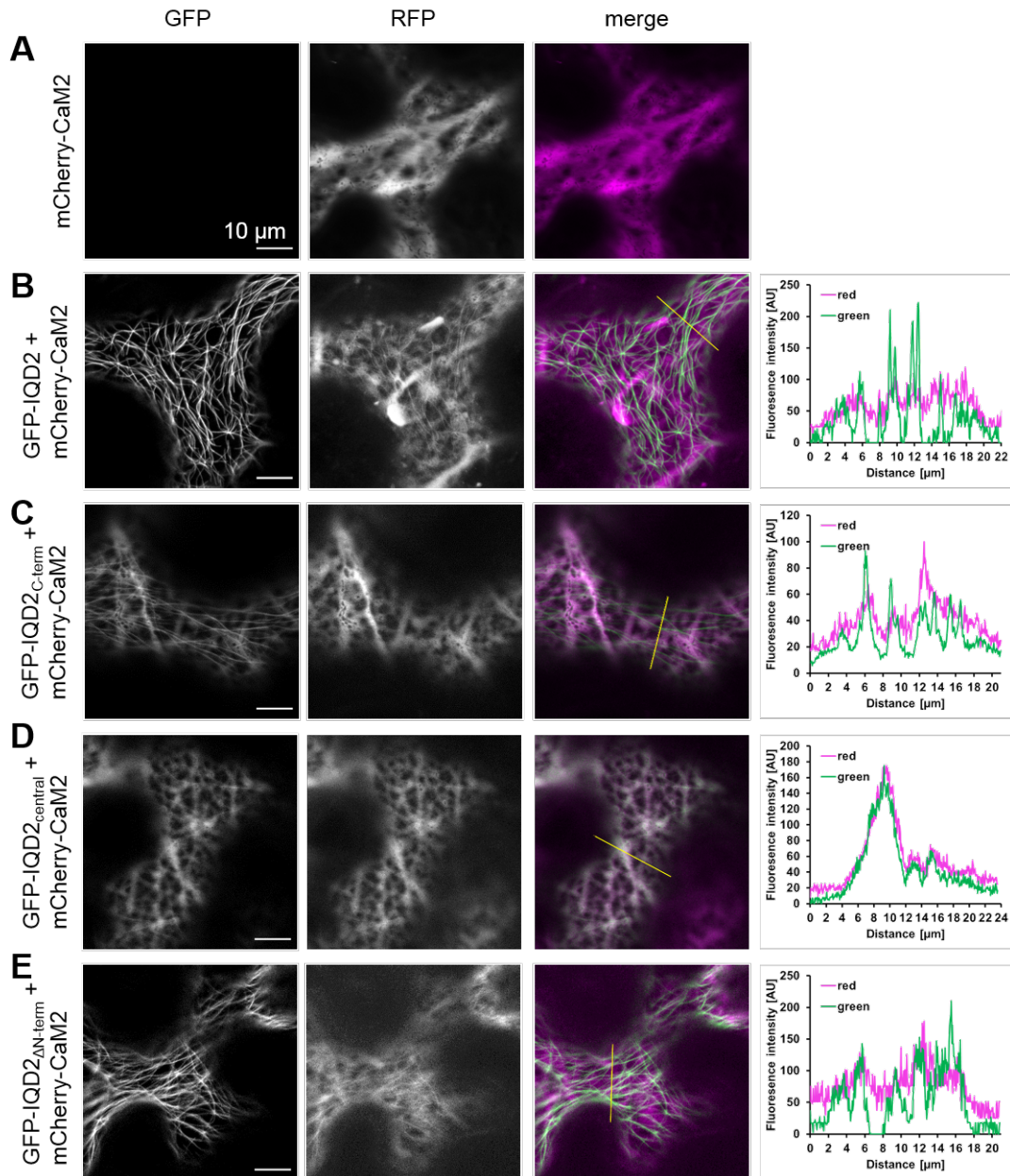


Figure 41: Co-localisation of IQD2 and CaM2 in *N. benthamiana* leaves. **A:** Subcellular localisation of mCherry-CaM2 under control of the 35S promoter. **B to E:** Co-expression of GFP-IQD2 and its truncations with mCherry-CaM2 under control of the 35S promoter. Scale bars represent 10 μm . Fluorescence profiles were generated along the yellow lines in the "merge" images.

to the cytosol (**Figs. 41 A, A.37 A, and A.38 A**). Co-expression of CaMs with GFP-IQD2, resulted in partial to complete recruitment of all CaMs to filamentous structures resembling microtubules (**Figs. 41 B, A.37 B, and A.38 B**). These data show that IQD2 recruits CaMs

to the cytoskeleton, consistent with previous findings [123] [34]. Co-expression of CaMs with GFP-IQD2_{central} resulted in loss of the previously observed partial microtubule association of GFP-IQD2_{central} in the case of mCherry-CaM2 (**Fig. 41 D**), while co-expression with RFP-CaM4 or -CaM7 did not result in a loss of microtubule-localisation. RFP-CaM4 and -CaM7 were recruited to the microtubules by GFP-IQD2_{central} (**Figs. A.37 D and A.38 D**). These data suggest that CaM2 is capable of out-competing the microtubule binding-capacity of GFP-IQD2_{central}, while CaM4 and CaM7 are not. When co-expressed with GFP-IQD2_{C-term}, the IQD2 construct maintained its partial microtubule labelling, and no CaMs were recruited to the microtubules (**Figs. 41 C, A.37 C, and A.38 C**), consistent with their lack of interaction. Co-expression of GFP-IQD2_{ΔN-term} with all CaMs resulted in their recruitment to the microtubule cytoskeleton comparable to full length GFP-IQD2 (**Figs. 41 E, A.37 E, and A.38 E**). These findings point to a mechanism of CaM-recruitment to the cytoskeleton, by which IQD2 interacts with CaMs via its IQ67 domain and recruits them to the microtubules via the DUF4005 domain in its C-terminus, i.e. MTB1. Furthermore, microtubule recruitment of CaM4 or CaM7 but not CaM2 by IQD2_{central} point toward differential integration of CaM-mediated Ca²⁺-signals at the microtubule cytoskeleton by IQD2 by different CaMs. These data further suggest a regulatory effect for the interaction of IQD2 with different CaM isoforms. The fact that neither CaM4, nor CaM7 out-competed the microtubule association of GFP-IQD2_{central} indicates a more efficient localisation to the microtubule cytoskeleton when these two CaM-isoforms are bound, while CaM2 may be more important for a reduction of IQD2-microtubule association.

2.6 Ternary interactions between KLCR1, IQD2, and CaMs

Our work established IQD2 and KLCR1 as *bona fide* CaM targets that physically interact with each other. Previous work suggested that ternary complexes between IQDs, KLCRs, and CaM can occur [36]. The stoichiometry of these complexes, and the contribution of IQDs and KLCRs to CaM-binding in these complexes, however, are still largely elusive. Notably, while KLCR1 and IQD2 both interact with holo-CaM, interaction with apo-CaM is specific for IQD2. Performing *in vitro* CaM-pulldown assays in the absence of Ca²⁺ thus allowed to assess if IQD2 can simultaneously bind KLCR1 and apo-CaM. KLCR-IQD-CaM complexes were additionally investigated *in vivo* by transient co-expression in *N. benthamiana* leaves.

To test ternary interactions between KLCRs, IQD2, and CaM, *in vitro* co-CaM-pulldowns with GST-KLCRs and His-IQD2 were carried out in the presence of 5 mM EGTA. CaM-pulldowns of His-IQD2, GST-KLCRs and a co-CaM-pulldown of His-IQD2 with GST alone served as positive and negative controls, respectively. His-IQD2 was detected with an anti-His antibody and GST-

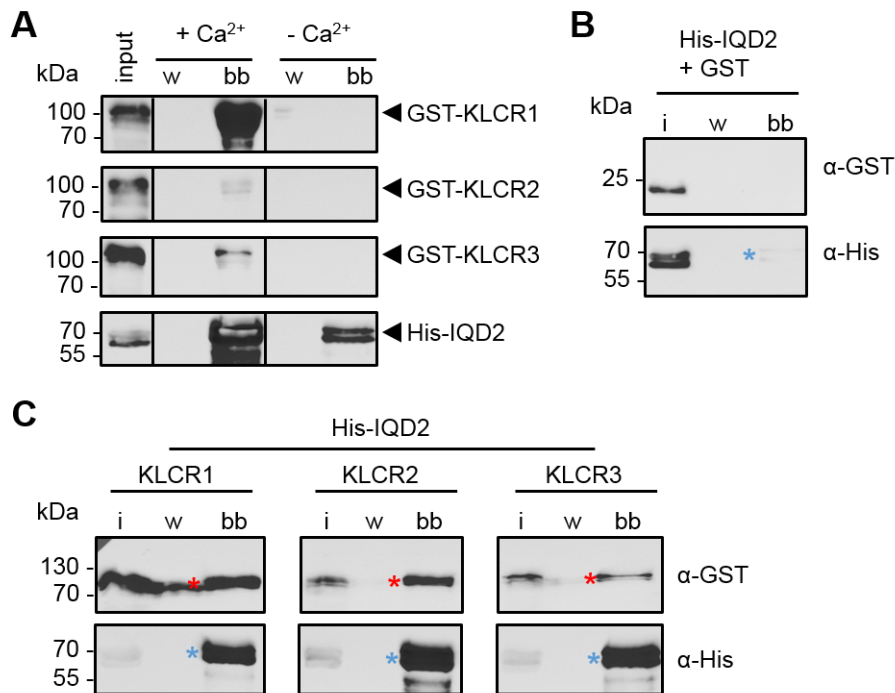


Figure 42: Co-interaction of IQD2 with KLCRs and CaM. **A:** Western blot of 15 % SDS-PAGE of CaM-pulldown of GST-KLCRs and His-IQD2 in the presence of 1 mM CaCl₂ (+ Ca²⁺) or 5 mM EGTA (– Ca²⁺). Expected positions of GST-KLCRs and His-IQD2 are marked with black arrowheads. **B:** Western blot of a CaM-pulldown of His-IQD2 together with GST in the absence of Ca²⁺. **C:** Western blot of a CaM-pulldown of His-IQD2 together with GST-KLCR1, -KLCR2, or -KLCR3 in the absence of Ca²⁺. His-IQD2 is marked with blue asterisks, GST-KLCRs with red asterisks. i: input, w: wash, bb: bead-bound.

KLCRs and GST were detected with an anti-GST antibody after western blotting. Consistent with earlier data, GST-KLCRs were recruited to holo-CaM, but not apo-CaM, while IQD2 was recruited to both, but weaker to apo-CaM (**Fig. 42 A**). These data suggest that GST-KLCRs possess the same CaM-binding properties as His-KLCRs. Co-incubation of His-IQD2 and GST with CaM-agarose and 5 mM EGTA resulted in weak recruitment of His-IQD2 to apo-CaM (**Figs. 42 B**) and no GST was recruited, suggesting that GST does not affect the apo-CaM-binding properties of IQD2 and does not bind to apo-CaM together with IQD2. Co-incubation of His-IQD2 and GST-KLCRs with CaM-agarose in the absence of Ca²⁺, resulted in recruitment of GST-KLCRs to apo-CaM, indicating simultaneous binding of IQD2 to apo-CaM and KLCRs. Co-incubation resulted in increased recruitment of KLCR1-IQD2 complexes to apo-CaM when compared to IQD2 alone, indicated by stronger bands in western blots (**Fig. 42 C**). These findings suggest that IQD2-KLCR-interaction affects their respective apo-CaM-binding affinity in a putatively cooperative binding mechanism. Possible causes for this increased affinity on the molecular level may be that either IQD2-KLCR-binding results in structural alterations in

KLCRs that affect their ability to bind apo-CaM, or vice-versa. Since only IQD2 is capable of apo-CaM-interaction on its own, it seemed more likely that IQD2 acts as the mediator of this increased binding affinity. The structural rigidity of KLCRs observed in cross-linking experiments with CaM2 further makes conformational changes in KLCRs unlikely.

To test, whether the observed altered apo-CaM binding of KLCR-IQD2-complexes was concentration dependent, co-CaM-pulldowns with gradual dilutions of the GST-KLCR- or GST-lysates co-incubated with undiluted IQD2-lysates were carried out. Decreasing the KLCR-concentration in co-pulldowns resulted in a gradual loss of the apo-CaM-affinity of KLCR-IQD2 complexes with all KLCRs (**Fig. A.39 A to C**). Dilution of the GST-lysate did not affect the apo-CaM affinity of His-IQD2 (**Fig. A.39 D**). These data hint at a possible sequential binding mode of IQD2 and KLCRs with apo-CaM. IQD2 and KLCRs may bind in solution, before recruiting to apo-CaM with increased affinity. These data are still preliminary and require further detailed assessment to draw solid conclusions from them.

The interaction between IQD2, KLCR1 and CaM are putatively charge-driven [285] [263]. High ionic strengths are known to disrupt electrostatic interactions in protein-protein complexes [286]. To assess the contribution of electrostatic interactions in the co-recruitment of KLCR-IQD2 complexes to apo-CaM further, *in vitro* His-pulldowns, CaM-pulldowns, and co-CaM-pulldowns with HS-IQD2 and GST-KLCR1 were carried out in buffers containing 1 M NaCl. Proteins were detected after western blotting using either anti-His or anti-GST antibodies. Incubation of GST-KLCR1 or HS-IQD2 with CaM-agarose in the presence of 1 mM CaCl₂ or of 5 mM EGTA resulted in recruitment of both GST-KLCR1 and HS-IQD2 to holo-CaM, suggesting resistance of holo-CaM binding to high ionic strength (**Fig. A.41 A**). Apo-CaM-recruitment of IQD2 was abolished in the presence of 1 M NaCl, suggesting susceptibility to the disruption of electrostatic interactions. These data are consistent with previous findings suggesting high resistance of holo-CaM-binding to target proteins to mechanisms of disrupting electrostatic interactions, e.g. by pH or changes in ionic strength [256] [257] [290]. Abolition of apo-CaM-binding of IQD2 is consistent with reported decreased interaction surfaces between apo-CaM and target proteins, and thus likely weaker interaction [256] [263]. High ionic strength was additionally shown to limit interactions of apo-CaM with target proteins by destabilising apo-CaM [290]. Co-incubation of GST-KLCR1 and HS-IQD2 with Ni-NTA agarose resulted in the successful immobilisation of HS-IQD2 and co-recruitment of GST-KLCR1, indicating that KLCR1-IQD2 binding is not affected by high ionic strength (**Fig. A.41 C**). Co-incubation of HS-IQD2 and GST-KLCR1 with CaM-agarose in the absence of Ca²⁺ resulted in no recruitment of either protein to apo-CaM (**Fig. A.41 B**), consistent with the abolished apo-CaM binding of IQD2.

The disruption of KLCR1-IQD2-co-recruitment to apo-CaM indicates that apo-CaM-interaction of IQD2 is necessary for co-recruitment of KLCR1-IQD2 complexes to apo-CaM. These data further support a role for IQD2 as a bridge between KLCR1 and apo-CaM in KLCR-IQD-apo-CaM interactions.

To validate that KLCR1 recruitment to apo-CaM is mediated by IQD2 and to determine the

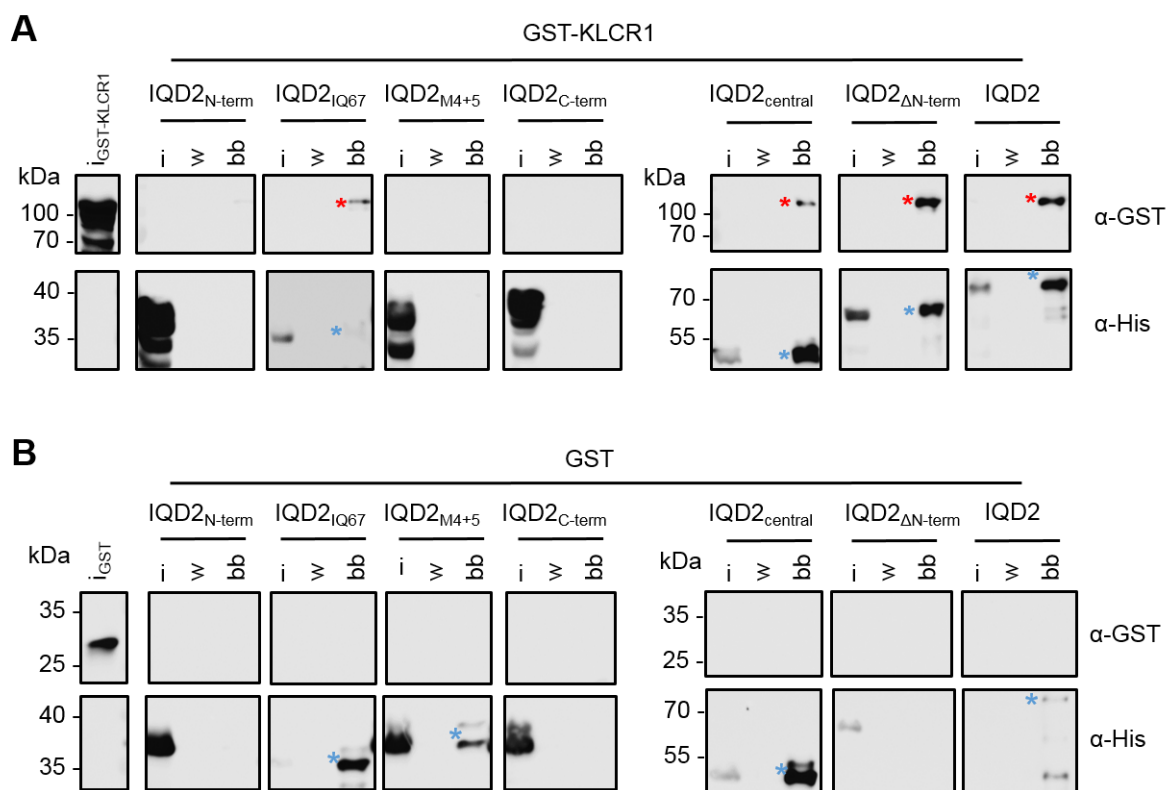


Figure 43: Apo-CaM pulldown assays with IQD2 truncations and KLCR1. Western blot of 12 % SDS-PAGEs of HS-IQD2 and its truncations (Fig. 29 A) together with GST-KLCR1 (**A**) or GST alone (**B**) in the absence of Ca²⁺ under high salt conditions (500 mM NaCl). HS-IQD2 and truncations are marked with blue asterisks, GST-KLCR1 is marked with red asterisks. i: input, w: wash, bb: bead-bound.

minimum required module in IQD2 required for co-recruitment, co-CaM-pulldowns of GST-KLCR1 with the truncated HS-IQD2 constructs were carried out in the absence of Ca²⁺. Standard buffer conditions resulted in inconclusive, unspecific protein-protein interactions (**Fig. A.40**). These pulldowns were thus carried out in the presence 500 mM NaCl to reduce unspecific interactions but still allow apo-CaM binding of IQD2. Co-CaM-pulldowns with GST served as the negative control. HS-IQD2 constructs were detected using an anti-His antibody and GST-KLCR1 and GST were detected with an anti-GST antibody after western blotting. Co-incubation of GST-KLCR1 with HS-IQD2, -IQD2_{IQ67}, -IQD2_{central}, and -IQD2_{ΔN-term} re-

sulted in recruitment of HS-IQD2 constructs and GST-KLCR1 to CaM-agarose, consistent with CaM-binding of these regions of IQD2. Co-incubation of GST-KLCR1 with HS-IQD2_{N-term}, IQD2_{M4+5}, or -IQD_{C-term} did not result in recruitment to CaM-agarose, consistent with their lack of CaM-binding (**Fig. 43 A**). IQD2_{IQ67} showed weak recruitment to apo-CaM in the presence of KLCR1, while recruitment of full length IQD2, IQD2_{central}, and IQD2_{ΔN-term} was comparable to the apo-CaM-recruitment of His-IQD2 with GST-KLCRs (**Fig. 42 C**). These data indicate co-interaction between KLCR1, IQD2_{IQ67}, and apo-CaM. They also suggest more efficient co-interaction of IQD2 constructs containing the central region of IQD2 and its C-terminus with KLCR1, compared to constructs lacking the C-terminus. Co-incubation of HS-IQD2 constructs with GST resulted in the CaM-binding properties observed previously for IQD2. HS-IQD2, -IQD2_{IQ67}, -IQD2_{M4+5}, and -IQD2_{central} were recruited to CaM-agarose, but no other HS-IQD2 construct, nor GST were (**Fig. 43 B**), indicating no effect of GST on apo-CaM binding of IQD2 or its truncations. These data suggest that the IQ67 domain and conserved motif #3 of IQD2 form the minimal necessary unit for co-recruitment of KLCR1 apo-CaM. The lack of co-recruitment of GST-KLCR1 and HS-IQD2_{M4+5} to apo-CaM suggests that both CaM- and KLCR-binding capacity in IQD2 are necessary to recruit KLCRs to apo-CaM. The stronger effect of all IQD2 constructs encompassing the IQ67 domain and conserved motifs #3 to #5 on KLCR1-co-recruitment to apo-CaM suggests, that co-recruitment is increased with stronger KLCR-interaction in IQD2 (**Fig. 35 A**). This is consistent with the preliminary observations of KLCR-concentration-dependency of IQD2-KLCR co-interaction with apo-CaM (**Fig. A.39**). Taken together, apo-CaM interaction is mediated by the IQ67 domain of IQD2, and adjacent motifs #3 to #5 are required for simultaneous binding of KLCR1 – consistent with the mapping of domains that mediate binary interactions of IQD2 with CaMs and KLCR1.

To assess ternary KLCR-IQD-CaM interactions *in vivo*, CFP-IQD2 was transiently co-expressed in *N. benthamiana* leaves with the KLCR1-CaM BiFC pairs (**Fig. 15**). Both VYNE-KLCR1 and VYCE-CaM2 and VYNE-KLCR1 and VYCE-CaM7 displayed diffuse fluorescence, indicating localisation to the cytosol, when expressed together, while CFP-IQD2 labelled the microtubule cytoskeleton (**Fig. 44 A to C**). Co-expression of VYNE-KLCR1 and VYCE-CaM2 or VYNE-KLCR1 and VYCE-CaM7 with CFP-IQD2 resulted in recruitment of YFP-fluorescence to the microtubule cytoskeleton (**Fig. 44 D and E**). These data suggest that recruitment of KLCR1 or CaMs to the microtubule cytoskeleton by IQD2 is not mutually exclusive and may have regulatory functions *in vivo*.

In conclusion, IQD2 can simultaneously interact with KLCR1 and apo-CaM. Furthermore, co-interaction increases the apparent affinity of KLCR1-IQD2 complexes for apo-CaM in a

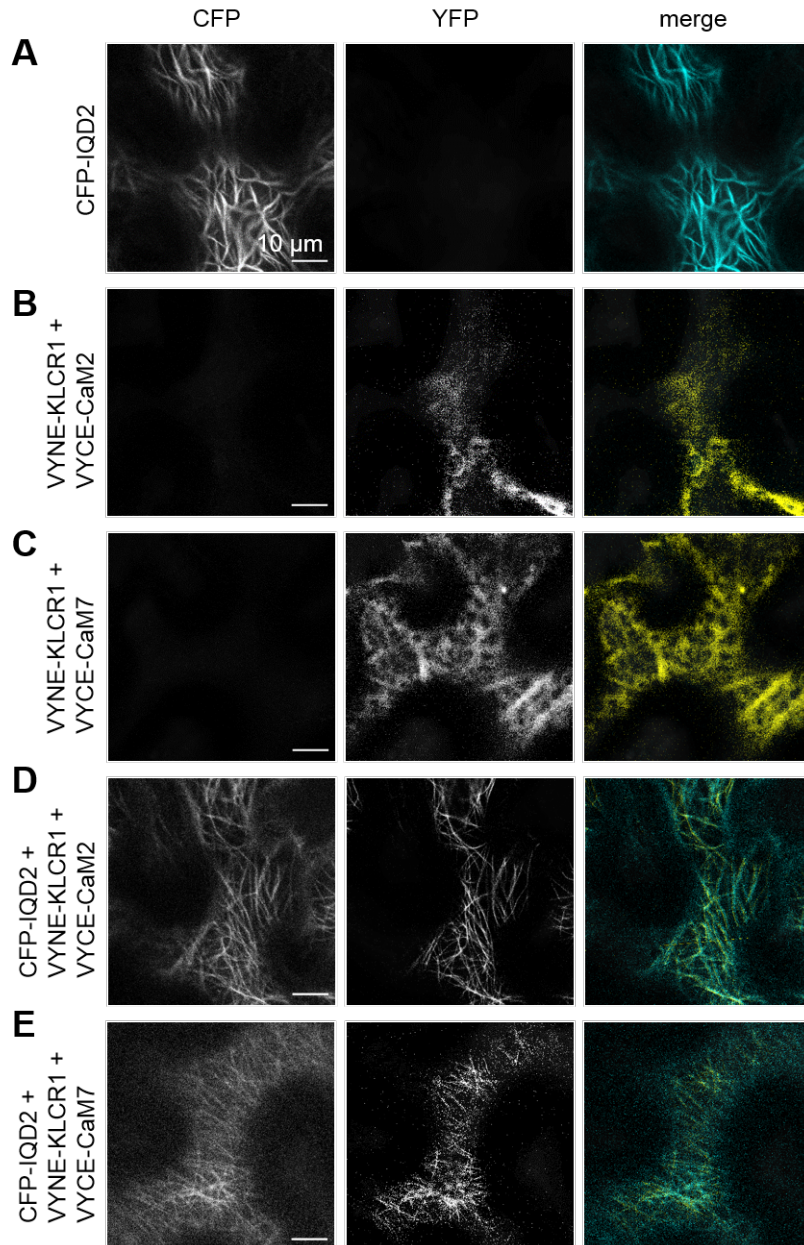


Figure 44: Subcellular localisation of KLCR1 and CaMs co-expressed with CFP-IQD2 in *N. benthamiana* leaves. **A:** Subcellular localisation of CFP-IQD2 under the control of the 35S promoter. **B** and **C:** Subcellular localisation of KLCR1-CaM2- or KLCR1-CaM7-complexes. **D** and **E:** Subcellular localisation of KLCR1-CaM-complexes co-expressed with CFP-IQD2. Scale bars represent 10 μm .

concentration-dependent manner, either by affecting binding affinity directly, or by the formation of complexes with KLCR-dimers that recruit additional IQD2 to apo-CaM. Fine-mapping of the minimum requirements for this co-interaction revealed that both CaM- and KLCR-binding capacity in IQD2 are necessary for co-recruitment, suggesting that IQD2 acts as a bridge between KLCR1 and apo-CaM. Stronger apo-CaM co-recruitment of truncated IQD2 versions that exhibited stronger KLCR-binding suggest that co-recruitment depends on the ability of IQD2 to efficiently interact with KLCRs and CaM.

2.7 KLCR-NET3 interactions

IQD-KLCR modules potentially act as hubs in macromolecular complex assembly that integrate CaM-mediated Ca^{2+} signaling at distinct subcellular sites. NET3 proteins, in particular NET3C, were recently identified as KLCR1 interacting proteins with predicted roles in linking IQD-KLCR modules to the actin cytoskeleton and EPCS [143] [27]. NET3C and related proteins thus are potential accessory subunits of *in planta* assembled KLCR-IQD mediated protein complexes. NET3s appear not to interact with IQD2, nor has CaM-interaction been shown prior to this thesis.

2.7.1 *In silico* assessment of NET3C

NET3C is a member of clade 3 of the NETWORKED protein family. No structural data of NET3s is available. To gain initial information on the characteristics of NET3C, its structure and biochemical properties were assessed *in silico* by interrogation of publicly available databases and bioinformatic tools.

NET3C is a protein of 225 amino acids and a molecular weight of approx. 26 kDa. NET3C contains the Networked Actin Binding (NAB) domain near its N-terminus and a coiled-coil domain near its C-terminus (**Fig. 45 A**). These domains are connected by a flexible linker. The N-terminus of NET3C and the linker between its domains are predicted to adopt no defined secondary structure (**Fig. 45 B**). The AlphaFold 2.0 model of NET3C predicts helical structures with medium high to high prediction confidence for the NAB domain and the coiled-coil domain. Prediction confidence outside of those domains is low and suggests loops or approximate helices for the rest of the protein sequence (**Fig. 45 C**). NET3C has a slightly acidic pI of 5.69 with negatively or positively charged amino acids arranged in alternating short acidic and basic patches. An over-representation of negatively charged amino acids is present in the flexible linker and the C-terminus is characterised by a poly-basic region (**Fig. 45 D and E**). CaM-

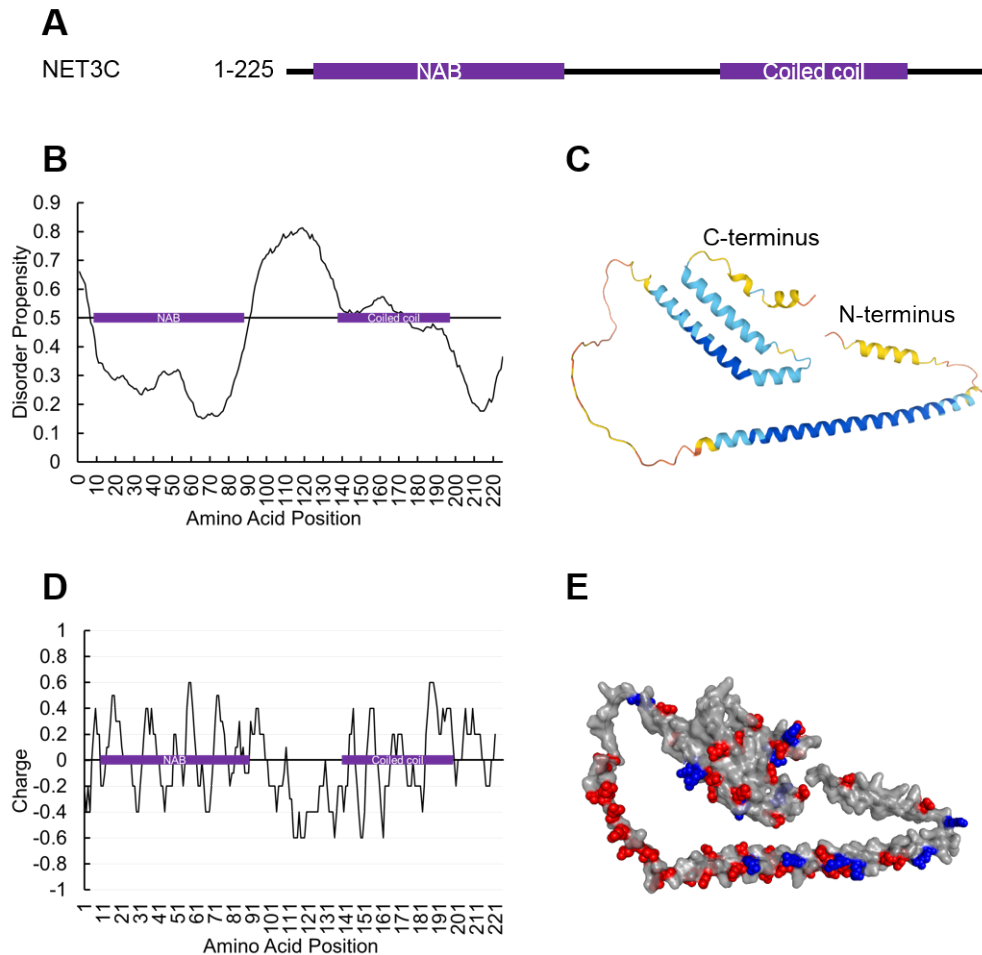


Figure 45: *In silico* analysis of NET3C. **A:** Schematic representation of NET3C with conserved domains and motifs depicted as violet boxes. **B:** Disorder prediction of NET3C with the protein's schematic representation superimposed. A disorder propensity above 0.5 represents a likely disordered region, while a value below 0.5 represents a likely structured region. **C:** AlphaFold 2.0 model of NET3C colored by prediction confidence from high (dark blue) to low (dark orange). **D:** Charge distribution of NET3C superimposed with the protein's schematic representation. **E:** AlphaFold 2.0 model of NET3C in cartoon depiction with a surface of 40% transparency superimposed. The negatively charged amino acids aspartic acid and glutamic acid are depicted as red spheres, while the positively charged amino acids arginine, histidine, and lysine are depicted as blue spheres.

binding scores of NET3C were evaluated to estimate the possibility of CaM-mediated regulation of NET3s. The CaM target database and the Calmodulation database predict a CaM-binding motif in the C-terminal end of the coiled-coil domain, while the Calmodulation data base also suggests CaM-binding capacity in the NAB domain of NET3C (**Fig. A.42 A**).

2.7.2 Interaction of NET3s with KLCRs

The interaction of NET3C with KLCRs had been shown in previous publications [27]. To test these findings, Y2H experiments and *in vitro* pulldowns were carried out. *In vitro* pulldowns were performed with NET3C and its closely related NETWORKED family member NET3A. NET3C was expressed as a DBD-fusion in Y2H experiments and KLCRs as AD-fusions. Yeast

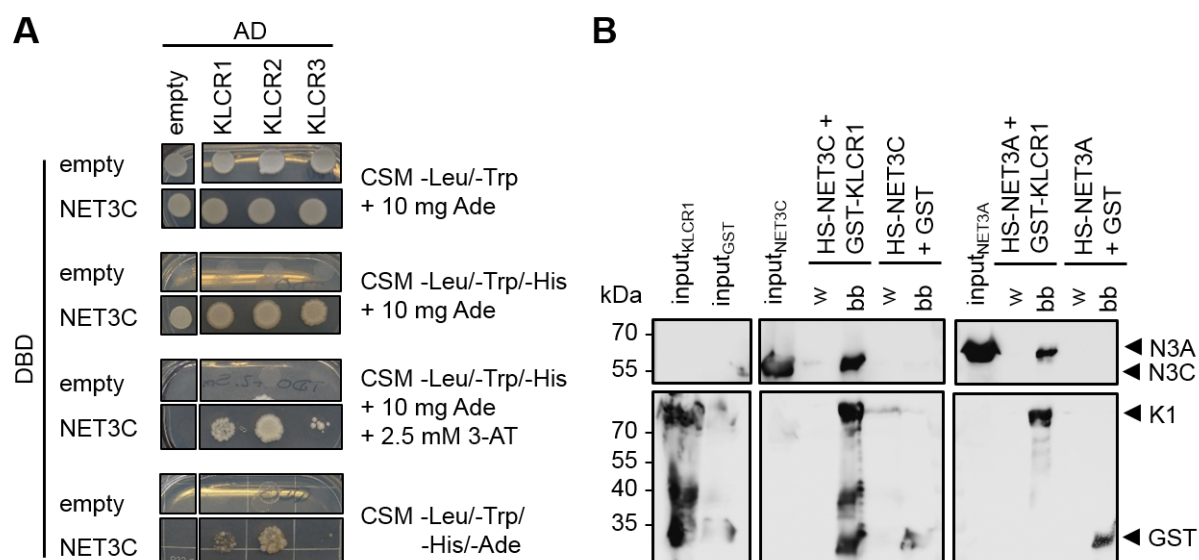


Figure 46: Y2H experiment and *in vitro* GST-pulldowns showing interaction of NET3s with KLCRs. **A:** Y2H DDO, TDO, TDO + 2.5 mM 3-AT and QDO medium (top to bottom) with NET3C as a DBD-fusion and KLCRs as AD fusions. The same negative controls for AD and DBD were used as in Fig. 34. **B:** Western blot of GST-pulldown of NET3A and NET3C with GST-KLCR1 or GST. Expected protein sizes are marked with black arrowheads. N3A: HS-NET3A, N3C: HS-NET3C, K1: GST-KLCR1. Pulldowns were carried out by Mariyam Gaysaeva.

colony growth served as the read-out for protein-protein interactions. Yeast grew on vector-selective DDO medium, showing successful transformation. Co-expression of NET3C with the AD showed auto-activation on TDO medium without 3-AT but not on TDO medium containing 2.5 mM 3-AT or on QDO medium (**Fig. 46 A**). Co-expression of NET3C with all KLCRs resulted in yeast growth on TDO medium with 2.5 mM 3-AT, confirming protein interaction. Yeast also grew on QDO medium for all co-expressions, except with KLCR3. Co-expression of

NET3C with KLCR3 resulted only in weak yeast growth on TDO medium with 3-AT. These data are consistent with the previously reported interaction of NET3C with all KLCRs and the reported binding preference for KLCR1 and KLCR2 over KLCR3 [27].

To test the direct interaction between the NET3s and KLCR1, *in vitro* GST-pulldowns of HS-NET3C and -NET3A were carried out with GST-KLCR1 and GST as a negative control. Successful immobilisation GST-KLCR1 or GST on GSH agarose was detected using an anti-GST antibody. Recruitment of NET3s was observed with an anti-His antibody after western-blotting. Co-incubation of NET3A or NET3C with GST-KLCR1 resulted in recruitment of NET3s to the GSH-agarose, showing as bands at 55 kDa for HS-NET3A and 50 kDa for NET3C (**Fig. 46 B**). Co-incubation of either NET3 with GST did not result in recruitment to GSH-agarose. These data are consistent with previously reported findings and suggest specific, direct interaction of NET3A and NET3C with KLCR1. In summary, these experiments confirmed the previously reported interaction between the NET3 proteins NET3C and NET3A and the KLCRs and show, that interaction with KLCR1 is a direct, physical interaction that persists *in vitro*.

2.7.3 CaM-mediated regulation of NET3s

Interaction of NET3s with CaMs was not previously reported. To assess the putative ability of NET3 proteins to bind CaMs, suggested by *in silico* CaM-binding site predictions in NET3C, Y2H experiments and *in vitro* CaM-pulldowns with NET3A and NET3C were carried out.

NET3C was expressed as a DBD-fusion in Y2H experiments and CaMs as AD-fusions. Yeast colony growth served as the read-out for protein-protein interactions. Yeast grew on vector-selective DDO medium, showing successful transformation. Co-expression of NET3C with the AD indicated auto-activation on TDO medium without 3-AT. This was abolished by the addition of 2.5 mM 3-AT, and on high-stringency QDO medium (**Fig. 47 A**). Co-expression of NET3C with all CaMs resulted in yeast growth on TDO medium with 2.5 mM 3-AT, indicating CaM-interaction. Yeast also grew on QDO medium for all co-expressions (**Fig. 47 A**). These data suggest interaction of NET3C with all CaM-isoforms found in *A. thaliana*.

To test direct interaction between NET3s and CaM, *in vitro* CaM-pulldowns in the presence of 1 mM CaCl₂ or 5 mM EGTA were carried out with both NET3s. HS-NET3s were detected with an anti-His antibody. Both HS-NET3s recruited to CaM-agarose in the presence of CaCl₂, but not in the presence of EGTA, indicating interaction of NET3A and NET3C with holo-CaM (**Fig. 47 B**). These data are consistent with the *in silico* CaM-binding predictions for NET3C. Direct interaction between NET3s and holo-CaM potentially links the connection of KLCR-IQD-modules to the actin cytoskeleton to regulation by CaM-mediated Ca²⁺-signalling.

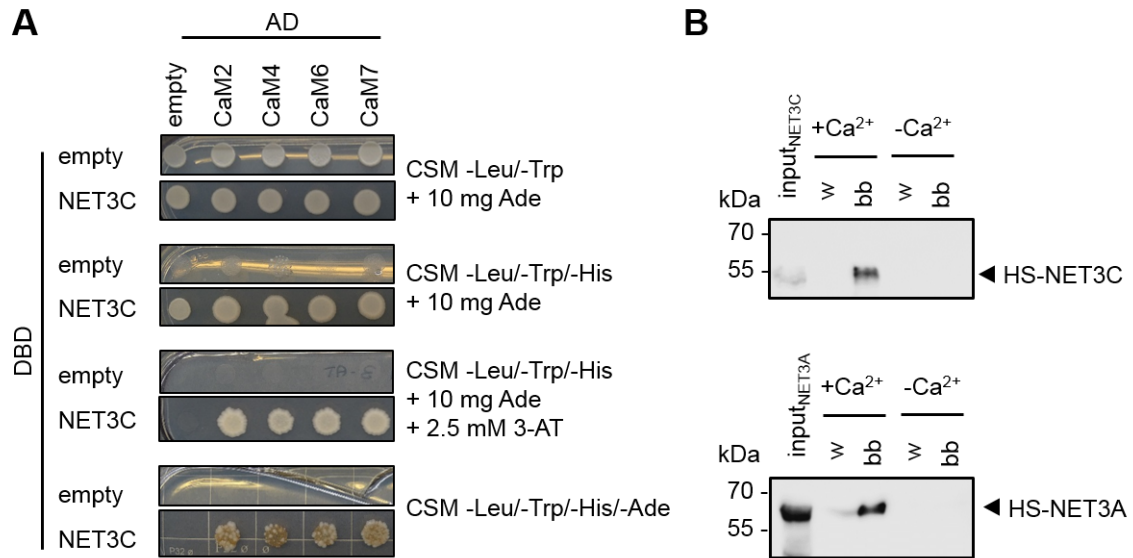


Figure 47: Y2H experiment and *in vitro* CaM-pulldowns showing interaction of NET3s with CaM. A: Y2H DDO, TDO, TDO + 2.5 mM 3-AT and QDO medium (top to bottom) with NET3C as a DBD-fusion and *At*CaMs as AD fusions. The same negative controls for AD and DBD were used as in Fig. 34. **A.** **B:** Western blot of CaM-pulldown of NET3A and NET3C in the presence of 1 mM CaCl₂ (+ Ca²⁺) or 5 mM EGTA (– Ca²⁺). Pulldowns were carried out by Mariyam Gaysaeva.

While no interaction between the NET3s and IQDs is known, these data further strengthen the putative role of IQD2 as a recruiter of apo-CaMs to KLCR1-IQD2-mediated multi-protein complexes for subsequent Ca²⁺-signal integration at the cytoskeleton.

3 Discussion

KLCR-IQD modules have been proposed to play a crucial role in linking the microtubules and the actin cytoskeleton to intracellular membrane systems and to integrate CaM-mediated Ca^{2+} -signalling at the cytoskeleton-PM-nexus. This work provides first insights into the mechanistic basis of the function of KLCR-IQD modules in macromolecular complex assembly. It uncovers the mode of interaction between two distinct scaffold proteins - an IDP and a tandem TPR protein. Furthermore, it provides initial data on the regulation of protein complex formation through Ca^{2+} by fine-mapping CaM-binding regions in IQD2 and KLCRs. In doing so, this thesis builds and expands on previous findings by Bürstenbinder *et al.* [123], Pflug [36], and Zang & Klemm *et al.* [27].

This thesis identified possible KLCR-dimerisation as a putative functionally relevant trait. It uncovered the structural determinants and dynamics of KLCR-CaM, KLCR-IQD2, and IQD2-CaM binding, and delved into a mechanistic understanding of ternary KLCR1-IQD2-CaM interactions. Additionally it confirmed previously reported binary protein-protein interactions between KLCRs and NET3s and linked actin-binding of NET3s to potential regulation by CaM. Furthermore, this thesis confirmed IQD2-microtubule binding, and recruitment of its interactors to microtubules. The combination of biochemical and structural biology approaches with methods of computational biology served to produce comprehensive insights into the mechanisms and dynamics of protein complex formation and regulation, using the KLCR1-IQD2 core module as a suitable model system.

3.1 TPR-mediated homo-interaction of KLCRs

Native purifications of KLCR1 and KLCR2 via gel filtration suggested the formation of KLCR-homo-dimers *in vitro* (**Figs. 11 and A.5 C**). GST-pulldown experiments confirmed these initial findings and hinted at the ability of KLCR1 and KLCR2 to form hetero-dimers in addition to homo-dimers (**Figs. 11 E**). BiFC experiments confirmed KLCR-hetero- and -homo-dimerisation *in vivo* and revealed that KLCR-dimers can be recruited to microtubules upon co-expression with IQD2 (**Figs. 12 and 38**). These data suggest that KLCR-dimers form *in planta* and that they can interact with IQD2 and possibly other IQD proteins.

KLCRs contain tandem-repeats of TPR motifs in their central to C-terminal region, forming a putatively helical TPR domain (**Figs. 8, A.3, and A.4**). Dimerisation and higher order oligomerisation of TPR-domains has been reported before for various proteins, including MamA from *Magnetospirillum* [62], CdC16/Cut9 from *S. pombe* [70], IpgC from *Shigella* [68], and

SGT1 from *A. thaliana* [67]. The magnetosome-associated protein MamA self-associates via its TPR domains and contributes to the outer hull of magnetosomes [71]. TPR-TPR-association of MamA does not hinder binding of other interactors, suggesting a stabilising role for these interactions, rather than a strictly regulatory one. Similar mechanisms for dimerisation have been described for CdC16/Cut9, IpgC, and SGT1. In all of these proteins the TPR domains interact via their N- or C-terminal helices, "twisting" into each other and interacting via the inner groove formed by three or more TPR motifs. The resulting increased protein-complex surface and concave shape may then be accessible for functionally relevant protein-protein interactions with other binding partners [70] [62]. This surface increase was shown to confer interaction between IpgC and its effector IpaB [68], as well as between CdC16/Cut9 and its binding partner Hcn1 [70]. Dimerisation may thus be crucial for the interaction of KLCRs with their binding partners. For SGT1, self-association has been shown to be concentration-dependent, where protein concentrations above 50 μM increased self-association in solution [67]. Furthermore, the dimerisation status of SGT1 was affected by pH and ROS-mediated oxidisation, possibly linking context-dependent regulation of protein self-interaction to plant defense. Oxidisation-dependent formation of dimeric or monomeric populations of SGT1 is believed to play a regulatory role in the association of SGT1 with components of the UPS and thereby context-dependent protein degradation. Considering the putative role of KLCRs as scaffold proteins, fine-tuning of their oligomerisation status through changes in protein abundance or electrostatic properties may serve to regulate their set of interactors for spatio-temporal control of complex assembly. The maintenance of monomeric or dimeric populations of KLCRs may further diversify functional fine-tuning of KLCR-mediated protein complexes.

TPR oligomerisation was also shown for artificially generated consensus TPR proteins (CTPRs). In these cases, self-association of TPR motifs was induced by the introduction of tyrosine residues in the flexible loops connecting the two α -helices of the interacting TPR motifs [69]. Experiments further suggested that the position of the C-terminal capping helix of these CTPRs may regulate the ability to self-associate. Upon self-association, the capping helix was disrupted, adopting a disordered fold. This disruption allowed for hydrophobic contacts between the helices of the interacting TPR motifs, resulting in dimerisation. The coiled-coil domain in the natural protein from which the CTPR was generated was believed to regulate self-association by steric inhibition. The predicted flexible N- and C-terminal regions present in all KLCRs may thus affect KLCR-KLCR interactions by regulating the accessibility of the termini of the TPR domain in a similar fashion. PTMs in these regions may be a means of directing KLCR-homo-interactions by changing the internal organisation of KLCRs. Phosphorylation of KLCRs

via MPKs may be crucial for this regulation by affecting the local electrostatic environment and therefore KLCR-KLCR interactions [272] [36]. Phosphorylation of KLCR2, but not other KLCRs in the C-terminal TPR motif may affect motif stability and thus possibly dimerisation, suggesting functional diversity of different KLCR-dimers (**Fig. A.29 C**). Data suggest that homo-dimerisation of KLCR1 is not affected in the splice variant lacking the C-terminal IDR (**Fig. 11 E**). This indicates that the absence of the C-terminal 78 amino acids does not alter the regulation of self-association of KLCR1 *in vitro* and points towards possible functions of the N-terminal IDR of KLCR1 for regulation of self-association.

In cross-linking experiments dimerisation of KLCR1 was not consistently observed (**Figs. 22 C and A.16**), suggesting additional means of regulating KLCR-self-association we have yet to understand. Similar to reports from SGT1, dimerisation of KLCR1 may be concentration-dependent [67]. A concentration-dependent effect of dimerisation is also supported by recent findings which demonstrated that protein complex assembly and retention is enhanced in crowded environments when compared to *in vitro* buffer conditions [291] [292]. The crowded cellular environment may thus support protein complex assembly and retention. *In vitro* these effects may be achieved by the addition of crowding-simulators, such as polyethylene glycol, to experiment buffers [293]. Ionic strength and pH of the experimental environment may also affect KLCR-self-association. The tag-free KLCR1, however, migrated in cross-linking buffer at a retention volume comparable to His-KLCR1 or GH-KLCR1 in different buffer conditions during gel-filtration (**Figs. 10 and 11 C**), suggesting that additional layers of regulation may contribute to KLCR-dimerisation. The successful establishment of conditions for the recombinant expression of KLCR1 and subsequent purification of tag-free variants provides an excellent starting point for detailed structural analyses, e.g. via x-ray crystallography, which may provide detailed information on the structure and dimerisation status of KLCR1. The high protein concentrations required for protein crystallisation may contribute to the formation of KLCR-dimers in protein crystals and allow insights into their 3D structure [64] [65].

The effects of TPR-domain oligomerisation on providing extended protein-protein interaction surfaces suggest that KLCR-dimerisation may be crucial for its function in KLCR-IQD modules [62]. Context-dependent regulation of TPR-self-association may play a role in maintaining monomeric or dimeric populations of KLCRs with different sets of interactors, or allow for switching between monomers and dimers to regulate binding properties [67]. The ability of KLCR-homo- and -hetero-dimers to occur, and interact with IQDs *in vivo* (**Figs. 12 and 38**), suggest a functional role for KLCR-dimers in protein-complex assembly. Differences in interaction partners between different KLCRs may allow for the assembly of diverse multi-protein

complexes through the incorporation of different KLCRs in KLCR-dimers.

3.2 Adaptors, scaffolds, and dockers

KLCRs and IQDs form the core protein-protein interaction module of a multi-protein complex linking the actin and the microtubule cytoskeleton, the plasma membrane, and the endoplasmic reticulum [27]. NET3s provide an extension of this core module by linking KLCRs and IQDs to the actin cytoskeleton. The experimental investigation of protein-protein-interactions in this thesis thus focused on IQDs, KLCRs, and NET3s, and their regulation via CaM-mediated Ca^{2+} -signalling. Interestingly, IQDs, NET3s, and KLCRs do not possess enzymatic activity [32] [143] [123]. Their structural and biochemical properties are indicative of functions as putative adaptors, scaffolds, or subcellular dockers [6]. IQDs would likely classify as IDPs with scaffolding functions, while KLCRs and NET3s would fit more into the category of ordered scaffold proteins (**Figs. 29, 8, and 45**). The KLCR-IQD-NET3 protein-protein interaction module would consequently be a super-hub of scaffold proteins, linking various crucial subcellular structures and potentially providing an assembly platform for signal integration at these sites by connecting Ca^{2+} -, hormone-, and kinase-signalling [35] [36]. Direct interaction between KLCR1 and NET3A as well as NET3C was shown in this thesis (**Fig. 46**), consistent with previous findings [27]. Since the NETWORKED protein family was already shown to directly associate with actin, thereby functioning as dockers, and linking the KLCR-IQD module to the actin cytoskeleton [143], assessments of subcellular localisation and its possible regulation concentrated on IQDs and KLCRs.

3.2.1 IQDs but not KLCRs associate directly with microtubules

GFP-KLCR1 and -KLCR2 both located to the microtubule cytoskeleton when expressed at low levels under control of the Ub10 promoter in *N. benthamiana* leaves (**Figs. 26 and A.26 A**), but not when expressed under control of the stronger 35S promoter (**Figs. A.25 and A.31 A**). Only those truncations of KLCR1 missing the N- or C-terminal disordered regions displayed microtubule localisation when expressed under control of the Ub10 promoter, but no other truncations did (**Fig. 26**). These data suggest that there may be no distinct direct microtubule binding site present in KLCRs and association with microtubules requires a large portion of the TPR domain to be intact. Additionally, no direct interaction between purified KLCR1 and microtubules was observed in *in vitro* microtubule spin-down assays, regardless of microtubule- or KLCR1-concentration (**Figs. 27 and 28**). The small percentage of KLCR1

consistently observed in the pellet after ultracentrifugation may point to susceptibility of KLCR1 for sedimentation at high g-forces, or may be the result of a "buffer shock" experienced when KLCRs are diluted in General Tubulin Buffer (GTB) for spin-downs. The latter may be addressed by purifying KLCRs in GTB for future experiments. While KLCRs were shown to co-localise with microtubules *in vivo* and directly bind them *in vitro* in recent studies [120], these findings could not be reproduced in this thesis. Microtubule localisation of KLCRs was shown in *A. thaliana* in our group, but likely relies on the presence microtubule adaptors (Sandra Klemm, unpublished data). These data also point to a possible tissue-specific subcellular localisation of KLCRs, likely dependent on the availability of putative adaptors. Taken together, these findings suggest that rather than directly interacting with microtubules, KLCRs are most likely recruited to the microtubule cytoskeleton by a docking protein [39]. Considering the known microtubule interaction of IQD proteins [34], as well as their interaction with KLCRs [123] [36], IQDs may act as microtubule dockers for KLCRs. KLCRs were shown to interact with a number of clade III IQDs, namely IQD1 [123], IQD2 [36], and IQD9 [189]. Due to the recent implication of IQD2 and KLCR1 as the central module for the assembly of the PINK complex, investigations focused on this particular protein combination [27].

IQD2 localised to the microtubule cytoskeleton when expressed under the control of the 35S promoter in *N. benthamiana* leaves (**Fig. 31 A**). Direct microtubule binding was demonstrated by co-sedimentation with microtubules in microtubule spin-down assays (**Fig. 32**), confirming direct interaction of IQD2 and the microtubule cytoskeleton (**Fig. 51 A**). Transient expression of truncations of IQD2 narrowed down the microtubule interaction sites in IQD2 to two distinct regions, namely its very C-terminal 134 amino acids, and the central region encompassing the IQ67 domain and conserved motifs #3 to #5 (**Figs. 29 A and 31 E to G**). The C-terminal microtubule binding site in IQD2 coincides with the presence of a recently reported microtubule binding DUF4005 domain in conserved motif #6 (MTB1) [199]. The central microtubule binding region of IQD2 contains the IQ67 domain and motifs #3 to #5 (MTB2) (**Fig. 49**). Motifs #3 and #4 had been implicated in microtubule binding of IQD13 in addition to motif #6 [204], consistent with these data. The polybasic regions in both MTBs may confer electrostatic interactions between IQD2 and the negatively charged tubulin tails, as described for other MAPs [294]. The presence of multiple microtubule binding domains was previously shown to confer particularly strong microtubule association in SPR1 [295], which is consistent with the stronger microtubule localisation of IQD2 constructs containing both MTB1 and MTB2 compared to those containing only one MTB. IQD2 may therefore serve as the docker for anchoring KLCRs to microtubules. The presence of multiple MTBs may also

point to other roles of IQD2 in bundling microtubules (**Fig. 51 A**) [296] [160].

The microtubule binding properties of the *A. thaliana* IQD family suggest that neither the presence of a DUF4005 domain, nor the presence of the IQ67 domain or conserved motifs #3 to #5 are sufficient for efficient microtubule localisation of IQDs [34]. Clade III IQDs IQD4, IQD5, IQD9, and IQD10 all possess MTB2, but not MTB1. IQD4, IQD9, and IQD10 show weak microtubule labelling, similar to constructs of IQD2 containing only one MTB. IQD5, on the other hand, strongly associates with microtubules. All other clade III IQDs contain both MTBs and exhibit strong microtubule labelling. IQD15 and IQD26, both possess MTB1, but not motifs #3 to #5 of MTB2. IQD26 shows strong microtubule labelling, while IQD15 does not. The minimal IQD protein IQD20, consisting only of the IQ67 domain, also does not label microtubules, indicating no role for the IQ67 domain in microtubule binding. These data point towards important roles for the conserved motifs in IQDs for microtubule binding, but also suggest additional regulatory layers to the subcellular localisation of IQD proteins beyond their conserved motifs. These may be located in the hyper-variable regions of IQDs, and/or be conferred by PTMs.

3.2.2 IQD2 binds KLCRs and recruits them to the microtubule cytoskeleton

IQD2 interacted with all three KLCRs and exhibited possible preferential binding for KLCR2 in Y2H assays (**Fig. 34**). Fine-mapping of IQD2-KLCR1 interactions revealed that the KLCR-binding site in IQD2 stretched from the IQ67 domain to #5, therefore overlapping with MTB2 (**Fig. 35 A**). Out of these motifs, motif #3 may have the strongest influence in KLCR1-binding, while motifs #4 and #5 may contribute a supporting effect for KLCR-binding (**Fig. 49**). Further findings in our group suggest that specifically motifs #3 to #5 are required for KLCR-interaction, as truncations of IQD1 missing only the conserved motifs, but not the surrounding amino acids or the IQ67 domain could not interact with KLCRs (Bürstenbinder *et al.*, unpublished data). The need for specific, conserved motifs in IQD2 for KLCR1-interaction is reminiscent of MORFs conferring protein-protein interaction in disordered scaffold proteins [84] [75] [297]. In KLCR1, on the other hand a certain number of TPR motifs, but no one concrete TPR motif, was sufficient for IQD2-interaction (**Fig. 36**). This is consistent with previous findings on TPR domain-ligand interactions, whereby structural conservation rather than sequence conservation is necessary for tandem-repeat proteins binding to their interactors [49] [42] [62]. These findings suggest that the formation of an inner groove assembled by more than three TPR motifs in sequence may be sufficient for scaffold-ligand interactions, causing the ligand to adopt an extended conformation upon binding to the tandem-repeat protein, while

the tandem-repeat protein remains rigid [42] [298]. The putative structural flexibility of IQD2 may allow for the required extended conformation upon binding to KLCRs. The strong positive charge in motif #3 of IQD2 and strong negative charge in TPR motifs #7, #9, and #10 of KLCR1 points towards these sites primarily conferring IQD2-KLCR1-binding via electrostatic interactions (**Figs. 30 and 9 A**). Charge-mediated protein-protein interactions are susceptible to high salt concentrations that disrupt the necessary electrostatic properties of the interacting proteins [286]. The persistence of IQD2-KLCR1 interactions even in the presence of 1 M NaCl suggests a particularly strong protein-protein interaction between the two, or a reliance on other binding mechanisms than electrostatic forces (**Fig. A.41 C**).

Transient co-expression of KLCRs with IQD2 in *N. benthamiana* resulted in the recruitment of all KLCRs from the cytosol to the microtubules (**Figs. 37 B, A.31 B, and A.32 B**), suggesting that IQD2 functions as the docker for KLCRs to the microtubule cytoskeleton (**Fig. 51 B**) [39]. Interestingly, microtubule binding of MTB2 alone was abolished by KLCR-co-expression, suggesting an out-competition and steric inhibition of microtubule association of the central region of IQD2 by KLCRs (**Figs. 37 D, A.31 D, and A.32 D**). MTB1 may therefore be crucial in anchoring IQD2-KLCR-complexes to microtubules, while KLCR-binding may serve as a regulatory mechanism for the subcellular relocation of IQD2. The subcellular localisation of IQD2-KLCR-complexes more closely resembled that of full-length IQD2 than that of the C-terminus of IQD2. This suggests that rather than completely abolishing the contribution of MTB2 to the microtubule localisation of IQD2, KLCR-interaction may still leave this contribution partially intact. Further insights into the exact mode of binding in IQD2-KLCR-complexes may uncover the structural mechanism by which this recruitment is achieved. Due to challenges in acquiring high amounts of pure IQD2 for *in vitro* studies (**Fig. A.27**), cross-linking experiments with IQD2 and different KLCRs may be the method of choice for structural approaches, due to their lower requirements for protein amounts and purity compared to e.g. crystallography. The simulation of crowded conditions may support the formation of stable IQD2-complexes *in vitro* [293], allowing for additional experimental investigation. Further research may also shed light onto the structural determinants underlying the differential binding between IQD2 and different KLCRs. Direct recruitment of KLCRs to microtubules by IQD2 may also be further investigated by performing *in vitro* co-microtubule-spin-downs. The structure of KLCR-IQD mediated protein complexes on microtubules may be investigated employing cryo-electron microscopy (EM) on *in vitro* assembled microtubules incubated with KLCRs, IQD2, and their interactors.

The differential interaction between IQD2 and different KLCRs as well as the interaction of

other clade III IQDs with KLCRs may be the basis for the formation of not just one KLCR-IQD mediated multi-protein complex but rather a set of different, context-dependent protein-complexes. The fact that both KLCR1 and KLCR2 could act as bridges between IQD2 and NET3C further supports the hypothesis of a diverse set of actin-microtubule bridging complexes mediated by KLCRs, as does the interaction of both NET3A and NET3C with KLCR1 and KLCR2 [27]. Phosphorylation of IQDs by MPKs and other kinases has been shown for a number of IQDs, including IQD1 and IQD2 [202] [36] [201]. Phosphorylation of both IQDs, and KLCRs may thus serve as a regulatory mechanism for charge-mediated protein-protein interactions as well as subcellular localisation of these proteins [36]. Phosphorylation of IQDs may additionally induce disorder-to-order switches, as shown for human 4E-BP2 [287]. Annotated phospho-sites in the disordered regions in IQD2 further support this hypothesis (**Fig. A.29 A**). The biochemical and structural assessment of putative KLCR-IQD-NET3-complexes may shed light on the structural properties of NET3s contributing to the assembly of extended KLCR-IQD-modules on the actin cytoskeleton. Lastly, it would allow for insights into possible competitive or cooperative protein-protein interactions within the KLCR-IQD-mediated protein complexes and their putative fine-tuning by PTMs.

3.3 CaM-mediated calcium-signalling as a regulatory mechanism of the KLCR-IQD core module

Previous work identified IQDs and KLCRs as CaM-interactors [32] [123] [36]. While IQDs contain a canonical CaM-interacting domain in the form of the IQ67 domain, no such conserved CaM-binding domains were known for KLCRs [123]. CaM-binding of NET3s had not been reported previously. CaM-interaction of the three members of the PINK complex investigated in this thesis was analysed comprehensively to assess the possibility of CaM-mediated regulation of the IQD-KLCR modules by Ca²⁺-signalling. CaM-pulldown experiments showed Ca²⁺-dependent CaM-binding for all KLCRs, as well as NET3A and NET3C (**Figs. 13 and 47 B**). IQD2 was shown to interact with both apo- and holo-CaM, albeit with a lower affinity for apo-CaM (**Fig. 40**), confirming previously reported findings [36]. IQD2 and KLCR1 were shown to interact directly with *AtCaM2* and *AtCaM7* in GST- or His-pulldowns, exhibiting comparative CaM-binding observed with commercially available CaM-agarose (**Figs. 14 and 40**), but showing a slight binding preference for CaM7 over CaM2. The interaction between *AtCaMs* and KLCRs was further supported by *in vivo* BiFCs assays and co-IPs (**Figs. 15 and A.11**). Overall, these findings firmly link three out of four contributors of the PINK-complex to CaM-mediated signalling, thereby cementing the role of Ca²⁺-signalling in the regulation of

KLCR-IQD-mediated multi-protein complex assembly and function.

3.3.1 Regulation of KLCRs by CaM-mediated calcium-signalling

KLCRs share similarity with animal KLCs in their TPR domain. Interestingly, CaM-binding is conserved within animal KLCs and plant KLCRs. In human KLCs, CaM-binding regulates kinesin activity by interacting with hydrophobic and basic residues in the C-terminus of KLCs and indirectly inhibiting the ATPase activity of the associated KHC [193]. Likewise, the C-terminus of plant KLCRs shows basic patches (**Fig. 9**). Bovine CaM and AtCaMs have pIs of approx. 4.1. In pH of 7 to 8, CaMs have thus been reported to carry a net charge of -15 [257]. The surface accessibility of negatively charged residues in holo-CaM may result in binding to polybasic regions in KLCR1 or KLCR2 by electrostatic interactions [256] (**Figs. 9 A, A.3 D, A.4 D, and A.10**). CaM-mediated regulation of KLCs is subject to regulation by phosphorylation by blocking CaM-binding to KLCs through changes in the electrostatic environment of the CaM-binding site [193]. As known MPK targets, KLCR-CaM-interaction may be subject to similar modes of regulation [36]. Phosphorylation of KLCRs as a mode of regulation is further supported by the identification of KLCRs as targets for calcium dependent protein kinases (CDPKs), MPKs, and sugar nonfermenting kinases (SnRK), and by the presence of multiple promiscuous kinase consensus sites in KLCR1 [93] [192]. Annotated phospho-sites in the C-terminus and in the N-terminal disordered region of all KLCRs further supports this hypothesis (**Fig. A.29 B to D**). Since the involvement of KLCRs in kinesin-mediated transport has yet to be shown, their CaM-interaction and phosphorylation points to a re-purposing of conserved regulatory mechanisms for different tasks in the plant kingdom.

The implied importance of the C-terminus of the TPR domain in KLCR1 and KLCR2 for CaM-interaction was confirmed by fine-mapping of their CaM-binding sites by CaM-pulldowns with truncations of both proteins (**Figs. 18 and 19**). Interestingly, both KLCRs showed CaM-binding in their C-terminus and an additional CaM-binding site in the N-terminus of their respective TPR domain, although CaM-binding in this region was much more pronounced in KLCR2 compared to KLCR1 (**Fig. 48**). CaM-binding in the N-terminal region of the TPR domain may be caused by an artificially generated CaM-binding site as a result of truncating the KLCRs. However, these findings agree with *in silico* CaM-binding site predictions, that also suggest differential CaM-binding sites in KLCR1 and KLCR2, and therefore possible functional diversification between different KLCRs (**Figs. A.14 and A.15**). The increase in apo-CaM binding capacity in KLCR1_{spl} compared to canonical KLCR1 suggests either a crucial role for the C-terminal disordered tail of KLCRs in CaM-binding regulation or the accessibility of a newly

formed CaM-binding site in this splice variant by changes in the chemical environment, as suggested by *in silico* predictions by the CaM-target database (**Fig. A.14**). The former would be similar to putative modes of regulation of the formation of KLCR-dimers by the flexible regions within the KLCRs, and would allow for PTM-mediated fine-tuning of CaM-interactions [69]. The altered CaM-binding of KLCR1_{spl} may allow for alterations of CaM-mediated regulation of KLCR1 functions in a tissue-specific manner, depending on the abundance of either splice variant.

Cross-linking experiments between KLCR1 and CaM2 largely confirmed the position of the CaM-binding site(s) in KLCR1 observed in pulldown experiments (**Fig. 23 B**). The majority of inter-molecular cross-links occurred in the C- or N-terminal flexible regions of KLCR1 and EF hands 1 and 3 in CaM2. The intra-molecular cross-links within KLCR1 suggest close proximity between the N- and C-terminus, making the apparent connection between CaM2 and both termini of KLCR1 more plausible (**Fig. 23 A**). Interestingly, the general pattern of intra-molecular cross-links within KLCR1 is almost identical between KLCR1 alone or KLCR1 complexed with CaM2 (**Fig. A.19**). This is consistent with previous observations regarding the structural rigidity of tandem-repeat proteins when bound to ligands [52] [42]. The formation of a largely similar pattern of inter-molecular cross-links between KLCR1 and CaM2 in the presence and absence of 1 mM added CaCl₂ is puzzling. No interaction between KLCR1 and CaM2, and therefore no cross-links were expected in the absence of Ca²⁺ (**Fig. A.19 B and C**). Possible explanations may be either the formation of an artificial KLCR1-CaM2 complex in the presence of added CaCl₂ due to a lack of incubation time prior to the addition of the cross-linker, the presence of residual Ca²⁺ within CaM2, which was sufficient for complex formation, or the stabilisation of a KLCR1-CaM2 complex that can still form in the absence of Ca²⁺ but would be too unstable to be observed by other means or be biologically relevant. Pre-incubation of KLCRs and CaMs with CaCl₂ prior to the addition of the cross-linker would be the most straightforward way of testing these possibilities, similar to how cross-linking-based structures of TIR1-AUX/IAA complexes were generated with pre-incubation of TIR1 and IAA7 or IAA12 with auxin [102]. Cross-linking experiments including KLCR2 and/or CaM7 may shed light on the structural determinants underlying differential protein-protein interactions, and therefore their possible regulatory effects in the context of the KLCR-IQD-module.

In silico modelling was used to visualise the spatial arrangement of KLCR1 and CaM2 in KLCR1-CaM2 complexes. Alphafold models of KLCR1 and CaM2 showed high confidence due to the availability of good templates for derived models of both proteins (**Figs. 24 and A.20**). A drawback of derived protein models is the lack of confidence when modelling flexible regions of

proteins of interest, as seen in the termini of KLCR1, or the linker between the EF-hand domains of CaM2. The lack of intra-molecular cross-links in CaM2 additionally complicated validation of CaM2-models with experimental data. Intra-molecular cross-links in KLCR1 confirm the compact fold of the TPR domain suggested by the AlphaFold 2.0 database. Violated cross-links between the C-terminus and the core of KLCR1 suggest an even more compact conformation of the protein than represented in the model. Manual refinement of the AlphaFold models using cross-linking data as distance restraints may resolve confidence issues and produce a model of KLCR1 with higher quality.

The generation of protein complex models produced the first data-based models of KLCR-CaM complexes. It also showed the advantages of HADDOCK-based modelling over AlphaFold multimer. Using the experimental cross-links as distance restraints during modelling, the HADDOCK models of KLCR1-CaM2 complexes agree with the fine-mapping of CaM-binding sites in KLCR1, placing CaM2 in the C-terminus of the TPR domain of KLCR1 (**Figs. 18 B and 25 A and C**). Violated intra-molecular cross-links in KLCR1 and inter-molecular cross-links between the core of KLCR1 and CaM2 may point towards a complex between a more compact conformation of KLCR1 and an extended conformation of CaM, as reported for other CaM-targets [263]. Binding energies calculated by HADDOCK suggest that electrostatic interactions are the main contributor to KLCR1-CaM2 binding (**Fig. A.22**). This is consistent with the regulation of CaM-binding in other TPR domain proteins by PTMs that affect surface charge, such as phosphorylation [193]. The contribution of electrostatic interactions to KLCR-CaM-binding may be further investigated by CaM-pulldowns in different pH conditions or salt concentrations. CaM-pulldowns of KLCR1 in the presence of 1 M NaCl suggest high resistance of KLCR-CaM-binding to ionic strength (**Fig. A.41 A**). Further experimental investigation may provide more detailed insights. AlphaFold multimer created a wide range of assemblies of CaM2 on KLCR1. The highest ranked model placed CaM2 near the core of the TPR domain, violating almost all experimental cross-links (**Fig. 25 B and D**). Taken together, these data show that cross-linking of KLCR1 and CaM2 coupled with MD simulations via HADDOCK produced satisfactory complex models. Improved cross-linking data resulting from pre-incubation of KLCRs and CaMs with CaCl₂ prior to the addition of DSBU may bolster the confidence of these models by providing higher quality restraints for the refinement of monomeric protein models, and HADDOCK MD simulations. The high quality of KLCR1-CaM2 complex models based on data from experiments without added CaCl₂ suggests that the residual Ca²⁺ present as a contamination in buffer solutions is sufficient to form holo-CaM-mediated protein complexes. Cross-linking experiments with lower concentrations of CaCl₂ may thus produce KLCR1-CaM2

complexes under more physiologically relevant conditions that may represent a more natural complex assembly [211].

Affinity measurements carried out by MST between KLCR1 and CaM2, CaM4, and CaM7 confirmed the differential binding between KLCR1 and different CaM-isoforms observed in *in vitro* pulldowns (**Fig. 17**). The calculated K_D values of 48 ± 23 nM between KLCR1 and holo-CaM7, 190 ± 65 nM for holo-CaM2, and 270 ± 109 nM for holo-CaM4 are within the physiologically relevant range, but suggest preferential binding for CaM7 over CaM2 over CaM4. Most holo-CaM binding affinities reported in literature lie between 1 and 600 nM [299] [300] [301] [302] [123] [303], although the effects of different methods of affinity determination on the resulting K_D must be taken into account. Furthermore, different CaM-binding motifs have different affinities for holo-CaM. Differential CaM-binding has been reported for other CaM-targets. KCBP showed an almost twofold stronger binding affinity for CaM2 over CaM4 and CaM6 [254]. Similar differences in target binding affinity were also described in soybean CaMs, despite identical target profiles [252]. Differential target-affinity may provide a mode of regulation of CaM-target-interactions, either by fine-tuning the relative abundance of different CaM-isoforms [252], or by making use of different Ca^{2+} -binding affinities of different CaMs or even different EF-hands in the same CaM [250] [251]. Following the latter hypothesis, affinity measurements with different KLCRs, or in the presence of different, physiologically relevant Ca^{2+} -concentrations may shed light on these modes of regulation. They may also provide insights into the role of CaM-mediated Ca^{2+} -signalling on the scaffolding function of KLCRs in KLCR-IQD-mediated protein complexes. Putative interaction of KLCRs with CMLs may serve as an additional layer of protein complex regulation *in planta*, as would the tissue-dependent regulation of the expression of different CaM- and CML-isoforms, and stress-dependent changes in the intracellular Ca^{2+} -signature.

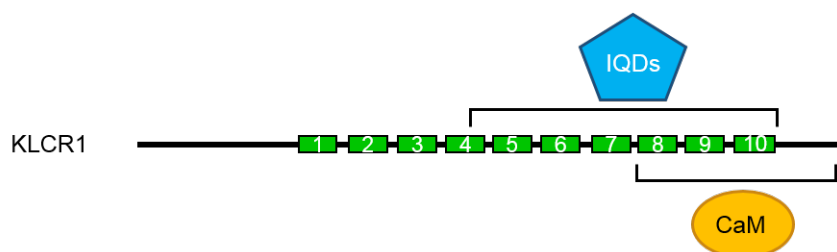


Figure 48: Putative binding regions for interaction partners in KLCR1. A: Putative binding regions of IQD2 and CaM in the TPR domain of KLCR1.

3.3.2 IQD2 as a mediator of CaM-signalling

IQ67 domain proteins comprise one of the largest classes of plant-specific CaM-targets [32]. Their CaM-interaction is conferred by their conserved IQ67 domain and believed to be mediated by up to three IQ motifs and a variable number of 1-5-10 and 1-8-14 motifs [32]. These different motifs potentially allow for interaction with both apo- and holo-CaM – in contrast to the exclusive holo-CaM interaction observed in KLCRs and NET3s. Due to their ability to recruit apo-CaM, IQDs may play a crucial role in the recruitment of apo-CaM to KLCR-IQD mediated protein-complexes, either as a means to rapidly confer CaM-mediated Ca^{2+} -signals to other complex members, as a Ca^{2+} -dependent molecular switch, or as a Ca^{2+} -independent means of complex regulation by apo-CaM [198]. Y2H experiments painted a clear picture of the CaM-binding sites in IQD2. Only constructs of IQD2 containing the IQ67 domain were capable of CaM-interaction (**Fig. 39**). These experimental data agree with *in silico* predictions of CaM-binding sites within IQD2, which place the highest CaM-binding score in the N-terminal half of the IQ67 domain, followed by the very N-terminus of IQD2, the region just C-terminal of the IQ67 domain, and lastly the C-terminus of IQD2 (**Fig. A.36**). They are also consistent with previously reported CaM-binding of the IQ67 domain of IQD1 [123]. In contrast to the IQD2-KLCR1-interaction, no difference was observed between the CaM-binding of only the IQ67 domain, or longer constructs containing this domain, suggesting that there are no additional motifs within IQD2 contributing to the CaM-interaction.

Although no CaM-interaction was shown for the IDRs of IQD2, they may play a role in fine-tuning the binding affinity of IQD2 for apo- or holo-CaM. Mechanisms of fine-tuning a protein-protein interaction by the inclusion of disordered regions of varying size and composition in one binding partner were reported in the case of the IDPs IAA7 and IAA12 in their auxin-dependent interaction with TIR1 [102]. Similar mechanisms may be at play in IQD proteins, contributing to differential CaM-binding of different IQDs. Additionally, IQ motifs in myosins were shown to adopt different conformations in complex with apo- or holo-CaM, indicating possible modes of structural regulation of IQDs by CaM-binding [289]. The abolition of apo-CaM-interaction but retention of holo-CaM-interaction of IQD2 in the presence of 1 M NaCl suggests strong binding between IQD2 and holo-CaM (**Fig. A.41 A**), consistent with previously reported strong interaction of holo-CaM with target proteins [256]. Holo-CaM binding was reported to be unaffected by mechanisms of disrupting electrostatic interactions, e.g. by pH or changes in ionic strength [256] [257] [290], consistent with experimental data. Abolition of apo-CaM-binding correlates with reported decreased interaction surfaces between apo-CaM and target proteins, and thus likely weaker interaction [256] [263]. High ionic strength was additionally

shown to result in destabilisation of apo-CaM [290], thus possibly limiting its interactions with target proteins further.

IQD2 was capable of recruiting all tested *AtCaM*-isoforms to the microtubule cytoskeleton (**Figs. 41 B, A.37 B, and A.38 B**) consistent with the microtubule localisation of other clade III IQDs [123] [36]. IQD2 also recruited CaM2 to microtubules in *in vitro* microtubule spin-downs, further confirming a direct, physical interaction between these proteins (**Fig. 32**). MTB2 of IQD2 partially overlaps with the IQ67 domain, the primary CaM-binding site in IQD2. Interestingly, CaM-binding resulted in the out-competition of microtubule binding of MTB2 when co-expressed with CaM2 in *N. benthamiana* (**Fig. 41 D**). This was not the case for CaM4 or CaM7 (**Figs. A.37 D and A.38 D**), suggesting possible modes of differential CaM-mediated regulation of the subcellular localisation of IQD2 by different CaM-isoforms. Similar to the regulation of KLCR-scaffold functions by CaMs, this may be achieved by regulation of the availability of different CaMs or differential Ca^{2+} -affinities and therefore the presence of different holo-CaMs in different cellular contexts [254] [252] [250] [251]. These findings suggest that IQD2 may not only function as a docker for KLCRs to the microtubule cytoskeleton, but also for different *AtCaM*-isoforms.

Co-expression and co-purification of IQD2 with CaM2 or CaM7 resulted in an increased yield of soluble IQD2 compared to expression and purification of IQD2 by itself (**Fig. A.27**), suggesting a stabilising effect of the IQD-CaM-interaction on IQD2, as described for other CaM-binding proteins [237] [264]. These co-expressions may be used for future cross-linking experiments to gain insight into the binding mode between IQD2 and different CaMs. In contrast to the cross-linking experiments carried out with KLCR1 and CaM2, tag-removal from IQD2 may not be possible due to the solubility-enhancing effect of the SUMO-tag used in most *in vitro* assays involving IQD2 in this thesis [304]. Biochemical assays with a reduced truncation of IQD2 encompassing only the IQ67 domain, i.e. amino acids 114 to 180, may provide further insights into its CaM-binding potential, possible regulation of IQD2-CaM-interactions by the IDRs of IQD2, and may allow for more detailed structural studies of differential binding between IQD2 and different CaMs, and therefore possible modes of conferring differential CaM-mediated Ca^{2+} -signalling to KLCR-IQD modules.

3.3.3 Calcium-signalling as a regulator of the subcellular localisation of NET3s

Here we showed that both NET3A and NET3C specifically interact with holo-CaM (**Fig. 47 B**). These findings suggest an additional layer of CaM-mediated regulation of the assembly and localisation of extended KLCR-IQD-NET3-modules and their localisation to the actin

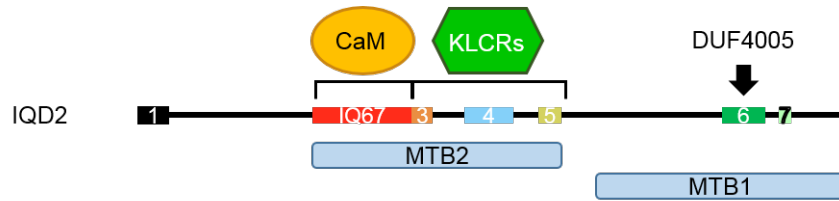


Figure 49: Putative binding regions for interaction partners in IQD2. Putative binding region of CaM in the IQ67 domain of IQD2, KLCRs in motifs #3 to #5, and microtubules in MTB1 and MTB2. The DUF4005 domain likely confers microtubule binding in MTB1.

cytoskeleton. Given the predicted possible position of CaM-binding sites in NET3C in its C-terminal coiled-coil domain and/or in the C-terminal half of its NAB domain, a mechanism of regulating the actin-association of NET3s similar to how CaM- and KLCR-binding may affect the microtubule localisation of IQDs seems plausible (**Fig. A.42 A**). Another possible function more connected to CaM-binding in the coiled-coil domain may be the regulation of interactions between NET3s and VAP27-1 or KLCRs, given the putative role of coiled-coil domains as protein-protein interaction domains [209]. Alternatively, CaM-binding in the coiled-coil domain may indirectly affect actin-binding by either masking or unmasking the NAB domain similar to how coiled-coil domains in other proteins can affect protein-protein interactions [69]. Similarity between *in silico* predictions of CaM-binding sites in NET3A and NET3C suggests possible general modes of NET3-regulation by CaM (**Fig. A.42 A and B**). In animals, Ca^{2+} -signals are known to promote the establishment and stabilisation of EPCS [305]. Furthermore, the ER provides a crucial intracellular Ca^{2+} -store and EPCS have been shown to be crucial to maintain Ca^{2+} -homeostasis by re-filling internal stores [224]. CaM-mediated regulation of NET3s may therefore influence the establishment and maintenance of EPCS and may regulate Ca^{2+} -homeostasis in plants.

Ultimately, further research into the exact function of NET3s and a mechanistic understanding of their interaction with VAP27-1 and actin is necessary to uncover their function in the regulation of KLCR-IQD modules and gain insight into the role of CaM-mediated Ca^{2+} -signalling in their regulation.

3.3.4 Assembly of calcium-signalling modules by ternary interactions between KLCRs, IQD2, and apo-CaM

The ability of IQD2 to recruit KLCRs to apo-CaM was shown in this thesis (**Fig. 42**). These data are consistent with previously reported ternary interactions between KLCRs, IQDs, and CaM [36]. They suggest a function in the pre-assembly of Ca^{2+} -signalling modules aided

by IQDs. Interestingly, the co-recruitment of IQDs and KLCRs to apo-CaM also resulted in an increase in apo-CaM-binding affinity of the respective IQDs, comparable to the affinity for holo-CaM. Contrary to the apparent preferential interaction of IQD2 with KLCR2 over KLCR1 and KLCR3, no strong preference in the co-recruitment of IQD2 with any KLCR became obvious in *in vitro* pulldowns (**Fig. 42**). *In vivo* BiFC assays further showed recruitment of KLCR1-CaM complexes to the microtubule cytoskeleton by IQD2, suggesting that KLCRs and CaMs may be recruited by IQDs at the same time and that their coupled binding does not hinder microtubule association of IQDs *in planta* (**Figs. 44 and 51 B**). While these *in vivo* assays likely featured holo-CaM due to Ca^{2+} present in plant cells, not apo-CaM, they suggest the assembly and subcellular recruitment of IQD-mediated Ca^{2+} -signalling modules *in planta*.

Preliminary experiments assessing the concentration dependency of KLCR-IQD2 co-recruitment to apo-CaM showed that gradual reduction of the amount of KLCRs in co-CaM-pulldowns with constant input amounts of IQD2 resulted in a gradual decrease of the apo-CaM affinity of IQD2, suggesting a concentration-dependent mechanism of increased apo-CaM affinity conferred by the interaction of IQD2 and KLCRs (**Fig. A.39**). While the interaction of KLCRs and IQDs may cause the increase in apo-CaM binding affinity, CaM-pulldowns in the presence of 1 M NaCl showed that an abolition of apo-CaM-binding of IQD2 also resulted in the abolition of the ability to co-recruit to apo-CaM with KLCR1. Possible explanations for this co-recruitment may be that either the interaction of IQD2 and KLCR1 results in the accessibility of a combined interaction surface for apo-CaM binding with increased affinity, or structural changes in IQD2 that result in this increased binding affinity (**Fig. 50 B**). Changes in the conformation of IQ-domains of myosins complexed with holo- or apo-CaM support conformation-specific binding mechanisms of IQD2 to CaM [289]. Alternatively IQD2 may bind to apo-CaM with its "normal" binding affinity and subsequently recruit KLCR-dimers that can then bind an additional IQD2, leading to an apparent increase in binding affinity that isn't really one (**Fig. 50 C**). While the former hypothesis seems more plausible, both of these hypotheses could be tested by a structural biology approach. Cross-linking of KLCR-IQD-CaM complexes in the presence and absence of Ca^{2+} may provide insights into the binding mechanisms underlying the formation of these complexes. Similar approaches, combining cross-linking data with computational biology, and existing 3D structures of components of a protein complex, have been successfully employed in recent years to generate 3D models of the endocytic TPLATE complex [276]. Existing crystal structures of holo- and apo-CaM and the high degree of structural conservation between TPR domains make this a very viable endeavour [246]. The challenges posed by *in vitro* handling of IQDs may also be addressed in this manner, as cross-linking was shown as a

suitable tool for protein complex stabilisation, potentially lowering the risk of IQD-degradation in solution [306]. The resulting structural information could be used to specifically generate mutants of IQDs or KLCRs which are incapable of some of their protein-protein interactions, to assess which interactions contribute to which function *in planta*.

To further understand the minimum required module that can still confer co-recruitment of

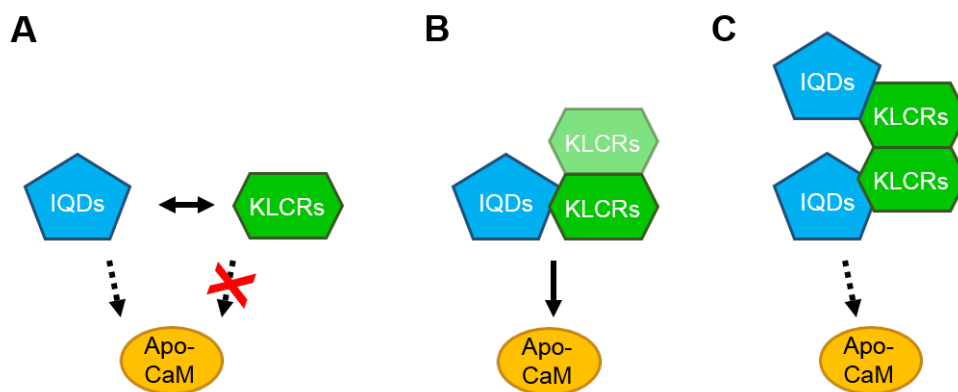


Figure 50: Modes of IQD-KLCR apo-CaM interaction. **A:** IQDs interact with apo-CaM, while KLCRs do not. **B:** IQDs and KLCRs may form complexes that result in an increased apo-CaM affinity compared to single proteins. **C:** IQDs may recruit KLCRs to apo-CaM. KLCR-homo-interaction may result in the recruitment of additional KLCRs and IQDs, resulting in an apparent increase in binding affinity.

IQD2 and KLCRs to apo-CaM, the previously described truncations of IQD2 were subjected to co-CaM-pulldowns with KLCR1. Constructs containing the IQ67 domain and conserved motif #3 of IQD2 were capable of co-recruiting KLCR1 to apo-CaM, suggesting that amino acids 98 to 198 of IQD2 form the minimum required module for this function (**Fig. 43**). Those constructs additionally containing conserved motifs #4 and #5 showed stronger apo-CaM co-recruitment, suggesting a supporting function of these motifs, similar to how motif #3 was sufficient for KLCR-binding of IQD2 in His-pulldowns, but motifs #4 and #5 enhanced the binding strength (**Fig. 35 A**). Motifs #4 and #5 alone were not capable of co-recruiting to apo-CaM with KLCR1, further confirming that both CaM- and KLCR-binding capacity within IQD2 are necessary for this ternary interaction. These findings are also consistent with the concentration dependency of IQD2-KLCR co-recruitment to apo-CaM, whereby increased IQD2-KLCR-interaction correlated with increased affinity for apo-CaM (**Fig. A.39**).

Taken together, these data suggest that IQDs may function as adaptors in the formation of ternary KLCR-IQD-CaM complexes, enforcing proximity between KLCRs and CaMs for subsequent Ca^{2+} -signal transfer between the two [37] [38]. They further point to an additional docking function for IQDs in recruiting KLCRs and CaMs to the microtubule cytoskeleton simul-

taneously [39]. IQDs may therefore act as scaffolds with docking function in Ca^{2+} -signalling. Since these interactions may be governed by electrostatic interactions, this function may be subject to regulation by PTMs that affect the local electrostatic environment of these proteins, such as phosphorylation [307] [36] [191]. Ca^{2+} -dependent transition from apo- to holo-CaM may serve as a molecular switch for changes in protein complex composition or structure. The structural flexibility of IQDs, and the N- and C-terminal regions of KLCRs may thus serve as a regulatory mechanism of protein complex formation by governing the steric accessibility of certain interaction sites and surfaces [74] [94]. These data provide a starting point for further in-depth characterisation of ternary interactions between KLCRs, IQDs, and CaMs to uncover mechanisms of multi-protein complex formation and their regulation.

3.4 Assembly and regulation of KLCR-IQD-mediated complexes by the interplay between docking, scaffolding, and cellular signalling

The KLCR-IQD core module serves as a central module for protein complex assembly. Its functions can be augmented and linked to specific subcellular sites by the inclusion of other binding partners, such as NET3s. IQDs may fulfil a dual function in KLCR-IQD-mediated protein complex assembly. Their ability to interact with microtubules and the PM highlights them as putative dockers of KLCR-IQD modules to these subcellular sites [34]. Their predicted disorder and ability to bind both KLCRs and CaMs simultaneously marks them as scaffolds or adaptors in protein complex assembly, enforcing proximity between its components and CaM for Ca^{2+} -signal integration. The interaction of IQDs with apo-CaM, specifically, suggests a function in the pre-assembly of Ca^{2+} -signalling modules for rapid signal processing. KLCRs bind IQDs, NET3s and CaM, highlighting them as the most central coordinator of KLCR-IQD modules that acts as a bridge between microtubule-binding and actin-binding components of assembled protein complexes. Lastly, NET3s likely act as dockers to the actin cytoskeleton and as adaptors to VAP27-1 and other components of the PINK complex [210] [27]. The capacity of all investigated proteins to interact with holo-CaM suggests a crucial role for CaM-mediated Ca^{2+} -signalling in the regulation of the assembly, organisation, or localisation of KLCR-IQD-mediated protein complexes (**Fig. 51 C**). It also points to the possibility of Ca^{2+} -signal transfer to other putative interactors of these complexes, therefore acting as a cellular signalling hub [35] [267]. As bridging complexes between both cytoskeleton components, the ER, and the PM, cell-cycle dependent regulation of KLCR-IQD modules may be critical to their correct function. CaM-mediated Ca^{2+} -signalling has been implicated in cell cycle regulation in the past, and the CaM-mediated initiation of cyclin-dependent phosphorylation has been suggested as a

regulatory mechanism [308] [309] [219]. As cyclin-dependent kinases (CDKs) share a recognition site with MPKs (S/TP), of which both IQDs and KLCRs are known targets [36], cell-cycle dependent PTMs may affect KLCR-IQD-mediated protein complex assembly and localisation in different cellular contexts.

Additionally, KLCR-IQD modules may be subject to compositional diversity as a regulatory mechanism. *A. thaliana* possesses 33 IQDs, of which more than ten are capable of differential interaction with different KLCRs, and all of which are capable of CaM-interaction (Bürstenbinder, unpublished data). The addition of four CaM-isoforms encoded by seven genes, two KLCRs capable of NET3-interaction [27], and two NET3s capable of KLCR-interaction [27], suggests a vast possible array of KLCR-IQD mediated protein complexes. These complexes may be subject to context-dependent regulation by different CaM-isoforms in different Ca²⁺-signatures. Co-immunoprecipitation of KLCR-IQD-mediated protein complexes from different plant tissues or plant cells in different stages of the cell cycle may provide insights into this diversity. Cross-linking in cell lysates may help stabilising the more transient interactions or less stable protein components of these complexes [306].

A structural biology approach combining x-ray crystallography, cross-linking experiments, and

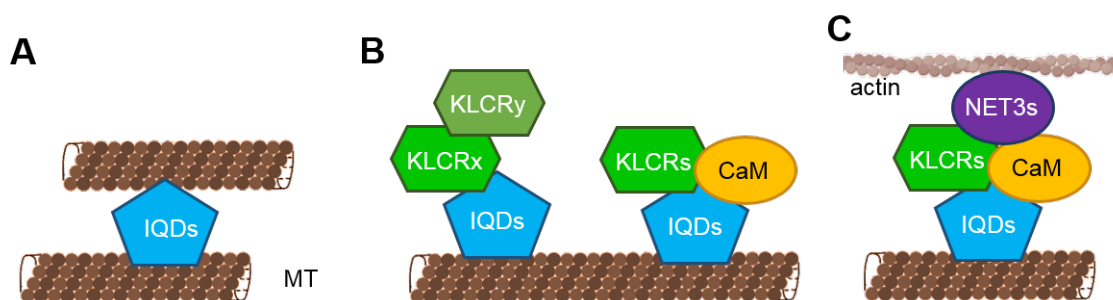


Figure 51: Configurations of KLCR-IQD complex components on the cytoskeleton. A: Microtubule bundling by IQDs. **B:** Recruitment of KLCRs and/or CaMs to microtubules by IQDs. **C:** A bridging complex consisting of IQDs, KLCRs, and NET3s connects microtubules and actin, subject to CaM-mediated regulation.

in silico modelling may also shed light onto the structural and functional characteristics of KLCR-IQD modules. Existing crystal structures of CaMs allow for molecular replacement for structure elucidation by crystallography [246]. The integration of these different approaches, and combination with cryo-EM may allow for the generation of a structural model of the whole KLCR-IQD core module and associated proteins in the future [276]. This is further aided by the increasing reliability of *in silico* structure predictions thanks to the recent advances made by AlphaFold and AlphaFold multimer [280] [310] [278], especially when combined with MD simulations using software like HADDOCK [281] or RosettaDock [311].

4 Materials and Methods

4.1 Equipment and consumables

Table 3: Equipment

Device	Model	Manufacturer
Autoclave	DX-200	Systec
Centrifuge	Centrifuge 5415 D Centrifuge 5424 Centrifuge 5804 R Centrifuge 5810 R Mikro 200 R Avanti J-26 XP Avanti J-30 I LE-80 Ultracentrifuge PicoFuge	Eppendorf Eppendorf Eppendorf Eppendorf Hettich Beckman Coulter Beckman Coulter Beckman Coulter Stratagene
Fluorescence imager	FluorChemQ	Alpha InnoTech
Gel electrophoresis	Protean Mini	Bio-Rad
Heating block	Thermomixer C Thermomixer 5436	Eppendorf Eppendorf
Incubator	Innova 4330 Innova 44 Unitron	New Brunswick Scientific New Brunswick Scientific Infors
Laser Scanning Microscopes	LSM780 LSM880 LSM900	Carl Zeiss Carl Zeiss Carl Zeiss
MST device	Monolith	Nanotemper
PCR cycler	T-Gradient SimpliAmp	Biometra Applied Biosystems
Photometer	BioPhotometer Plus DU800 Infinite M200 Infinite M1000	Eppendorf Beckman Coulter Tecan Tecan

Device	Model	Manufacturer
Rotator	Rotator Mixer	Starlab
Rotors	JA 30.50 Ti JLA 8.1000 TLA 110	Beckman Coulter Beckman Coulter Beckman Coulter
Sonicator	Sonopuls TS102 & TS106	Bandelin
UV detection	Gel Doc XR +	Bio-Rad
Western blotting	Trans-Blot SD Semi-Dry transfer cell	Bio-Rad

4.1.1 Chromatography

Proteins were purified by (GSH) affinity chromatography, Immobilised Metal Affinity Chromatography (IMAC), ion exchange chromatography, or SEC. Protein purifications were carried out using an ÄKTApure Fast Protein Liquid Chromatography (FPLC) system by Cytiva, formerly known as GE Healthcare Life Sciences, or gravity flow columns with appropriate agarose resin. Chromatography columns and resins were provided by GE Healthcare, Macherey-Nagel, Serva Electrophoresis GmbH, Sigma Aldrich, or Thermo Fisher Scientific.

Table 4: Resins

Resin	Method	Provider
Glutathione agarose resin	Affinity	Serva
Protino Ni-NTA agarose	IMAC	Macherey-Nagel
Cobalt agarose	IMAC	Macherey-Nagel
CaM agarose	Affinity	Sigma Aldrich

Table 5: ÄKTApure columns

Column	Method	Size	Provider
HiPrep Sephacryl S-100 HR	Gel filtration	16/60	GE Healthcare
HiLoad 16/60 Superdex 75 pg	Gel filtration	16/60	GE Healthcare
HiLoad 16/600 Superdex 200 pg	Gel filtration	16/600	GE Healthcare
MonoQ 5/50 GL	Ion exchange	1 ml	GE Healthcare

Table 6: Standards, kits, and specialised consumables

Standard/Kit/Consumable	Provider
Amicon Ultra 15 ml Centrifugal Filter	Merck Millipore
Roche cOmplete TM Protease Inhibitor Cocktail	Merck
GeneJET Plasmid Miniprep-Kit	Thermo Fisher Scientific
GeneJET Gel Extraction and DNA Cleanup Micro Kit	Thermo Fisher Scientific
Microtubule Binding Protein Spin-Down Assay Biochem Kit	Cytoskeleton Inc.
Protein Labeling Kit RED-NHS	Nanotemper
Protein Labeling Kit RED-NHS 2nd Generation	Nanotemper
PageRuler TM Prestained Protein Ladder	Thermo Fisher Scientific
Spectra TM Multicolor Broad Range Protein Ladder	Thermo Fisher Scientific
GeneRuler TM 1 kb DNA Ladder	Thermo Fisher Scientific
Cytiva Amersham TM ECL Select TM Western Blotting Detection Reagent	Thermo Fisher Scientific
Cytiva Amersham TM ECL Prime TM Western Blotting Detection Reagent	Thermo Fisher Scientific

4.1.2 Chemicals & software

All chemicals used in this thesis are commercially available and were purchased from Bio-rad, Carl Roth, Duchefa, gibco, Merck, Miltenyi Biotec, New England Biolabs (NEB), Otto Nordwald, QIAGEN, Serva, Sigma Aldrich, St. John's Laboratory, Thermo Fisher Scientific, or VWR. Primers and expression constructs were generated and analysed using the Clone Manager Suite, the SnapGene ViewerTM, or Benchling. Primers were purchased from Eurofins Genomics. Multiple Sequence Alignments were carried out with the help of ClustalO or Muscle using default settings, and visualised using JalView Desktop. ImageJ [312] was used to quantify protein amounts in denaturing PAGEs and for general image processing. The HeliQuest server was used for helical wheel projections [313]. Laser Scanning Microscopes were operated using the Zen software provided by Zeiss. MST experimental data was processed using the MO.Control and MO.Affinity Analysis software by NanoTemper. Statistical analyses were carried out using Graphpad PRISM [314] or MS Excel. Cross-linking LC/MS/MS data were analysed using the software MeroX [315], and plots were generated with the xVis Crosslink Analysis Web-server [316]. Plots generated by xVis were processed using Inkscape. 3D protein models based

on the cross-linking data were generated using a local installation of AlphaFold [310], processed with Python, and molecular docking was carried out with HADDOCK [281] using the cross-links as distance restraints [282]. Conserved motifs in IQD proteins were identified using the MEME suite [317] using default settings, except for a maximum window width of 67. Protein disorder predictions were generated using the servers IUPRED [318], MFDp2 [319], PONDR [320], PrDOS [321], and PsiPred [322]. A disorder prediction consensus was generated as the average of their respective predictions. Protein 3D models were obtained from the AlphaFold 2.0 database [269], or generated using the MODELLER server [323], and visualised using PyMol [324]. Charge plots were generated using the EMBOSS charge tool [325]. Online databases used in this thesis were The *Arabidopsis* Information Resource (TAIR) [326], the Uniprot database [327], the CaM-target database, the Calmodulation database [328], and the RCSB Protein Data Bank (PDB) [329]. This thesis was written using L^AT_EX.

4.2 Buffers and media

Table 7: Buffers – protein work and purifications

Buffer	Recipe
Standard buffer	50 mM Tris-HCl pH 8.0, 200 mM NaCl
His lysis buffer	Standard buffer, 10 mM imidazole, 1 mM PMSF, 1x Roche cOmplete protease inhibitor cocktail
His wash buffer 1	Standard buffer, 25 mM imidazole
His wash buffer 2	Standard buffer, 50 mM imidazole, 1 M NaCl
His wash buffer 3	Standard buffer, 100 mM imidazole, 20 mM MgCl ₂ , 5 mM ATP
His elution buffer	Standard buffer, 250 mM imidazole, 10 % (v/v) glycerol
GST lysis buffer	Standard buffer, 5 mM DTT or DTE, 1 mM PMSF, 1x Roche cOmplete protease inhibitor cocktail
GST wash buffer 1 & 3	Standard buffer, 5 mM DTT or DTE
GST wash buffer 2	Standard buffer, 1 M NaCl, 5 mM DTT or DTE
GST elution buffer	Standard buffer, 5 mM DTT or DTE, 10 mM GSH, 10 % (v/v) glycerol
<i>A. tumefaciens</i> infiltration buffer	10 mM MES-KOH pH 5.3, 10 mM MgCl ₂ , 150 µg /ml acetosyringone

Buffer	Recipe
<i>In vivo</i> pulldown buffer	20 mM HEPES-KOH pH 7.5, 40 mM KCl, 1 mM EDTA, 1x Roche cOmplete protease inhibitor cocktail, 1 mM PMSF, 10 % (v/v) glycerol, 0.1 % (v/v) Triton-X100 (only for lysis)
CaM-binding-buffer	5.8 mM Tris-HCl pH 8.0, 2.7 mM KCl, 137 mM NaCl, 0.1 % (v/v) Tween20, 0.002 % (w/v) NaN ₃ optional: 1 mM CaCl ₂ or 5 mM EGTA if used in CaM-PDs or MST measurements involving CaM
High-salt CaM-binding-buffer	CaM-binding-buffer, 500 mM NaCl
Max. salt CaM-binding-buffer	CaM-binding-buffer, 1 M NaCl
MST-buffer	50 mM Tris-HCl pH 8.0, 150 mM NaCl, 10 mM MgCl ₂ , 0.05 % (v/v) Tween20 optional: 1 mM CaCl ₂ or 5 mM EGTA if used in CaM-PDs or MST measurements involving CaM
Cross-linking buffer	20 mM HEPES-KOH pH 7.5, 50 mM NaCl, 10 % (v/v) glycerol

Table 8: Buffers – general utility

Buffer	Recipe
4x Laemmli buffer [330]	250 mM Tris-HCl pH 6.8, 8 % (w/v) SDS, 40 % (v/v) glycerol, 20 % (v/v) β-Mercaptoethanol, 0.02 % (w/v) bromophenol blue
SDS-running buffer [330]	25 mM Tris-HCl pH 8.3, 192 mM glycine, 0.1 % (w/v) SDS
Towbin buffer	25 mM Tris-HCl pH 8.3, 192 mM glycine, 20 % (v/v) methanol, 0.1 % (w/v) SDS
Coomassie staining solution & destainer	40 % (v/v) ethanol, 10 % (v/v) acetic acid, 0.1 % (w/v) Coomassie Brilliant Blue (for staining solution only)
PonceauS staining solution	10 ml milliQ H ₂ O, 0.3 ml glacial acetic acid, 0.033 g PonceauS, milliQ H ₂ O to 30 ml final volume

Buffer	Recipe
TBS(-T)	50 mM Tris-HCl pH 7.8, 150 mM NaCl, 0.1 % (v/v) Tween20 (for TBS-T only)
PBS(-T)	137 mM NaCl, 2.7 mM KCl, 10 mM Na ₂ HPO ₄ , 1.8 mM KH ₂ PO ₄ , 0.1 % (v/v) Tween20 (for PBS-T only)
Column regeneration buffer (for Ni-NTA & Cobalt agarose)	20 mM MES-NaOH pH 5.0, 100 mM NaCl
50x TAE buffer	2 M Tris-HCl pH 8.3, 1 M glacial acetic acid, 50 mM EDTA
DNA loading buffer	10 mM EDTA, 10 % (v/v) glycerol, 0.025 % (w/v) bromophenol blue, 0.025 % (v/v) xylene cyanole

Table 9: Buffers – MS/MS analysis

Buffer	Recipe
ABC solution	100 mM ammonium bi-carbonate
DTT solution	10 mM DTT in ABC solution
IAA solution	55 mM iodoacetamide in ABC solution
Trypsin solution	12.5 ng/μl trypsin in ABC solution
AspN solution	2 to 5 ng/μl AspN
TFA solution	5 % (v/v) trifluoroic acid
Extraction buffer	1:2 (v/v) TFA solution in acetonitrile

Table 10: Media

Medium	Recipe
Lysogene Broth (LB) [331]	1 % (w/v) Bacto Tryptone, 0.5 % (w/v) Yeast extract, 1 % (w/v) NaCl, 1.5 % (w/v) agarose (for solid medium only)
S.O.C medium	2 % (w/v) Bacto Tryptone, 0.5 % (w/v) Yeast extract, 0.05 % (w/v) NaCl, 2.5 mM KCl, 10 mM MgCl ₂ , 20 mM Glucose
Terrific Broth (TB) [332]	1.2 % (w/v) Bacto Tryptone, 2.4 % (w/v) Yeast extract, 0.4 % (v/v) glycerol, 10 % (v/v) 10x KPi buffer

Medium	Recipe
10x KPi buffer	720 mM K ₂ HPO ₄ · 3 H ₂ O; 170 mM KH ₂ PO ₄
YPDA medium	2 % (w/v) Difco Peptone, 1 % (w/v) Yeast extract, 0.01 % (w/v) Adenine hemisulfate, 2 % (w/v) glucose
Drop-out media	0.68 % (w/v) YNB media, 0.5 % (w/v) glucose, appropriate DO mix (DDO, TDO, QDO), 0.001 % Adenine hemisulfate (for DDO and TDO), 2.5 mM 3-AT (for TDO with 3-AT), 1.7 % (w/v) bacto-agar

4.2.1 Bacterial strains, cell cultures, and plant material

All recombinantly expressed proteins used in *in vitro* studies were expressed in *E. coli* strain KRX. Plasmids were generated and amplified using *E. coli* strains TOP10, XLBlue, or DB3.1. *E. coli* were grown in LB (for propagation) or TB (for expression) medium (**Tab. 10**) at 37 °C over night if not stated otherwise. *A. tumefaciens* strains GV3101 (for constructs with kanamycin resistance) or GV3101pK (for constructs without kanamycin resistance) (**Tab. 12**) were used for transient expression of (fluorescent) proteins in *N. benthamiana*. *A. tumefaciens* were grown in LB medium at 28 °C for two days. *N. benthamiana* plants were grown under long-day conditions (16 h light, 8 h dark) at 18 to 20 °C and a relative humidity of 55 to 60 %. Soil mixed with vermiculite (1 to 2 mm) in a 4:1 ratio was used as growing substrate. Yeast strain PJ69-4a was used for Yeast-Two-Hybrid experiments. Yeast was grown in liquid YPDA (**Tab. 10**) at 30 °C over night or on drop-out media plates (**Tab. 10**) at 30 °C for several days until colonies showed.

4.3 Primers

Table 11: List of primers used in this thesis. Non-gene specific overhangs are marked as *italic*.

Primer name	Number	Sequence (5' to 3')
IQD2 fwd	2543	<i>G GGG ACA AGT TTG TAC AAA AAA GCA GGC TTC CTG GTG CCA CGC GGT AGT ATG GGG AAA AAA GCT AAA TGG TTT T</i>
IQD2 rev	2544	<i>GGG GAC CAC TTT GTA CAA GAA AGC TGG GTC TCA GCT GCC TGC TCC GTT</i>

Primer name	Number	Sequence
IQD2 F1 fwd	2461	<i>TTT GAA TTC CTG GTG CCA CGC GGT AGT ATG GGG AAA AAA GCT AAA T</i>
IQD2 F1 rev	2462	<i>TTT CTC GAG CTC TAA GGA GCA GAT GAA GAT G</i>
IQD2 F2 fwd	2463	<i>TTT GAA TTC CTG GTG CCA CGC GGT AGT GGT GTT GTT CGT CG</i>
IQD2 F2 rev	2464	<i>TTT CTC GAG CTC TAC TCT TTA GCA TGT TTC TGA A</i>
IQD2 F3 fwd	2465	<i>TTT GAA TTC CTG GTG CCA CGC GGT AGT CTA GCT GGC TTG AAG AA</i>
IQD2 F3 rev	2466	<i>TTT CTC GAG CTC TAG GTC CCT CTT GCG G</i>
IQD2 F4 fwd	2467	<i>TTT GAA TTC CTG GTG CCA CGC GGT AGT CCA AGA AAC AAA AAC AGT TT</i>
IQD2 F4 rev	2468	<i>TTT TCT AGA TTC AGC TGC CTG CT</i>
IQD2 F9 fw	2542	<i>G GGG ACA AGT TTG TAC AAA AAA GCA GGC TTC CTG GTG CCA CGC GGT AGT GGT GTT GTT CGT CGC GCT</i>
KLCR1 pET41a(+) fwd	2523	<i>CGG TGA TGA CGA CGA CAA GAG TCC CAT GGG AAT GCC AGC AAT GCC AGG</i>
KLCR1 pET41a(+) rev	2524	<i>GTG GTG GTG GTG CTC GAG TGC GGC CGC TCA GAA CTT GAA ACC GAG GC</i>
CaM2 pET41a(+) fwd	2525	<i>CGG TGA TGA CGA CGA CAA GAG TCC CAT GGC GGA TCA GCT CAC</i>
CaM2 pET41a(+) rev	2526	<i>GTG GTG GTG GTG CTC GAG TGC GGC CGC TCA CTT AGC CAT CAT AAC CTT CA</i>

4.4 Cloning

4.4.1 Vectors

Most protein constructs used were generated using the Gateway Cloning System [333]. Newly generated constructs were cloned into Gateway ENTR vectors and mobilised and expressed in DEST vectors. Restriction cloning was used to generate constructs in the pENTR3C vector. Constructs in the pET41a(+) vector were generated using Circular Polymerase Extension Cloning (CPEC). All expression vectors used N-terminal affinity or fluorescence tags. Most vectors used for transient expression in *N. benthamiana* expressed proteins under control of the 35S promoter. An exception to this is the pUBN-vector, using the UB10 promoter. Antibiotics used were kanamycin (Kan), gentamycin (Gent), carbenicillin (Carb), and spectinomycin (Spec).

Table 12: Vectors used in this thesis.

Method	Vector	Tag	Resistance
Gateway ENTRY vectors	pENTR3C	N/A	50 µg /ml Kan
	pDONR207	N/A	25 µg /ml Gent
	pDONR221	N/A	50 µg /ml Kan
Recombinant protein expression	pDEST15	GST	50 µg /ml Carb
	pDEST-N110	10xHis	50 µg /ml Carb
	pDEST-SUMO	8xHis-SUMO	50 µg /ml Carb
	pET41a(+)	GST-6xHis	50 µg /ml Kan
Transient expression in <i>N. benthamiana</i>	pB7WGF2	GFP	75 µg /ml Spec
	pB7WGC2	CFP	75 µg /ml Spec
	pGWB455N	RFP	75 µg /ml Spec
	pJOG393	mCherry	75 µg /ml Spec
	pDEST-VYNE	N-YFP	50 µg /ml Kan
	pDEST-VYCE	C-YFP	50 µg /ml Kan
	pUBN-GFP	GFP	75 µg /ml Spec
Yeast expression vectors	pDEST22	Gal4 AD	50 µg /ml Carb
	pDEST32	Gal4 DBD	25 µg /ml Gent

4.4.2 PCR & Protein fragment generation

Expression constructs of IQD2 featuring an N-terminal thrombin-cleavage-site for use in the Gateway cloning system, and constructs of KLCR1, CaM2, and CaM7 for cloning into the vector pET41a(+) via CPEC were generated by Phusion PCR. Truncated versions of IQD2 featuring an N-terminal thrombin cleavage-site were newly generated (**Tab. 11**). Truncated versions of KLCR1 and KLCR2 had been generated previously by Dr. Paul Pflug, Dr. Dipannita Mitra, or Anshu Khatri.

Table 13: Protein constructs

Protein	AA positions	Trivial name	Primers	T_m (°C)
KLCR1	1 to 610	N/A	2523 & 2524	55
CaM2 & CaM7	1 to 149	N/A	2525 & 2526	55
IQD2	1 to 461	N/A	2543 & 2544	56
	1 to 97	N-term	2461 & 2462	56
	98 to 198	IQ67	2463 & 2464	56
	199 to 327	M4+5	2465 & 2466	56
	328 to 461	C-term	2467 & 2468	56
	98 to 327	central	2463 & 2466	56
	98 to 461	Δ N-term	2542 & 2544	56

Phusion PCR was carried out using the Phusion High Fidelity PCR kit. PCR-products were separated via 1 % agarose gels [1 % (w/v) agarose, 1x TAE, 0.1 μ g /ml DNA stain G] and extracted according to manufacturer instructions using the GeneJET Gel Extraction and DNA Cleanup Micro Kit.

Table 14: Phusion PCR mix and program for fragment generation

PCR:		Program:		
		T (°C)	t	
5x Phusion buffer	10 μ l	98	30 s	30x
40 mM dNTPs	1 μ l	98	10 s	
10 mM Fw primer	2.5 μ l	T_m	30 s	
10 mM Rv primer	2.5 μ l	72	15 s/kb	
DNA template	1–50 μ g	72	10 min	
Phusion polymerase	0.5 μ l	4	∞	
milliQ H ₂ O	to 50 μ l			

4.4.3 Restriction cloning

Constructs of IQD2 featuring thrombin-cleavage-sites, except full length IQD2 and IQD2 $_{\Delta N-term}$, were cloned into the Gateway pENTR3C vector via restriction cloning. Inserts and vector were digested with the restriction enzymes in **Tab. 15**.

Table 15: Restriction digest of IQD2 constructs for cloning

PCR product or vector	Enzymes	Exp. size [kb]
IQD2 N-term	EcoRI & XhoI	0.32
IQD2 IQ67	EcoRI & XhoI	0.33
IQD2 M4+5	EcoRI & XhoI	0.42
IQD2 C-term	EcoRI & XbaI	0.43
IQD2 central	EcoRI & XhoI	0.72
pENTR3C	EcoRI & XhoI	2.28
	EcoRI & XbaI	2.27

Restriction digestions were carried out at 37 °C for 30 minutes (**Tab. 16**). FastAP was only added for vector digestion, not insert digestion, to avoid spontaneous re-ligation. Digested DNA products were separated by 1 % agarose gel, purified as above, and subjected to ligation using a T4 DNA ligase by either NEB, Promega, or Thermo Fisher Scientific (**Tab. 17**). Molar ratios were calculated using the NEBcalculator (<https://nebiocalculator.neb.com/>).

Table 16: Restriction digest

Digest:

Plasmid DNA	1 µg
10x Thermo Scientific FastDigest Buffer	2 µl
FastDigest Restriction Enzyme(s)	1 µl each
FastAP Thermosensitive Alkaline Phosphatase	1 µl
milliQ H ₂ O	to 20 µl

10 µl of the cloning reaction were directly transformed into *E. coli* TOP10 as described below. Individual colonies were picked from the plates and transferred into liquid LB medium with vector-specific antibiotics (**Tab. 12**). After over-night cultivation at 37 °C bacteria were subjected to plasmid preparation according to manufacturer instructions using the GeneJET

Plasmid Miniprep Kit. Ligation products were analysed via control digest using the enzyme combinations for cloning, and — if positive — were sent for sequencing by Eurofins Genomics to validate fidelity of the vector insert.

Table 17: Ligation setup

Sticky end ligation:	
Linear vector DNA	20-100 ng
Insert DNA	1:1 to 5:1 molar ratio over vector
10x T4 DNA Ligase Buffer	2 μ l
T4 DNA ligase	1 unit
milliQ H ₂ O	to 20 μ l

4.4.4 Gateway cloning

Constructs of full length IQD2 and IQD2 _{Δ N-term} featuring a thrombin cleavage site in the vector pDONR221 were generated via BP-reaction (**Tab. 18**). BP reaction mixes were incubated at room temperature (RT) for one to two hours. 5 μ l reaction mix were subsequently transformed into *E. coli* TOP10. Positive clones were confirmed via control digest and sequencing by Eurofins Genomics. Most expression vectors were generated using the Gateway

Table 18: BP-reaction

BP-reaction:	
DONR-vector	1–2 μ l (approx. 150 ng)
PCR product	1–2 μ l (approx. 150 ng)
BP clonase II	1 μ l
TE-buffer	to 10 μ l

cloning system. Except for those specified above, ENTRY-vectors for most constructs were already available. LR-reactions were carried out to mobilise expression constructs into vectors pDEST-N110, pDEST15, or pDEST-SUMO for recombinant protein expression, into the vectors pB7WGF2, pGWB455N, or pUBN-GFP for transient transformation of *N. benthamiana*, or into vectors pDEST22 or pDEST32 for Y2H experiments (**Tab 12**). LR reactions were carried out at RT for one to two hours and were subsequently transformed into *E. coli* TOP10 as described below (**Tab. 19**). Positive clones were identified via control digest.

Table 19: LR-reaction

LR-reaction:	
ENTRY-vector	1–2 μ l (approx. 150 ng)
DEST-vector	1–2 μ l (approx. 150 ng)
LR clonase II	1 μ l
TE-buffer	to 5 μ l

4.4.5 Circular Polymerase Extension Cloning

KLCR1, CaM2, and CaM7 were cloned into the vector pET41a(+) using the CPEC method modified from Quan *et al.* [334]. Inserts were generated via Phusion PCR as described above. The target vector was digested with restriction enzymes NcoI and NotI. PCR products and digested vector were purified via gel extraction (see above) and subjected to Phusion PCR for cloning (**Tab. 20**). Part of the PCR mix was directly used for transformation of *E. coli* TOP10, and part was analysed via 1 % agarose gel to assess successful cloning. CPEC products were analysed by control digest and – if positive – sequenced by Eurofins Genomics.

Table 20: CPEC PCR

PCR:		Program:		
		T (°C)	t	
5x Phusion buffer	10 μ l	98	30 s	30x
40 mM dNTPs	1 μ l	98	10 s	
10 mM Fw primer	2.5 μ l	T_m	30 s	
10 mM Rv primer	2.5 μ l	72	15 s/kb	
DNA template	1–50 μ g	72	10 min	
Phusion polymerase	0.5 μ l	4	∞	
milliQ H ₂ O	to 50 μ l			

4.4.6 Generation of chemically competent *E. coli*

For the generation of chemically competent bacteria, *E. coli* TOP10 or KRX were cultivated in 50 ml LB medium without antibiotics at 37 °C over night. Cells were sedimented by centrifugation for 10 min at 4 °C and 3,500 g. The supernatant was discarded and cells were re-suspended in 25 ml sterile 100 mM MgCl₂ and incubated for 60 min on ice. Cells were subsequently sedimented again and the supernatant discarded. Cells were re-suspended in 25 ml sterile 100 mM CaCl₂ and incubated on ice for 60 min. Washing with CaCl₂ was repeated twice with incubation times of 45 and 30 min. Cells were finally re-suspended in 4 ml sterile 100 mM CaCl₂ in 10 % (v/v) glycerol. Cells were aliquotted into 50 μ l aliquots, flash frozen, and stored

at $-80\text{ }^{\circ}\text{C}$.

4.4.7 Heat-shock mediated transformation of *E. coli*

50 μl chemically competent *E. coli* cells were thawed on ice for 5 min. Plasmid DNA or cloning mixes were added and cells were incubated on ice for 30 min. Following 40 s of heat shock at $42\text{ }^{\circ}\text{C}$ competent cells were incubated on ice for another 2 min. 200 μl sterile LB or SOC medium (**Tab. 10**) were added and the cells incubated at $37\text{ }^{\circ}\text{C}$ for a minimum of one hour. Cells were then incubated on solid LB medium (**Tab. 10**) containing vector-selective antibiotics at $37\text{ }^{\circ}\text{C}$ over night (**Tab. 12**). Colonies were picked from plates, grown in liquid medium containing the appropriate antibiotics, and either used for expression or plasmid propagation. pDEST-SUMO-IQD2 was co-transformed into *E. coli* KRX with pET41a(+)-CaM2 and -CaM7 for co-expression and -purification, as were pDEST-SUMO-KLCR1, -KLCR2, and -KLCR1_{spl} co-transformed with pET41a(+)-KLCR1 for co-expression and GST-pulldowns.

4.4.8 Generation of chemically competent *A. tumefaciens*

For the generation of chemically competent *A. tumefaciens*, strains GV3101 or GV3101pk were grown in LB medium (**Tab. 10**) at $28\text{ }^{\circ}\text{C}$ over night. Main cultures were inoculated in 100 ml LB and grown to an OD_{600} of 0.5 to 1. Cells were cooled on ice and subsequently sedimented by centrifugation at $4\text{ }^{\circ}\text{C}$ and 2,700 g for 20 min. Cells were re-suspended in 5 ml cold TE-buffer and sedimented as before. Cells were subsequently re-suspended in 1 ml 20 mM CaCl_2 , incubated on ice for 30 min, and sedimented as before. Cells were then re-suspended in 10 ml LB containing 10 % (v/v) glycerol, aliquotted into 100 μl aliquots, flash frozen, and stored at $-80\text{ }^{\circ}\text{C}$.

4.4.9 Heat-shock mediated transformation of *A. tumefaciens*

50 μl chemically competent *A. tumefaciens* cells were thawed on ice for 5 min. 5 μl of plasmid DNA were added and cells were incubated on ice for another 30 min. Following 5 min cold-shock in liquid nitrogen cells were heat-shocked for at $37\text{ }^{\circ}\text{C}$ 3 min. Cells were then placed on ice for 2 min. 200 μl LB medium were added and cells were grown at $28\text{ }^{\circ}\text{C}$ for minimum 1 hour. Cells were incubated on solid LB containing vector-selective antibiotics (**Tab. 12**) at $28\text{ }^{\circ}\text{C}$ for two days. Positive colonies were validated by colony PCR using insert-specific primers.

4.5 Protein production

4.5.1 Protein expression

For protein expression *E. coli* KRX were transformed with the respective expression construct and grown in liquid TB medium (**Tab. 10**) with appropriate antibiotics (**Tab. 12**). Pre-cultures were grown at 37 °C over night. Main expression cultures were inoculated with 1:40 to 1:100 dilutions of the over-night pre-cultures and grown at 37 °C for two to three hours for cold expression, or over night for warm expression (**Tab. 21**). Protein expression was induced with 0.5 mM IPTG and 1.4 mM rhamnose. For cold expression cells were grown at 16 °C for 20 hours. For warm expression growth time was approx. four hours at 37 °C. The main culture was subsequently sedimented by centrifugation for 15 min at 4,500 g. Cells were collected in 50 ml reaction tubes and either flash frozen in liquid nitrogen and stored at –20 °C or used directly for protein purification.

Table 21: Expression constructs and expression conditions

Protein	Vector	Expression conditions
IQD2	pDEST-N110	16 °C , 20 h
	pDEST-SUMO	37 °C , 4 h
IQD2 fragments	pDEST-N110	37 °C , 4 h
	pDEST-SUMO	37 °C , 4 h
KLCR1, KLCR2, & KLCR3	pDEST-N110	16 °C , 20 h
	pDEST15	16 °C , 20 h
	pET41a(+)	16 °C , 20 h
CaM2, CaM4, & CaM7	pDEST-N110	37 °C , 4 h
	pET41a(+)	37 °C , 4 h
NET3C	pDEST-SUMO	37 °C , 4 h
NET3A	pDEST-SUMO	37 °C , 4 h
GST	pDEST15	37 °C , 4 h

4.5.2 Native protein purification

For protein purification *E. coli* KRX cells containing the respective protein(s) were re-suspended in appropriate lysis buffer (**Tab. 7**). Cell pellet from 1 litre expression culture was filled up with lysis buffer to a total volume of 30 ml. Cell pellet from 50 ml expression culture was re-suspended in 2 ml lysis buffer. The re-suspended cells were lysed through sonication

(TS106, 15 min, 3 s pulse, 3 s pause, 95 % amplitude for 1 l; TS102, 2 min, no pulsation, 85 % amplitude) and the cell debris sedimented via centrifugation for 20 min at 4 °C above 20,000 g.

For affinity purification via gravity flow columns, 1 ml glutathione (GSH)-agarose resin (for GST-fusions) or Ni-NTA or Cobalt agarose resin (for His-fusions) per 50 ml cell lysate were equilibrated with ten bed volumes of the respective lysis buffer. The cleared cell lysate was poured over the column bed repeatedly (up to three times) and the flow-through collected. The column bed was subsequently washed three times with ten bed volumes of the respective wash buffer(s) (**Tab. 7**). Bound proteins were eluted up to five times with one bed volume elution buffer (**Tab. 7**). Crude extract, wash, and elution fractions were analysed via denaturing PAGE and protein eluates were concentrated to below 5 ml for further purification steps where necessary. For proteins that did not require further purification, buffers were exchanged by centrifugation in Amicon Ultra Centrifugal Filters (**Tab. 6**) to remove imidazole or GSH and transfer them into storage buffers containing 10 % (v/v) glycerol. Tandem affinity purification was carried out to produce pure GH-KLCR1, GH-CaMs, or for co-purification of HS-IQD2 with GH-CaMs. Two steps of affinity purification, one via Ni-NTA agarose, one via GSH-agarose, were performed as described above, followed by SEC for GH-KLCR1 and GH-CaMs. Purification buffers for co-purification of HS-IQD2 and GH-CaMs consistently contained 1 mM CaCl₂. For the generation of tag-free KLCR1 or Calmodulin, GH-KLCR1 or -CaM2 were purified via Ni-NTA agarose as described above. The elution fractions containing the protein of interest (POI) were then immobilised on GSH-agarose and incubated with 50 U thrombin at 4 °C for two hours. Three POI fractions were collected and immediately subjected to SEC for thrombin removal.

4.5.3 Chromatography

Proteins were subjected to size exclusion chromatography (SEC) using an ÄKTA pure FPLC system. KLCRs and full length IQDs were purified via a HiLoad 16/600 Superdex 200 pg column, CaM2, CaM4 and IQD fragments either via a HiPrep Sephacryl S-100 HR column and CaM7 via a HiLoad 16/60 Superdex 75 pg column. Chromatography buffer was chosen according to experimental needs. For binding assays, proteins were purified in CaM-binding-buffer and for cross-linking and microtubule spin-downs assays in cross-linking buffer (**Tab. 7**). In addition to purification, SEC was used to assess the apparent molecular weight of proteins via their Stokes' radii [335], relative to their expected molecular weight, which indirectly provides information regarding their folding or multimerisation status.

After SEC, elution fractions were assessed via denaturing PAGE (see below), fractions containing the protein of interest were combined and concentrated by centrifugation in Amicon Ultra Centrifugal Filters (**Tab. 6**) as needed. Protein concentrations were determined in denaturing PAGEs via BSA calibration or measured in a UV/vis photo-spectrometer.

4.5.4 Denaturing polyacrylamide gel electrophoresis (PAGE)

Purified protein samples and samples from *in vitro* biochemical assays were analysed via denaturing PAGE [336]. Gels containing 10 %, 12 %, or 15 % polyacrylamide were used. Recipes for 12 ml separating gel solution and 5 ml stacking gel solution sufficed for two gels (**Tab. 22**).

Protein samples were denatured in 4x Laemmli buffer (**Tab. 8**) by boiling at 95 °C for

Table 22: Recipe – SDS-PAGEs

Components	10 %	12 %	15 %	18 %	4.5 %
milliQ H ₂ O	5.0 ml	4.20 ml	3.0 ml	1.80 ml	3.0 ml
30 % acrylamide/bisacrylamide	4.0 ml	4.80 ml	6.0 ml	7.20 ml	0.75 ml
1.5 M Tris-HCl pH 8.8, 0.4 % SDS	3.0 ml	3.0 ml	3.0 ml	3.0 ml	—
0.5 M Tris-HCl pH 6.8, 0.4 % SDS	—	—	—	—	1.25 ml
Optional: Trichloroethanol (TCE)	60 µl	60 µl	60 µl	60 µl	—
10 % APS	60 µl	60 µl	60 µl	60 µl	20 µl
TEMED	13 µl	13 µl	13 µl	13 µl	16 µl

five minutes. PAGEs were run in SDS running buffer (**Tab. 8**). Gels were either stained in Coomassie staining solution (**Tab. 8**) and destained in the same solution sans Coomassie Brilliant Blue (CBB), or subjected to semi-dry western blotting. TCE in-gel fluorescence was used for fluorescent detection of proteins with sufficient tryptophan content in gels under UV light after short incubation with UV light. For higher staining sensitivity, PAGEs were subjected to silver staining by incubation in water for 30 min, followed by 10 min incubation in destaining solution (**Tab. 8**). Gels were subsequently incubated for 5 min in 50 % (v/v) ethanol, 2 min in Sensitiser [0.02 % (w/v) Na₂S₂O₃ · 5H₂O], and 2 min in water. For staining, gels were incubated for 20 min in ice-cold 0.1 % (w/v) AgNO₃, washed twice with water, and developed with Developer solution [2 % (w/v) Na₂CO₃, 0.04 % (v/v) 37 % CH₂O, 4 % (v/v) sensitiser] by incubation for 1 min upwards.

4.5.5 Semi-dry Western blotting

For semi-dry Western blotting, gels from denaturing PAGEs, four slices of Whatman paper, and one piece of nitrocellulose membrane were equilibrated in Towbin buffer (**Tab. 8**). Subsequently a stack of two pieces of Whatman paper, the nitrocellulose membrane, the gel, and two pieces of Whatman paper (bottom to top) was placed in a semi-dry blotter. The blot was run for a minimum of one hour at 20 to 25 V. Subsequently, the blot was disassembled and the membrane stained with PonceauS (**Tab. 8**) to control for successful protein transfer. The membrane was blocked with 2 % (w/v) BSA and 2 % (w/v) milk powder in TBS (**Tab. 8**). Appropriate (primary) antibodies (**Tab. 23**) were added in blocking solution, and the blot was incubated at 4 °C over night.

For protein detection or addition of the secondary antibody, blots were washed three times for 10 min with TBS-T, and once for 5 min with TBS. Afterwards, proteins were either directly detected, or – if necessary – a secondary antibody was added in 2 % (w/v) BSA and 2 % (w/v) milk powder in TBS. Blots were incubated with secondary antibodies for a minimum of one hour and subsequently washed as described before. Horseradish peroxidase (HRP) coupled antibodies were used for chemi-luminescence detection in a fluorescence imager using the Cytiva AmershamTM kits (**Tab. 6**). 1:1 mixtures of the ECL SelectTM and the ECI PrimeTM kit were used to optimise detection quality.

Table 23: Antibodies

Antibody	Detection method	Dilution	Manufacturer	Cat. Number
His-Antibody	HRP	1:10,000	Miltenyi Biotec	130-092-785
Anti-GST-Tag antibody	–	1:5,000	St. John's Laboratory	STJ96909
Anti-mouse IgG	HRP	1:20,000	Sigma Aldrich	A9044

4.5.6 Protein identification via LC/MS/MS

Tag-free KLCR1 and CaM2 were subjected to protein identification via LC/MS/MS by Dr. Susanne Matschi and Carsten Proksch. Proteins were digested with trypsin and desalted as described by Majovsky *et al.* [337]. Dried peptides were dissolved in 5 % (v/v) ACN, 0.1 % (v/v) TFA, and 2 µg were injected into an EASY-nLC 1000 liquid chromatography system

(Thermo Fisher Scientific). Peptides were separated using liquid chromatography C18 reverse phase chemistry employing a 120 min gradient from 5 % to 40 % (v/v) ACN in 0.1 % (v/v) TFA, and a flow rate of 250 nl/min. Eluted peptides were electrosprayed on-line into a QExactive Plus mass spectrometer (Thermo Fisher Scientific). The spray voltage was 1.9 kV, the capillary temperature 275 °C and the Z-Lens voltage 240 V. A full MS survey scan was carried out with chromatographic peak width set to 15 s, resolution 70000, automatic gain control (AGC) 3E+06 and a max injection time (IT) of 100 ms. MS/MS peptide sequencing was performed using a Top10 TDA scan strategy with HCD fragmentation. Mass to charge ratios (m/z) between 400 and 1300 of tryptic peptides of KLCR1 or CaM2 bearing up to 3 charges and tolerating up to 2 missed cleavages with fixed carbamidomethyl modification of cysteine and variable methionine oxidation were placed on the inclusion list. The machine was programmed to pick ions if none of the specified were present. MS/MS scans were acquired with resolution 17500, AGC 5E+04, IT 50 ms, isolation width 1.6 m/z , normalized collision energy 28, under fill ratio 3 %, dynamic exclusion duration 20 s, and an intensity threshold of 3E+04. Peptides were identified using the Mascot software v2.5.0 (Matrix Science) linked to Proteome Discoverer v1.4 or 2.1 (Thermo Fisher Scientific). A precursor ion mass error of 5 ppm and a fragment ion mass error of 0.02 Da were tolerated in searches of the TAIR database amended with common contaminants. Carbamidomethylation of cysteine (C) was set as fixed modification and oxidation of methionine (M) was tolerated as a variable modification. A spectrum (PSM), peptide and protein level false discovery rate (FDR) was calculated for all annotated PSMs, peptide groups and proteins based on the target-decoy database model. PSMs, peptide groups and proteins with scores surpassing the significance threshold of $\alpha = 0.05$ were considered identified.

4.6 Biochemical assays

4.6.1 *In vitro* pulldown assays

Pulldown assays were carried out in CaM-binding-buffer (**Tab. 7**) (unless otherwise specified) to qualitatively assess protein-protein interactions. GST-tagged proteins immobilised on GSH-agarose [338] or His-tagged proteins immobilised on Ni-NTA agarose were used to capture putative binding partners, or commercially available CaM-agarose was used to assess CaM-binding ability [274]. For pulldowns, *E. coli* KRX containing the proteins of interest were lysed in CaM-binding buffer and cell debris was sedimented as described previously. Alternatively, purified protein was used for pulldowns where specified. CaM-pulldowns of tag-free KLCR1 were carried out in cross-linking buffer. Pulldowns were carried out in High salt buffer containing

500 mM NaCl to reduce unspecific electrostatic interactions where specified (**Tab. 7**). NaCl concentration was increased to 1 M to fully disrupt electrostatic interactions with Max. salt buffer (**Tab. 7**).

For CaM-pulldowns, CaM-agarose was equilibrated with assay buffer containing either 1 mM CaCl₂ or 5 mM EGTA. Cleared cell lysate(s) or protein solution(s) containing CaCl₂ or EGTA were added to the agarose and incubated at 4 °C for one hour to over night. The agarose was sedimented via centrifugation for 5 min at 500 g and 4 °C and washed three times with ten bed volumes of the appropriate assay buffer composition. Proteins were "eluted" by boiling the agarose in one bed volume 2x Laemmli buffer for 5 min. Protein samples were assessed via denaturing PAGE and semi-dry Western blotting.

For GST- and His-pulldowns, GSH- or Ni-NTA agarose was equilibrated with CaM-binding buffer (containing 10 mM imidazole in the case of His-pulldowns). Cleared cell lysate(s) or protein solution(s) containing a GST- or His-tagged protein of interest (POI) (and – if applicable – a binding partner of interest) were added to the agarose and incubated at 4 °C for at least two hours to over night. If the binding partner of interest was not already present in the initial setup, the agarose was sedimented as described above, washed three times, and incubated over night with cell lysate(s) or protein solution(s) containing the binding partner(s) of interest if necessary. Washing, "elution", and analysis were carried out as described for CaM-pulldowns. GST alone was used as a negative control during GST-pulldowns or when GST-tagged proteins were pulled down in His-pulldowns.

4.6.2 *In vivo* pulldowns

In vivo pulldowns were carried out by Gina Stamm to qualitatively assess protein-protein interactions under natural conditions. For *in vivo* pulldowns, *N. benthamiana* material was ground to a fine powder in liquid nitrogen followed by re-suspension in *In vivo* pulldown buffer (**Tab. 7**). Cell debris was sedimented by centrifugation at 4 °C and 15,000 g for 10 min. The resulting supernatant was centrifuged again to remove residual cell debris. RFP-traps were equilibrated in *in vivo* pulldown buffer by washing five times with five bed volumes of buffer. The cleared plant cell lysate was incubated with equilibrated RFP-traps at 4 °C for 12 to 16 hours. After incubation, the beads were washed five times with PBS-T (**Tab. 8**). After the last washing step, bound proteins were "eluted" and analysed as described for *in vitro* pulldowns.

4.6.3 Microscale Thermophoresis (MST)

Microscale Thermophoresis was carried out on a Nanotemper Monolith in order to assess protein binding affinities [275]. His-KLCR1 was labelled using the Monolith Protein Labeling Kit RED-NHS or Monolith Protein Labeling Kit RED-NHS 2nd Generation according to manufacturer instructions to achieve optimum labelling efficiency. Concentration of labelled protein and degree of labelling (DOL) were determined using a UV/vis photo-spectrometer (**Tab. 24**). Measurements were performed in CaM-binding-buffer (**Tab. 7**) containing 1 mM CaCl₂ or 5 mM EGTA. Premium Coated Capillaries provided by Nanotemper were used due to target protein adhesion to Standard Capillaries. Experiments were carried out according to the instructions provided by the MO.Control software used for operating the Monolith.

Table 24: MST labelling results

Protein	Concentration [μ M]	DOL
His-KLCR1	2.2 to 6.9	0.77 to 1.33

4.6.4 Chemical cross-linking

Chemical cross-linking was carried out to stabilise protein complexes and to gain insight into regions conferring interaction. Cross-linking was performed according to a protocol established in the group of Prof. Andrea Sinz [277]. Proteins were chemically cross-linked using the cleavable cross-linker DSBU/BuUrBu, a molecule of 12.5 Å length. Due to DSBU's reactivity with primary amines, cross-linking reactions were carried out in a HEPES-based cross-linking buffer (**Tab. 7**). If CaMs were involved in cross-linking reactions, the buffer was supplemented with 1 mM CaCl₂. Concentrations of proteins were adjusted to 5 μ M and subsequently mixed in a 1:1 molar ratio with one another and 30x or 100x molar excess of DSBU in DMSO. The mixtures were incubated at RT for one hour, three hours, or four hours, and subsequently analysed via 10 or 12 % denaturing PAGE.

Tryptic digest and LC/MS/MS analysis of the cross-linking results were carried out by Dr. Christain Ihling according to the following protocol: Solutions were used as specified above (**Tab. 9**). Stained SDS-gels were washed with water for 30 min. Stained bands corresponding to the cross-linking products were excised, cut into cubes of 1 mm size, and sedimented. Gel pieces were incubated with 500 μ l acetonitrile (ACN) for 10 min at RT. After liquid removal, gel pieces were incubated in 50 μ l DTT solution for 30 min at 56 °C, followed by addition of 500 μ l ACN and 10 min incubation at RT. After liquid removal, 50 μ l IAA solution (**Tab.9**)

were added and gel pieces incubated at RT in the dark for 20 min, followed by addition of 500 μ l ACN and 10 min incubation at RT and liquid removal. The remaining gel pieces were incubated in 100 μ l ABC/ACN (1:1) and incubated for 10 to 30 min. After addition of 500 μ l ACN and 10 min incubation at RT all liquid was removed.

For digestion 78 μ l ABC solution were mixed with 40 μ l AspN solution. 20 μ l of the resulting solution were added to the gel pieces and incubated at 4 °C over night. After incubation at 37 °C for 4 hours, the gel pieces were incubated with trypsin as described for the AspN solution at 4 °C for 4 hours. Gel pieces were then incubated with 80 μ l extraction buffer at 37 °C for 15 min. Solid components were sedimented and the supernatant subjected to LC/MS/MS analysis.

4.6.5 LC/MS/MS analysis of cross-linking data

Digested samples were analyzed by LC/MS/MS using an UltiMate 3000 RSLC nano-HPLC system (Thermo Fisher Scientific) coupled to a timsTOF Pro mass spectrometer equipped with CaptiveSpray source (Bruker Daltonics). Peptides were trapped on a C18 column (pre-column Acclaim PepMap 100, 300 μ m \times 5 mm, 5 μ m, 100 Å (Thermo Fisher Scientific) and separated on a μ PAC 50 column (PharmaFluidics). After trapping, peptides were eluted by a 90 min water-ACN gradient from 3 % (v/v) to 35 % (v/v) ACN at a flow rate of 600 nl/min.

For the timsTOF Pro settings, the following parameters were adapted, starting from the PASEF method for standard proteomics: Scan range was set between 0.6 and 1.6 Vs/cm² with a ramp time of 166 ms. 14 PASEF MS/MS scans were triggered per cycle (2.57 s) with a maximum of 7 precursors per mobilogram. Precursor ions in an m/z range between 100 and 1700 with charge states greater or equal to 2+ and greater or equal to 8+ were selected for fragmentation. Values for mobility-dependent collision energy ramping were set to 95 eV at an inverted reduced mobility ($1/k_0$) of 1.6 Vs/cm² and 23 eV at 0.73 Vs/cm². Target intensity per individual PASEF precursor was set to 20,000. Active exclusion was enabled for 0.4 min (mass width 0.015 Th, $1/k_0$ width 0.015 Vs/cm²).

Cross-links were identified using the MeroX software with the following settings: Proteolytic cleavage C-terminal at Lys and Arg, and N-terminal at Asp and Glu; peptide lengths of 4 to 50 amino acids; modifications: alkylation of Cys by IAA, oxidation of Met; cross-linker specificity Lys, Ser, Thr, Tyr, N-terminus; search algorithm in RISEUP mode; precursor mass accuracy of 15 ppm; fragment ion mass accuracy of 20 ppm; signal-to-noise ratio greater 1.5; precursor mass correction enabled; 10 % intensity as pre-score cutoff; 1 % false-discovery rate cutoff; minimum score of 60. The resulting cross-linking files were visualised as bar plots or circle plots

using xVis.

4.6.6 *In silico* modelling of KLCR1-CaM2 complexes

Protein complex models were generated and curated by Dr. Christian Tüting. All analyses were carried out with Python. Models were curated using PyMol [324]. Monomeric models of KLCR1 and CaM2 were generated using a local installation of Alphafold v2.2 with default parameters. Residues with an IDDT below 50 were removed for subsequent analysis. The HADDOCK web server 2.2 (guru interface) was used for docking, generating dimeric structures of KLCR1-CaM2 complexes. Cross-links were defined as unambiguous distance restraints between the C α -atoms of the cross-linked amino acid residues with a permitted distance of 0 to 30 Å. Cluster analysis was performed with a custom Python script. C α distances were determined by extracting the coordinates of each C α atom from the .pdb files generated by Alphafold or HADDOCK. Distances d were calculated as

$$d = \sqrt{(x_1 - x_2)^2 + (y_1 - y_2)^2 + (z_1 - z_2)^2}.$$

A cross-link was considered satisfied with a C α -distance d below 30 Å.

4.6.7 Microtubule spin-down assays

Microtubule spin-down assays were performed with purified GH-KLCR1, GH-CaMs, HS-IQD2, and tag-free KLCR1 according to the protocol provided in the "Microtubule Binding Protein Spin-Down Assay Biochem Kit" by Cytoskeleton Inc. (BK029). For qualitative spin-downs, instructions were followed, using 2 or 5 μ g purified protein, except in the case of HS-IQD2/GH-CaM2. Because no exact protein concentrations of HS-IQD2 could be determined, the protein solution after affinity purification was mixed with tubulin either without prior dilution, or diluted 1:1 in CaM-binding buffer. Ultracentrifugation was carried out at 50,000 g. For concentration curves, microtubule concentration in the microtubule stock solution was doubled by diluting two 20 μ l tubulin aliquots after polymerisation in General Tubulin Buffer (GTB) with taxol, and decreasing the amount of GTB added from 200 to 180 μ l accordingly. BSA and a MAPF fraction were used as negative and positive controls, respectively, according to the kit's instructions.

4.6.8 GAL4 Yeast-two-hybrid (Y2H) experiments

For Y2H experiments *S. cerevisiae* PJ69-4a was inoculated in YPDA medium (**Tab. 10**) and grown at 30 °C over night to an OD₆₀₀ of 0.5 to 1.0. Cells were harvested by centrifugation at 3,500 g for 5 min. Yeast cells from 50 ml liquid cultures were washed twice with sterile H₂O (10 ml and 1 ml) and once with 1x TE/LiOAc [10 mM Tris-HCl pH 7.5, 1 mM EDTA, 100 mM LiOAc] (1 ml) before re-suspension in 0.25 ml 1x TE/LiOAc. 20 µl yeast cell suspension was mixed with a 5 g/l stock ssDNA to a final concentration of 0.83 g/l ssDNA and the entire mixture incubated with a 1:1 mixture of AD- and DBD-fusion constructs for co-expression amounting to 100 ng vector DNA per construct. Subsequently 100 µl PEG solution [10 mM Tris-HCl pH 7.5, 1 mM EDTA, 100 mM LiOAc, 40 % (v/v) PEG4000] were added to the mixture. Cells were incubated at 30 °C for one hour followed by heat-shock at 42 °C for 15 min. Cells were sedimented, 100 µl liquid removed, washed with 180 µl 1x TE [10 mM Tris-HCl pH 7.5, 1 mM EDTA], followed by immediate removal of 130 µl solution and re-suspension in the remaining solution. 10 µl of the remaining solution were plated on vector-selective DDO medium and grown at 30 °C over night or for several days until single colonies showed. Single colonies were picked and grown at 30 °C over night in 1x TE. 10 µl of the cell-suspension were spotted on DDO (SD/-Leu/-Trp) medium, and interaction selective TDO (SD/-Leu/-Trp/-His) medium with medium stringency, or QDO (SD/-Leu/-Trp/-His/-Ade) medium with high stringency, and grown at 30 °C until colonies showed.

4.7 Microscopy

4.7.1 Transient transformation of *N. benthamiana*

For transient expression of fluorescent proteins in *N. benthamiana* leaves, *A. tumefaciens* GV3101 or GV3101pK containing the desired constructs or the silencing inhibitor p19 (kanamycin) were grown at 28 °C in LB medium containing the appropriate antibiotics (**Tab. 12**) and rifampicin for two days prior to infiltration. Cells were sedimented by centrifugation at 9,300 g for 2 min, washed twice with infiltration buffer (**Tab. 7**), and re-suspended in infiltration buffer. Cells containing the constructs for transient (co-)expression were mixed with equal amounts of p19 (e.g. GFP-IQD2 with one equivalent of p19, GFP-IQD2 together with RFP-KLCR1 with two equivalents p19), and the total concentration adjusted to between an OD₆₀₀ of 0.5 and 1.0. For BiFC, OD₆₀₀s of all BiFC constructs were adjusted to exactly 0.5, while CFP-IQD2 was adjusted to an OD₆₀₀ of 1.0 due to lower fluorescence strength. Diluted cells were incubated at 18 °C for one hour and subsequently infiltrated into the abaxial side of *N. benthamiana*

leaves using 2 ml syringes. Fluorescence images were taken after two or three days for transient (co-)expressions and after two days for BiFC experiments.

4.7.2 Confocal laser scanning microscopy (LSM)

Leaf discs were excised from infiltrated leaf areas and mounted in water. Fluorescence images were recorded using an LSM780, LSM880, or LSM900 inverted confocal laser scanning microscope, using a 40x water immersion objective or a 10x objective. GFP fluorescence was excited with a 488 nm laser, and detected with a band-pass filter between 493 and 535 nm. RFP and mCherry fluorescence were excited with a 561 nm laser and detected between 570 and 633 nm. CFP fluorescence was excited with a 405 nm laser and detected between 463 and 493 nm, and YFP fluorescence was excited with a 514 nm laser and detected between 531 and 620 nm. Channels were recorded in the sequential scanning mode at a resolution of 1024 x 1024 pixels. Z-stacks were generated with an aperture adjusted to one airy unit (AU) and the corresponding optimal interval suggested by Zeiss' Zen software. The T-PMT channel served as a pseudo-bright field channel.

Images were analysed and processed using Fiji/ImageJ. Brightness and contrast were adjusted via their lookup tables. Where necessary, channels were split using the "image/color/split channels" option and merged via the "image/color/merge channels" function. Z-stacks were generated as maximum intensity projections using the "image/stacks/Z project/" option. Scale bars were added via the "analyze/tools/scale bar" option. Fluorescence profiles were generated along a line inserted into the image, fluorescence intensities read out via the "analyze/plot profile" option, and analysed via MS Excel. For BiFC, all images were recorded and processed identically.

5 References

- [1] T. Gabaldón, “Origin and early evolution of the eukaryotic cell,” *Annual review of microbiology*, vol. 75, pp. 631–647, 2021.
- [2] R. Milo, “What is the total number of protein molecules per cell volume? A call to rethink some published values,” *BioEssays*, vol. 35, no. 12, 2013.
- [3] T. Itoh, T. Tanaka, R. A. Barrero, C. Yamasaki, Y. Fujii, P. B. Hilton, B. A. Antonio, H. Aono, R. Apweiler, R. Bruskiwich, T. Bureau, F. Burr, A. C. De Oliveira, G. Fuks, T. Habara, G. Haberer, B. Han, E. Harada, A. T. Hiraki, H. Hirochika, D. Hoen, H. Hokari, S. Hosokawa, Y. I. Hsing, H. Ikawa, K. Ikeo, T. Imanishi, Y. Ito, P. Jaiswal, M. Kanno, Y. Kawahara, T. Kawamura, H. Kawashima, J. P. Khurana, S. Kikuchi, S. Komatsu, K. O. Koyanagi, H. Kubooka, D. Lieberherr, Y. C. Lin, D. Lonsdale, T. Matsumoto, A. Matsuya, W. R. McCombie, J. Messing, A. Miyao, N. Mulder, Y. Nagamura, J. Nam, N. Namiki, H. Numa, S. Nurimoto, C. O’Donovan, H. Ohyanagi, T. Okido, S. Oota, N. Osato, L. E. Palmer, F. Quetier, S. Raghuvanshi, N. Saichi, H. Sakai, Y. Sakai, K. Sakata, T. Sakurai, F. Sato, Y. Sato, H. Schoof, M. Seki, M. Shibata, Y. Shimizu, K. Shinozaki, Y. Shinso, N. K. Singh, B. Smith-White, J. I. Takeda, M. Tanino, T. Tatusova, S. Thongjuea, F. Todokoro, M. Tsugane, A. K. Tyagi, A. Vanavichit, A. Wang, R. A. Wing, K. Yamaguchi, M. Yamamoto, N. Yamamoto, Y. Yu, H. Zhang, Q. Zhao, K. Higo, B. Burr, T. Gojobori, and T. Sasaki, “Curated genome annotation of *Oryza sativa* ssp. *japonica* and comparative genome analysis with *Arabidopsis thaliana*: The Rice Annotation Project,” *Genome Res.*, vol. 17, no. 2, 2007.
- [4] B. Alberts, A. Johnson, J. Lewis, M. Raff, K. Roberts, and P. Walter, “Signaling in plants,” in *Molecular Biology of the Cell. 4th edition*, Garland Science, 2002.
- [5] D. A. Fletcher and R. D. Mullins, “Cell mechanics and the cytoskeleton,” *Nature*, vol. 463, no. 7280, pp. 485–492, 2010.
- [6] L. Buday and P. Tompa, “Functional classification of scaffold proteins and related molecules,” *The FEBS journal*, vol. 277, no. 21, pp. 4348–4355, 2010.
- [7] K. Y. Chol, B. Satterberg, D. M. Lyons, and E. A. Elion, “Ste5 tethers multiple protein kinases in the MAP kinase cascade required for mating in *S. cerevisiae*,” *Cell*, vol. 78, no. 3, 1994.
- [8] Y. Mugabo and G. E. Lim, “Scaffold proteins: from coordinating signaling pathways to metabolic regulation,” *Endocrinology*, vol. 159, no. 11, pp. 3615–3630, 2018.
- [9] A. S. Shaw and E. L. Filbert, “Scaffold proteins and immune-cell signalling,” *Nature Reviews Immunology*, vol. 9, no. 1, pp. 47–56, 2009.

- [10] A. Levchenko, J. Bruck, and P. W. Sternberg, "Scaffold proteins may biphasically affect the levels of mitogen-activated protein kinase signaling and reduce its threshold properties," *Proc. Natl. Acad. Sci. U. S. A.*, vol. 97, no. 11, 2000.
- [11] J. E. Ferrell Jr, "What do scaffold proteins really do?," *Science's STKE*, vol. 2000, no. 52, pp. pe1–pe1, 2000.
- [12] A. Saha and R. J. Deshaies, "Multimodal Activation of the Ubiquitin Ligase SCF by Nedd8 Conjugation," *Mol. Cell*, vol. 32, no. 1, 2008.
- [13] W. Wong and J. D. Scott, "Akap signalling complexes: focal points in space and time," *Nature reviews Molecular cell biology*, vol. 5, no. 12, pp. 959–970, 2004.
- [14] E. C. Greenwald, J. M. Redden, K. L. Dodge-Kafka, and J. J. Saucerman, "Scaffold state switching amplifies, accelerates, and insulates protein kinase c signaling," *J. Biol. Chem.*, vol. 289, no. 4, 2014.
- [15] J. W. Locasale, A. S. Shaw, and A. K. Chakraborty, "Scaffold proteins confer diverse regulatory properties to protein kinase cascades," *Proc. Natl. Acad. Sci. U. S. A.*, vol. 104, no. 33, 2007.
- [16] W. Engström, A. Ward, and K. Moorwood, "The role of scaffold proteins in jnk signalling," *Cell proliferation*, vol. 43, no. 1, pp. 56–66, 2010.
- [17] M. C. Good, J. G. Zalatan, and W. A. Lim, "Scaffold proteins: hubs for controlling the flow of cellular information," *Science*, vol. 332, no. 6030, pp. 680–686, 2011.
- [18] H. Jeong, S. P. Mason, A.-L. Barabási, and Z. N. Oltvai, "Lethality and centrality in protein networks," *Nature*, vol. 411, no. 6833, pp. 41–42, 2001.
- [19] J.-D. J. Han, N. Bertin, T. Hao, D. S. Goldberg, G. F. Berriz, L. V. Zhang, D. Dupuy, A. J. Walhout, M. E. Cusick, F. P. Roth, *et al.*, "Evidence for dynamically organized modularity in the yeast protein–protein interaction network," *Nature*, vol. 430, no. 6995, pp. 88–93, 2004.
- [20] A. Zeke, M. Lukács, W. A. Lim, and A. Reményi, "Scaffolds: interaction platforms for cellular signalling circuits," *Trends in cell biology*, vol. 19, no. 8, pp. 364–374, 2009.
- [21] T. Pawson and J. D. Scott, "Signaling through scaffold, anchoring, and adaptor proteins," *Science (80-.)*, vol. 278, no. 5346, 1997.
- [22] R. P. Bhattacharyya, A. Reményi, B. J. Yeh, and W. A. Lim, "Domains, motifs, and scaffolds: the role of modular interactions in the evolution and wiring of cell signaling circuits," *Annu. Rev. Biochem.*, vol. 75, pp. 655–680, 2006.

- [23] M. G. Wuo and P. S. Arora, "Engineered protein scaffolds as leads for synthetic inhibitors of protein-protein interactions," *Current opinion in chemical biology*, vol. 44, pp. 16–22, 2018.
- [24] Z. Su, K. Dhusia, and Y. Wu, "Understand the Functions of Scaffold Proteins in Cell Signaling by a Mesoscopic Simulation Method," *Biophys. J.*, vol. 119, no. 10, 2020.
- [25] J. Guo, B. Jiansheng Liang, and B. Jin-Gui Chen, "RACK1, a Versatile Scaffold Protein in Plants?," *Int. J. Plant Dev. Biol.*, vol. 1, no. 1, 2007.
- [26] S. Abel, K. Bürstenbinder, and J. Müller, "The emerging function of IQD proteins as scaffolds in cellular signaling and trafficking," *Plant Signal. Behav.*, vol. 8, no. 6, 2013.
- [27] J. Zang, S. Klemm, C. Pain, P. Duckney, Z. Bao, G. Stamm, V. Kriechbaumer, K. Bürstenbinder, P. J. Hussey, and P. Wang, "A novel plant actin-microtubule bridging complex regulates cytoskeletal and ER structure at ER-PM contact sites," *Curr. Biol.*, vol. 31, no. 6, 2021.
- [28] H. Ullah, E. L. Scappini, A. F. Moon, L. V. Williams, D. L. Armstrong, and L. C. Pedersen, "Structure of a signal transduction regulator, RACK1, from *Arabidopsis thaliana*," *Protein Sci.*, vol. 17, no. 10, 2008.
- [29] K. Hyodo, N. Suzuki, and T. Okuno, "Hijacking a host scaffold protein, RACK1, for replication of a plant RNA virus," *New Phytol.*, vol. 221, no. 2, 2019.
- [30] X. Guo and J. Dong, "To divide or differentiate: it is about scaffolding," *Trends in plant science*, vol. 24, no. 6, pp. 481–484, 2019.
- [31] C. Bolle, "The role of gras proteins in plant signal transduction and development," *Planta*, vol. 218, no. 5, pp. 683–692, 2004.
- [32] S. Abel, T. Savchenko, and M. Levy, "Genome-wide comparative analysis of the IQD gene families in *Arabidopsis thaliana* and *Oryza sativa*," *BMC Evol. Biol.*, vol. 5, 2005.
- [33] M. Levy, Q. Wang, R. Kaspi, M. P. Parrella, and S. Abel, "Arabidopsis *iqd1*, a novel calmodulin-binding nuclear protein, stimulates glucosinolate accumulation and plant defense," *The Plant Journal*, vol. 43, no. 1, pp. 79–96, 2005.
- [34] K. Bürstenbinder, B. Möller, R. Plötner, G. Stamm, G. Hause, D. Mitra, and S. Abel, "The IQD Family of Calmodulin-Binding Proteins Links Calcium Signaling to Microtubules, Membrane Subdomains, and the Nucleus," *Plant Physiol.*, vol. 173, no. 3, pp. 1692–1708, 2017.
- [35] K. Bürstenbinder, D. Mitra, and J. Quegwer, "Functions of *iqd* proteins as hubs in cellular calcium and auxin signaling: a toolbox for shape formation and tissue-specification in plants?," *Plant signaling & behavior*, vol. 12, no. 6, pp. 1692–1708, 2017.

- [36] F. P. Pflug, "Biochemical analysis of arabidopsis thaliana iq67-domain protein 1 and related proteins," 2019.
- [37] A. Alexa, J. Varga, and A. Remenyi, "Scaffolds are 'active' regulators of signaling modules," *The FEBS journal*, vol. 277, no. 21, pp. 4376–4382, 2010.
- [38] J. S. Logue and J. D. Scott, "Organizing signal transduction through a-kinase anchoring proteins (akaps)," *The FEBS journal*, vol. 277, no. 21, pp. 4370–4375, 2010.
- [39] T. Brummer, C. Schmitz-Peiffer, and R. J. Daly, "Docking proteins," *The FEBS journal*, vol. 277, no. 21, pp. 4356–4369, 2010.
- [40] L. Buday, L. Wunderlich, and P. Tamás, "The nck family of adapter proteins: regulators of actin cytoskeleton," *Cellular signalling*, vol. 14, no. 9, pp. 723–731, 2002.
- [41] T. Pawson, "Dynamic control of signaling by modular adaptor proteins," *Current opinion in cell biology*, vol. 19, no. 2, pp. 112–116, 2007.
- [42] T. Z. Grove, A. L. Cortajarena, and L. Regan, "Ligand binding by repeat proteins: natural and designed," *Current opinion in structural biology*, vol. 18, no. 4, pp. 507–515, 2008.
- [43] L. K. Mosavi, T. J. Cammett, D. C. Desrosiers, and Z.-y. Peng, "The ankyrin repeat as molecular architecture for protein recognition," *Protein science*, vol. 13, no. 6, pp. 1435–1448, 2004.
- [44] M. Peifer, S. Berg, and A. B. Reynolds, "A repeating amino acid motif shared by proteins with diverse cellular roles," *Cell*, vol. 76, no. 5, pp. 789–791, 1994.
- [45] M. R. Groves, N. Hanlon, P. Turowski, B. A. Hemmings, and D. Barford, "The structure of the protein phosphatase 2a pr65/a subunit reveals the conformation of its 15 tandemly repeated heat motifs," *Cell*, vol. 96, no. 1, pp. 99–110, 1999.
- [46] P. Enkhbayar, M. Kamiya, M. Osaki, T. Matsumoto, and N. Matsushima, "Structural principles of leucine-rich repeat (lrr) proteins," *Proteins: Structure, Function, and Bioinformatics*, vol. 54, no. 3, pp. 394–403, 2004.
- [47] A. K. Das, P. T. Cohen, and D. Barford, "The structure of the tetratricopeptide repeats of protein phosphatase 5: implications for tpr-mediated protein–protein interactions," *The EMBO journal*, vol. 17, no. 5, pp. 1192–1199, 1998.
- [48] T. F. Smith, C. Gaitatzes, K. Saxena, and E. J. Neer, "The wd repeat: a common architecture for diverse functions," *Trends in biochemical sciences*, vol. 24, no. 5, pp. 181–185, 1999.
- [49] T. J. Magliery and L. Regan, "Sequence variation in ligand binding sites in proteins," *BMC bioinformatics*, vol. 6, no. 1, pp. 1–11, 2005.

- [50] E. R. Main, Y. Xiong, M. J. Cocco, L. D'Andrea, and L. Regan, "Design of stable α -helical arrays from an idealized tpr motif," *Structure*, vol. 11, no. 5, pp. 497–508, 2003.
- [51] A. L. Cortajarena, T. Kajander, W. Pan, M. J. Cocco, and L. Regan, "Protein design to understand peptide ligand recognition by tetratricopeptide repeat proteins," *Protein Engineering Design and Selection*, vol. 17, no. 4, pp. 399–409, 2004.
- [52] A. L. Cortajarena and L. Regan, "Ligand binding by tpr domains," *Protein Science*, vol. 15, no. 5, pp. 1193–1198, 2006.
- [53] U. S. Cho and W. Xu, "Crystal structure of a protein phosphatase 2a heterotrimeric holoenzyme," *Nature*, vol. 445, no. 7123, pp. 53–57, 2007.
- [54] C. U. Stirnimann, E. Petsalaki, R. B. Russell, and C. W. Müller, "Wd40 proteins propel cellular networks," *Trends in biochemical sciences*, vol. 35, no. 10, pp. 565–574, 2010.
- [55] B. D. Johnson, R. J. Schumacher, E. D. Ross, and D. O. Toft, "Hop modulates hsp70/hsp90 interactions in protein folding," *Journal of Biological Chemistry*, vol. 273, no. 6, pp. 3679–3686, 1998.
- [56] W. B. Pratt, P. Krishna, and L. J. Olsen, "Hsp90-binding immunophilins in plants: the protein movers," *Trends in plant science*, vol. 6, no. 2, pp. 54–58, 2001.
- [57] A. L. Schapire, V. Valpuesta, and M. A. Botella, "TPR proteins in plant hormone signaling," *Plant Signal. Behav.*, vol. 1, no. 5, 2006.
- [58] M. Sharma and G. K. Pandey, "Expansion and function of repeat domain proteins during stress and development in plants," *Frontiers in plant science*, vol. 6, p. 1218, 2016.
- [59] G. L. Blatch and M. Lässle, "The tetratricopeptide repeat: a structural motif mediating protein-protein interactions," *Bioessays*, vol. 21, no. 11, pp. 932–939, 1999.
- [60] A. L. Morris, M. W. MacArthur, E. G. Hutchinson, and J. M. Thornton, "Stereochemical quality of protein structure coordinates," *Proteins: Structure, Function, and Bioinformatics*, vol. 12, no. 4, pp. 345–364, 1992.
- [61] A. L. Bakkum and R. B. Hill, "Removal of a consensus proline is not sufficient to allow tetratricopeptide repeat oligomerization," *Protein Sci.*, vol. 26, no. 10, 2017.
- [62] N. Zeytuni and R. Zarivach, "Structural and functional discussion of the tetra-trico-peptide repeat, a protein interaction module," *Structure*, vol. 20, no. 3, pp. 397–405, 2012.

- [63] A. Perez-Riba and L. S. Itzhaki, "The tetratricopeptide-repeat motif is a versatile platform that enables diverse modes of molecular recognition," *Current opinion in structural biology*, vol. 54, pp. 43–49, 2019.
- [64] H. Zhu, H. Y. Lee, Y. Tong, B. S. Hong, K. P. Kim, Y. Shen, K. J. Lim, F. Mackenzie, W. Tempel, and H. W. Park, "Crystal structures of the tetratricopeptide repeat domains of Kinesin light chains: Insight into cargo recognition mechanisms," *PLoS One*, vol. 7, no. 3, 2012.
- [65] Q. Nguyen, M. Chenon, F. Vilela, C. Velours, M. Aumont-Nicaise, J. Andreani, P. F. Varela, P. Llinas, and J. Ménétrey, "Structural plasticity of the N-terminal capping helix of the TPR domain of kinesin light chain," *PLoS One*, vol. 12, no. 10, 2017.
- [66] N. C. Strynadka and M. N. James, "Crystal structures of the helix-loop-helix calcium-binding proteins," *Annual review of biochemistry*, vol. 58, no. 1, pp. 951–999, 1989.
- [67] A. Nyarko, K. Mosbahi, A. J. Rowe, A. Leech, M. Boter, K. Shirasu, and C. Kleanthous, "TPR-mediated self-association of plant SGT1," *Biochemistry*, vol. 46, no. 40, 2007.
- [68] M. Lunelli, R. K. Lokareddy, A. Zychlinsky, and M. Kolbe, "Ipab–ipgc interaction defines binding motif for type iii secretion translocator," *Proceedings of the National Academy of Sciences*, vol. 106, no. 24, pp. 9661–9666, 2009.
- [69] A. M. Krachler, A. Sharma, and C. Kleanthous, "Self-association of TPR domains: Lessons learned from a designed, consensus-based TPR oligomer," *Proteins Struct. Funct. Bioinforma.*, vol. 78, no. 9, 2010.
- [70] Z. Zhang, K. Kulkarni, S. J. Hanrahan, A. J. Thompson, and D. Barford, "The apc/c subunit cdc16/cut9 is a contiguous tetratricopeptide repeat superhelix with a homo-dimer interface similar to cdc27," *The EMBO journal*, vol. 29, no. 21, pp. 3733–3744, 2010.
- [71] N. Zeytuni, E. Ozyamak, K. Ben-Harush, G. Davidov, M. Levin, Y. Gat, T. Moyal, A. Brik, A. Komeili, and R. Zarivach, "Self-recognition mechanism of mama, a magnetosome-associated tpr-containing protein, promotes complex assembly," *Proceedings of the National Academy of Sciences*, vol. 108, no. 33, pp. E480–E487, 2011.
- [72] I. D. Small and N. Peeters, "The ppr motif—a tpr-related motif prevalent in plant organellar proteins," *Trends in biochemical sciences*, vol. 25, no. 2, pp. 45–47, 2000.
- [73] X. Wang, Y. An, P. Xu, and J. Xiao, "Functioning of ppr proteins in organelle rna metabolism and chloroplast biogenesis," *Frontiers in plant science*, vol. 12, p. 1, 2021.

- [74] M. S. Cortese, V. N. Uversky, and A. K. Dunker, "Intrinsic disorder in scaffold proteins: getting more from less," *Progress in biophysics and molecular biology*, vol. 98, no. 1, pp. 85–106, 2008.
- [75] M. Fuxreiter, P. Tompa, and I. Simon, "Local structural disorder imparts plasticity on linear motifs," *Bioinformatics*, vol. 23, no. 8, pp. 950–956, 2007.
- [76] J. Liu, H. Tan, and B. Rost, "Loopy proteins appear conserved in evolution," *Journal of molecular biology*, vol. 322, no. 1, pp. 53–64, 2002.
- [77] I. Yruela and B. Contreras-Moreira, "Protein disorder in plants: a view from the chloroplast," *BMC plant biology*, vol. 12, no. 1, pp. 1–13, 2012.
- [78] H. Hegyi, E. Schad, and P. Tompa, "Structural disorder promotes assembly of protein complexes," *BMC structural biology*, vol. 7, no. 1, pp. 1–9, 2007.
- [79] Z. Dosztanyi, J. Chen, A. K. Dunker, I. Simon, and P. Tompa, "Disorder and sequence repeats in hub proteins and their implications for network evolution," *Journal of proteome research*, vol. 5, no. 11, pp. 2985–2995, 2006.
- [80] A. K. Dunker, C. J. Brown, J. D. Lawson, L. M. Iakoucheva, and Z. Obradović, "Intrinsic disorder and protein function," *Biochemistry*, vol. 41, no. 21, pp. 6573–6582, 2002.
- [81] Z. Ma, Y. Sun, X. Zhu, L. Yang, X. Chen, and Y. Miao, "Membrane nanodomains modulate formin condensation for actin remodeling in Arabidopsis innate immune responses," *Plant Cell*, vol. 34, no. 1, 2022.
- [82] V. N. Uversky, C. J. Oldfield, and A. K. Dunker, "Showing your id: intrinsic disorder as an id for recognition, regulation and cell signaling," *Journal of Molecular Recognition: An Interdisciplinary Journal*, vol. 18, no. 5, pp. 343–384, 2005.
- [83] B. W. Pontius, "Close encounters: why unstructured, polymeric domains can increase rates of specific macromolecular association," *Trends in biochemical sciences*, vol. 18, no. 5, pp. 181–186, 1993.
- [84] M. Fuxreiter, I. Simon, P. Friedrich, and P. Tompa, "Preformed structural elements feature in partner recognition by intrinsically unstructured proteins," *Journal of molecular biology*, vol. 338, no. 5, pp. 1015–1026, 2004.
- [85] Y. Ivarsson and P. Jemth, "Affinity and specificity of motif-based protein–protein interactions," *Current opinion in structural biology*, vol. 54, pp. 26–33, 2019.

- [86] J. G. Olsen, K. Teilum, and B. B. Kragelund, "Behaviour of intrinsically disordered proteins in protein–protein complexes with an emphasis on fuzziness," *Cellular and Molecular Life Sciences*, vol. 74, no. 17, pp. 3175–3183, 2017.
- [87] W. Luo, H. Zou, L. Jin, S. Lin, Q. Li, Z. Ye, H. Rui, and S.-C. Lin, "Axin contains three separable domains that confer intramolecular, homodimeric, and heterodimeric interactions involved in distinct functions," *Journal of Biological Chemistry*, vol. 280, no. 6, pp. 5054–5060, 2005.
- [88] M. E. Fealey, B. P. Binder, V. N. Uversky, A. Hinderliter, and D. D. Thomas, "Structural impact of phosphorylation and dielectric constant variation on synaptotagmin's idr," *Biophysical journal*, vol. 114, no. 3, pp. 550–561, 2018.
- [89] A.-C. Gingras, S. P. Gygi, B. Raught, R. D. Polakiewicz, R. T. Abraham, M. F. Hoekstra, R. Aebersold, and N. Sonenberg, "Regulation of 4e-bp1 phosphorylation: a novel two-step mechanism," *Genes & development*, vol. 13, no. 11, pp. 1422–1437, 1999.
- [90] R. W. Lim and S. Halpain, "Regulated association of microtubule-associated protein 2 (map2) with src and grb2: evidence for map2 as a scaffolding protein," *Journal of Biological Chemistry*, vol. 275, no. 27, pp. 20578–20587, 2000.
- [91] V. Pejaver, W. L. Hsu, F. Xin, A. K. Dunker, V. N. Uversky, and P. Radivojac, "The structural and functional signatures of proteins that undergo multiple events of post-translational modification," *Protein Sci.*, vol. 23, no. 8, pp. 1077–1093, 2014.
- [92] A. L. Darling and V. N. Uversky, "Intrinsic disorder and posttranslational modifications: the darker side of the biological dark matter," *Frontiers in genetics*, vol. 9, p. 158, 2018.
- [93] H. L. Rust and P. R. Thompson, "Kinase consensus sequences: a breeding ground for crosstalk," *ACS chemical biology*, vol. 6, no. 9, pp. 881–892, 2011.
- [94] V. N. Uversky, "A decade and a half of protein intrinsic disorder: biology still waits for physics," *Protein Science*, vol. 22, no. 6, pp. 693–724, 2013.
- [95] F. Meng, V. Uversky, and L. Kurgan, "Computational prediction of intrinsic disorder in proteins," *Curr. Protoc. Protein Sci.*, vol. 2017, 2017.
- [96] F. Pazos, N. Pietrosevoli, J. A. García-Martín, and R. Solano, "Protein intrinsic disorder in plants," *Frontiers in plant science*, vol. 4, p. 363, 2013.
- [97] M. Marin and T. Ott, "Intrinsic disorder in plant proteins and phytopathogenic bacterial effectors," *Chemical reviews*, vol. 114, no. 13, pp. 6912–6932, 2014.

- [98] A. A. Covarrubias, C. L. Cuevas-Velazquez, P. S. Romero-Pérez, D. F. Rendón-Luna, and C. C. Chater, "Structural disorder in plant proteins: where plasticity meets sessility," *Cellular and Molecular Life Sciences*, vol. 74, no. 17, pp. 3119–3147, 2017.
- [99] B. B. Kragelund, M. K. Jensen, and K. Skriver, "Order by disorder in plant signaling," *Trends in plant science*, vol. 17, no. 11, pp. 625–632, 2012.
- [100] A. A. Covarrubias, P. S. Romero-Perez, C. L. Cuevas-Velazquez, and D. F. Rendon-Luna, "The functional diversity of structural disorder in plant proteins," *Archives of biochemistry and biophysics*, vol. 680, p. 108229, 2020.
- [101] X. Sun, W. T. Jones, and E. H. Rikkerink, "Gras proteins: the versatile roles of intrinsically disordered proteins in plant signalling," *Biochemical Journal*, vol. 442, no. 1, pp. 1–12, 2012.
- [102] M. Niemeyer, E. Moreno Castillo, C. H. Ihling, C. Iacobucci, V. Wilde, A. Hellmuth, W. Hohenwarter, S. L. Samodelov, M. D. Zurbriggen, P. L. Kastritis, *et al.*, "Flexibility of intrinsically disordered degrons in aux/iaa proteins reinforces auxin co-receptor assemblies," *Nature communications*, vol. 11, no. 1, pp. 1–18, 2020.
- [103] F. Van den Ent and J. Lowe, "Crystal structure of the cell division protein FtsA from *Thermotoga maritima*," *EMBO J.*, vol. 19, no. 20, 2000.
- [104] P. Wintrebert, "La rotation immédiate de l'oeuf pondu et la rotation d'activation chez *discoglossus pictus* otth," *CR Soc. Biol.*, vol. 106, pp. 439–442, 1931.
- [105] B. Kost and N.-H. Chua, "The plant cytoskeleton: vacuoles and cell walls make the difference," *Cell*, vol. 108, no. 1, pp. 9–12, 2002.
- [106] R. E. Goldstein and J. W. van de Meent, "A physical perspective on cytoplasmic streaming," *Interface Focus*, vol. 5, no. 4, 2015.
- [107] W. F. Marshall and J. L. Rosenbaum, "Cell division: The renaissance of the centriole," *Current biology*, vol. 9, no. 6, pp. R218–R220, 1999.
- [108] A. Smertenko, F. Assaad, F. Baluška, M. Bezanilla, H. Buschmann, G. Drakakaki, M.-T. Hauser, M. Janson, Y. Mineyuki, I. Moore, *et al.*, "Plant cytokinesis: terminology for structures and processes," *Trends in cell biology*, vol. 27, no. 12, pp. 885–894, 2017.
- [109] F. Huber, J. Schnauß, S. Rönicke, P. Rauch, K. Müller, C. Fütterer, and J. Käs, "Emergent complexity of the cytoskeleton: from single filaments to tissue," *Advances in physics*, vol. 62, no. 1, pp. 1–112, 2013.

- [110] M. J. Deeks, M. Fendrych, A. Smertenko, K. S. Bell, K. Oparka, F. Cvrčková, V. Žárský, and P. J. Hussey, "The plant formin atfh4 interacts with both actin and microtubules, and contains a newly identified microtubule-binding domain," *Journal of cell science*, vol. 123, no. 8, pp. 1209–1215, 2010.
- [111] F. He, H. Chen, and R. Han, "The Plant Cytoskeleton and Crosslinking Factors," *CellBio*, vol. 09, no. 02, 2020.
- [112] D. B. Szymanski and D. J. Cosgrove, "Dynamic coordination of cytoskeletal and cell wall systems during plant cell morphogenesis," *Current Biology*, vol. 19, no. 17, pp. R800–R811, 2009.
- [113] A. Sampathkumar, P. Krupinski, R. Wightman, P. Milani, A. Berquand, A. Boudaoud, O. Hamant, H. Jönsson, and E. M. Meyerowitz, "Subcellular and supracellular mechanical stress prescribes cytoskeleton behavior in Arabidopsis cotyledon pavement cells," *Elife*, vol. 3, 2014.
- [114] D. Mitra, S. Klemm, P. Kumari, J. Quegwer, B. Möller, Y. Poeschl, P. Pflug, G. Stamm, S. Abel, and K. Bürstenbinder, "Microtubule-associated protein iq67 domain5 regulates morphogenesis of leaf pavement cells in arabidopsis thaliana," *Journal of experimental botany*, vol. 70, no. 2, pp. 529–543, 2019.
- [115] B. A. Palevitz, "Actin in the preprophase band of allium cepa.," *The Journal of cell biology*, vol. 104, no. 6, pp. 1515–1519, 1987.
- [116] Y. Mineyuki and B. A. Palevitz, "Relationship between preprophase band organization, F-actin and the division site in Allium. Fluorescence and morphometric studies on cytochalasin-treated cells," *J. Cell Sci.*, vol. 97, no. 2, 1990.
- [117] B. E. Gunning and S. M. Wick, "Preprophase bands, phragmoplasts, and spatial control of cytokinesis.," *J. Cell Sci. Suppl.*, vol. 2, 1985.
- [118] B. Kost, J. Mathur, and N.-H. Chua, "Cytoskeleton in plant development," *Current opinion in plant biology*, vol. 2, no. 6, pp. 462–470, 1999.
- [119] L. Bashline, L. Lei, S. Li, and Y. Gu, "Cell wall, cytoskeleton, and cell expansion in higher plants," *Molecular Plant*, vol. 7, no. 4, pp. 586–600, 2014.
- [120] Z. Liu, R. Schneider, C. Kesten, Y. Zhang, M. Somssich, Y. Zhang, A. R. Fernie, and S. Persson, "Cellulose-Microtubule Uncoupling Proteins Prevent Lateral Displacement of Microtubules during Cellulose Synthesis in Arabidopsis," *Dev. Cell*, vol. 38, no. 3, pp. 305–315, 2016.
- [121] A. Geitmann and A. Nebenführ, "Navigating the plant cell: intracellular transport logistics in the green kingdom," *Molecular Biology of the Cell*, vol. 26, no. 19, pp. 3373–3378, 2015.

- [122] N. Lian, X. Wang, Y. Jing, and J. Lin, "Regulation of cytoskeleton-associated protein activities: Linking cellular signals to plant cytoskeletal function," *Journal of Integrative Plant Biology*, vol. 63, no. 1, pp. 241–250, 2021.
- [123] K. Bürstenbinder, T. Savchenko, J. Müller, A. W. Adamson, G. Stamm, R. Kwong, B. J. Zipp, D. C. Dinesh, and S. Abel, "Arabidopsis calmodulin-binding protein iq67-domain 1 localizes to microtubules and interacts with kinesin light chain-related protein-1," *J. Biol. Chem.*, vol. 288, no. 3, pp. 1871–1882, 2013.
- [124] W. D. Halliburton, "On Muscle-Plasma," *J. Physiol.*, vol. 8, no. 3-4, 1887.
- [125] B. Geissler, D. Shiomi, and W. Margolin, "The *ftsA** gain-of-function allele of *Escherichia coli* and its effects on the stability and dynamics of the Z ring," *Microbiology*, vol. 153, no. 3, 2007.
- [126] A. Paez-Garcia, J. A. Sparks, L. de Bang, and E. B. Blancaflor, "Plant actin cytoskeleton: New functions from old scaffold," in *Plant Cell Monogr.*, vol. 23, Springer, 2018.
- [127] W. Kabsch, H. G. Mannherz, D. Suck, E. F. Pai, and K. C. Holmes, "Atomic structure of the actin: DNase I complex," *Nature*, vol. 347, no. 6288, 1990.
- [128] F. B. Straub and G. Feuer, "Adenosinetriphosphate the functional group of actin," *BBA - Biochim. Biophys. Acta*, vol. 4, no. C, 1950.
- [129] T. Oda, M. Iwasa, T. Aihara, Y. Maéda, and A. Narita, "Erratum: The nature of the globular-to fibrous-actin transition (*Nature* (2009) 457 (441-445)),", 2009.
- [130] K. C. Holmes, D. Popp, W. Gebhard, and W. Kabsch, "Atomic model of the actin filament," *Nature*, vol. 347, no. 6288, 1990.
- [131] T. D. Pollard and E. D. Korn, "Acanthamoeba myosin. I. Isolation from *Acanthamoeba castellanii* of an enzyme similar to muscle myosin," *J. Biol. Chem.*, vol. 248, no. 13, 1973.
- [132] Q. Lu, J. Li, F. Ye, and M. Zhang, "Structure of myosin-1c tail bound to calmodulin provides insights into calcium-mediated conformational coupling," *Nat. Struct. Mol. Biol.*, vol. 22, no. 1, pp. 81–87, 2015.
- [133] T. Hodge, M. Jamie, and T. Cope, "A myosin family tree," *Journal of cell science*, vol. 113, no. 19, pp. 3353–3354, 2000.
- [134] A. S. Reddy and I. S. Day, "Analysis of the myosins encoded in the recently completed *Arabidopsis thaliana* genome sequence.," *Genome Biol.*, vol. 2, no. 7, 2001.

- [135] S. Reichelt, A. E. Knight, T. P. Hodge, F. Baluska, J. Samaj, D. Volkmann, and J. Kendrick-Jones, "Characterization of the unconventional myosin VIII in plant cells and its localization at the post-cytokinetic cell wall," *Plant J.*, vol. 19, no. 5, 1999.
- [136] H. Sun, F. Furt, and L. Vidali, "Myosin XI localizes at the mitotic spindle and along the cell plate during plant cell division in *Physcomitrella patens*," *Biochem. Biophys. Res. Commun.*, vol. 506, no. 2, 2018.
- [137] A. Sattarzadeh, J. Krahmer, A. D. Germain, and M. R. Hanson, "A myosin XI tail domain homologous to the yeast myosin vacuole-binding domain interacts with plastids and stromules in *Nicotiana benthamiana*," *Mol. Plant*, vol. 2, no. 6, 2009.
- [138] M. Abu-Abied, E. Belausov, S. Hagay, V. Peremyslov, V. Dolja, and E. Sadot, "Myosin XI-K is involved in root organogenesis, polar auxin transport, and cell division," *J. Exp. Bot.*, vol. 69, no. 12, pp. 2869–2881, 2018.
- [139] R. B. Meagher, E. C. McKinney, and M. Kandasamy, "Isovariant dynamics expand and buffer the responses of complex systems: the diverse plant actin gene family," *The Plant Cell*, vol. 11, no. 6, pp. 995–1005, 1999.
- [140] Y. Fu, "The actin cytoskeleton and signaling network during pollen tube tip growth," *Journal of integrative plant biology*, vol. 52, no. 2, pp. 131–137, 2010.
- [141] F. G. Woodhouse and R. E. Goldstein, "Cytoplasmic streaming in plant cells emerges naturally by microfilament self-organization," *Proc. Natl. Acad. Sci. U. S. A.*, vol. 110, no. 35, 2013.
- [142] M. Diao and S. Huang, "An update on the role of the actin cytoskeleton in plasmodesmata: A focus on formins," *Frontiers in Plant Science*, vol. 12, p. 191, 2021.
- [143] M. J. Deeks, J. R. Calcutt, E. K. Ingle, T. J. Hawkins, S. Chapman, A. C. Richardson, D. A. Mentlak, M. R. Dixon, F. Cartwright, A. P. Smertenko, K. Oparka, and P. J. Hussey, "A superfamily of actin-binding proteins at the actin-membrane nexus of higher plants," *Curr. Biol.*, vol. 22, no. 17, 2012.
- [144] P. Duckney, J. T. Kroon, M. R. Dixon, T. J. Hawkins, M. J. Deeks, and P. J. Hussey, "NETWORKED2-subfamily proteins regulate the cortical actin cytoskeleton of growing pollen tubes and polarised pollen tube growth," *New Phytol.*, vol. 231, no. 1, 2021.
- [145] M. Pilhofer, M. S. Ladinsky, A. W. McDowall, G. Petroni, and G. J. Jensen, "Microtubules in Bacteria: Ancient tubulins build a five-protofilament homolog of the eukaryotic cytoskeleton," *PLoS Biol.*, vol. 9, no. 12, 2011.

- [146] M. C. Ledbetter and K. R. Porter, "A "microtubule" in plant cell fine structure," *J. Cell Biol.*, vol. 19, no. 1, 1963.
- [147] R. C. Weisenberg, "Microtubule formation in vitro in solutions containing low calcium concentrations," *Science (80-.)*, vol. 177, no. 4054, 1972.
- [148] J. Löwe, H. Li, K. H. Downing, and E. Nogales, "Refined structure of α β -tubulin at 3.5 Å resolution," *J. Mol. Biol.*, vol. 313, no. 5, 2001.
- [149] A. Desai and T. J. Mitchison, "Microtubule polymerization dynamics," *Annual review of cell and developmental biology*, vol. 13, no. 1, pp. 83–117, 1997.
- [150] P. Findeisen, S. Mühlhausen, S. Dempewolf, J. Hertzog, A. Zietlow, T. Carlomagno, and M. Kollmar, "Six subgroups and extensive recent duplications characterize the evolution of the eukaryotic tubulin protein family," *Genome biology and evolution*, vol. 6, no. 9, pp. 2274–2288, 2014.
- [151] S. Chaaban and G. J. Brouhard, "A microtubule bestiary: structural diversity in tubulin polymers," *Molecular biology of the cell*, vol. 28, no. 22, pp. 2924–2931, 2017.
- [152] A. Roll-Mecak, "Intrinsically disordered tubulin tails: complex tuners of microtubule functions?," in *Seminars in cell & developmental biology*, vol. 37, pp. 11–19, Elsevier, 2015.
- [153] H. Sui and K. H. Downing, "Structural basis of interprotofilament interaction and lateral deformation of microtubules," *Structure*, vol. 18, no. 8, 2010.
- [154] D. Chretien, F. Metoz, F. Verde, E. Karsenti, and R. H. Wade, "Lattice defects in microtubules: Protofilament numbers vary within individual microtubules," *J. Cell Biol.*, vol. 117, no. 5, 1992.
- [155] R. A. Walker, E. T. O'Brien, N. K. Pryer, M. F. Soboeiro, W. A. Voter, H. P. Erickson, and E. D. Salmon, "Dynamic instability of individual microtubules analyzed by video light microscopy: rate constants and transition frequencies.," *J. Cell Biol.*, vol. 107, no. 4, 1988.
- [156] H. V. Goodson and E. M. Jonasson, "Microtubules and microtubule-associated proteins," *Cold Spring Harb. Perspect. Biol.*, vol. 10, no. 6, 2018.
- [157] E. Mandelkow and E. M. Mandelkow, "Microtubules and microtubule-associated proteins," *Curr. Opin. Cell Biol.*, vol. 7, no. 1, 1995.
- [158] D. W. Ehrhardt and S. L. Shaw, "Microtubule dynamics and organization in the plant cortical array," *Annu. Rev. Plant Biol.*, vol. 57, pp. 859–875, 2006.
- [159] F. Bartolini, *The retinitis pigmentosa 2 protein and catastrophin: Overlapping functions with tubulin-specific chaperones*. New York University, 2004.

- [160] V. Makrides, M. R. Massie, S. C. Feinstein, and J. Lew, "Evidence for two distinct binding sites for tau on microtubules," *Proceedings of the national academy of sciences*, vol. 101, no. 17, pp. 6746–6751, 2004.
- [161] J. Al-Bassam and F. Chang, "Regulation of microtubule dynamics by tog-domain proteins xmap215/dis1 and clasp," *Trends in cell biology*, vol. 21, no. 10, pp. 604–614, 2011.
- [162] L. Halat, K. Gyte, and G. Wasteneys, "The microtubule-associated protein clasp is translationally regulated in light-dependent root apical meristem growth," *Plant Physiology*, vol. 184, no. 4, pp. 2154–2167, 2020.
- [163] T. Vavrdová, J. Samaj, and G. Komis, "Phosphorylation of plant microtubule-associated proteins during cell division," *Frontiers in Plant Science*, vol. 10, p. 238, 2019.
- [164] N. Hirokawa, "Kinesin and dynein superfamily proteins and the mechanism of organelle transport," *Science*, vol. 279, no. 5350, pp. 519–526, 1998.
- [165] N. Hirokawa, Y. Noda, Y. Tanaka, and S. Niwa, "Kinesin superfamily motor proteins and intracellular transport," *Nature reviews Molecular cell biology*, vol. 10, no. 10, pp. 682–696, 2009.
- [166] N. Hirokawa, K. K. Pfister, H. Yorifuji, M. C. Wagner, S. T. Brady, and G. S. Bloom, "Sub-molecular domains of bovine brain kinesin identified by electron microscopy and monoclonal antibody decoration," *Cell*, vol. 56, no. 5, pp. 867–878, 1989.
- [167] Y.-R. J. Lee, W. Qiu, and B. Liu, "Kinesin motors in plants: from subcellular dynamics to motility regulation," *Current opinion in plant biology*, vol. 28, pp. 120–126, 2015.
- [168] J. C. Ambrose, W. Li, A. Marcus, H. Ma, and R. Cyr, "A minus-end-directed kinesin with plus-end tracking protein activity is involved in spindle morphogenesis," *Molecular biology of the cell*, vol. 16, no. 4, pp. 1584–1592, 2005.
- [169] T. Miki, H. Naito, M. Nishina, and G. Goshima, "Endogenous localizome identifies 43 mitotic kinesins in a plant cell," *Proceedings of the National Academy of Sciences*, vol. 111, no. 11, pp. E1053–E1061, 2014.
- [170] Z. Shen, A. R. Collatos, J. P. Bibeau, F. Furt, and L. Vidali, "Phylogenetic analysis of the kinesin superfamily from physcomitrella," *Frontiers in plant science*, vol. 3, p. 230, 2012.
- [171] E. Lipka and S. Müller, "Potential roles for kinesins at the cortical division site," *Frontiers in plant science*, vol. 3, p. 158, 2012.

- [172] E. Lipka, A. Gadeyne, D. Stockle, S. Zimmermann, G. De Jaeger, D. W. Ehrhardt, V. Kirik, D. Van Damme, and S. Muller, "The Phragmoplast-Orienting Kinesin-12 Class Proteins Translate the Positional Information of the Preprophase Band to Establish the Cortical Division Zone in *Arabidopsis thaliana*," *Plant Cell*, vol. 26, no. 6, pp. 2617–2632, 2014.
- [173] T. I. Baskin and W. Z. Cande, "The structure and function of the mitotic spindle in flowering plants," *Annu. Rev. Plant Physiol. Plant Mol. Biol.*, vol. 41, no. 1, 1990.
- [174] C. E. Walczak and R. Heald, "Mechanisms of mitotic spindle assembly and function," *International review of cytology*, vol. 265, pp. 111–158, 2008.
- [175] C. G. Rasmussen, A. J. Wright, and S. Müller, "The role of the cytoskeleton and associated proteins in determination of the plant cell division plane," *Plant J.*, vol. 75, no. 2, 2013.
- [176] E. Lipka, A. Herrmann, and S. Mueller, "Mechanisms of plant cell division," *Wiley Interdisciplinary Reviews: Developmental Biology*, vol. 4, no. 4, pp. 391–405, 2015.
- [177] M. Yamada and G. Goshima, "Mitotic spindle assembly in land plants: molecules and mechanisms," *Biology*, vol. 6, no. 1, p. 6, 2017.
- [178] G. Jürgens, "Cytokinesis in higher plants," *Annu. Rev. Plant Biol.*, vol. 56, pp. 281–299, 2005.
- [179] A. P. Smertenko, B. Piette, and P. J. Hussey, "The origin of phragmoplast asymmetry," *Current biology*, vol. 21, no. 22, pp. 1924–1930, 2011.
- [180] M. Sasabe and Y. Machida, "Map65: a bridge linking a map kinase to microtubule turnover," *Current opinion in plant biology*, vol. 9, no. 6, pp. 563–570, 2006.
- [181] M. Sasabe, K. Kosetsu, M. Hidaka, A. Murase, and Y. Machida, "Arabidopsis thaliana MAP65-1 and MAP65-2 function redundantly with MAP65-3/PLEIADE in cytokinesis downstream of MPK4," *Plant Signal. Behav.*, vol. 6, no. 5, pp. 743–747, 2011.
- [182] M. Sasabe and Y. Machida, "Regulation of organization and function of microtubules by the mitogen-activated protein kinase cascade during plant cytokinesis," *Cytoskeleton*, vol. 69, no. 11, pp. 913–918, 2012.
- [183] H. Buschmann and S. Müller, "Update on plant cytokinesis: rule and divide," *Current opinion in plant biology*, vol. 52, pp. 97–105, 2019.
- [184] P. Kumari, P. Dahiya, P. Livanos, L. Zergiebel, M. Kölling, Y. Poeschl, G. Stamm, A. Hermann, S. Abel, S. Müller, and K. Bürstenbinder, "IQ67 DOMAIN proteins facilitate preprophase band formation and division-plane orientation," *Nat. Plants*, vol. 7, no. 6, 2021.

- [185] H. Ma and M. Liu, "The microtubule cytoskeleton acts as a sensor for stress response signaling in plants," *Molecular Biology Reports*, vol. 46, no. 5, pp. 5603–5608, 2019.
- [186] L. Wang, E. Sadeghnezhad, P. Guan, and P. Gong, "Microtubules monitor calcium and reactive oxygen species signatures in signal transduction," *Plant Science*, vol. 304, p. 110589, 2021.
- [187] Y. Wang, B. Wang, S. Gilroy, E. Wassim Chehab, and J. Braam, "Cml24 is involved in root mechanoresponses and cortical microtubule orientation in arabidopsis," *Journal of Plant Growth Regulation*, vol. 30, no. 4, pp. 467–479, 2011.
- [188] M. Kölling, P. Kumari, and K. Bürstenbinder, "Calcium-and calmodulin-regulated microtubule-associated proteins as signal-integration hubs at the plasma membrane–cytoskeleton nexus," *Journal of Experimental Botany*, vol. 70, no. 2, pp. 387–396, 2019.
- [189] B. Yang, G. Stamm, K. Bürstenbinder, and C. Voiniciuc, "Microtubule-associated iqd9 guides cellulose synthase velocity to shape seed mucilage," *bioRxiv*, 2021.
- [190] M. S. Mukhtar, A.-R. Carvunis, M. Dreze, P. Epple, J. Steinbrenner, J. Moore, M. Tasan, M. Galli, T. Hao, M. T. Nishimura, *et al.*, "Independently evolved virulence effectors converge onto hubs in a plant immune system network," *science*, vol. 333, no. 6042, pp. 596–601, 2011.
- [191] A. Ganguly, C. Zhu, W. Chen, and R. Dixit, "FRA1 kinesin modulates the lateral stability of cortical microtubules through cellulose synthase–Microtubule uncoupling proteins," *Plant Cell*, vol. 32, no. 8, 2020.
- [192] N. Rayapuram, J. Bigeard, H. Alhoraibi, L. Bonhomme, A.-M. Hesse, J. Vinh, H. Hirt, and D. Pflieger, "Quantitative phosphoproteomic analysis reveals shared and specific targets of arabidopsis mitogen-activated protein kinases (mapks) mpk3, mpk4, and mpk6," *Molecular & Cellular Proteomics*, vol. 17, no. 1, pp. 61–80, 2018.
- [193] H. J. Matthies, R. J. Miller, and H. C. Palfrey, "Calmodulin binding to and cAMP-dependent phosphorylation of kinesin light chains modulate kinesin ATPase activity," *J. Biol. Chem.*, vol. 268, no. 15, 1993.
- [194] L. Feng, Z. Chen, H. Ma, X. Chen, Y. Li, Y. Wang, and Y. Xiang, "The IQD gene family in soybean: Structure, phylogeny, evolution and expression," *PLoS One*, vol. 9, no. 10, 2014.
- [195] R. Cai, C. Zhang, Y. Zhao, K. Zhu, Y. Wang, H. Jiang, Y. Xiang, and B. Cheng, "Genome-wide analysis of the IQD gene family in maize," *Mol. Genet. Genomics*, vol. 291, no. 2, pp. 543–558, 2016.

- [196] Z. Huang, J. Van Houten, G. Gonzalez, H. Xiao, and E. Van Der Knaap, "Genome-wide identification, phylogeny and expression analysis of SUN, OFP and YABBY gene family in tomato," *Mol. Genet. Genomics*, vol. 288, no. 3-4, pp. 111–129, 2013.
- [197] Q. Ke, H. Sun, M. Tang, R. Luo, Y. Zeng, M. Wang, Y. Li, Z. Li, and L. Cui, "Genome-wide identification, expression analysis and evolutionary relationships of the iq67-domain gene family in common wheat (*triticum aestivum* L.) and its progenitors," *BMC genomics*, vol. 23, no. 1, pp. 1–21, 2022.
- [198] L. A. Jurado, P. S. Chockalingam, and H. W. Jarrett, "Apocalmodulin," *Physiol Rev*, vol. 79, no. 3, pp. 661–682, 1999.
- [199] Y. Li, Y. Huang, Y. Wen, D. Wang, H. Liu, Y. Li, J. Zhao, L. An, F. Yu, and X. Liu, "The domain of unknown function 4005 (DUF4005) in an Arabidopsis IQD protein functions in microtubule binding," *J. Biol. Chem.*, vol. 297, no. 1, 2021.
- [200] J. Liu, J. Chen, X. Zheng, F. Wu, Q. Lin, Y. Heng, P. Tian, Z. J. Cheng, X. Yu, K. Zhou, X. Zhang, X. Guo, J. Wang, H. Wang, and J. Wan, "GW5 acts in the brassinosteroid signalling pathway to regulate grain width and weight in rice," *Nat. Plants*, vol. 3, 2017.
- [201] J. Van Leene, C. Han, A. Gadeyne, D. Eeckhout, C. Matthijs, B. Cannoot, N. De Winne, G. Persiau, E. Van De Slijke, B. Van de Cotte, *et al.*, "Capturing the phosphorylation and protein interaction landscape of the plant tor kinase," *Nature Plants*, vol. 5, no. 3, pp. 316–327, 2019.
- [202] M. K. Choudhary, Y. Nomura, L. Wang, H. Nakagami, and D. E. Somers, "Quantitative circadian phosphoproteomic analysis of arabidopsis reveals extensive clock control of key components in physiological, metabolic, and signaling pathways," *Molecular & Cellular Proteomics*, vol. 14, no. 8, pp. 2243–2260, 2015.
- [203] B. Yang, J. R. Wendrich, B. De Rybel, D. Weijers, and H.-W. Xue, "Rice microtubule-associated protein iq67-domain14 regulates grain shape by modulating microtubule cytoskeleton dynamics," *Plant biotechnology journal*, vol. 18, no. 5, pp. 1141–1152, 2020.
- [204] Y. Sugiyama, M. Wakazaki, K. Toyooka, H. Fukuda, and Y. Oda, "A Novel Plasma Membrane-Anchored Protein Regulates Xylem Cell-Wall Deposition through Microtubule-Dependent Lateral Inhibition of Rho GTPase Domains," *Curr. Biol.*, 2017.
- [205] H. Liang, Y. Zhang, P. Martinez, C. G. Rasmussen, T. Xu, and Z. Yang, "The microtubule-associated protein IQ67 DOMAIN5 modulates microtubule dynamics and pavement cell shape," *Plant Physiol.*, 2018.

- [206] J. Wendrich, B.-J. Yang, P. Mijnhout, H.-W. Xue, B. D. Rybel, and D. Weijers, "IQD proteins integrate auxin and calcium signaling to regulate microtubule dynamics during Arabidopsis development," *bioRxiv*, p. 275560, 2018.
- [207] T. J. Hawkins, M. J. Deeks, P. Wang, and P. J. Hussey, "The evolution of the actin binding NET superfamily," *Front. Plant Sci.*, vol. 5, no. JUN, 2014.
- [208] A. J. Saurin, K. L. Borden, M. N. Boddy, and P. S. Freemont, "Does this have a familiar ring?," *Trends in biochemical sciences*, vol. 21, no. 6, pp. 208–214, 1996.
- [209] H. Peng, G. E. Begg, D. C. Schultz, J. R. Friedman, D. E. Jensen, D. W. Speicher, and F. J. Rauscher III, "Reconstitution of the krab-kap-1 repressor complex: a model system for defining the molecular anatomy of ring-box-coiled-coil domain-mediated protein-protein interactions," *Journal of molecular biology*, vol. 295, no. 5, pp. 1139–1162, 2000.
- [210] P. Wang, T. J. Hawkins, C. Richardson, I. Cummins, M. J. Deeks, I. Sparkes, C. Hawes, and P. J. Hussey, "The plant cytoskeleton, NET3C, and VAP27 mediate the link between the plasma membrane and endoplasmic reticulum," *Curr. Biol.*, vol. 24, no. 12, 2014.
- [211] D. E. Clapham, "Calcium signaling," *Cell*, vol. 131, no. 6, pp. 1047–1058, 2007.
- [212] T. Yang and B. Poovaiah, "Calcium/calmodulin-mediated signal network in plants," *Trends in plant science*, vol. 8, no. 10, pp. 505–512, 2003.
- [213] P. K. Hepler, "Calcium: A Central Regulator of Plant Growth and Development," *PLANT CELL ONLINE*, vol. 17, no. 8, pp. 2142–2155, 2005.
- [214] A. Perochon, D. Aldon, J.-P. Galaud, and B. Ranty, "Calmodulin and calmodulin-like proteins in plant calcium signaling," *Biochimie*, vol. 93, no. 12, pp. 2048–2053, 2011.
- [215] L. Steinhorst and J. Kudla, "Calcium and reactive oxygen species rule the waves of signaling," *Plant physiology*, vol. 163, no. 2, pp. 471–485, 2013.
- [216] D. Aldon, M. Mbengue, C. Mazars, and J.-P. Galaud, "Calcium signalling in plant biotic interactions," *International journal of molecular sciences*, vol. 19, no. 3, p. 665, 2018.
- [217] P. Wang, C. Hawes, C. Richardson, and P. J. Hussey, "Characterization of proteins localized to plant er-pm contact sites," in *The Plant Endoplasmic Reticulum*, pp. 23–31, Springer, 2018.
- [218] E. Kordyum, "Calcium signaling in plant cells in altered gravity," *Advances in Space Research*, vol. 32, no. 8, pp. 1621–1630, 2003.
- [219] C. R. Kahl and A. R. Means, "Regulation of cell cycle progression by calcium/calmodulin-dependent pathways," *Endocrine reviews*, vol. 24, no. 6, pp. 719–736, 2003.

- [220] N. Nagasaki, R. Tomioka, and M. Maeshima, "A hydrophilic cation-binding protein of *Arabidopsis thaliana*, AtPCaP1, is localized to plasma membrane via N-myristoylation and interacts with calmodulin and the phosphatidylinositol phosphates PtdIns(3,4,5)P3 and PtdIns(3,5)P2," *FEBS J.*, vol. 275, no. 9, pp. 2267–2282, 2008.
- [221] P. K. Hepler, "The cytoskeleton and its regulation by calcium and protons," *Plant Physiology*, vol. 170, no. 1, pp. 3–22, 2016.
- [222] T. Li, A. Yan, N. Bhatia, A. Altinok, E. Afik, P. Durand-Smet, P. T. Tarr, J. I. Schroeder, M. G. Heisler, and E. M. Meyerowitz, "Calcium signals are necessary to establish auxin transporter polarity in a plant stem cell niche," *Nat. Commun.*, vol. 10, no. 1, 2019.
- [223] A. Costa, L. Navazio, and I. Szabo, "The contribution of organelles to plant intracellular calcium signalling," *Journal of Experimental Botany*, vol. 69, no. 17, pp. 4175–4193, 2018.
- [224] T. Cremer, J. Neefjes, and I. Berlin, "The journey of Ca^{2+} through the cell—pulsing through the network of er membrane contact sites," *Journal of Cell Science*, vol. 133, no. 24, p. jcs249136, 2020.
- [225] N. H. Evans, M. R. McAinsh, and A. M. Hetherington, "Calcium oscillations in higher plants," *Current opinion in plant biology*, vol. 4, no. 5, pp. 415–420, 2001.
- [226] J. F. Harper, "Dissecting calcium oscillators in plant cells," *Trends in plant science*, vol. 6, no. 9, pp. 395–397, 2001.
- [227] A. N. Dodd, J. Kudla, and D. Sanders, "The Language of Calcium Signaling," *Annu. Rev. Plant Biol.*, vol. 61, no. 1, pp. 593–620, 2010.
- [228] A. M. Hetherington and C. Brownlee, "The generation of Ca^{2+} signals in plants," *Annu. Rev. Plant Biol.*, vol. 55, no. 1, pp. 401–427, 2004.
- [229] K. H. Edel, E. Marchadier, C. Brownlee, J. Kudla, and A. M. Hetherington, "The evolution of calcium-based signalling in plants," *Current Biology*, vol. 27, no. 13, pp. R667–R679, 2017.
- [230] V. S. Reddy and A. S. Reddy, "Proteomics of calcium-signaling components in plants," *Phytochemistry*, vol. 65, no. 12, pp. 1745–1776, 2004.
- [231] M. Kato, N. Nagasaki-Takeuchi, Y. Ide, and M. Maeshima, "An *Arabidopsis* hydrophilic Ca^{2+} -binding protein with a pevk-rich domain, pcap2, is associated with the plasma membrane and interacts with calmodulin and phosphatidylinositol phosphates," *Plant Cell Physiol.*, vol. 51, no. 3, pp. 366–379, 2010.

- [232] M. Kato, T. Aoyama, and M. Maeshima, "The Ca²⁺-binding protein PCaP2 located on the plasma membrane is involved in root hair development as a possible signal transducer," *Plant J.*, vol. 74, no. 4, pp. 690–700, 2013.
- [233] E. McCormack, Y.-C. Tsai, and J. Braam, "Handling calcium signaling: arabidopsis cams and cmls," *Trends in plant science*, vol. 10, no. 8, pp. 383–389, 2005.
- [234] J.-J. Zou, F.-J. Wei, C. Wang, J.-J. Wu, D. Ratnasekera, W.-X. Liu, and W.-H. Wu, "Arabidopsis Calcium-Dependent Protein Kinase CPK10 Functions in Abscisic Acid- and Ca²⁺-Mediated Stomatal Regulation in Response to Drought Stress," *PLANT Physiol.*, vol. 154, no. 3, pp. 1232–1243, 2010.
- [235] S. Luan, J. Kudla, M. Rodriguez-Concepcion, S. Yalovsky, and W. Gruissem, "Calmodulins and calcineurin b-like proteins: Calcium sensors for specific signal response coupling in plants," *The Plant Cell*, vol. 14, no. suppl_1, pp. S389–S400, 2002.
- [236] V. La Verde, P. Dominici, and A. Astegno, "Towards understanding plant calcium signaling through calmodulin-like proteins: A biochemical and structural perspective," *International journal of molecular sciences*, vol. 19, no. 5, p. 1331, 2018.
- [237] R. E. Cheney and M. S. Mooseker, "Unconventional myosins," *Current opinion in cell biology*, vol. 4, no. 1, pp. 27–35, 1992.
- [238] T. A. DeFalco, K. W. Bender, and W. A. Snedden, "Breaking the code: Ca²⁺ sensors in plant signalling," *Biochem. J.*, vol. 425, no. 1, pp. 27–40, 2010.
- [239] W. A. Snedden and H. Fromm, "Calmodulin, calmodulin-related proteins and plant responses to the environment," *Trends in Plant Science*, vol. 3, no. 8, pp. 299–304, 1998.
- [240] R. E. Zielinski, "CALMODULIN AND CALMODULIN-BINDING PROTEINS IN PLANTS," *Annu. Rev. Plant Physiol. Plant Mol. Biol.*, vol. 49, no. 1, pp. 697–725, 1998.
- [241] O. Batistič and J. Kudla, "Analysis of calcium signaling pathways in plants.," *Biochim. Biophys. Acta*, vol. 1820, no. 8, pp. 1283–93, 2012.
- [242] J. Kudla, O. Batistic, and K. Hashimoto, "Calcium Signals: The Lead Currency of Plant Information Processing," *Plant Cell*, vol. 22, no. 3, pp. 541–563, 2010.
- [243] J. Michiels, C. Xi, J. Verhaert, and J. Vanderleyden, "The functions of ca²⁺ in bacteria: a role for ef-hand proteins?," *Trends in microbiology*, vol. 10, no. 2, pp. 87–93, 2002.
- [244] K. W. Bender and W. A. Snedden, "Calmodulin-Related Proteins Step Out from the Shadow of Their Namesake," *PLANT Physiol.*, vol. 163, no. 2, pp. 486–495, 2013.

- [245] M. A. Schumacher, M. Crum, and M. C. Miller, "Crystal structures of apocalmodulin and an apocalmodulin/sk potassium channel gating domain complex," *Structure*, vol. 12, no. 5, pp. 849–860, 2004.
- [246] S. Kumar, M. Mazumder, N. Gupta, S. Chattopadhyay, and S. Gourinath, "Crystal structure of arabidopsis thaliana calmodulin7 and insight into its mode of dna binding," *FEBS letters*, vol. 590, no. 17, pp. 3029–3039, 2016.
- [247] A. Houdusse, J.-F. Gaucher, E. Kremntsova, S. Mui, K. M. Trybus, and C. Cohen, "Crystal structure of apo-calmodulin bound to the first two iq motifs of myosin v reveals essential recognition features," *Proceedings of the National Academy of Sciences*, vol. 103, no. 51, pp. 19326–19331, 2006.
- [248] H. Tidow, L. R. Poulsen, A. Andreeva, M. Knudsen, K. L. Hein, C. Wiuf, M. G. Palmgren, and P. Nissen, "A bimodular mechanism of calcium control in eukaryotes," *Nature*, vol. 491, no. 7424, pp. 468–472, 2012.
- [249] A. Crivici and M. Ikura, "Molecular and structural basis of target recognition by calmodulin," *Annual review of biophysics and biomolecular structure*, vol. 24, no. 1, pp. 85–116, 1995.
- [250] J. L. Gifford, M. P. Walsh, and H. J. Vogel, "Structures and metal-ion-binding properties of the ca²⁺-binding helix–loop–helix ef-hand motifs," *Biochemical Journal*, vol. 405, no. 2, pp. 199–221, 2007.
- [251] J. L. Gifford, M. Jamshidiha, J. Mo, H. Ishida, and H. J. Vogel, "Comparing the calcium binding abilities of two soybean calmodulins: towards understanding the divergent nature of plant calmodulins," *The Plant Cell*, vol. 25, no. 11, pp. 4512–4524, 2013.
- [252] S. H. Lee, M. C. Kim, W. D. Heo, J. C. Kim, W. S. Chung, C. Y. Park, H. C. Park, Y. H. Cheong, C. Y. Kim, S. H. Lee, K. J. Lee, J. D. Bahk, S. Y. Lee, and M. J. Cho, "Competitive binding of calmodulin isoforms to calmodulin-binding proteins: implication for the function of calmodulin isoforms in plants," *Biochim. Biophys. Acta - Protein Struct. Mol. Enzymol.*, vol. 1433, no. 1-2, pp. 56–67, 1999.
- [253] D. Chin and A. R. Means, "Calmodulin: a prototypical calcium sensor," *Trends in cell biology*, vol. 10, no. 8, pp. 322–328, 2000.
- [254] V. S. Reddy, F. Safadi, R. E. Zielinski, and A. S. Reddy, "Interaction of a kinesin-like protein with calmodulin isoforms from arabidopsis," *Journal of Biological Chemistry*, vol. 274, no. 44, pp. 31727–31733, 1999.

- [255] P. Zhang, S. Tripathi, H. Trinh, and M. S. Cheung, "Opposing intermolecular tuning of Ca^{2+} affinity for calmodulin by neurogranin and camkii peptides," *Biophysical journal*, vol. 112, no. 6, pp. 1105–1119, 2017.
- [256] P. L. Wintrode and P. L. Privalov, "Energetics of target peptide recognition by calmodulin: a calorimetric study," *Journal of molecular biology*, vol. 266, no. 5, pp. 1050–1062, 1997.
- [257] I. André, T. Kesvatera, B. Jönsson, K. S. Åkerfeldt, and S. Linse, "The role of electrostatic interactions in calmodulin-peptide complex formation," *Biophysical journal*, vol. 87, no. 3, pp. 1929–1938, 2004.
- [258] S. C. Popescu, G. V. Popescu, S. Bachan, Z. Zhang, M. Seay, M. Gerstein, M. Snyder, and S. P. Dinesh-Kumar, "Differential binding of calmodulin-related proteins to their targets revealed through high-density Arabidopsis protein microarrays," *Proc. Natl. Acad. Sci.*, vol. 104, no. 11, pp. 4730–4735, 2007.
- [259] J. Li, X. Wang, T. Qin, Y. Zhang, X. Liu, J. Sun, Y. Zhou, L. Zhu, Z. Zhang, M. Yuan, and T. Mao, "MDP25, A Novel Calcium Regulatory Protein, Mediates Hypocotyl Cell Elongation by Destabilizing Cortical Microtubules in Arabidopsis," *Plant Cell*, vol. 23, no. 12, pp. 4411–4427, 2011.
- [260] T. Qin, J. Li, M. Yuan, and T. Mao, "Characterization of the role of calcium in regulating the microtubule-destabilizing activity of MDP25," *Plant Signal. Behav.*, vol. 7, no. 7, pp. 708–710, 2012.
- [261] R. K. Sharma and S. Parameswaran, "Calmodulin-binding proteins: A journey of 40 years," *Cell Calcium*, vol. 75, pp. 89–100, 2018.
- [262] A. P. Yamniuk and H. J. Vogel, "Structural investigation into the differential target enzyme regulation displayed by plant calmodulin isoforms," *Biochemistry*, vol. 44, no. 8, pp. 3101–3111, 2005.
- [263] H. Tidow and P. Nissen, "Structural diversity of calmodulin binding to its target sites," *The FEBS journal*, vol. 280, no. 21, pp. 5551–5565, 2013.
- [264] M. Rainaldi, A. P. Yamniuk, T. Murase, and H. J. Vogel, "Calcium-dependent and-independent binding of soybean calmodulin isoforms to the calmodulin binding domain of tobacco mapk phosphatase-1," *Journal of biological chemistry*, vol. 282, no. 9, pp. 6031–6042, 2007.
- [265] P. Adams, M. Ben-Johny, I. Dick, T. Inoue, and D. Yue, "Apocalmodulin itself promotes ion channel opening and Ca^{2+} regulation," *Cell*, vol. 159, no. 3, 2014.

- [266] M. Bähler and A. Rhoads, "Calmodulin signaling via the iq motif," *FEBS letters*, vol. 513, no. 1, pp. 107–113, 2002.
- [267] A. Villalobo, H. Ishida, H. J. Vogel, and M. W. Berchtold, "Calmodulin as a protein linker and a regulator of adaptor/scaffold proteins," *Biochimica Et Biophysica Acta (BBA)-Molecular Cell Research*, vol. 1865, no. 3, pp. 507–521, 2018.
- [268] R. J. CYR, "Calcium/calmodulin affects microtubule stability in lysed protoplasts," *Journal of Cell Science*, vol. 100, no. 2, pp. 311–317, 1991.
- [269] M. Varadi, S. Anyango, M. Deshpande, S. Nair, C. Natassia, G. Yordanova, D. Yuan, O. Stroe, G. Wood, A. Laydon, *et al.*, "AlphaFold protein structure database: Massively expanding the structural coverage of protein-sequence space with high-accuracy models," *Nucleic acids research*, vol. 50, no. D1, pp. D439–D444, 2022.
- [270] M. Gundogdu, S. Llabrés, A. Gorelik, A. T. Ferenbach, U. Zachariae, and D. M. van Aalten, "The O-GlcNAc Transferase Intellectual Disability Mutation L254F Distorts the TPR Helix," *Cell Chem. Biol.*, vol. 25, no. 5, 2018.
- [271] P. Durek, R. Schmidt, J. L. Heazlewood, A. Jones, D. MacLean, A. Nagel, B. Kersten, and W. X. Schulze, "Phosphat: the arabidopsis thaliana phosphorylation site database. an update," *Nucleic acids research*, vol. 38, no. suppl_1, pp. D828–D834, 2010.
- [272] V. A. Assimon, D. R. Southworth, and J. E. Gestwicki, "Specific binding of tetratricopeptide repeat proteins to heat shock protein 70 (hsp70) and heat shock protein 90 (hsp90) is regulated by affinity and phosphorylation," *Biochemistry*, vol. 54, no. 48, pp. 7120–7131, 2015.
- [273] S. Drevensek, M. Goussot, Y. Duroc, A. Christodoulidou, S. Steyaert, E. Schaefer, E. Duvernois, O. Grandjean, M. Vantard, D. Bouchez, *et al.*, "The arabidopsis trm1–ton1 interaction reveals a recruitment network common to plant cortical microtubule arrays and eukaryotic centrosomes," *The Plant Cell*, vol. 24, no. 1, pp. 178–191, 2012.
- [274] K. S. Kaleka, A. N. Petersen, M. A. Florence, and N. Z. Gerges, "Pull-down of Calmodulin-binding Proteins," *J. Vis. Exp.*, vol. 59, no. 59, 2012.
- [275] M. Jerabek-Willemsen, T. André, R. Wanner, H. M. Roth, S. Duhr, P. Baaske, and D. Breitsprecher, "MicroScale Thermophoresis: Interaction analysis and beyond," *J. Mol. Struct.*, vol. 1077, 2014.
- [276] K. Yperman, J. Wang, D. Eeckhout, J. Winkler, L. D. Vu, M. Vandorpe, P. Grones, E. Mylle, M. Kraus, R. Merceron, *et al.*, "Molecular architecture of the endocytic tplate complex," *Science Advances*, vol. 7, no. 9, p. eabe7999, 2021.

- [277] M. Q. Müller, F. Dreiocker, C. H. Ihling, M. Schäfer, and A. Sinz, "Cleavable cross-linker for protein structure analysis: Reliable identification of cross-linking products by tandem MS," *Anal. Chem.*, vol. 82, no. 16, 2010.
- [278] J. Jumper, R. Evans, A. Pritzel, T. Green, M. Figurnov, O. Ronneberger, K. Tunyasuvunakool, R. Bates, A. Žídek, A. Potapenko, *et al.*, "Highly accurate protein structure prediction with alphafold," *Nature*, vol. 596, no. 7873, pp. 583–589, 2021.
- [279] V. Mariani, M. Biasini, A. Barbato, and T. Schwede, "Iddt: a local superposition-free score for comparing protein structures and models using distance difference tests," *Bioinformatics*, vol. 29, no. 21, pp. 2722–2728, 2013.
- [280] R. Evans, M. O'Neill, A. Pritzel, N. Antropova, A. W. Senior, T. Green, A. Žídek, R. Bates, S. Blackwell, J. Yim, *et al.*, "Protein complex prediction with alphafold-multimer," *BioRxiv*, 2021.
- [281] G. Van Zundert, J. Rodrigues, M. Trellet, C. Schmitz, P. Kastiris, E. Karaca, A. Melquiond, M. van Dijk, S. De Vries, and A. Bonvin, "The haddock2. 2 web server: user-friendly integrative modeling of biomolecular complexes," *Journal of molecular biology*, vol. 428, no. 4, pp. 720–725, 2016.
- [282] A. M. Bonvin, E. Karaca, P. L. Kastiris, and J. P. Rodrigues, "Defining distance restraints in haddock," *Nature protocols*, vol. 13, no. 7, pp. 1503–1503, 2018.
- [283] D. D. Fisher, S. Gilroy, and R. J. Cyr, "Evidence for opposing effects of calmodulin on cortical microtubules," *Plant Physiology*, vol. 112, no. 3, pp. 1079–1087, 1996.
- [284] E. T. O'Brien, E. Salmon, and H. P. Erickson, "How calcium causes microtubule depolymerization," *Cell motility and the cytoskeleton*, vol. 36, no. 2, pp. 125–135, 1997.
- [285] F. B. Sheinerman, R. Norel, and B. Honig, "Electrostatic aspects of protein–protein interactions," *Current opinion in structural biology*, vol. 10, no. 2, pp. 153–159, 2000.
- [286] H.-X. Zhou and X. Pang, "Electrostatic interactions in protein structure, folding, binding, and condensation," *Chemical reviews*, vol. 118, no. 4, pp. 1691–1741, 2018.
- [287] A. Bah, R. M. Vernon, Z. Siddiqui, M. Krzeminski, R. Muhandiram, C. Zhao, N. Sonenberg, L. E. Kay, and J. D. Forman-Kay, "Folding of an intrinsically disordered protein by phosphorylation as a regulatory switch," *Nature*, vol. 519, no. 7541, pp. 106–109, 2015.
- [288] J. L. Hilton, "Inhibitions of growth and metabolism by 3-amino-1, 2, 4-triazole (amitrole)," *Journal of Agricultural and Food Chemistry*, vol. 17, no. 2, pp. 182–198, 1969.

- [289] K. M. Trybus, M. I. Gushchin, H. Lui, L. Hazelwood, E. B. Kremntsova, N. Volkmann, and D. Hanein, "Effect of calcium on calmodulin bound to the iq motifs of myosin v," *Journal of Biological Chemistry*, vol. 282, no. 32, pp. 23316–23325, 2007.
- [290] Q. Wang, K.-C. Liang, A. Czader, M. N. Waxham, and M. S. Cheung, "The effect of macromolecular crowding, ionic strength and calcium binding on calmodulin dynamics," *PLoS computational biology*, vol. 7, no. 7, p. e1002114, 2011.
- [291] B. Köhn and M. Kovermann, "All atom insights into the impact of crowded environments on protein stability by nmr spectroscopy," *Nature communications*, vol. 11, no. 1, pp. 1–10, 2020.
- [292] S. L. Speer, W. Zheng, X. Jiang, I.-T. Chu, A. J. Guseman, M. Liu, G. J. Pielak, and C. Li, "The intracellular environment affects protein–protein interactions," *Proceedings of the National Academy of Sciences*, vol. 118, no. 11, 2021.
- [293] F. Zosel, A. Soranno, K. J. Buholzer, D. Nettels, and B. Schuler, "Depletion interactions modulate the binding between disordered proteins in crowded environments," *Proceedings of the National Academy of Sciences*, vol. 117, no. 24, pp. 13480–13489, 2020.
- [294] J. Lefèvre, K. G. Chernov, V. Joshi, S. Delga, F. Toma, D. Pastré, P. A. Curmi, and P. Savarin, "The c terminus of tubulin, a versatile partner for cationic molecules: binding of tau, polyamines, and calcium," *Journal of Biological Chemistry*, vol. 286, no. 4, pp. 3065–3078, 2011.
- [295] R. Balkunde, L. Foroughi, E. Ewan, R. Emenecker, V. Cavalli, and R. Dixit, "Mechanism of microtubule plus-end tracking by the plant-specific spr1 protein and its development as a versatile plus-end marker," *Journal of Biological Chemistry*, vol. 294, no. 44, pp. 16374–16384, 2019.
- [296] W. Zauner, J. Kratz, J. Staunton, P. Feick, and G. Wiche, "Identification of two distinct microtubule binding domains on recombinant rat map 1b.," *European journal of cell biology*, vol. 57, no. 1, pp. 66–74, 1992.
- [297] P. Tompa, N. E. Davey, T. J. Gibson, and M. M. Babu, "A million peptide motifs for the molecular biologist," *Molecular cell*, vol. 55, no. 2, pp. 161–169, 2014.
- [298] H. Takayanagi, S. Yuzawa, and H. Sumimoto, "Structural basis for the recognition of the scaffold protein frmpd4/preso1 by the tpr domain of the adaptor protein lgn," *Acta Crystallographica Section F: Structural Biology Communications*, vol. 71, no. 2, pp. 175–183, 2015.
- [299] P. G. Gillespie and J. L. Cyr, "Calmodulin binding to recombinant myosin-1c and myosin-1c iq peptides," *BMC biochemistry*, vol. 3, no. 1, pp. 1–17, 2002.

- [300] T. A. DeFalco, C. B. Marshall, K. Munro, H.-G. Kang, W. Moeder, M. Ikura, W. A. Snedden, and K. Yoshioka, "Multiple calmodulin-binding sites positively and negatively regulate arabidopsis cyclic nucleotide-gated channel12," *The Plant Cell*, vol. 28, no. 7, pp. 1738–1751, 2016.
- [301] I. Corbacho, M. Berrocal, K. Török, A. M. Mata, and C. Gutierrez-Merino, "High affinity binding of amyloid β -peptide to calmodulin: Structural and functional implications," *Biochemical and Biophysical Research Communications*, vol. 486, no. 4, pp. 992–997, 2017.
- [302] C. R. Archer, B. T. Enslow, A. B. Taylor, V. De la Rosa, A. Bhattacharya, and M. S. Shapiro, "A mutually induced conformational fit underlies ca^{2+} -directed interactions between calmodulin and the proximal c terminus of *kcnq4* k^+ channels," *Journal of Biological Chemistry*, vol. 294, no. 15, pp. 6094–6112, 2019.
- [303] C. Seeger, V. O. Talibov, and U. H. Danielson, "Biophysical analysis of the dynamics of calmodulin interactions with neurogranin and ca^{2+} /calmodulin-dependent kinase ii," *Journal of Molecular Recognition*, vol. 30, no. 8, p. e2621, 2017.
- [304] D. Kuo, M. Nie, and A. J. Courey, "Sumo as a solubility tag and in vivo cleavage of sumo fusion proteins with *ulp1*," in *Protein Affinity Tags*, pp. 71–80, Springer, 2014.
- [305] E. M. Bayer, I. Sparkes, S. Vanneste, and A. Rosado, "From shaping organelles to signalling platforms: the emerging functions of plant er–pm contact sites," *Current Opinion in Plant Biology*, vol. 40, pp. 89–96, 2017.
- [306] J. Rappsilber, "The beginning of a beautiful friendship: cross-linking/mass spectrometry and modelling of proteins and multi-protein complexes," *Journal of structural biology*, vol. 173, no. 3, pp. 530–540, 2011.
- [307] A. J. Guseman, S. L. Speer, G. M. Perez Goncalves, and G. J. Pielak, "Surface charge modulates protein–protein interactions in physiologically relevant environments," *Biochemistry*, vol. 57, no. 11, pp. 1681–1684, 2018.
- [308] K. P. Lu and A. R. Means, "Regulation of the cell cycle by calcium and calmodulin," *Endocrine reviews*, vol. 14, no. 1, pp. 40–58, 1993.
- [309] A. R. Means, "Calcium, calmodulin and cell cycle regulation," *FEBS letters*, vol. 347, no. 1, pp. 1–4, 1994.
- [310] J. Jumper, R. Evans, A. Pritzel, T. Green, M. Figurnov, O. Ronneberger, K. Tunyasuvunakool, R. Bates, A. Žídek, A. Potapenko, A. Bridgland, C. Meyer, S. A. Kohl, A. J. Ballard, A. Cowie, B. Romera-Paredes, S. Nikolov, R. Jain, J. Adler, T. Back, S. Petersen, D. Reiman, E. Clancy,

- M. Zielinski, M. Steinegger, M. Pacholska, T. Berghammer, D. Silver, O. Vinyals, A. W. Senior, K. Kavukcuoglu, P. Kohli, and D. Hassabis, "Applying and improving AlphaFold at CASP14," *Proteins Struct. Funct. Bioinforma.*, vol. 89, no. 12, 2021.
- [311] S. Lyskov and J. J. Gray, "The rosettadock server for local protein–protein docking," *Nucleic acids research*, vol. 36, no. suppl_2, pp. W233–W238, 2008.
- [312] C. A. Schneider, W. S. Rasband, and K. W. Eliceiri, "Nih image to imagej: 25 years of image analysis," *Nature methods*, vol. 9, no. 7, pp. 671–675, 2012.
- [313] R. Gautier, D. Douguet, B. Antonny, and G. Drin, "Heliquet: a web server to screen sequences with specific α -helical properties," *Bioinformatics*, vol. 24, no. 18, pp. 2101–2102, 2008.
- [314] J. M. Miller, "GraphPad PRISM," *Analysis*, vol. 52, no. 1, 2003.
- [315] C. Iacobucci, M. Götze, C. H. Ihling, C. Piotrowski, C. Arlt, M. Schaefer, C. Hage, R. Schmidt, and A. Sinz, "A cross-linking/mass spectrometry workflow based on ms-cleavable cross-linkers and the merox software for studying protein structures and protein–protein interactions," *Nature protocols*, vol. 13, no. 12, pp. 2864–2889, 2018.
- [316] M. Grimm, T. Zimniak, A. Kahraman, and F. Herzog, "xvis: a web server for the schematic visualization and interpretation of crosslink-derived spatial restraints," *Nucleic acids research*, vol. 43, no. W1, pp. W362–W369, 2015.
- [317] T. L. Bailey, M. Boden, F. A. Buske, M. Frith, C. E. Grant, L. Clementi, J. Ren, W. W. Li, and W. S. Noble, "MEME Suite: Tools for motif discovery and searching," *Nucleic Acids Res.*, vol. 37, no. SUPPL. 2, 2009.
- [318] Z. Dosztányi, V. Csizmok, P. Tompa, and I. Simon, "IUPred: Web server for the prediction of intrinsically unstructured regions of proteins based on estimated energy content," *Bioinformatics*, vol. 21, no. 16, 2005.
- [319] M. J. Mizianty, V. Uversky, and L. Kurgan, "Prediction of intrinsic disorder in proteins using MFDp2," *Methods Mol. Biol.*, vol. 1137, pp. 147–162, 2014.
- [320] K. Peng, S. Vucetic, P. Radivojac, C. J. Brown, A. K. Dunker, and Z. Obradovic, "Optimizing long intrinsic disorder predictors with protein evolutionary information," *J. Bioinform. Comput. Biol.*, vol. 3, no. 1, 2005.
- [321] T. Ishida and K. Kinoshita, "PrDOS: Prediction of disordered protein regions from amino acid sequence," *Nucleic Acids Res.*, vol. 35, no. SUPPL.2, 2007.

- [322] D. W. Buchan and D. T. Jones, "The PSIPRED Protein Analysis Workbench: 20 years on," *Nucleic Acids Res.*, vol. 47, no. W1, 2019.
- [323] B. Webb and A. Sali, "Comparative protein structure modeling using MODELLER," *Curr. Protoc. Bioinforma.*, vol. 2016, 2016.
- [324] W. L. Delano, "The PyMOL Molecular Graphics System," *CCP4 Newsl. protein Crystallogr.*, vol. 40, no. 1, 2002.
- [325] P. Rice, I. Longden, and A. Bleasby, "Emboss: the european molecular biology open software suite," *Trends in genetics*, vol. 16, no. 6, pp. 276–277, 2000.
- [326] R. L. Poole, "The TAIR database.," *Methods Mol. Biol.*, vol. 406, pp. 179–212, 2007.
- [327] . The Uniprot Consortium, "UniProt: a worldwide hub of protein knowledge The UniProt Consortium," *Nucleic Acids Res.*, vol. 47, no. Issue D1, 2019.
- [328] K. Mruk, B. M. Farley, A. W. Ritacco, and W. R. Kobertz, "Calmodulation meta-analysis: Predicting calmodulin binding via canonical motif clustering," *Journal of general physiology*, vol. 144, no. 1, pp. 105–114, 2014.
- [329] B. Nieves, "PDB-101: Educational Portal of the RCSB Protein Database," *Am. Biol. Teach.*, vol. 83, no. 2, 2021.
- [330] U. K. LAEMMLI, "Cleavage of structural proteins during the assembly of the head of bacteriophage t4," *nature*, vol. 227, no. 5259, pp. 680–685, 1970.
- [331] G. Bertani, "Studies on lysogenesis i: the mode of phage liberation by lysogenic escherichia coli," *Journal of bacteriology*, vol. 62, no. 3, pp. 293–300, 1951.
- [332] K. Tartof and C. Hobbs, "Improved media for growing plasmid and cosmid clones," *Focus*, vol. 9, 1987.
- [333] F. Katzen, "Gateway® recombinational cloning: a biological operating system," *Expert opinion on drug discovery*, vol. 2, no. 4, pp. 571–589, 2007.
- [334] J. Quan and J. Tian, "Circular polymerase extension cloning," *Methods Mol. Biol.*, vol. 1116, pp. 103–117, 2014.
- [335] Z. Wasyl, E. Luchter, and W. Bielański, "Determination of the effective radius of protein molecules by thin-layer gel filtration," *BBA - Protein Struct.*, vol. 243, no. 1, pp. 11–18, 1971.
- [336] J. L. Brunelle and R. Green, "One-dimensional SDS-polyacrylamide gel electrophoresis (1D SDS-PAGE)," *Methods Enzymol.*, vol. 541, pp. 151–159, 2014.

- [337] P. Majovsky, C. Naumann, C.-W. Lee, I. Lassowskat, M. Trujillo, N. Dissmeyer, and W. Hoehener, "Targeted proteomics analysis of protein degradation in plant signaling on an Itq-orbitrap mass spectrometer," *Journal of proteome research*, vol. 13, no. 10, pp. 4246–4258, 2014.
- [338] M. B. Einarson, E. N. Pugacheva, and J. R. Orlinick, "GST Pull-down," *Cold Spring Harb. Protoc.*, vol. 2007, no. 8, pp. pdb.prot4757–pdb.prot4757, 2007.
- [339] J. P. Rodrigues, M. Trellet, C. Schmitz, P. Kastiris, E. Karaca, A. S. Melquiond, and A. M. Bonvin, "Clustering biomolecular complexes by residue contacts similarity," *Proteins: Structure, Function, and Bioinformatics*, vol. 80, no. 7, pp. 1810–1817, 2012.

A Appendix

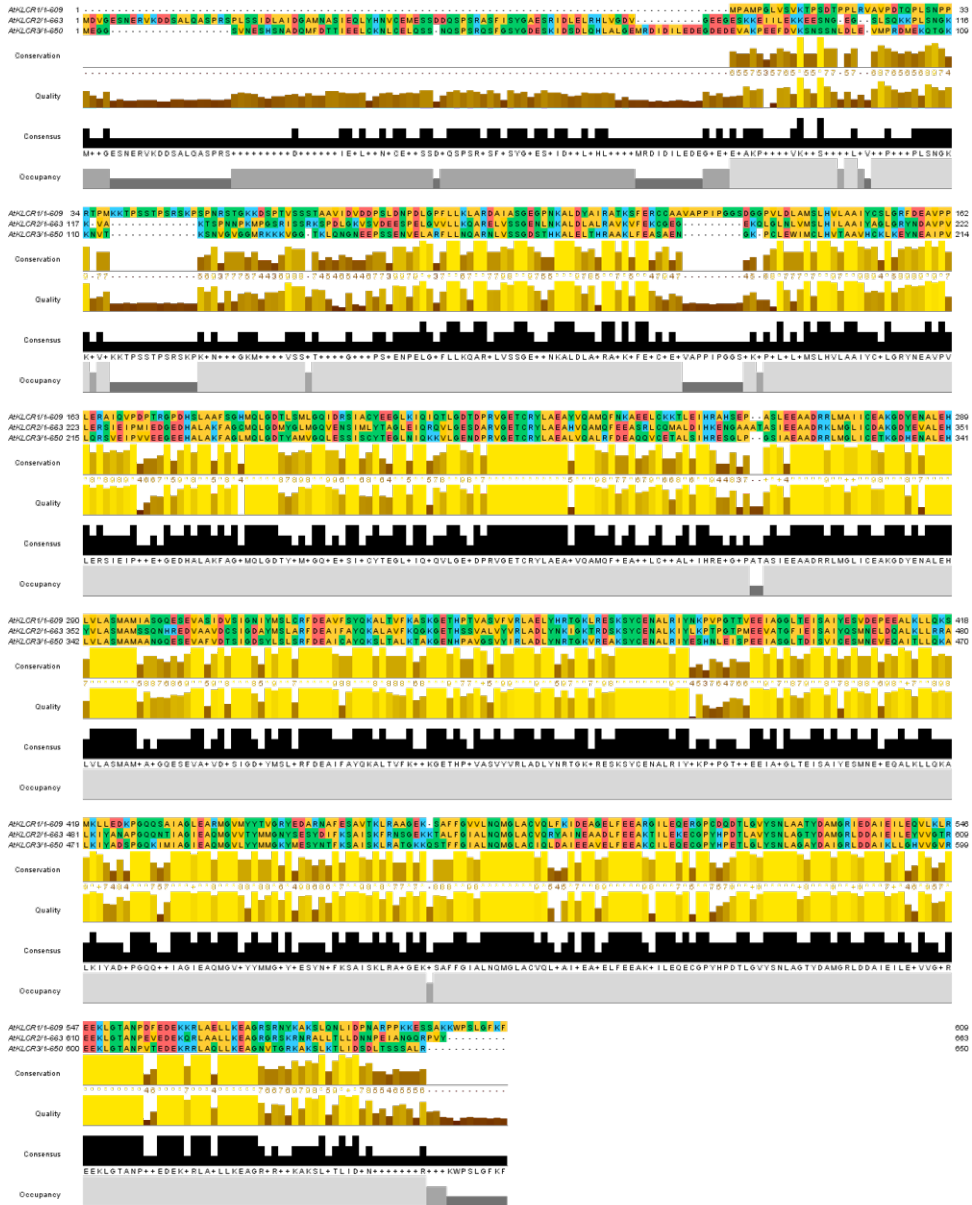


Figure A.1: Alignment of KLCR1, KLCR2, and KLCR3. The alignment was generated with the Clustal Omega algorithm using default parameters and displayed in Jalview. Non-polar amino acids are coloured yellow, polar ones in green. Acidic amino acids are coloured in red, basic ones in blue.

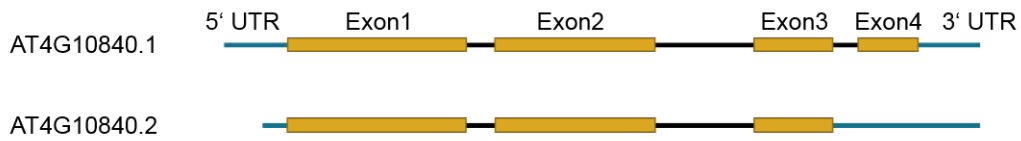


Figure A.2: Gene model of KLCR1 and its splice variant. Untranslated regions are depicted in blue, exons as yellow boxes, and introns in black.

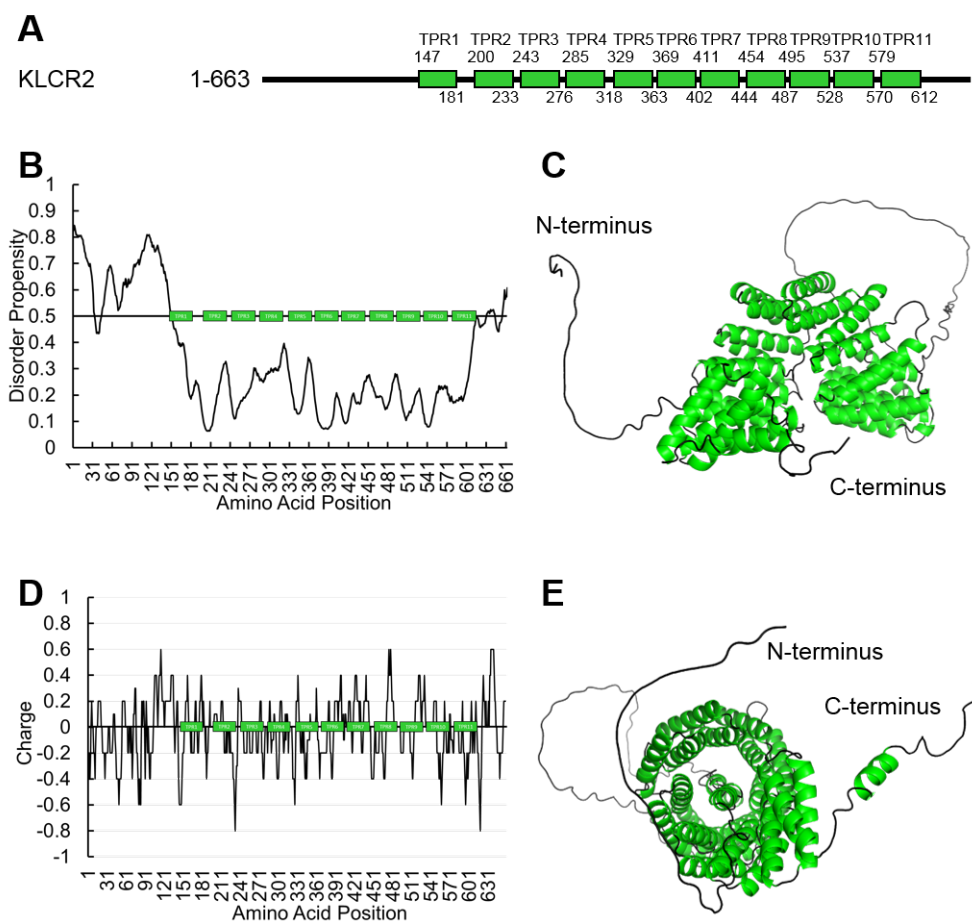


Figure A.3: *In silico* analysis of KLCR2. **A:** Schematic representation of KLCR2. TPR motifs are depicted as green boxes. First and last amino acid position are provided above and below each motif. **B:** Disorder prediction of KLCR2 with the protein schematic superimposed. A disorder propensity above 0.5 is considered to be likely disordered, while value below 0.5 suggests an ordered secondary structure. **C:** AlphaFold 2.0 model of KLCR2 in cartoon presentation. Helices are coloured green, while loops are coloured grey. **D:** Charge plot of KLCR2 generated with the EMBOSS charge tool superimposed with the protein schematic. **E:** "Top down" view of the model shown in **C**, showing the inner cylinder formed by KLCR2.

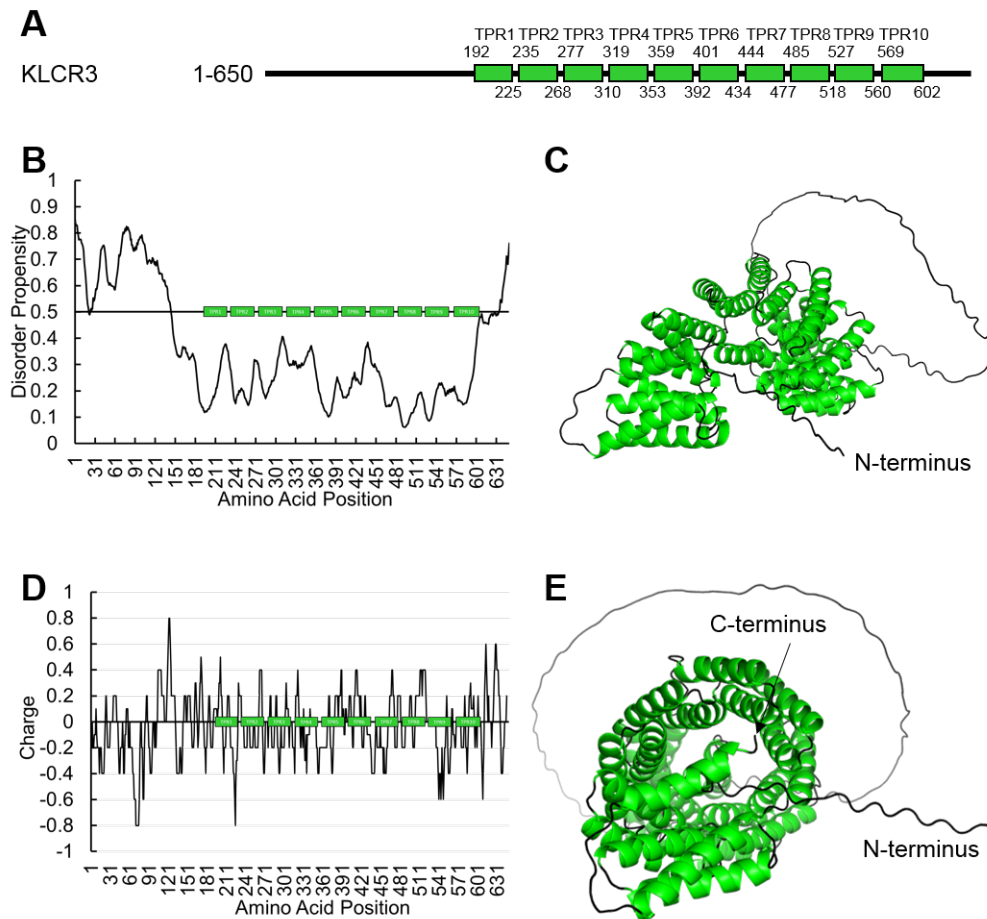


Figure A.4: *In silico* analysis of KLCR3. **A:** Schematic representation of KLCR3. TPR motifs are depicted as green boxes. First and last amino acid position are provided above and below each motif. **B:** Disorder prediction of KLCR3 with the protein schematic superimposed. A disorder propensity above 0.5 is considered to be likely disordered, while value below 0.5 suggests an ordered secondary structure. **C:** AlphaFold 2.0 model of KLCR3 in cartoon presentation. Helices are coloured green, while loops are coloured grey. **D:** Charge plot of KLCR3 generated with the EMBOSS charge tool superimposed with the protein schematic. **E:** "Top down" view of the model shown in **C**, showing the inner cylinder formed by KLCR3.

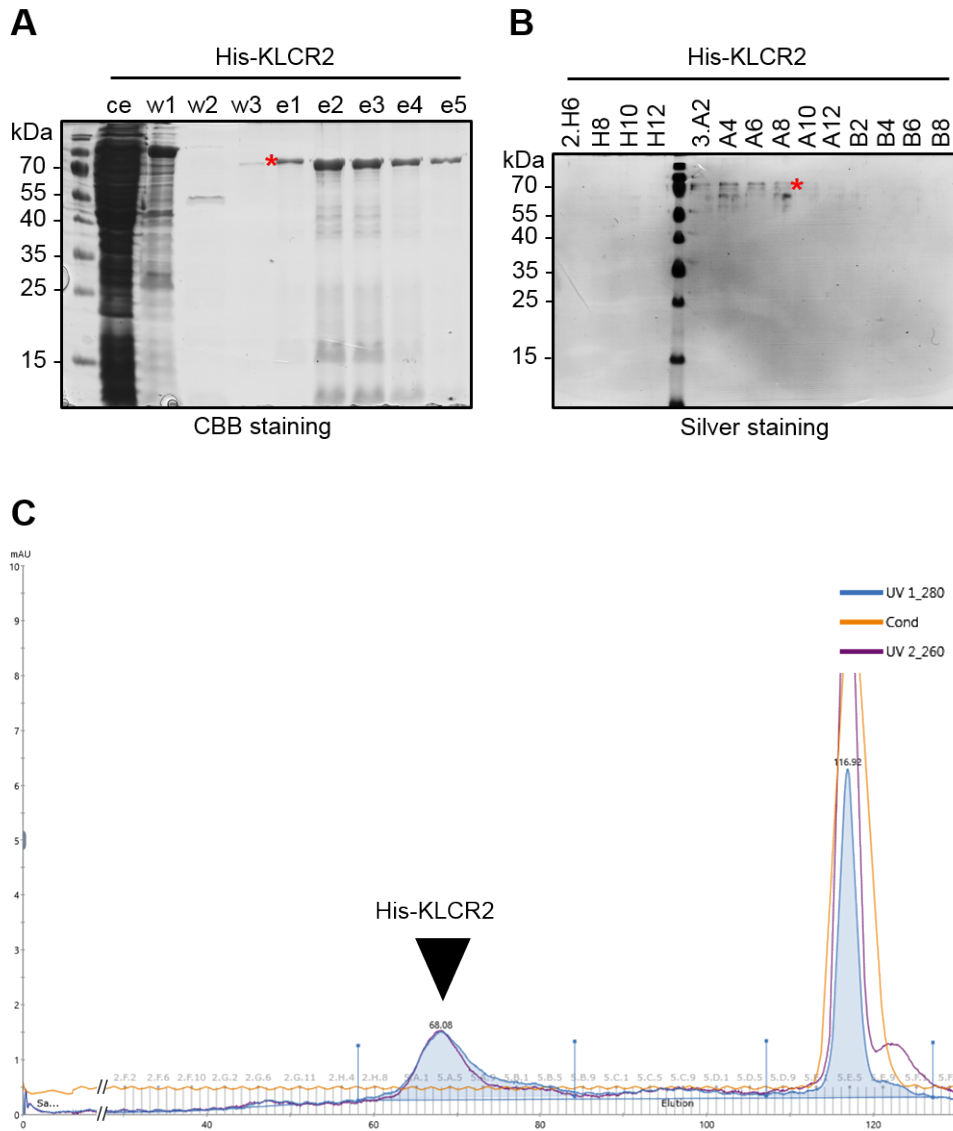


Figure A.5: Analysis of His-KLCR2 regarding homo-dimerisation. **A:** 15 % SDS-PAGE of affinity purification of His-KLCR2 via Ni-NTA agarose. His-KLCR2 is marked with a red asterisk. **B:** 15 % SDS-PAGE of the marked peak from **C** after silver staining. His-KLCR2 is marked with a red asterisk. **C:** Chromatogram of SEC of His-KLCR2 on HiLoad 16/600 Superdex 200 pg showing absorption at 280 nm (blue), absorption at 260 nm (violet), and conductivity (orange) plotted against the retention volume. The peak corresponding to His-KLCR2 is marked with a black arrowhead.

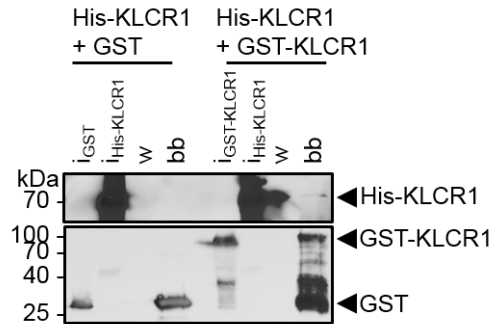


Figure A.6: GST-pulldown of His-KLCR1 with GST-KLCR1. Western blot of 15 % SDS-PAGE of GST-pulldown of His-KLCR1 with GST-KLCR1 or GST as negative control. Protein of interest are marked with black arrowheads. i: input, w: wash, bb: bead-bound.

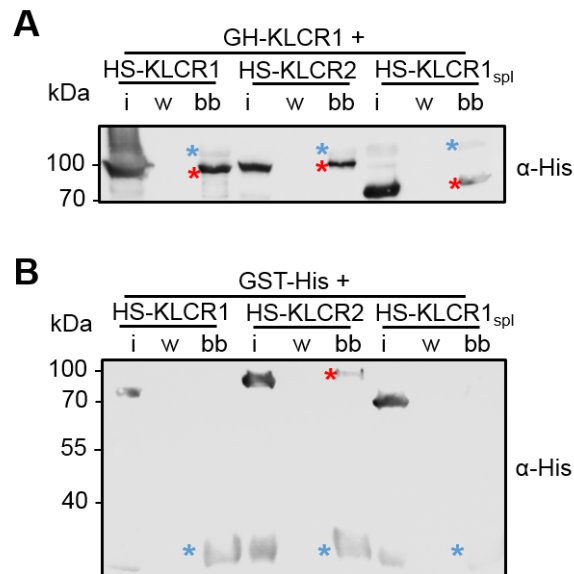


Figure A.7: Uncropped western blots from Fig. 11. Western blots of GST-pulldowns of HS-KLCR1, -KLCR2, and KLCR1_{spl} with GH-KLCR1 (A) or GH as negative control (B). Blue asterisks mark the bait constructs, red asterisks the prey constructs. i: input, w: wash, bb: bead-bound.

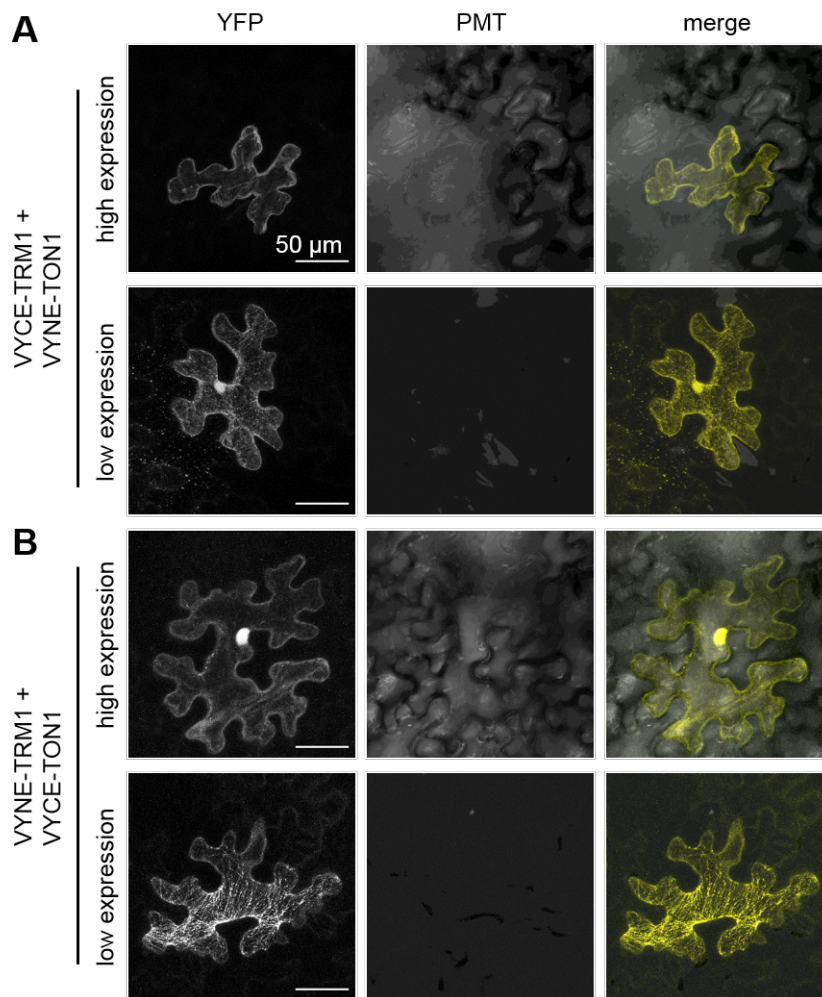


Figure A.8: BiFC of TRM1 and TON1 control in *N. benthamiana* leaves. Co-expression of VYCE-TRM1 and VYNE-TON1 (A) or VYNE-TRM1 and VYCE-TON1 (B) with high and low expression strength. YFP signal indicates protein interaction, while the T-PMT channel acts as a pseudo bright-field image. Scale bars represent 50 μm . The same TRM1-TON1 positive control was used for all BiFC experiments.

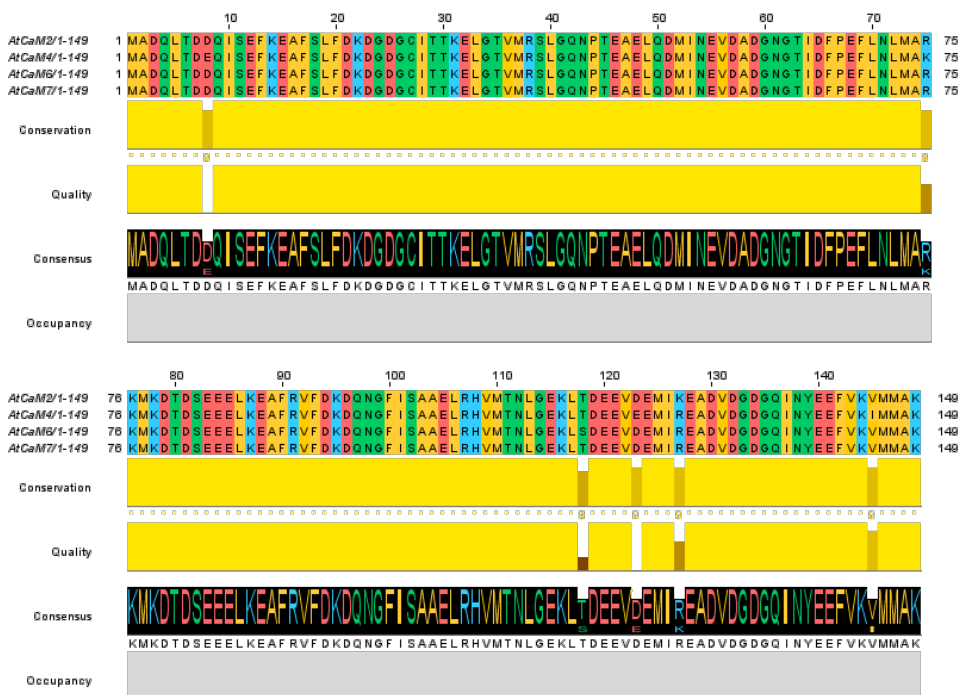


Figure A.9: Alignment of all *A. thaliana* CaM isoforms. The alignment was generated with the Clustal Omega algorithm using default parameters and displayed in Jalview. Non-polar amino acids are coloured yellow, polar ones in green. Acidic amino acids are coloured in red, basic ones in blue.

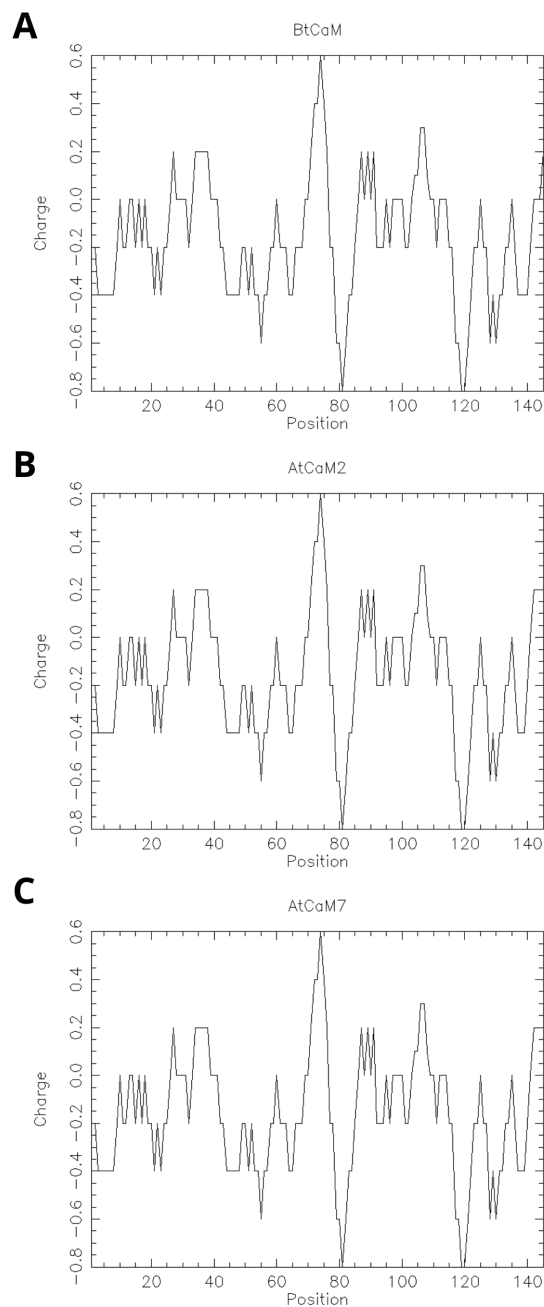


Figure A.10: Charge plots of *BtCaM*, *AtCaM2*, and *AtCaM7*. Bovine CaM (**A**), *AtCaM2* (**B**), and *AtCaM7* (**C**) are characterised by a strong negative charge throughout most of the protein sequence, except for a short patch of positive charge in the linker between the EF-hand domains. The negative charge of EF-hands 1 and 3 is less pronounced than that of EF-hands 2 and 4. Charge profiles do not differ between different CaMs due to their high sequence identity.

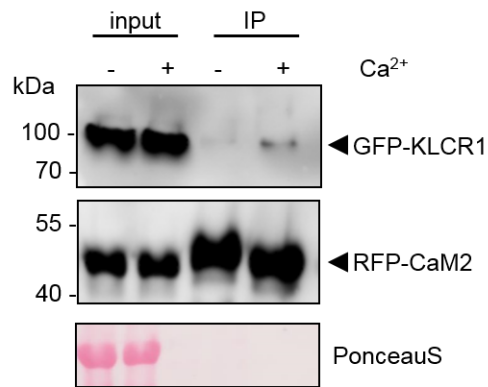


Figure A.11: Co-IP of KLCR1 with CaM2 from *N. benthamiana* leaves. Western blot of co-IP of GFP-KLCR1 with RFP-CaM2 using RFP-trap beads in the presence or absence of Ca²⁺. Expected positions of GFP-KLCR1 and RFP-CaM2 are marked with black arrowheads. Co-IPs were carried out by Gina Stamm.

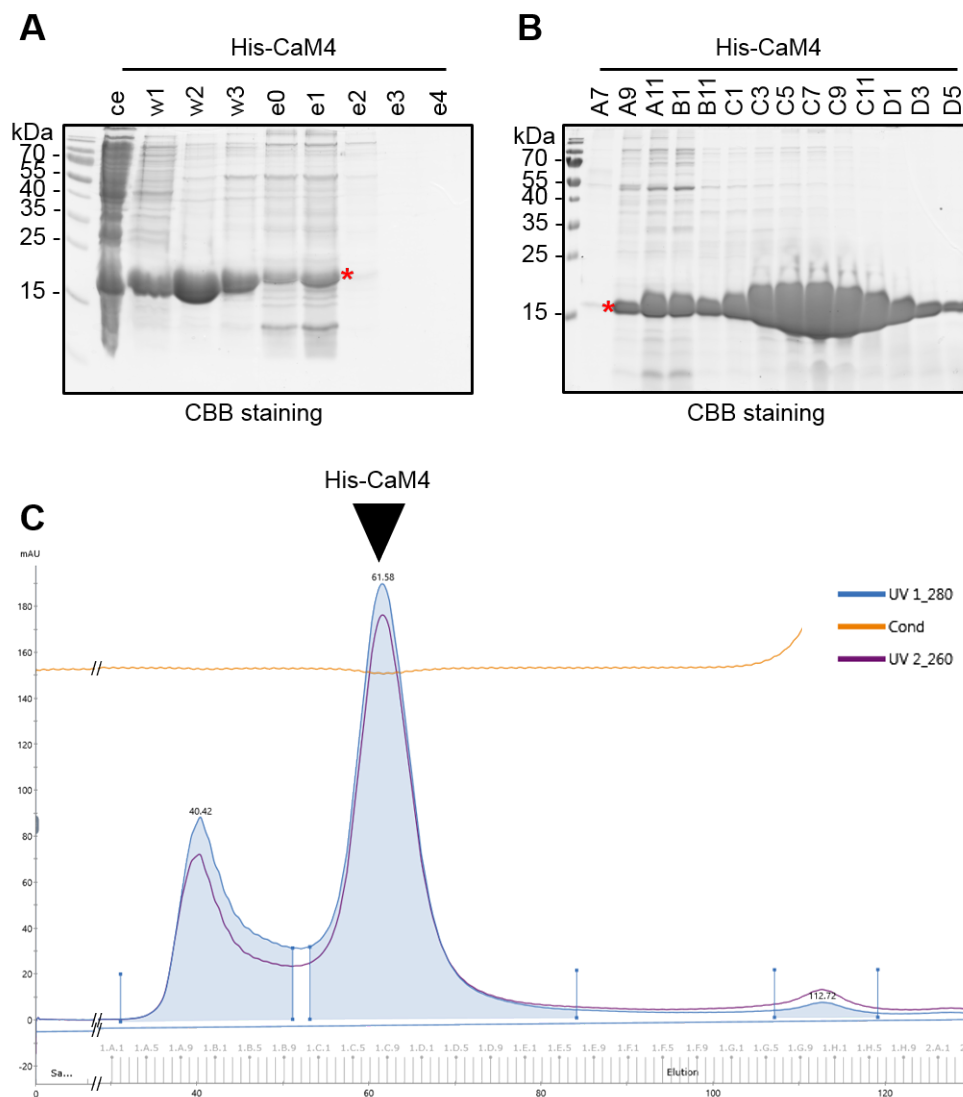


Figure A.12: Purification of His-CaM4. **A:** 15 % SDS-PAGE of crude extract (ce), wash fractions (w1 to w3), and elution fractions (e0 to e4) after affinity purification via Ni-NTA agarose. His-CaM4 is marked with a red asterisk. **B:** 15 % SDS-PAGE of peak fractions of SEC of His-CaM4. His-CaM4 is marked with a red asterisk. **C:** Chromatogram of SEC of His-CaM4 on a HiPrep 16/60 Sephacryl S100 HR column showing absorption at 280 nm (blue), 260 nm (violet), and conductivity (orange) plotted against the retention volume. The fractions analysed in **B** correspond to the peak at 61.58 ml.

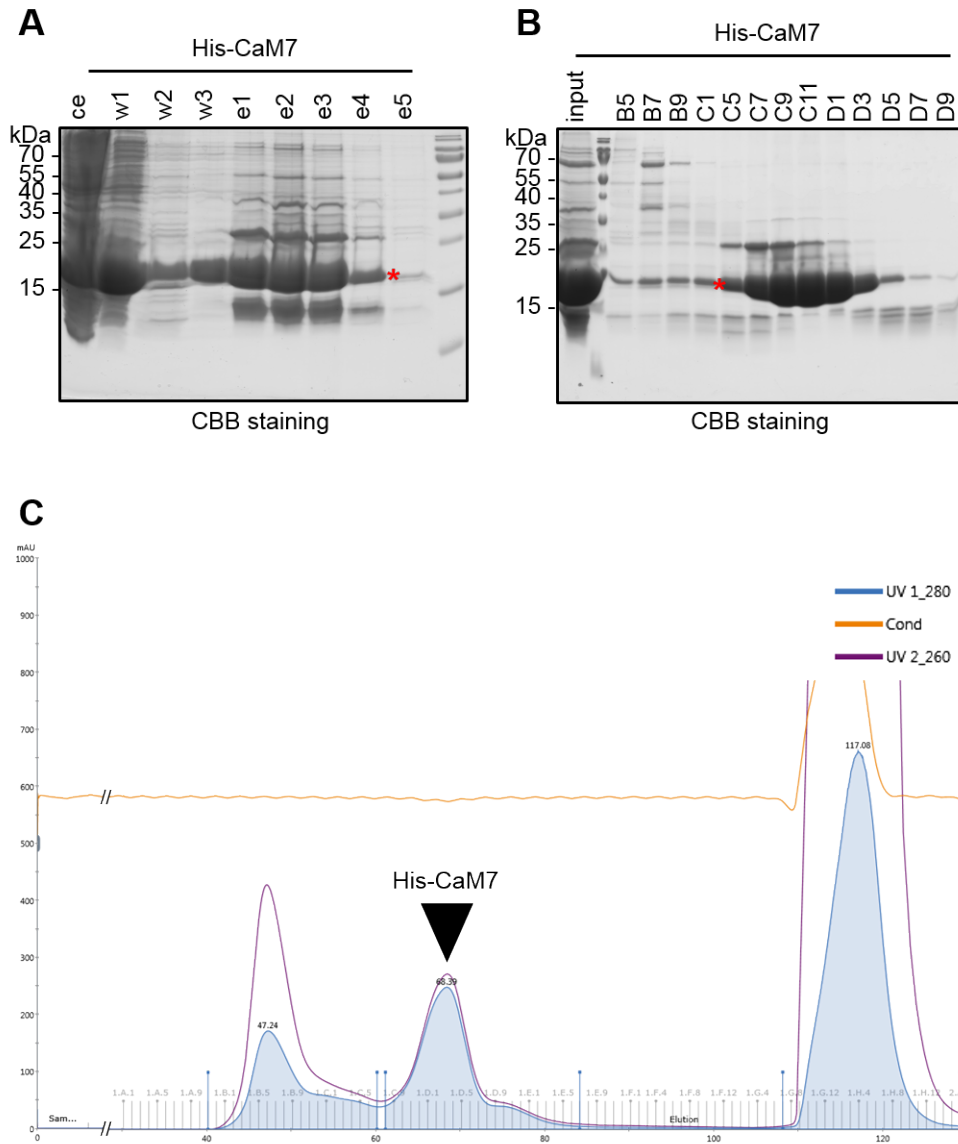


Figure A.13: Purification of His-CaM7. **A:** 15 % SDS-PAGE of crude extract (ce), wash fractions (w1 to w3), and elution fractions (e0 to e4) after affinity purification via Ni-NTA agarose. His-CaM7 is marked with a red asterisk. **B:** 15 % SDS-PAGE of peak fractions of SEC of His-CaM7. His-CaM7 is marked with a red asterisk. **C:** Chromatogram of SEC of His-CaM7 on a HiLoad 16/60 Superdex 75 column showing absorption at 280 nm (blue), 260 nm (violet), and conductivity (orange) plotted against the retention volume. The fractions analysed in **B** correspond to the peak at 68.39 ml.

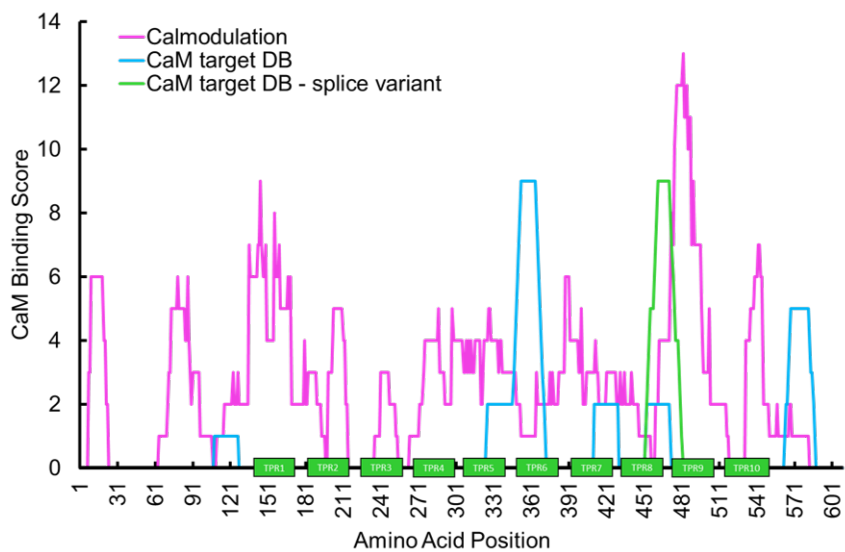


Figure A.14: CaM-binding score of KLCR1. CaM-binding scores from the Calmodulation database (magenta) or the CaM-target database (blue and green) plotted against the amino acids sequence of KLCR1 superimposed with the protein schematic. The green peak represents a difference in CaM-binding score in the CaM-target database between KLCR1 and its splice variant.

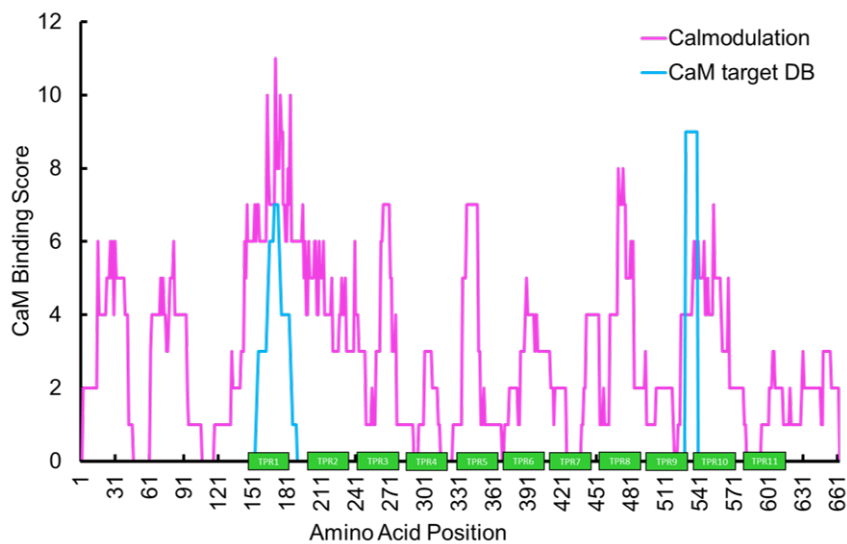


Figure A.15: CaM-binding score of KLCR2. CaM-binding scores from the Calmodulation database (magenta) or the CaM-target database (blue) plotted against the amino acids sequence of KLCR2 superimposed with the protein schematic.

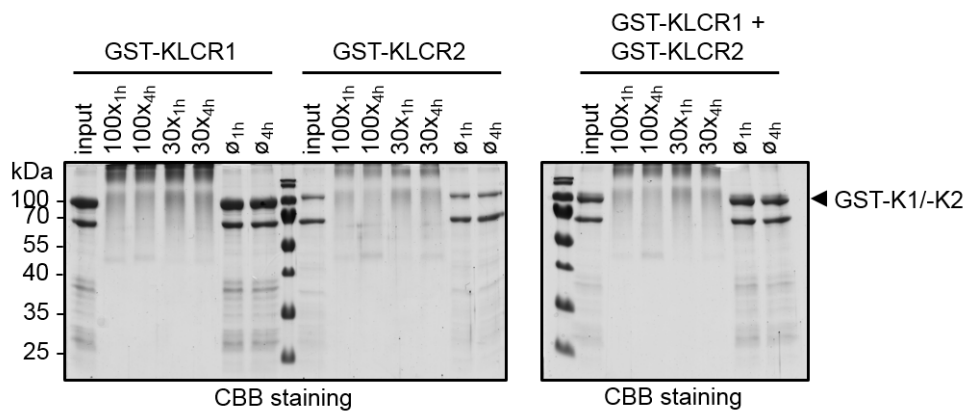


Figure A.16: Cross-linking of KLCR1 and KLCR2. 12 % SDS-PAGE of cross-linking results of 5 μ M GST-KLCR1 (K1) and GST-KLCR2 (K2) either by themselves or mixed together after one or four hours of incubation without cross-linker (\emptyset) or with 100- or 30-fold molar excess of cross-linker DSBU. Expected position of GST-tagged KLCRs is marked with a black arrowhead.

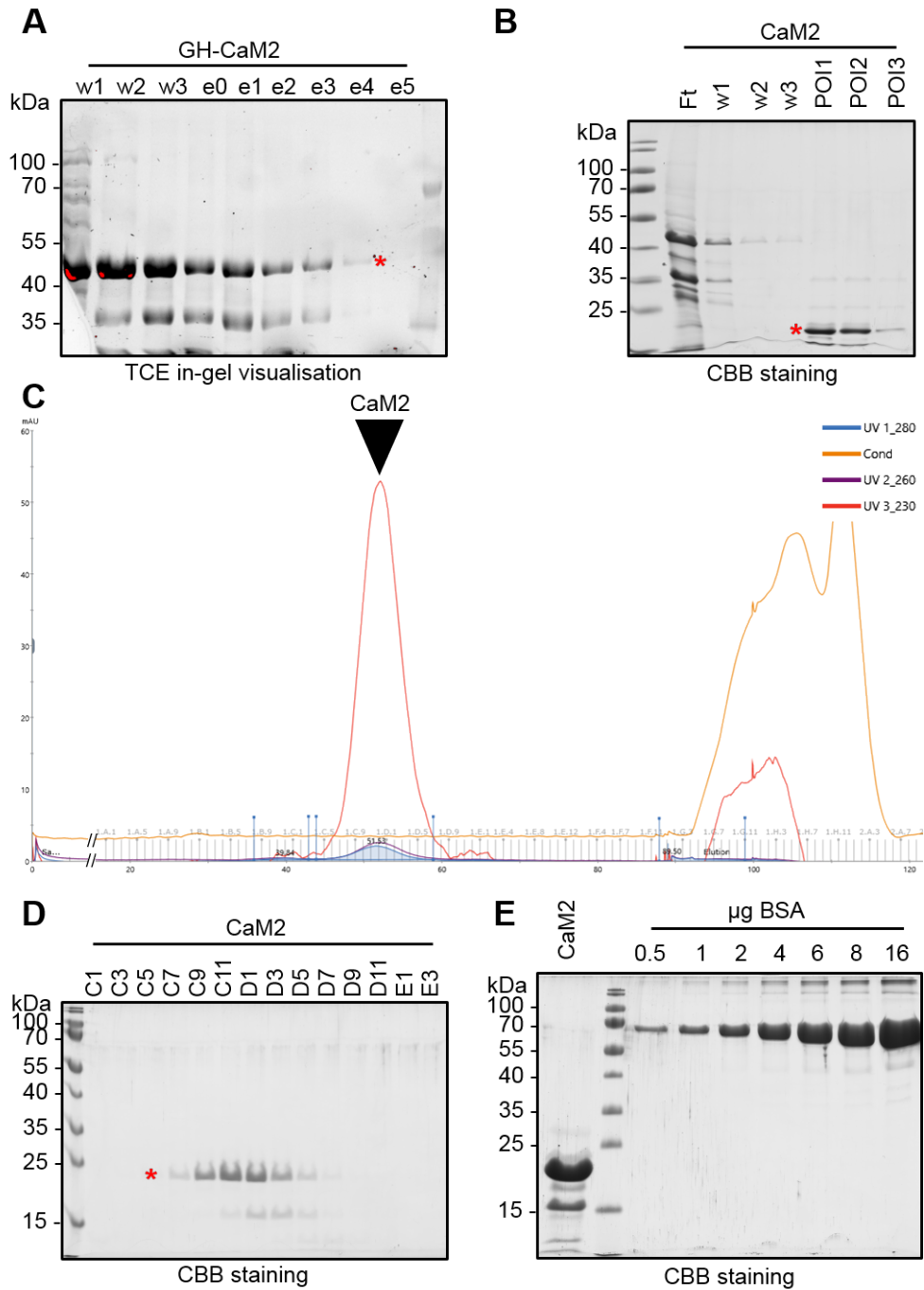


Figure A.17: Generation of tag-free CaM2. **A:** 12 % SDS-PAGE of wash (w1 to w3) and elution (e0 to e5) fractions of affinity purification of GST-His-CaM2 (GH-CaM2) via Ni-NTA agarose. GH-CaM2 is marked with a red asterisk. **B:** 12 % SDS-PAGE of flow-through (Ft), wash (w1 to w3) and protein-of-interest (POI1 to POI3) fractions after tag-removal from GH-CaM2. **C:** SEC of tag-free CaM2 on HiLoad 16/600 Superdex 200 pg. The peak corresponding to CaM2 is marked with a black arrowhead. **D:** 12 % SDS-PAGE of peak fractions of the SEC in **C**. Tag-free CaM2 is marked with a red asterisk. **E:** Concentrated peak fractions of CaM2 with a BSA calibration curve for concentration determination. CaM2 can be found at approx. 20 kDa.



Figure A.18: Mass spectrometric identification of tag-free KLCR1 and CaM2. Mass spectrometry results identifying tag-free KLCR1 and CaM2 from Figs. 21 and A.17. Identified peptides are mapped to the protein sequence and highlighted in green and yellow. Protein identification via MS/MS analysis was carried out by Carsten Proksch and Dr. Susanne Matschi.

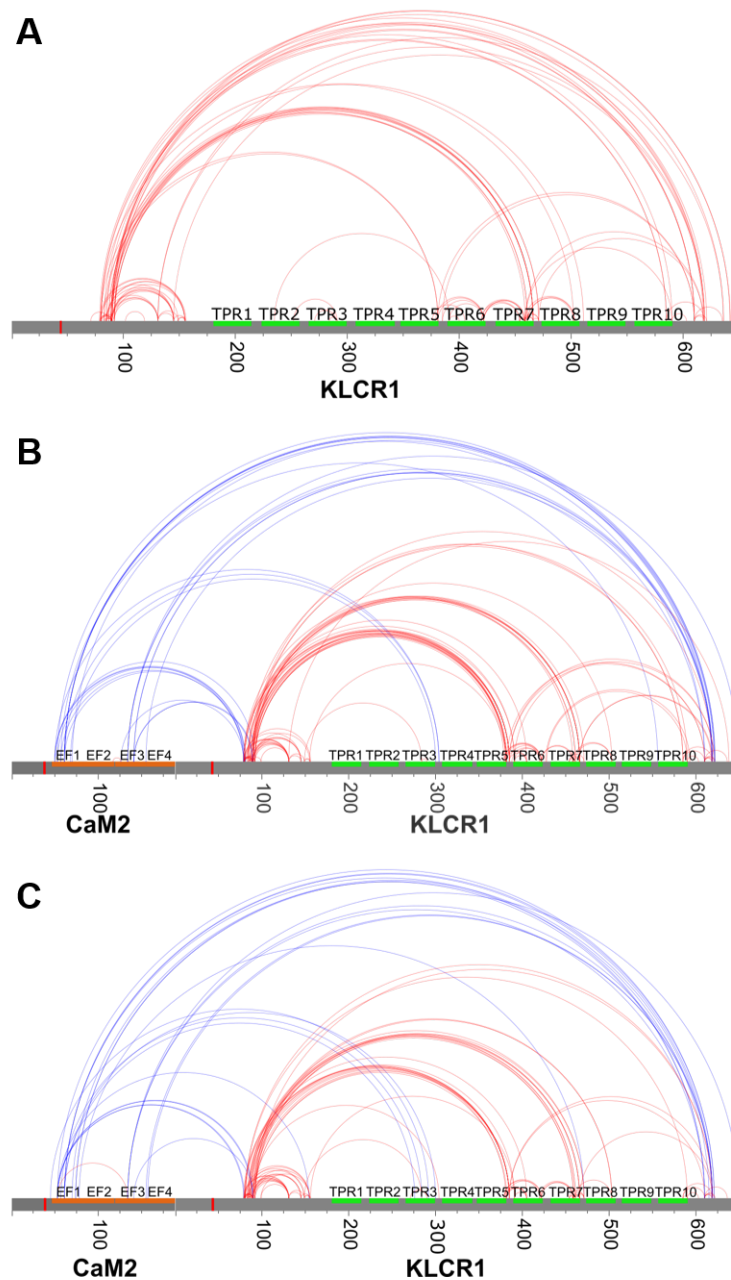


Figure A.19: Cross-linking results of tag-free KLCR1 and CaM2 as bar plots. A: Intra-molecular cross-links within KLCR1, identified using the MeroX software after LC/MS/MS analysis and visualised using xVis as a bar plot. The TPR motifs of KLCR1 are marked as green boxes. Red lines represent cross-links identified in three independent experiments. **B:** Inter-molecular cross-links between KLCR1 and holo-CaM2 and intra-molecular cross-links within KLCR1 and CaM2. Green boxes represent the TPR motifs in KLCRs, orange boxes the EF-hands in CaM2. **C:** Inter-molecular cross-links between KLCR1 and putatively apo-CaM2 and intra-molecular cross-links within KLCR1 and CaM2. Cross-links identified in three independent experiments are represented as red (intra) and blue (inter) lines. The bold red lines in **A**, **B**, and **C** mark the end of the remaining protein tag after tag-removal. LC/MS/MS measurements and analysis with MeroX were carried out by Dr. Christian Ihling.

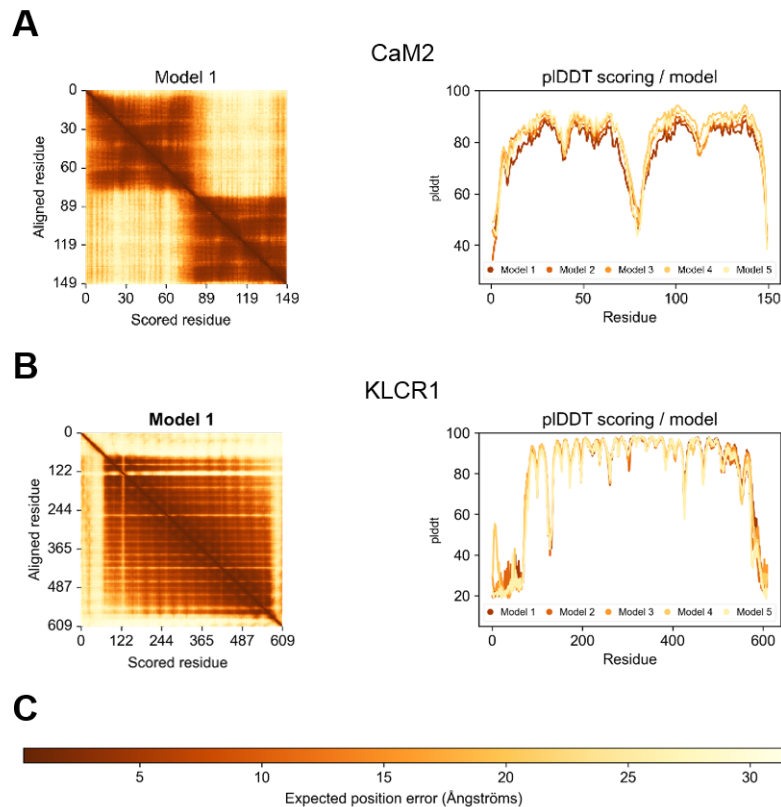


Figure A.20: Quality scores of the AlphaFold generated models of CaM2 and KLCR1. AlphaFold PAE (left) and pLDDT (right) scores of *in silico* models of CaM2 (**A**) and KLCR1 (**B**) mapped against the amino acid sequence. Dark areas in 2D plots indicate a low expected position error, thus high model confidence (**C**) when comparing the predicted and true structures (i.e. model and template). Two compact domains were identified in CaM2 and multiple small motifs in KLCR1, consistent with the EF-hands of CaMs and the TPR motifs in KLCR1. pLDDT scores plotted against the amino acid sequence of CaM2 and KLCR1 indicate high model confidence in the EF-hands of CaM2 and the TPR motifs of KLCR1, but low confidence in the linker between the EF-hands and the termini of KLCR1. Models were assessed by Dr. Christian Tüting.

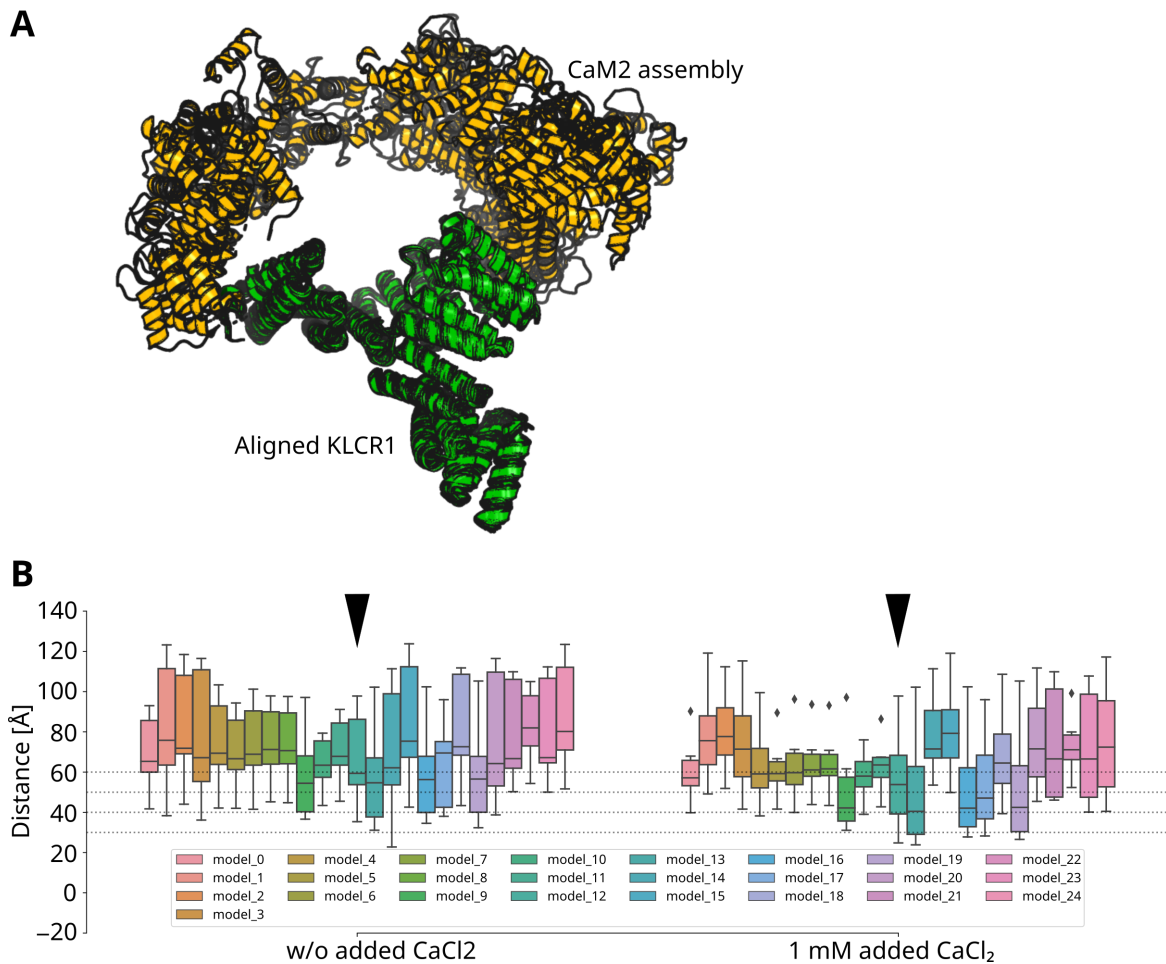


Figure A.21: AlphaFold multimer models of KLCR1-CaM2 complexes. **A:** Overlay of KLCR1-CaM2 complex models created by AlphaFold multimer, aligned to the position of KLCR1 (green). The CaM2 assembly (orange) shows a wide range of positions on the surface of KLCR1. **B:** $C\alpha_{avg}$ of AlphaFold multimer models generated of KLCR1-CaM2 complexes. Dashed lines indicate $C\alpha$ -distances of 30 Å, 40 Å, 50 Å, and 60 Å. Black arrowheads mark model 13 used for comparison to HADDOCK models. Models were generated and curated by Dr. Christian Tüting.

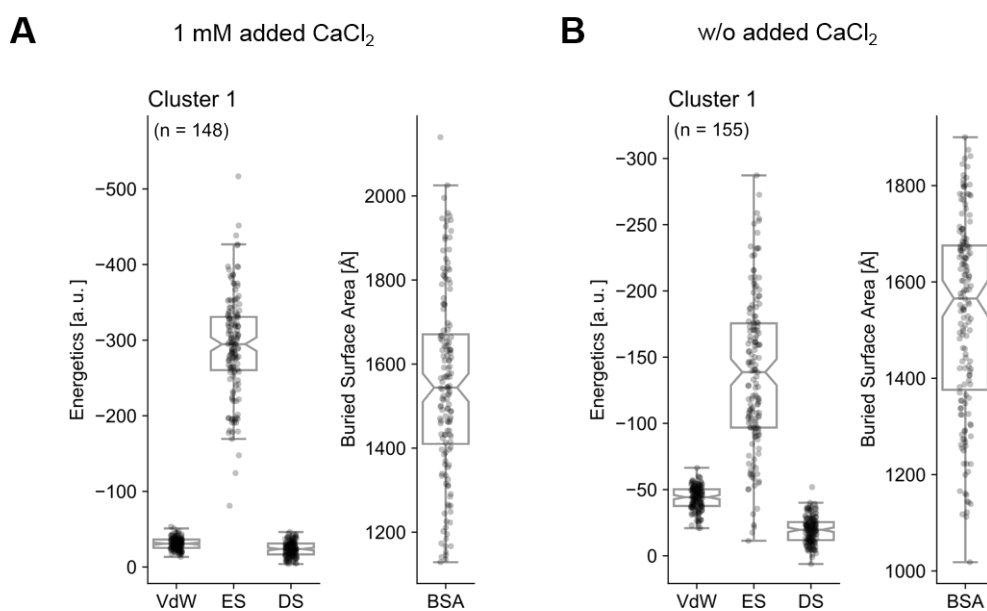


Figure A.22: Energy variations in HADDOCK MD simulations of KLRC1-CaM2 complexes. Energy variation of the main cluster in HADDOCK MD simulations of KLRC1-CaM2 complexes in the presence **(A)** or absence **(B)** of 1 mM added CaCl₂. VdW and DS energies show little variation, but ES energy and buried surface area (BSA) show variation between models. Models were assessed by Dr. Christian Tüting.

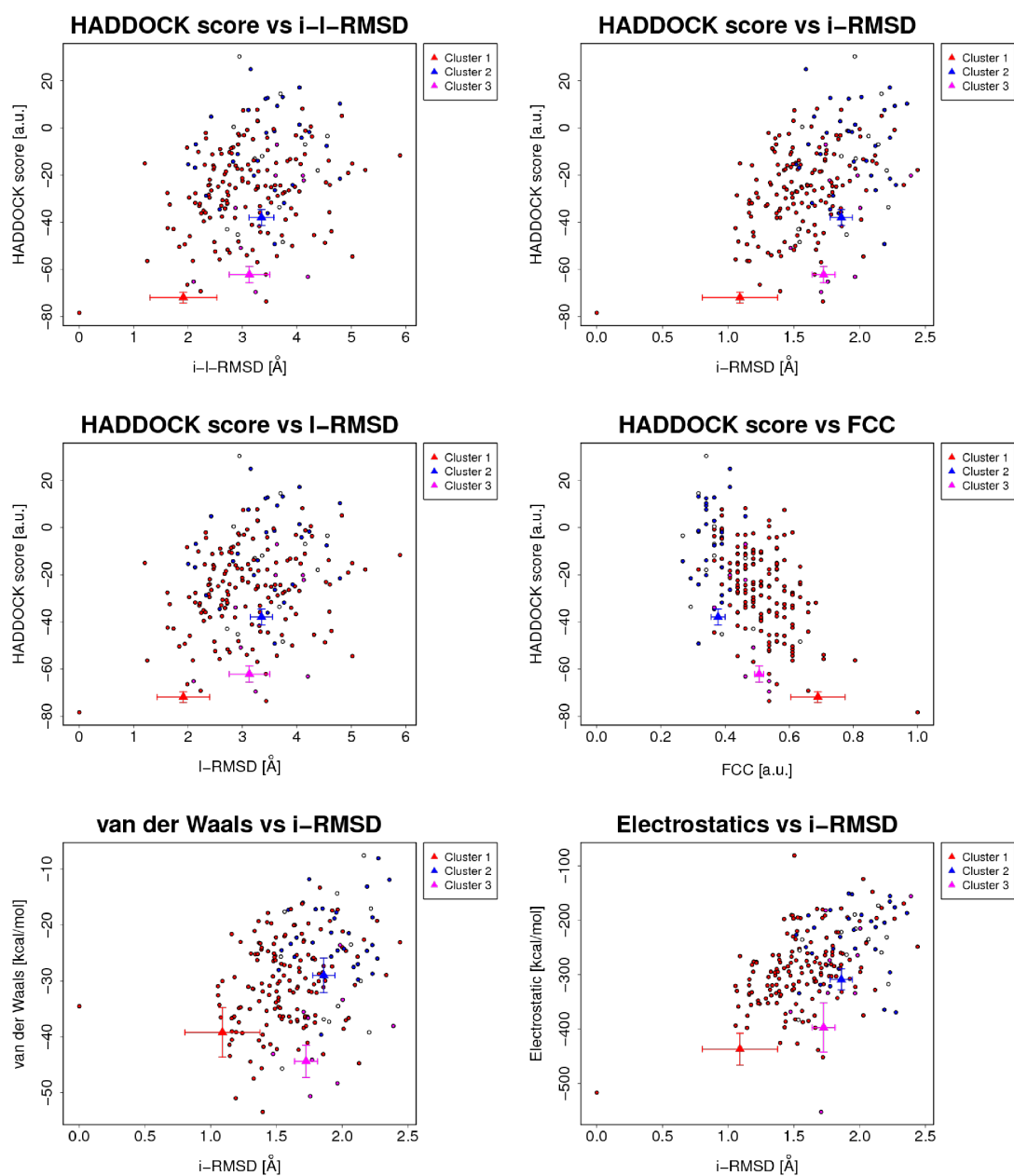


Figure A.23: HADDOCK scores of KLCR1-CaM2 models generated in the presence of 1 mM CaCl₂. 188 HADDOCK models generated with cross-links obtained in the presence of 1 mM CaCl₂ grouped into three clusters containing 148 (cluster 1), 31 (cluster 2), and 9 (cluster 3) models. Cluster averages and standard deviations of the four best models by HADDOCK score are shown as coloured symbols with error bars. i-RMSD: Interface RMSD, calculated on the backbone atoms of all residues involved in inter-molecular contacts with a 10 Å cutoff; I-RMSD: Ligand RMSD, calculated on the backbone atoms of all molecules after fitting on the backbone atoms of the first model; FCC: Fraction of Common Contacts, inter-molecular contacts defined based on best HADDOCK model using a 5 Å cutoff [339]; a.u.: Arbitrary Units.

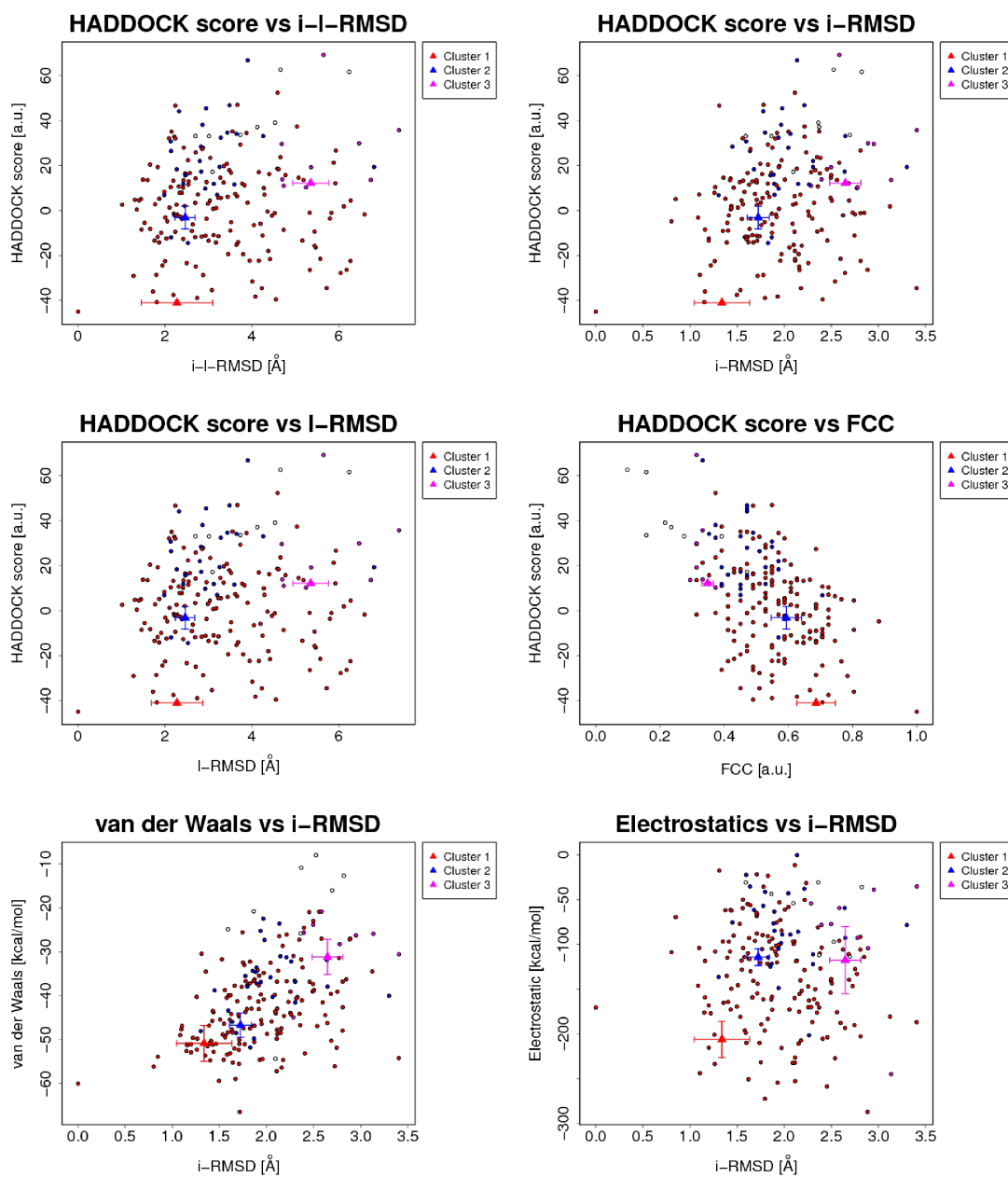


Figure A.24: HADDOCK scores of KLCR1-CaM2 models generated in the absence of added CaCl_2 . 188 HADDOCK models generated with cross-links obtained in the absence of added CaCl_2 grouped into three clusters containing 155 (cluster 1), 28 (cluster 2), and 9 (cluster 3) models. Cluster averages and standard deviations of the four best models by HADDOCK score are shown as coloured symbols with error bars. i-RMSD: Interface RMSD, calculated on the backbone atoms of all residues involved in inter-molecular contacts with a 10 Å cutoff; I-RMSD: Ligand RMSD, calculated on the backbone atoms of all molecules after fitting on the backbone atoms of the first model; FCC: Fraction of Common Contacts, inter-molecular contacts defined based on best HADDOCK model using a 5 Å cutoff [339]; a.u.: Arbitrary Units.

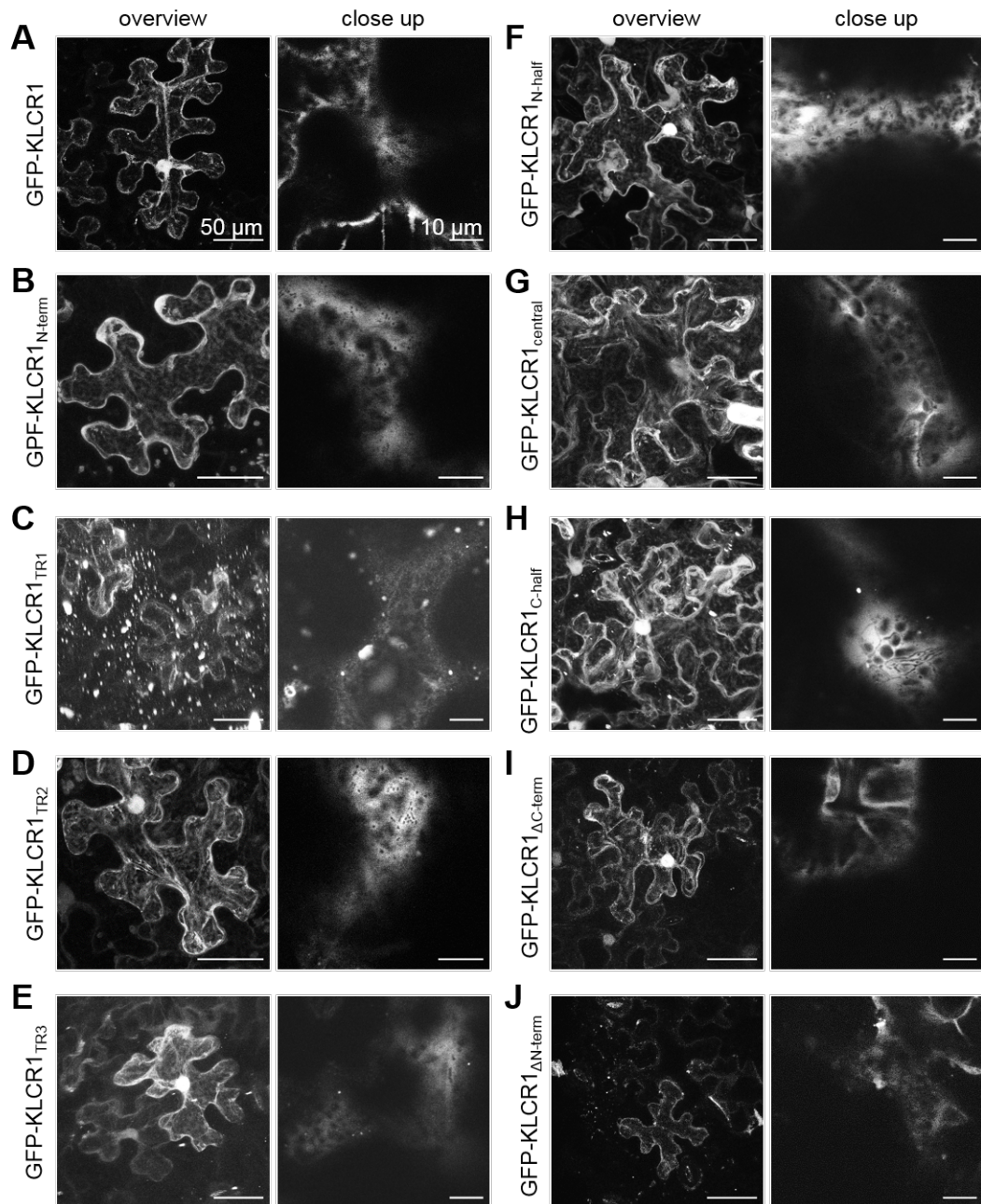


Figure A.25: Sub-cellular localisation of GFP-KLCR1 and its truncations. Sub-cellular localisation of GFP-KLCR1 (A) or its truncations according to Fig. 18 A (B to J) under the control of the constitutive 35S promoter. Scale bars in the overview images represent 50 μm , those in the close up images represent 10 μm .

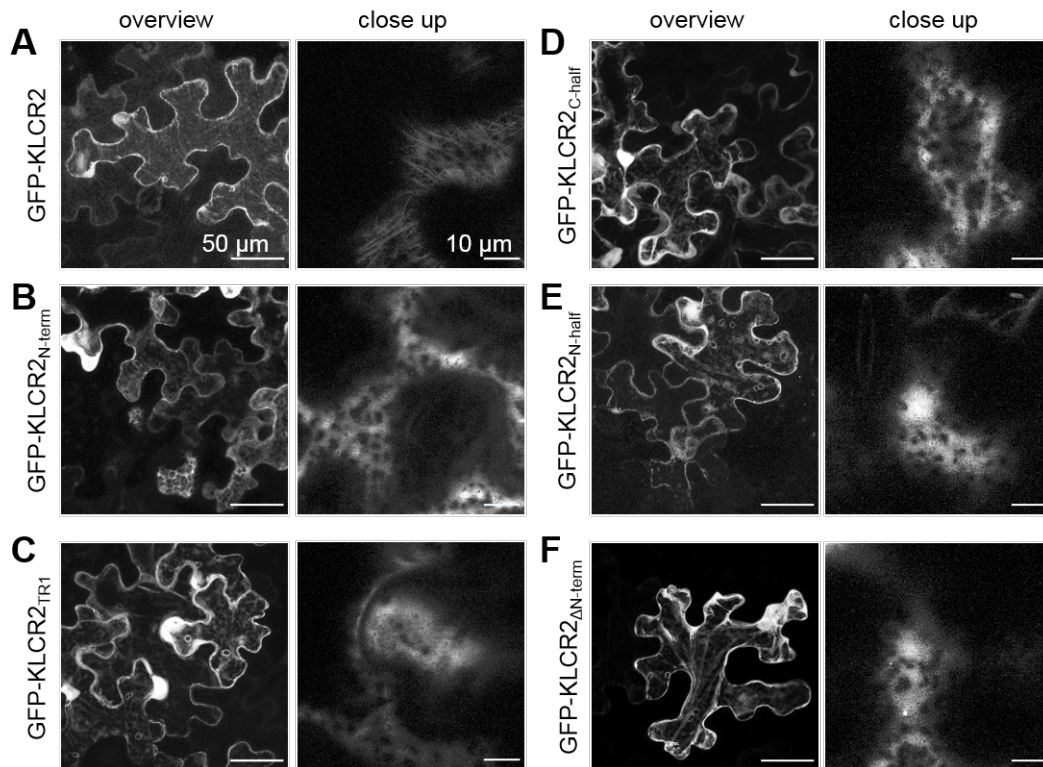


Figure A.26: Sub-cellular localisation of GFP-KLCR2 and its truncations. Sub-cellular localisation of GFP-KLCR1 (A) or its truncations according to Fig. 19 A (B to F) under the control of the constitutive Ub10 promoter. Scale bars in the overview images represent 50 μm , those in the close up images represent 10 μm .

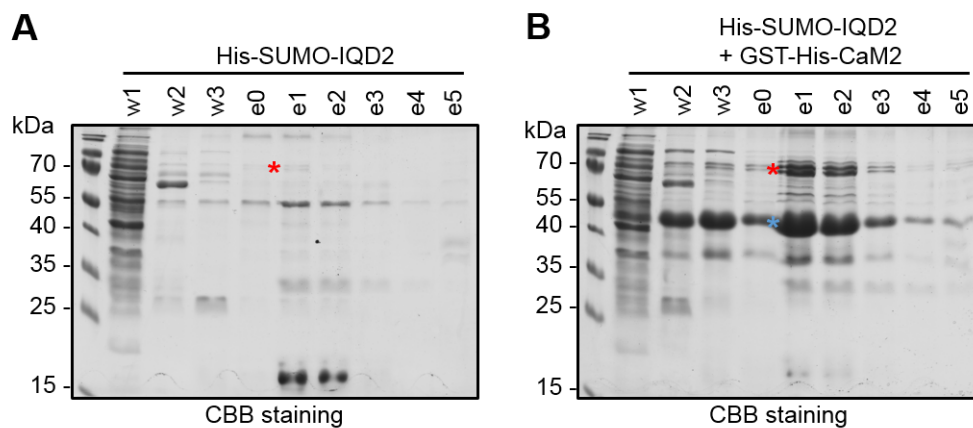


Figure A.27: Purification of His-SUMO-IQD2. 15 % SDS-PAGEs of wash (w1 to w3) and elution (e0 to e5) fractions of affinity purification of HS-IQD2 (A) or HS-IQD2 together with GH-CaM2 (B) via Ni-NTA agarose. Bands corresponding to HS-IQD2 are marked with red asterisks, those corresponding to GH-CaM2 with blue asterisks.

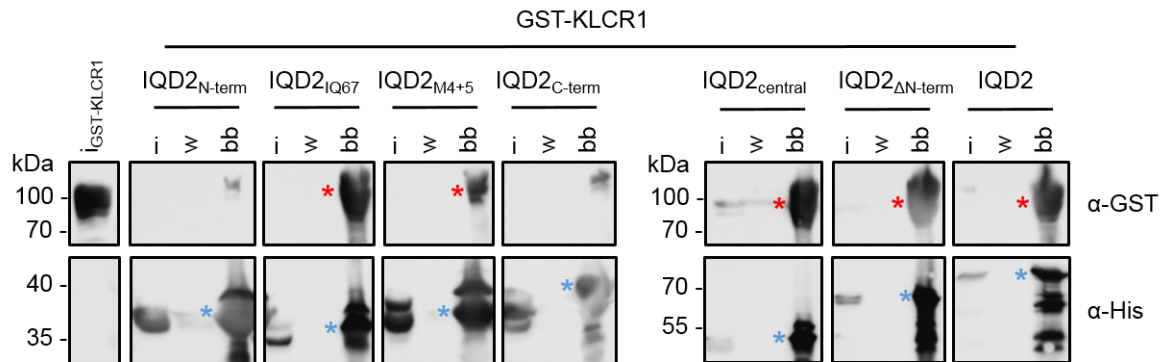


Figure A.28: His-pulldown of GST-KLCR1 with HS-IQD2 and its truncations under low salt conditions. Western blot of 12 % SDS-PAGE of His-pulldown of GST-KLCR1 with HS-IQD2 or its truncations according to Fig. 29 A carried out with 137 mM NaCl. Bait constructs are marked with blue asterisks, prey constructs with red asterisks. i: input, w: wash, bb: bead-bound.

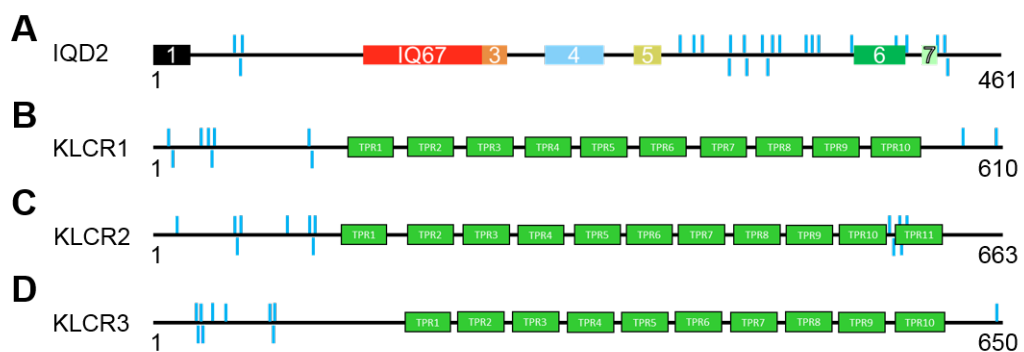


Figure A.29: Phospho-sites in IQD2 and the KLCRs annotated in the PhosPhAt database. Experimentally confirmed phospho-sites in IQD2 (A), KLCR1 (B), KLCR2 (C), and KLCR3 (D) annotated in the PhosPhAt database [271]. Phosphorylated amino acids are marked with blue lines. The AS positions of the first and last amino acid of each protein are labelled. Proteins are not scaled accurately relative to each other.

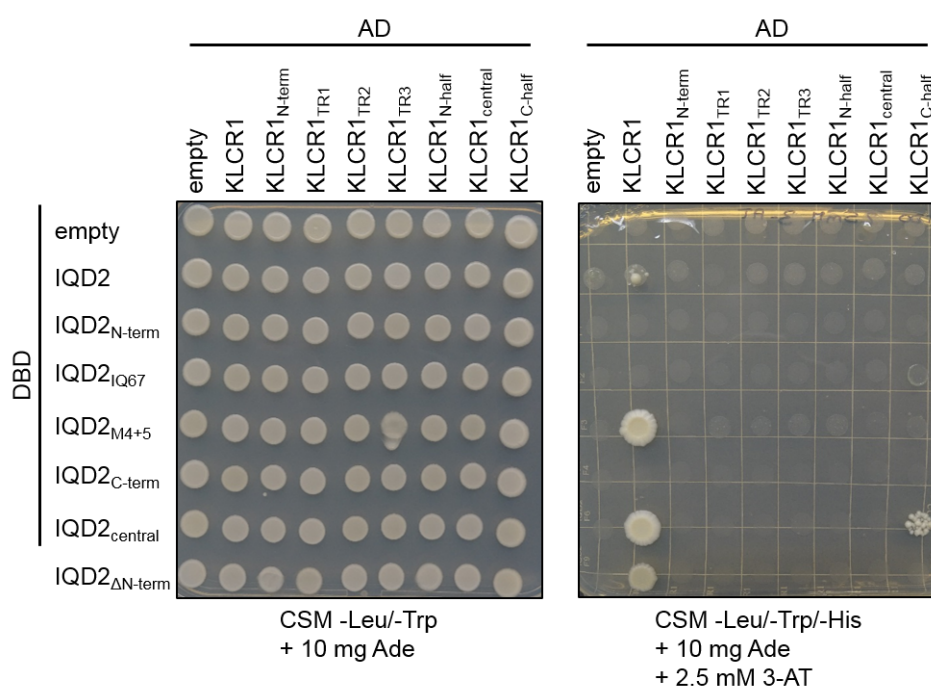


Figure A.30: Y2H experiment showing interaction of IQD2 truncations with KLCR1 truncations. DDO (left) and TDO + 2.5 mM 3-AT (right) plates with IQD2 and its truncations as DBD fusions and KLCR1 and its truncations as AD fusions.

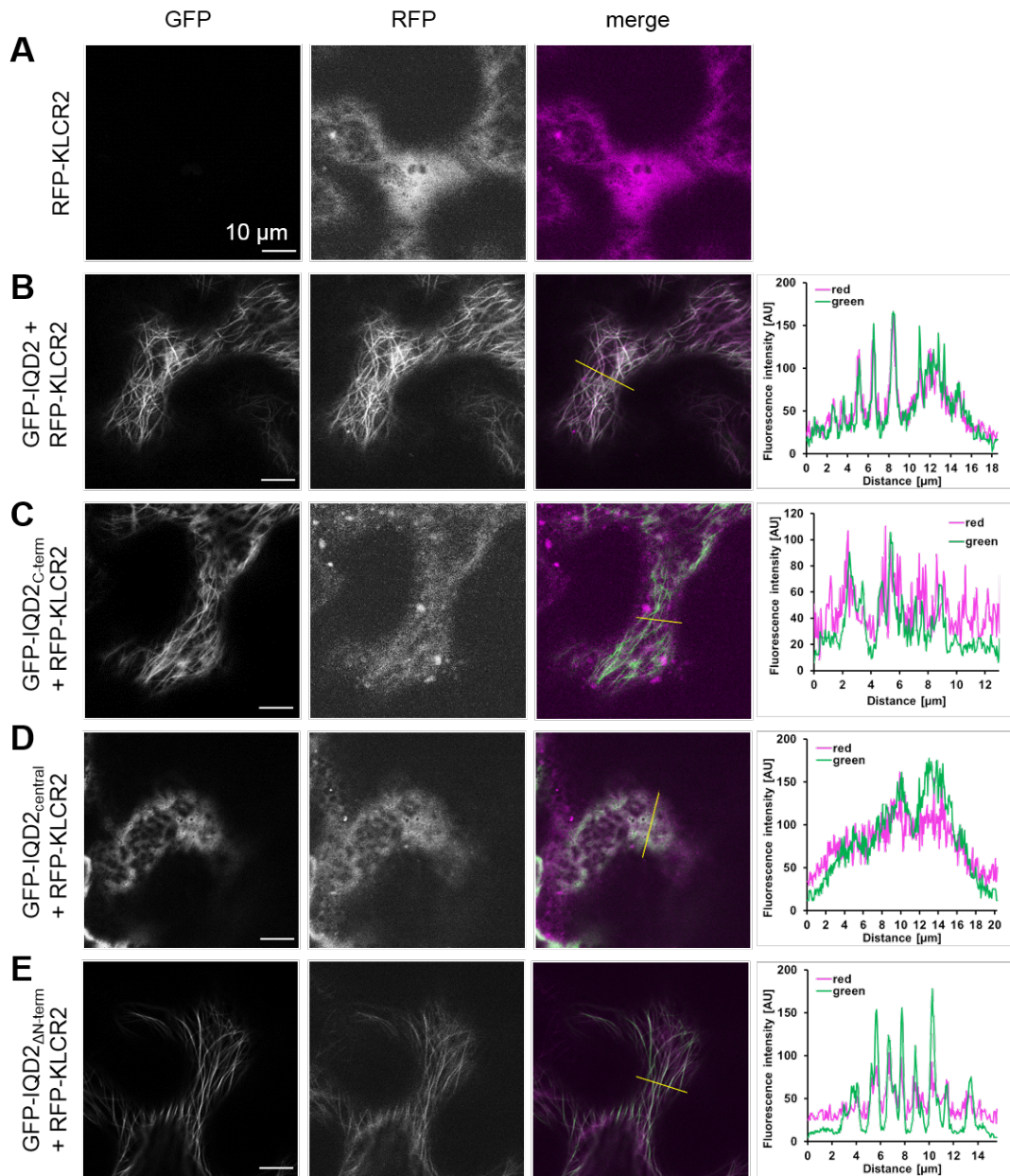


Figure A.31: Co-localisation of IQD2 and KLCR2 in *N. benthamiana* leaves. **A:** Sub-cellular localisation of RFP-KLCR2 under control of the 35S promoter. **B to E:** Co-expression of GFP-IQD2 and its truncations with RFP-KLCR2 under control of the 35S promoter. Scale bars represent 10 μm . Fluorescence profiles were generated along the yellow lines in the "merge" images.

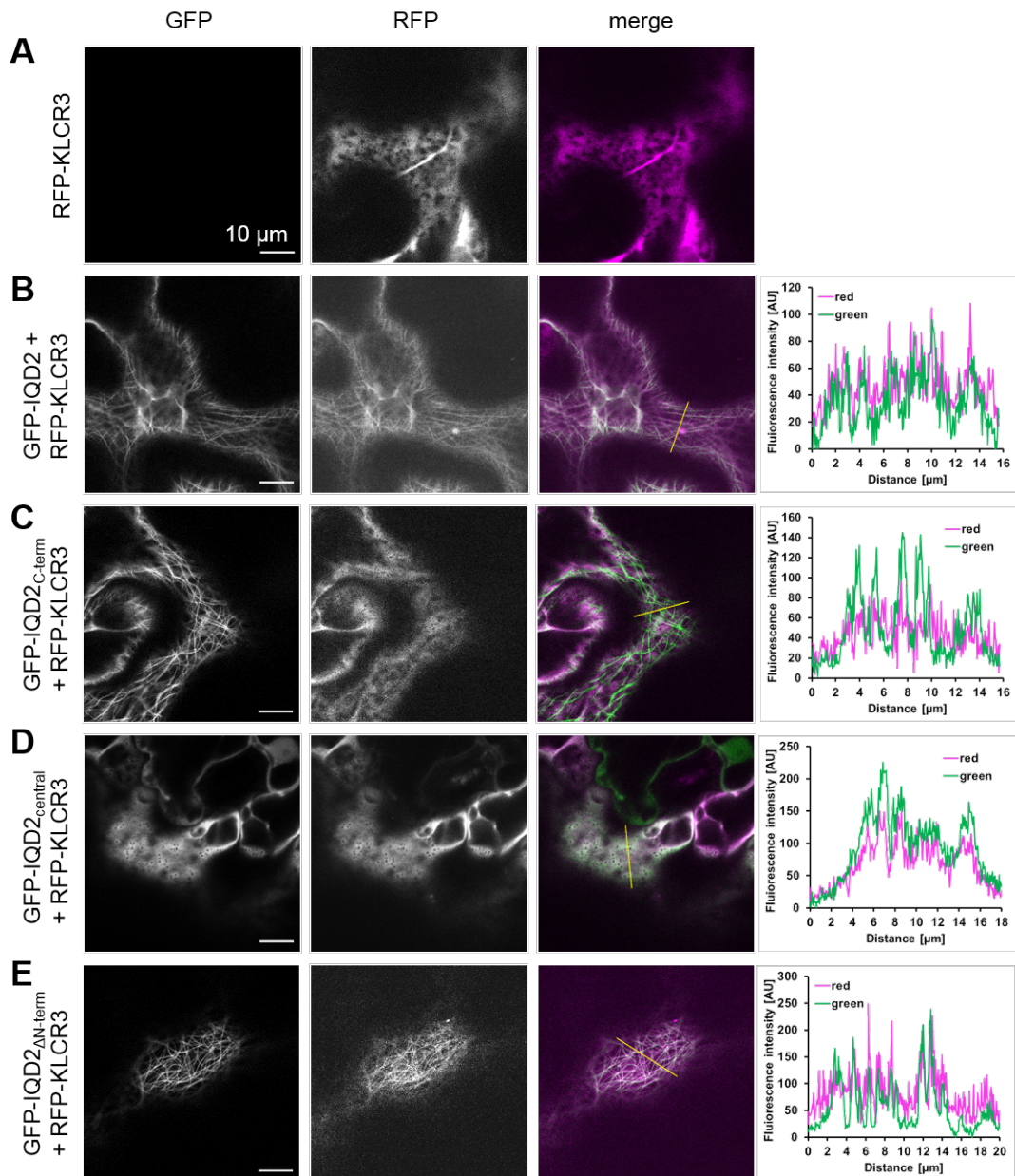


Figure A.32: Co-localisation of IQD2 and KLCR3 in *N. benthamiana* leaves. **A:** Sub-cellular localisation of RFP-KLCR3 under control of the 35S promoter. **B to E:** Co-expression of GFP-IQD2 and its truncations with RFP-KLCR3 under control of the 35S promoter. Scale bars represent 10 μm . Fluorescence profiles were generated along the yellow lines in the "merge" images.

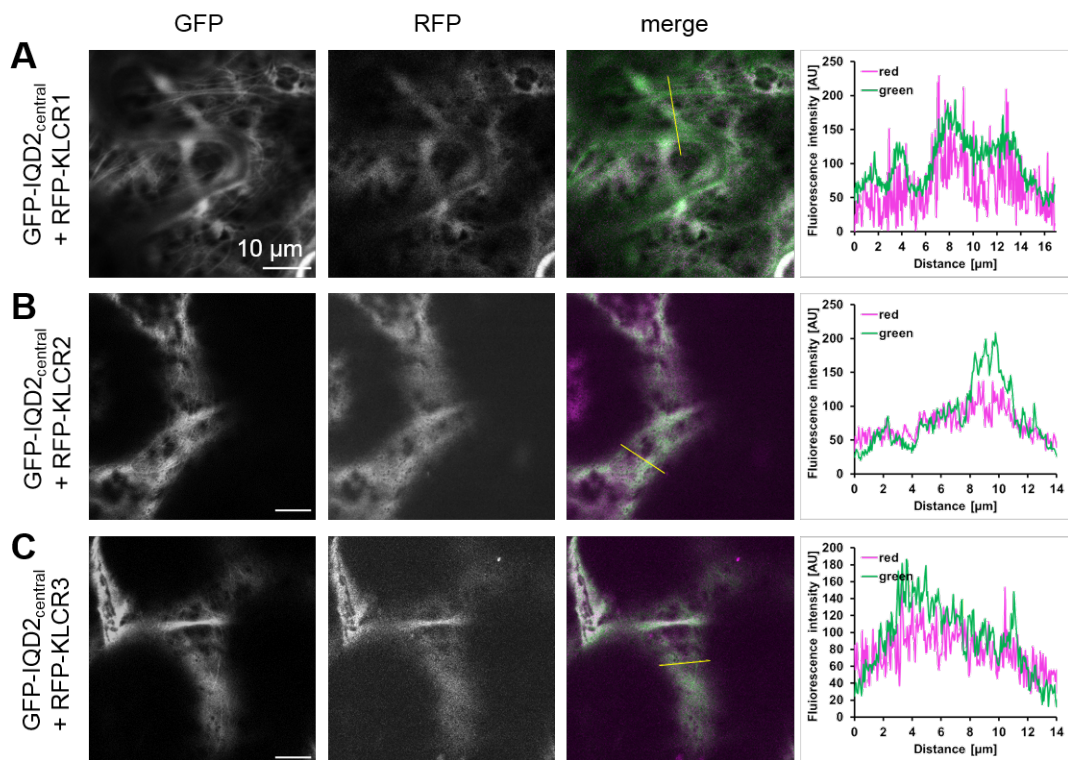


Figure A.33: Co-localisation of IQD2₉₈₋₃₂₇ and all KLCRs in *N. benthamiana* leaves. Co-expression of GFP-IQD2₉₈₋₃₂₇ with RFP-KLCR1 (**A**), RFP-KLCR2 (**B**), and RFP-KLCR3 (**C**) under control of the 35S promoter. Scale bars represent 10 μm . Fluorescence profiles were generated along the yellow lines in the "merge" images.

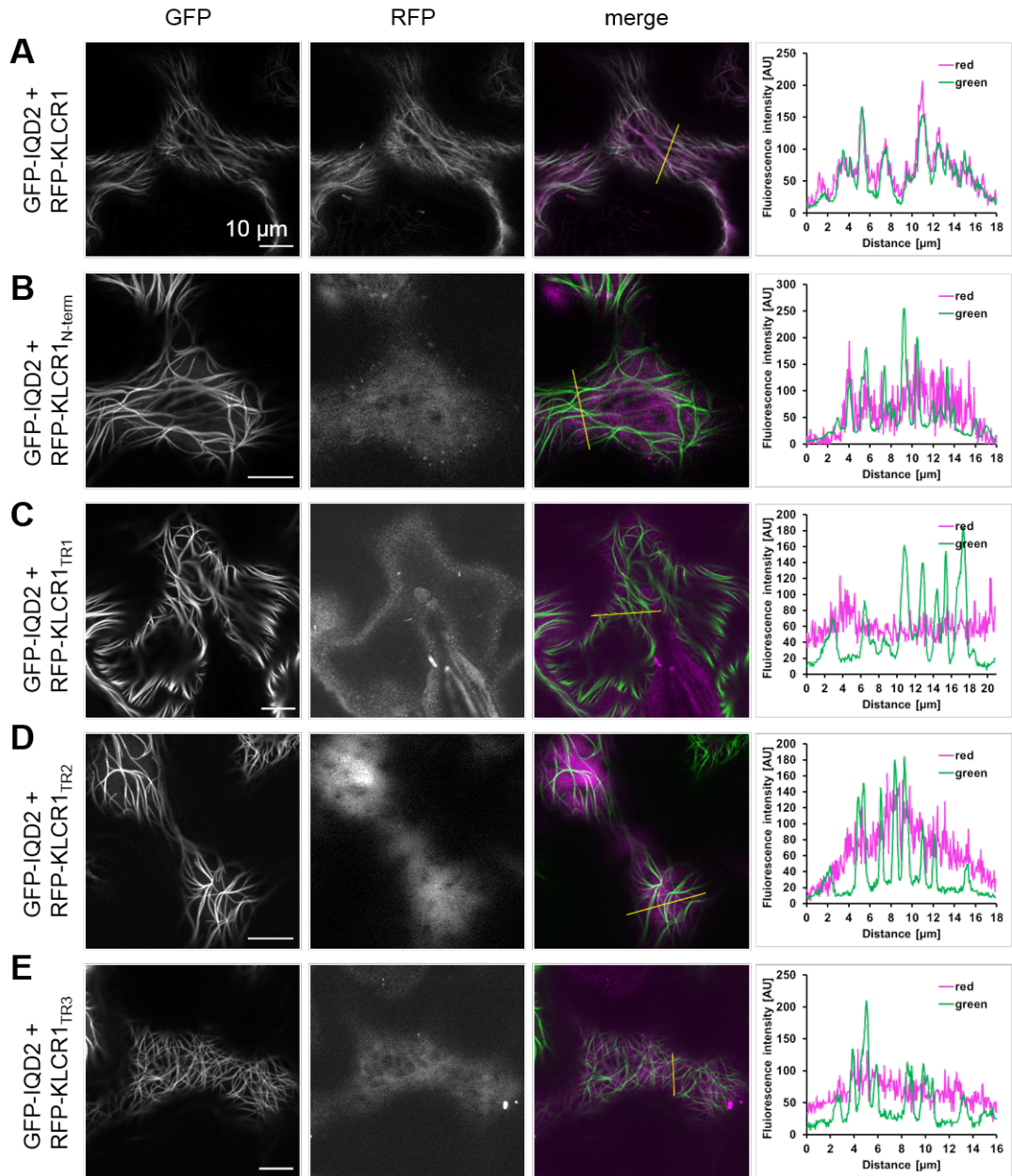


Figure A.34: Co-localisation of IQD2 and KLCR1 truncations in *N. benthamiana* leaves. A to E: Co-expression of GFP-IQD2 with RFP-KLCR1 and its truncations N-term to TR3 (Fig. 18 A) under control of the 35S promoter. Scale bars represent 10 μm . Fluorescence profiles were generated along the yellow lines in the "merge" images.

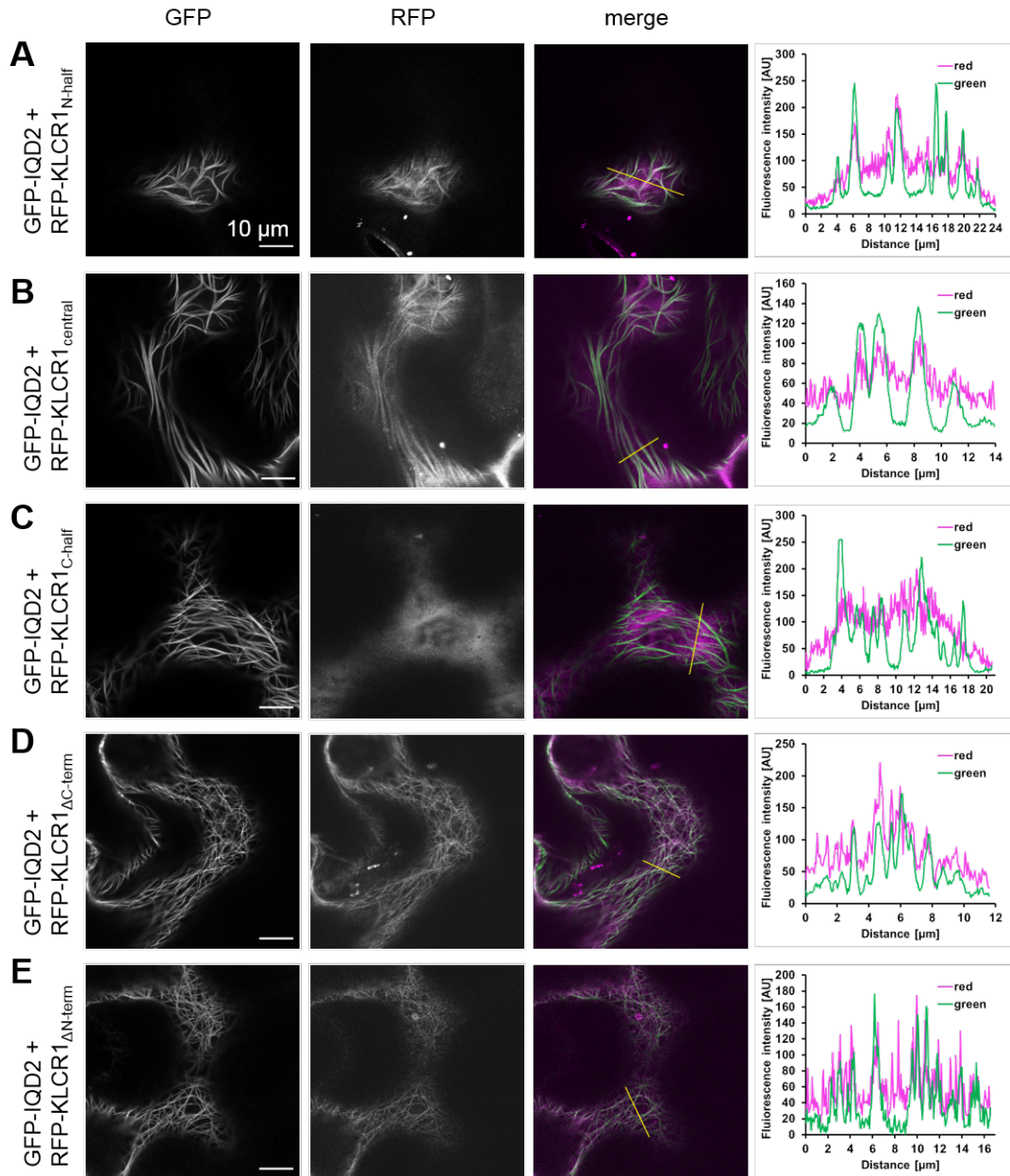


Figure A.35: Co-localisation of IQD2 and KLCR1 truncations in *N. benthamiana* leaves. A to E: Co-expression of GFP-IQD2 with RFP-KLCR1 truncations N-half to Δ N-term (Fig. 18 A) under control of the 35S promoter. Scale bars represent 10 μ m . Fluorescence profiles were generated along the yellow lines in the "merge" images.

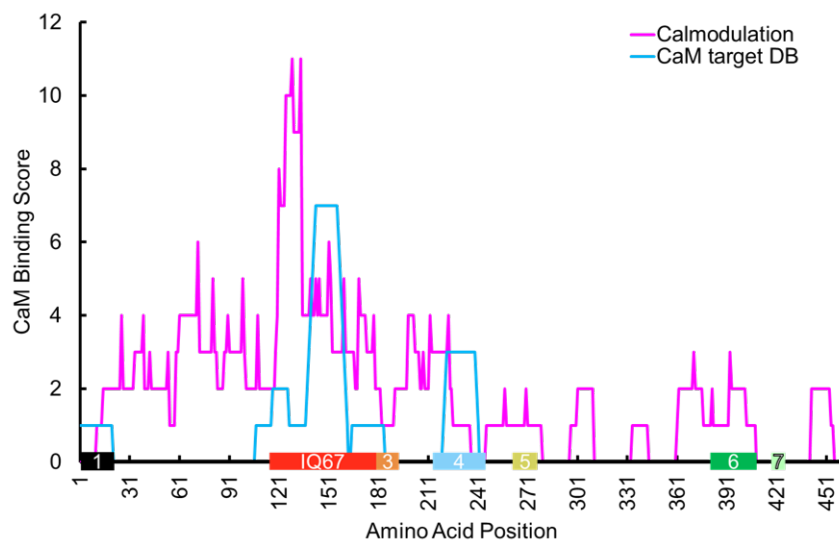


Figure A.36: CaM-binding score of IQD2. CaM-binding scores from the Calmodulation database (magenta) or the CaM-target database (blue) plotted against the amino acids sequence of IQD2 superimposed with the protein schematic.

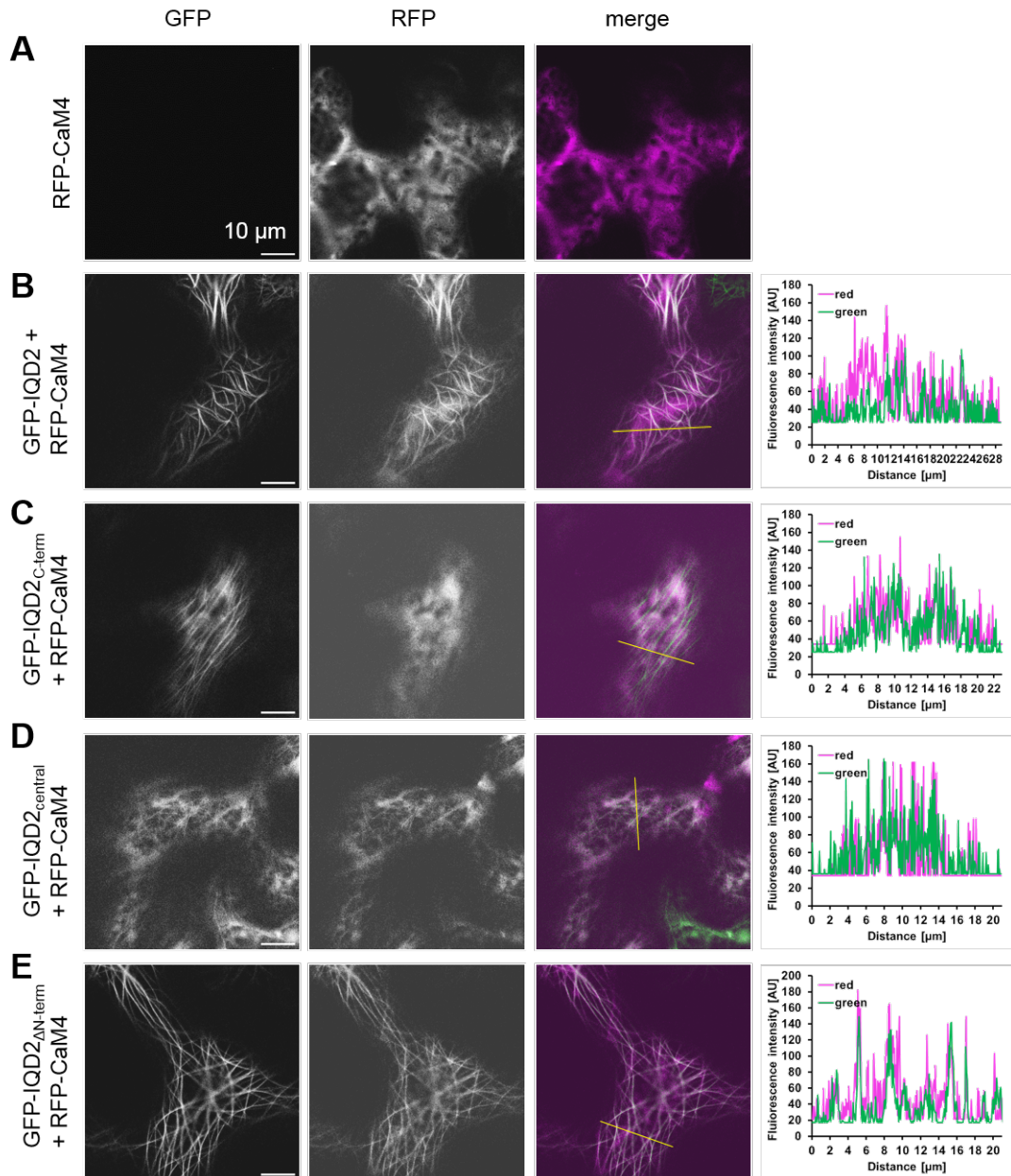


Figure A.37: Co-localisation of IQD2 and CaM4 in *N. benthamiana* leaves. **A:** Sub-cellular localisation of RFP-CaM4 under control of the 35S promoter. **B to E:** Co-expression of GFP-IQD2 and its truncations with RFP-CaM4 under control of the 35S promoter. Scale bars represent 10 μm . Fluorescence profiles were generated along the yellow lines in the "merge" images.

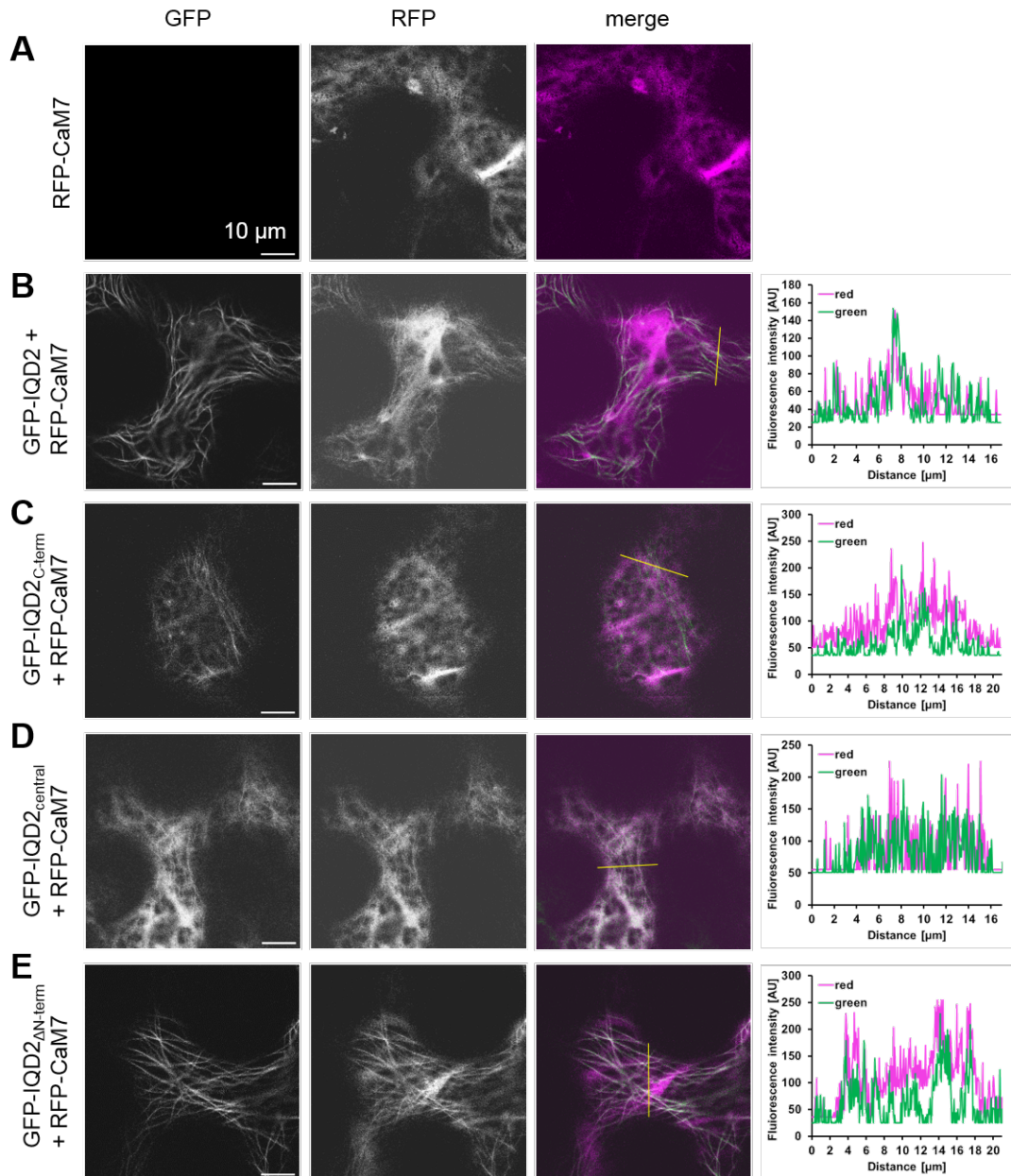


Figure A.38: Co-localisation of IQD2 and CaM7 in *N. benthamiana* leaves. **A:** Sub-cellular localisation of RFP-CaM7 under control of the 35S promoter. **B to E:** Co-expression of GFP-IQD2 and its truncations with RFP-CaM7 under control of the 35S promoter. Scale bars represent 10 μm . Fluorescence profiles were generated along the yellow lines in the "merge" images.

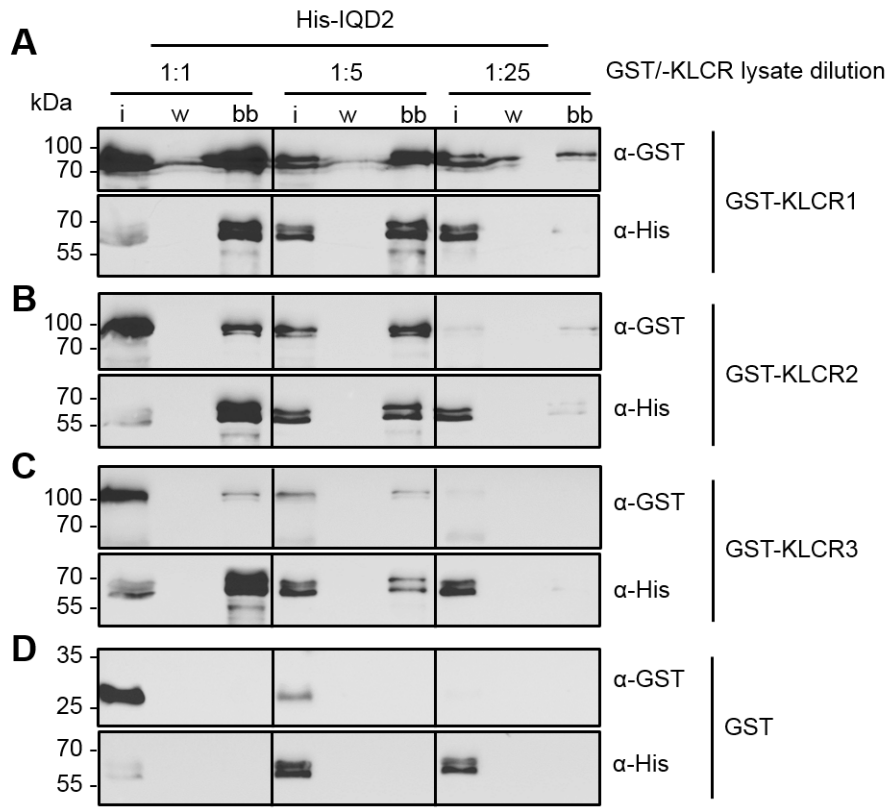


Figure A.39: Concentration dependency of the co-interaction of IQD2 with KLCRs and CaM. Western blot of a CaM-pulldown of His-IQD2 together with GST-KLCR1 (A), GST-KLCR2 (B), GST-KLCR3 (C), or GST alone (D) in the absence of Ca^{2+} with the bacterial lysate containing the the GST-tagged proteins either undiluted or diluted 1:5 or 1:25. i: input, w: wash, bb: bead-bound.

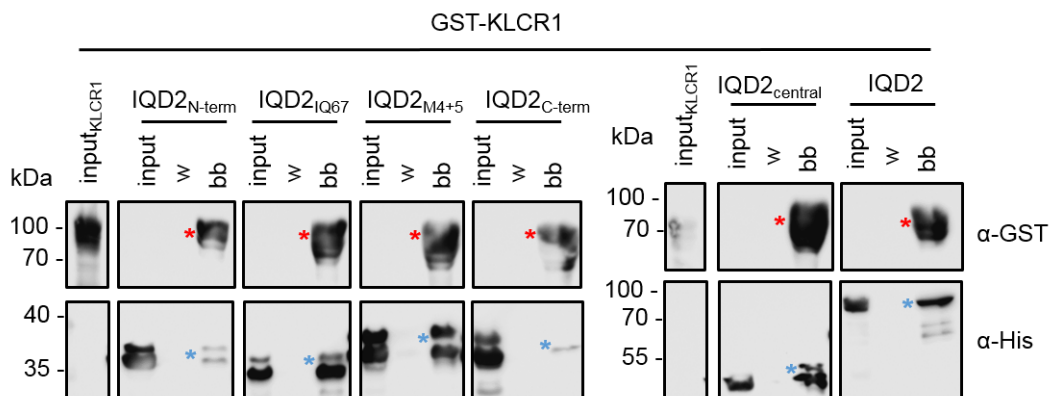


Figure A.40: Fine-mapping of IQD2-KLCR1-CaM interactions. Western blot of 12 % SDS-PAGEs of HS-IQD2 and its truncations (Fig. 29 A) together with GST-KLCR1 in the absence of Ca^{2+} under low salt conditions (137 mM NaCl). HS-IQD2 and truncations are marked with blue asterisks, GST-KLCR1 is marked with red asterisks. i: input, w: wash, bb: bead-bound.

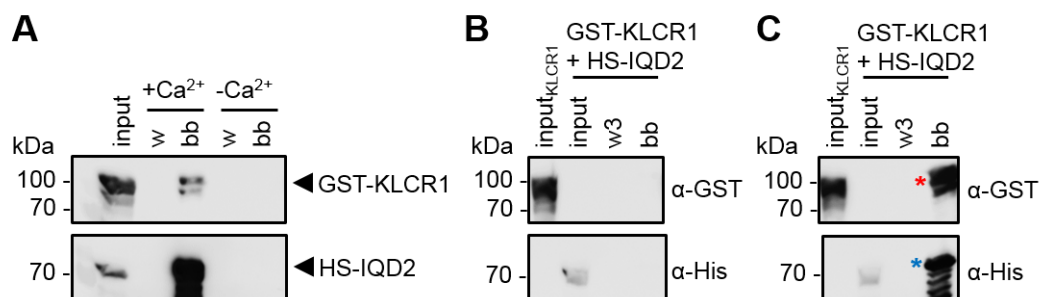


Figure A.41: Pulldowns with IQD2 and KLCR1 in the presence of 1 M NaCl. **A:** CaM-pulldowns of HS-IQD2 or GST-KLCR1 with CaM-agarose in the presence of 1 mM CaCl₂ (+ Ca²⁺) or 5 mM EGTA (– Ca²⁺). **B:** Co-CaM-pulldown of HS-IQD2 and GST-KLCR1 in the presence of 5 mM EGTA. **C:** His-pulldown of GST-KLCR1 with HS-IQD2. HS-IQD2 is marked with a blue asterisks, GST-KLCR1 is marked with a red asterisk. i: input, w: wash, bb: bead-bound.

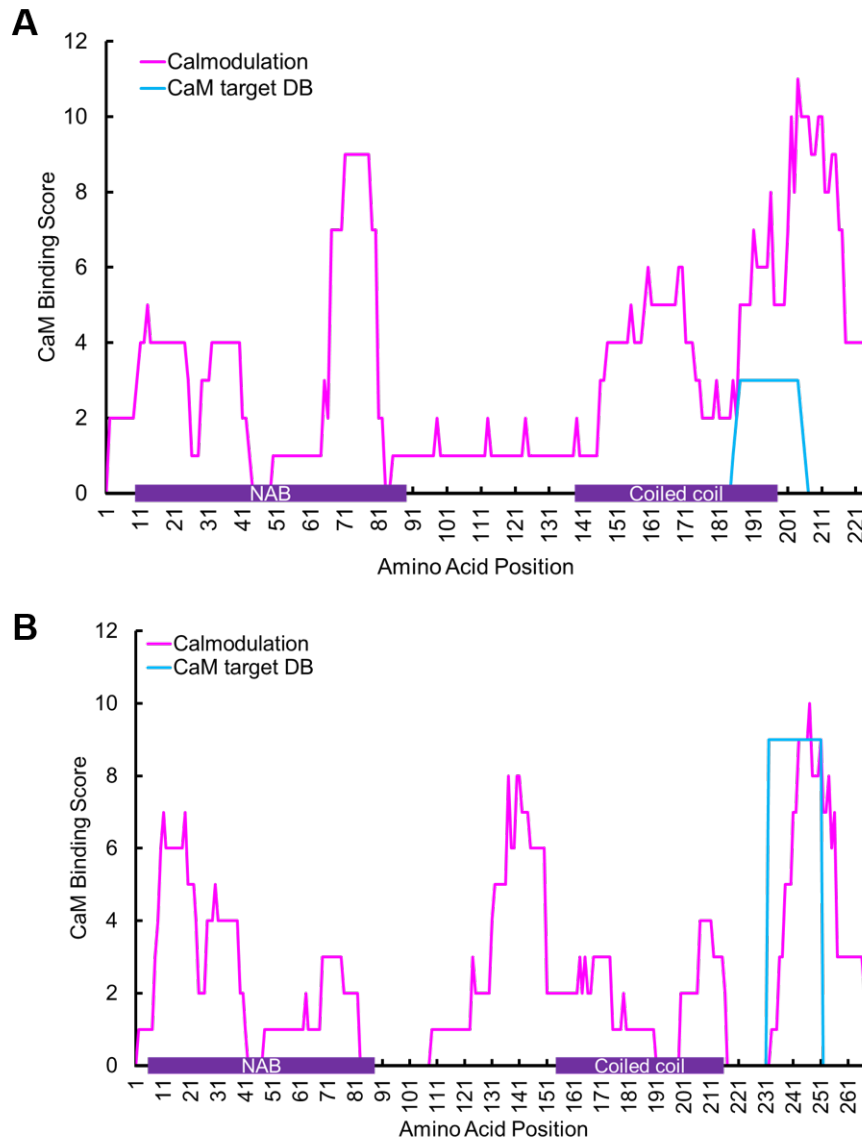


Figure A.42: CaM-binding score of NET3A and NET3C. CaM-binding scores from the Calmodulation database (magenta) or the CaM-target database (blue) plotted against the amino acids sequence of NET3C (**A**) and NET3A (**B**) superimposed with the protein schematic.

B Publications

M. Kölling, P. Kumari, and K. Bürstenbinder, "Calcium-and calmodulin-regulated micro-tubule associated proteins as signal-integration hubs at the plasma membrane–cytoskeleton nexus", *Journal of Experimental Botany*, vol. 70, no. 2, pp. 387–396, 2019.

Contribution: Literature research and writing.

P. Kumari, P. Dahiya, P. Livanos, L. Zergiebel, **M. Kölling**, Y. Poeschl, G. Stamm, A. Hermann, S. Abel, S. Müller, and K. Bürstenbinder, "IQ67 DOMAIN proteins facilitate pre-prophase band formation and division-plane orientation", *Nature Plants*, vol. 7, no. 6, 2021.

Contribution: GST-pulldowns of His-POK1/-POK2 and His-PHGAP1/-PHGAP2 with GST-IQD8_{159–414} and negative control GST; analysis by denaturing PAGE and western blotting; included in **Fig. 3 i and j**.

C Curriculum vitae

Name: Malte Kölling

Geb.: 07.07.1993, Itzehoe

Mai 2018 – heute	Doktorand am Leibniz Institut für Pflanzenbiochemie Abteilung "Molekular Signalverarbeitung" Forschungsgruppe "Zelluläre Koordination"
Okt. 2015 – Apr. 2018	Masterstudium "Biochemie" an der Martin-Luther-Universität Halle-Wittenberg
Okt. 2012 – Sep. 2015	Bachelorstudium "Biochemie" an der Georg-August-Universität Göttingen
2003 – 2011	Abitur am Sophie-Scholl-Gymnasium Itzehoe